DEVELOPMENT OF THE INNOVATIVE POSITRON EMISSION TOMOGRAPHY FOR BEAM RANGE MONITORING IN PROTON RADIOTHERAPY

JAKUB BARAN

SUPERVISORS:
PROF. PAWEŁ OLKO (IFJ PAN)
PROF. ANDRZEJ URBANIK (UJ CM)

CO-SUPERVISOR:
ANTONI RUCIŃSKI, PH.D. (IFJ PAN)

The Henryk Niewodniczański Institute of Nuclear Physics Polish Academy of Science
Department of Radiation Research and Proton Radiotherapy

Kraków, 2021

THIS WORK WAS PREPARED UNDER THE FRAMEWORK OF THE INTERDOKMED PROJECT NO. POWR.03.02.00-00-I013/16

THIS WORK WAS PARTIALLY FUNDED BY THE NATIONAL CENTRE FOR RESEARCH AND DEVELOPMENT (NCBIR), GRANT NO. LIDER/26/0157/L-8/16/NCBR/2017

Bądź zimny albo gorący,
nigdy letni.

— ks. Piotr Pawlukiewicz

ACKNOWLEDGEMENTS

First of all, I would like to thank Prof. Paweł Olko, Dr. Antoni Ruciński and prof. Andrzej Urbanik without whose supervision this thesis would not exist. I would like to express my greatest gratitude to Paweł who was always able to find the solution to every problem I had during my PhD journey. I would like to thank Antoni for an opportunity to work on his project and his expertise.

I would also like to extend my appreciation to Prof. Janusz Swakoń for constructive comments and fruitful discussions, Dr. Leszek Grzanka for his patience and help in understanding the intricacies of the Monte Carlo simulations and allowing me to use his time on the Prometheus cluster when I needed it the most, Dr. Jan Gajewski for helping with the beam model used in this work and for helping to understand the data formats used in radiotherapy.

Additionally, I want to give thanks to all members of the J-PET collaboration and its boss - prof. Paweł Moskal for their continuous willingness to help and chance to take part in Thursday's group meetings. I would like to thank especially prof. Paweł Moskal for his kindness and valuable discussions, Szymon Niedźwiecki and Monika Pawlik-Niedźwiecka for explaining me all aspects of the J-PET project I need and even more, their attitude and kindness, Wojciech Krzemień for help with the image reconstruction and preparation for the conference talk, Mateusz Bała, Paweł Kowalski and Nikodem Krawczyk for fruitful discussions about the practical aspects of the Monte Carlo simulations.

Special thanks to my friends and colleagues from CCB: Dawid Krzempek, Katarzyna Krzempek, Marzena Rydygier, Wiktor Komenda, Hubert Jabłoński, Natalia Mojżeszek, Marta Bałamut, Bartłomiej Sadowski and others for your kindness and good atmosphere during official and unofficial meetings and during our football games. I would like to thank especially Dawid, Kasia, Marzena and Wiktor for your expertise in clinical practice which you are always willing to share with me.

I also thank all the people I met during my internship at Sapienza University in Rome: prof. Alessio Sarti, prof. Vincenzo Patera, prof. Angelo

Schiavi, Giacomo, Michela, Marta, Micol, Eliana, Ricardo, Matteo and Alessandro. Special thanks to prof. Alessio Sarti and prof. Vinzenzo Patera for organizing my visit there. I would also like to express my deepest gratitude to Elena Romani and Luciano Flori who allowed me to spend this time in their apartment in Ostia, for your care and valuable discussions about life, politics and religion. I really appreciate it. I also thank Alicja and Sergio for your kindness and help during my stay in Rome.

A lot of thanks to my colleagues from the lab: Magdalena, Monika, Agata, Agnieszka, Kinga, Agata, David and Kasia. We fought this battle together and I will never forget about it.

I would like to thank Ola for her kind help in improving the English in the thesis.

Chciałbym serdecznie podziękować moim Rodzicom za cały ich trud wychowania i zaszczepienie we mnie pasji do nauk ścisłych od najmłodszych lat.

Last but not least I would like to express my greatest thanks to my best friend and wife Patrycja for being my support for all these years, for your faith in me and your willingness to keep pushing us to make our dreams come true, and to my beloved daughters: Ania for her lovely smile which makes my day everyday and Ola, for being the most important motivation to finish the PhD. I love you very much.

ABSTRACT

Proton therapy is a radiation therapy technique where the proton beams accelerated to between 60 MeV and 250 MeV are applied. It enables excellent dose conformity leading to reduction of the dose in the Organs at Risk (OAR), increasing the dose to target volume and reducing late side effects. The high dose conformity achievable thanks to the steep distal dose fall-off at the end of the Bragg peak is, however, a source of uncertainty of proton range in a patient. This may lead to underexposure of the target or overexposure of an OAR. This disadvantage may be overcome by applying range monitoring, which is currently still not available in the clinical routine. In one of the proposed methods, β^+radioisotopes originating from proton interactions with tissue could be detected with a Positron Emission Tomography (PET) and used to monitor the range of the proton beam. The aim of the work was to investigate the feasibility of the Jagiellonian Positron Emission Tomography (J-PET) system based on the plastic scintillators for range monitoring of therapeutic scanning proton beams.

The workflow consisting of the Monte Carlo transport calculations with GATE and PET data reconstruction with CASToR software was proposed. Six geometrical configurations of PET scanners based on 24, 48 and 72 J-PET modules arranged in the barrel and dual-head setup configurations were investigated. The efficiency factor η was derived to determine the efficiency of each specific setup. The range detection uncertainty and the optimisation of the PET image reconstruction parameters was based on the Maximum Likelihood Expectation-Maximization (MLEM) iterations and dedicated smoothing filters.

The reconstruction methodology was validated for a water phantom with uniformly distributed activity. Monte Carlo studies of PET detected activity range in PMMA phantom revealed that the accuracy for a range assessment of the single proton beam was at the level of 0.82 - 1.25 mm. The double layer dual-head configuration was found a compromise of the image quality, range estimation precision and the ability to integrate the detector in the treatment room. The modelling of PET signal detected by the J-PET system for a patient treated at the Cyclotron Centre Bronowice (CCB) proton therapy centre demonstrated that it is possible to reconstruct the activity distribution maps produced in patients. The Pearson Correlation Coefficient (PCC) was used as a metric to determine the optimal smoothing approach for PET images. It was shown that opti-

mal filtering of the activity maps can be performed using the Gaussian filtering with a 1x1x1 kernel size.

The results demonstrate the feasibility of the J-PET technology for the in-room range monitoring for proton radiotherapy. The proposed system with larger FOV, lighter, with minimized electronic read-out and lower price makes the J-PET technology cost-effective and promising system for proton beam range monitoring in hadrontherapy.

STRESZCZENIE

Radioterapia protonowa jest jedną z metod radioterapii, w której stosuje się wiązki protonów przyspieszonych do energii od 60 MeV do 250 MeV. Radioterapia protonowa pozwala uzyskać bardzo dobry rozkład przestrzenny dawki, a w konsekwencji zredukować dawki do organów krytycznych, zwiększyć w razie potrzeby dawki w targecie i zmniejszyć późne efekty uboczne leczenia. Jedną z największych wad radioterapii protonowej jest niepewność zasięgu protonów w czasie napromieniania pacjenta. Niepewności te mogą prowadzić do znaczącego obniżenia dawki w objętości tarczowej lub jej zawyżenia dla organów krytycznych. W literaturze znanych jest kilka metod mających na celu zredukowanie tego efektu poprzez monitorowanie faktycznego zasięgu wiązki protonowej podczas radioterapii. Jedna z metod wykorzystuje β^+promieniotwórcze radioizotopy, powstające w wyniku oddziaływania protonów z tkanką, których rozpad może być zmierzony przy użyciu skanera pozytonowej tomografii emisyjnej (PET). Celem pracy było zbadanie możliwości wykorzystania systemu PET rozwijanego na Uniwersytecie Jagiellońskim, wykorzystującego nowatorskie detektory zbudowane w oparciu o scyntylatory plastikowe do monitorowania zasięgu terapeutycznej wiązki protonowej.

W ramach pracy przygotowano sześć konfiguracji skanera PET na bazie 24, 48 oraz 72 modułów J-PET w formie skanerów cylindrycznych oraz dwugłowicowych. Opracowano metodę badań uwzględniającą obliczenia Monte Carlo z użyciem oprogramowania GATE oraz rekonstrukcję danych PET z użyciem oprogramowania CASToR. Dla każdej konfiguracji geometrycznej skanera wyznaczono współczynnik wydajności η. Ostatnia część pracy polegała na oszacowaniu niepewności wyznaczenia zasięgu oraz optymalizacji parametrów rekonstrukcji: liczby iteracji algorytmu Maximum Likelihood Estimation-Maximization (MLEM) oraz filtru wygładzania.

Metodologia rekonstrukcji danych PET została zwalidowana z użyciem fantomu wodnego wypełnionego jednorodną aktywnością radioizotopu β^+. Symulacje Monte Carlo wariancji zasięgu aktywności PET w fantomie PMMA pokazały dokładność oceny zasięgu pojedynczej ołówkowej wiązki protonowej na poziomie 0.82-1.25 mm. Stwierdzono, że kompromisem pomiędzy jakością obrazu PET, dokładnością oszacowania zasięgu oraz technologiczną możliwością zintegrowania skanera w pokoju leczenia jest dwuwarstwowy układ dwugłowicowy.

Przeprowadzone symulacje oraz rekonstrukcja danych PET z użyciem zanonimizowanych danych pacjenta leczonego w Centrum Cyklotronowym Bronowice, pokazały możliwość rekonstrukcji mapy aktywności PET w sytuacji klinicznej. W celu znalezienia optymalnego filtru wygładzania tej mapy obliczono współczynnik korelacji Pearson'a pomiędzy zrekonstruowaną a symulowaną mapą aktywności. Analiza wykazała, że optymalnym filtrem jest filtr Gaussowski z jądrem 1x1x1.

Technologia J-PET jest technologią tańszą, lżejszą, wykazującą się większym polem widzenia oraz z mniejszą ilością elektroniki, w porównaniu do standardowych systemów PET, co czyni ją obiecującą techniką do zastosowania do pomiaru zasięgu w hadronoterapii.

CONTENTS

ACRONYMS

BEV Beam's Eye-View

CASToR Customizable and Advanced Software for Tomographic Reconstruction

CCB Cyclotron Centre Bronowice

CNAO Centro Nazionale di Adroterapia Oncologica

CSDA Continuous Slowing Down Approximation

CT Computed Tomography

DICOM Digital Imaging and COmmunications in Medicine

FBP Filtered Back Projection

FOV Field Of View

FPGA Field Programmable Gate Array

FWHM Full Width at Half Maximum

GATE Geant4 Application for Emission Tomography

GSI Gesellschaft fuer Schwerionenforschung

HIT Heidelberg Ion-Beam Therapy Centre

HU Hounsfield Unit

IARC International Agency for Research on Cancer

INFN Instituto Nazionale di Fisica Nucleare

INSIDE Innovative Solutions for In-beam DosimEtry in hadrontherapy

J-PET Jagiellonian Positron Emission Tomography

LOR Line of Response

MGH Massachusetts General Hospital

MLEM Maximum Likelihood Expectation-Maximization

MONDO MOnitor for Neutron Dose in hadrOntherapy

NRMSD Normalized Root Mean Square Deviation

OAR Organs at Risk

OSEM Ordered Subset Expectation-Maximization

OV Overall View

PCC Pearson Correlation Coefficient

pCT proton Computed Tomography

PBS Pencil Beam Scanning

PBT Proton Beam Therapy

PET Positron Emission Tomography

PGPI Prompt Gamma Peak Integral

PGS Prompt Gamma Spectroscopy

PGT Prompt Gamma Timing

PMMA Polymethyl-methacrylate

PTV Planning Treatment Volume

ROI Region Of Interest

SNR Signal to Noise Ratio

SOBP Spread-Out Bragg Peak

SPECT Single-Photon Emission Computed Tomography

STIR Software for Tomographic Image Reconstruction

TDC Time-to-Digital Converters

TOF Time-Of-Flight

TPS Treatment Planning System

WHO World Health Organization

1 INTRODUCTION

Nowadays, one of the leading causes of death around the world is cancer. The *International Agency for Research on Cancer* (IARC), which is an agenda of the *World Health Organization* (WHO), reports in an IARC document from 2014 the rapidly increasing trend of the diagnosed cancers worldwide [1]. In 2012, cancer was diagnosed in 14.1 million patients with mortality at the 58% level (8.2 million people). Six years later, in 2018, the same agenda reported that expected numbers for 2018 were 18.1 million diagnosed cases and 9.6 million deaths due to cancer [2]. The increasing trend of deaths due to cancer is also visible in Poland, with 140.6 thousand and 164.9 thousand cancer cases diagnosed in 2010 and 2017, respectively [3].

Radiation therapy is one of the most frequently applied cancer treatment methods. Among many radiation modalities, accelerated protons produce an excellent depth dose distribution characterized by maximum dose deposition at the end of their range [4]. This enables them to reduce the dose to OAR, increase the dose to the target volume (therapeutic window) and reduce late side effects. This makes proton radiotherapy the first choice of treatment [5] for the deeply situated brain, and head and neck tumours [6].

One of the major limitations of proton therapy is uncertainties in assessing of proton range [4], which might lead to overexposure of the OAR to the therapeutic dose or underexposure of the target volume. To tackle this problem, several range verification approaches are proposed. Firstly, it is possible to verify the irradiation delivery *in-vivo* during or shortly after the treatment. This can be done with a detector that measures the beam range in real-time, allowing interrupting beam delivery if the proton range is different from the predicted in the treatment plan. Secondly, the solutions based on the range measurement after the treatment are used. In such cases, a compensation of the range error is applied in the subsequent dose fractions applying adaptive treatment approaches [7]. The *in-vivo* range monitoring techniques rely on the detection of secondary radiation or induced radioactivity during or after the irradiation, e.g. by prompt gamma imaging [8], secondary charged particles tracking [9–12] or positron emission tomography (PET) [13–15].

The PET technique offers a localisation of proton-induced β^+radioisotopes. The coordinates of the annihilation of β^+emitters can be directly correlated with the proton beam range. The first clinical application of PET

technology for the range verification of ^{12}C ion beams took place at Gesellschaft fuer Schwerionenforschung (GSI), Darmstadt, Germany in 1994 [16]. A dedicated PET camera with two flat parallel panels of detectors installed in the treatment room was collecting signals immediately after switching off the beam. In the Heidelberg Ion-Beam Therapy Centre (HIT), activity induced in the patient was measured with the conventional PET scanner after completing the irradiation. Despite several attempts, the range monitoring system based on PET technology is still not used in clinical routine.

Nowadays, cost-effective, total-body PET technology (J-PET) based on long, organic plastic scintillator strips is under development at the Jagiellonian University (Cracow, Poland). Photons passing through the strips deposit their energy via Compton scattering and produce scintillations converted into the electrical signal at the photomultipliers placed at the ends of the scintillator. In contrast to the conventionally used PET scanners, one plastic strip can replace a whole row of the crystal scintillators in an axial direction and needs only two dedicated read-out electronic devices at its ends. The potential applications of the J-PET scanner are not limited only to the total body imaging [17]. However, they are also dedicated to physics studies on positronium imaging in cancer diagnostics [18], quantum entanglement research [19, 20] and discrete symmetries studies [21, 22]. The elongated J-PET plastic strips are potentially an interesting tool for measuring the spatial distribution of β^+radioisotopes induced by proton beams in tissue [23].

1.1 AIM AND OUTLINE

In order to investigate the feasibility of J-PET technology for the proton beam range verification, Monte Carlo simulations of proton irradiation, J-PET technology and PET data reconstruction have to be tested and validated. First, a reconstruction workflow must be established either with existing open-source software or a dedicated solution. Secondly, the simulation framework for the proton beam irradiation with phantom has to be set, and the range accuracy and efficiency of the system assessed. Lastly, patient irradiation has to be simulated and the results of β^+signal reconstruction analyzed.

This thesis aims to establish and test a methodology for the application of a set of J-PET detectors for proton beam range verification using Monte Carlo simulations. This general goal will be reached in the following steps:

1. Development of the dedicated Monte Carlo framework for characterization of the J-PET detector using the Geant4 Application for Emission Tomography (GATE) software package.

2. Validation of the PET data reconstruction framework validation with the Customizable and Advanced Software for Tomographic Reconstruction (CASToR).

3. Monte Carlo based study of the response of various J-PET detector configurations for proton irradiation of Polymethyl-methacrylate (PMMA) phantom.

4. Preparation of the Monte Carlo based simulations methodology to monitor beam range during the patient treatment at the Cyclotron Centre Bronowice (CCB).

The content of the thesis is listed below:

Chapter 2 introduces a research background on proton radiotherapy, PET imaging, and proton beam range monitoring.

Chapter 3 describes the concept of the J-PET technology, PET data reconstruction software requirements for the J-PET data reconstruction. The chapter introduces the J-PET setup configurations for proton range verification, CCB beam model and describes the properties and limitations of the CASToR, PET image reconstruction software used in the dissertation.

Chapter 4 addresses the PET data reconstruction workflow and workflow validation details, including attenuation and sensitivity corrections. This is done for setup based on one-layer and multi-layer J-PET scanners built like a barrel or dual-heads configurations. The efficiency factor η defined as a ratio of registered coincidences and simulated back-to-back gamma rays is defined and calculated.

Simulations of proton beam irradiation of a PMMA phantom are described in Chapter 5. The efficiency factor for measuring the induced activity in different geometrical configurations (barrel, dual-head), examples of images reconstructed based on Monte Carlo simulations, differences between the dose, produced activity and reconstructed emission profiles and their uncertainties are presented.

In Chapter 6, details of the Monte Carlo simulation workflow and methodology validation of the irradiation plan for a patient treated at CCB are introduced. The beam model, delivered dose, CT calibration, raw treatment plan conversion and Monte Carlo simulations setup are presented. The efficiency factor for various geometrical configurations is calculated. Reconstructed PET images from β^+signal obtained during the after-treatment phase from the patient irradiation are presented, A

Pearson Correlation Coefficient (PCC) is calculated as a final criterion for the correctness of the presented methodology.

The last chapter - Chapter 7 - states the conclusions and summarizes the whole thesis.

This thesis is limited to the Monte Carlo simulation studies only. No experimental validation was performed as at the moment of the thesis preparation, the J-PET system was not available in all these configurations at the CCB.

2

RESEARCH BACKGROUND

The main advantage of proton therapy is the specific depth dose profile of proton beam with a low entrance dose, the highest energy deposition at the depth close to the proton range and practically zero dose for distances exceeding the range. However, this sharp distal edge of the depth dose profile may lead, in case of the range uncertainty, to an overexposure of the OAR or underexposure of the tumour in case of the range uncertainty.

This chapter introduces to physics of proton interactions with the matter for energies and elemental composition relevant for proton radiotherapy. Particular attention is paid to the production of short–living β^+isotopes and methods of their localisation in the body using PET. Feasibility studies for applying of the novel PET technique based on organic scintillators for the range verification in proton therapy are the main subject of the thesis.

2.1 PROTON INTERACTIONS WITH MATTER

In radiation therapy, proton beams with maximal energies of 230 - 250 MeV are applied. Protons interact with tissue mainly composed of low-Z elements like H, C, N and O. Up to 99% of proton energy is lost in inelastic Coulomb interactions with atomic electrons. However, for the range verification and production of β^+isotopes, non-elastic nuclear reactions are essential.

Inelastic Coulomb interactions

Protons with the energies typically used for radiotherapy are losing their energy mostly via the inelastic Coulomb interactions with atomic electrons. The energy loss of the primary beam per length unit (stopping power) is determined by the Bethe-Bloch formula [24, 25] and is considered adequate for proton energies from 2 MeV [26]. Bethe-Bloch formula is given by:

$$-\frac{dE}{dx} = 2\pi N_e r_e^2 m_e c^2 \frac{Z^2}{\beta^2}[\ln\frac{2m_e c^2\gamma^2\beta^2 W_{max}}{I^2} - 2\beta^2 - 2\frac{C(\beta)}{Z_t} - \delta(\beta)] \quad (1)$$

where N_e, r_e and m_e are electron density, radius and rest mass, c is light velocity, Z is particle charge, β is relative velocity equal $\beta = v/c$, $\gamma =$

$\frac{1}{\sqrt{1-1/\beta^2}}$, W_{max} is the maximum kinetic energy, which can be transferred to a free electron in a single collision, I is the mean ionization potential of the material, C is a shell correction term, Z_t is the atomic number and δ is the density correction.

Several corrections are applied for energies lower than 2 MeV (when the particle velocity is comparable with the velocity of orbital electrons). The formula has to be extended for Lindhard theory [27, 28], Anderson-Ziegler model [29] or analytical models [30].

Elastic and inelastic nuclear interactions

Apart from inelastic Coulomb phenomena, protons can interact with human tissue via elastic and non-elastic nuclear reactions. Proton Bremsstrahlung emission in tissue is negligible [31].

Elastic nuclear interactions are responsible for the smearing of the initial concentrated dose, causing broadening lateral beam width by deflecting the initial proton trajectory. In the elastic interaction, the nucleus itself remains intact. As the mass of interacting particles is similar, the energy loss is relatively high. The process is dominated by the multiple Coulomb scattering [32, 33].

The most important interactions from the *in-vivo* range monitoring perspective are inelastic nuclear reactions. Primary protons are removed from the beam and secondary particles such as gamma-rays, neutrons, secondary charged particles (protons, deuterons, tritons, ^{3}He, ^{4}He, etc.) are produced. Prompt gamma-rays (called later prompt gammas), originated from the nuclei deexcitation, are currently one of the main research areas of interest for range assessment [8]. Methods based on prompt gammas rely on detecting their discrete lines from residual ^{12}C nucleus at 4.44 MeV - mostly ^{12}C(p,p′)^{12}C and ^{16}O(p,p′α)^{12}C reactions - and residual ^{16}O nucleus at 6.13 MeV - ^{16}O(p,p′)^{16}O reaction (Figure 1). The 2.2 MeV line (deexcitation of deuterium) is not considered as its space distribution is not correlated with the proton beam range [8]. Different types of position-sensitive detectors can detect secondary charged particles. For clinical use, the so-called Dose Profiler [9] is under construction, aiming to detect the position of gamma quanta emission. Additionally, MOnitor for Neutron Dose in hadrOntherapy (MONDO) neutron tracker [11] is also under development. A more extensive description of the *in-vivo* proton range verification methods is given in Section 2.7.

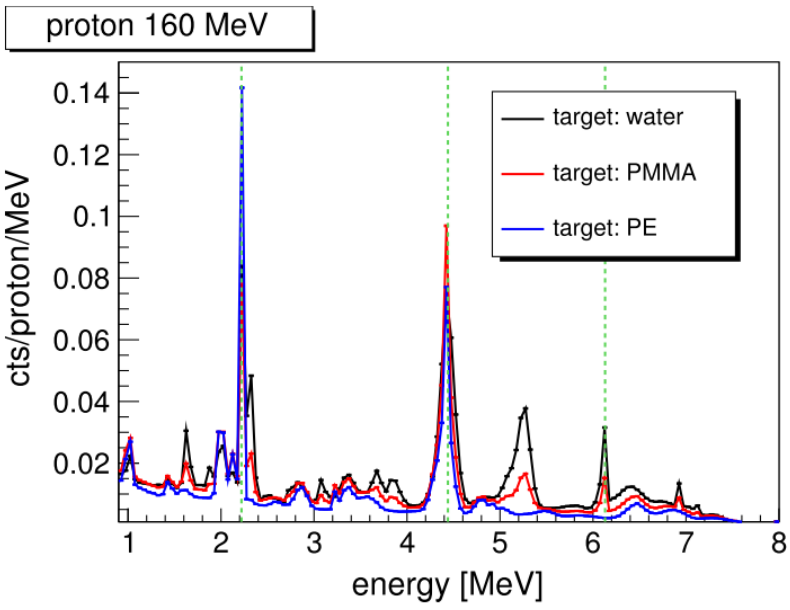

Figure 1: Energy spectra of prompt gammas generated in water, polyethene and PMMA cylinder targets (15 cm diameter, 25 cm length) irradiated by a 160 MeV proton beam. Discrete lines from residual ^{12}C nucleus at 4.44 MeV, residual ^{16}O nucleus at 6.13 MeV and deexcitation of deuterium at 2.2 MeV are shown. Reprinted from [8].

As a result of the non-elastic nuclear reactions in proton radiotherapy, β^+radioisotopes are produced in the irradiated tissue. The most important of them are presented in Table 1. In the therapeutic proton beam interacting with the human body, three nuclear reaction channels produce up to 95% of the β^+nuclei [34]:

- $^{16}O(p,pn)^{15}O$
- $^{12}C(p,pn)^{11}C$
- $^{16}O(p,3p3n)^{11}C$

Radioactive nuclei obey β^+decay as following:

$$^{A}_{Z}X \rightarrow ^{A}_{Z-1}Y + e^+ + \nu$$

As the bound proton transits into a bound neutron, energy is released and divided between positron and neutrino. Due to the three-body kinetics, the energy spectra of both particles are continuous. Positrons can travel even up to several millimetres in the human body (R_{max}). However, due to multiple scattering, their path is not straight, and the mean range (R_{mean}) is smaller than R_{max}. The intrinsic properties of several positrons produced during proton irradiation are presented in Table 2.

Table 1: Nuclear reaction channels and main β^+radioisotopes characteristic produced in human tissues. Table adapted from [34].

TARGET	NUCLEAR REACTION CHANNELS	β^+ ISOTOPES	HALF-LIFE
C	$^{12}C(p,pn)^{11}C$, $^{12}C(p,p2n)^{10}C$	^{10}C, ^{11}C	19.29 s, 20.33 min
N	$^{14}N(p,2p2n)^{11}C$, $^{14}N(p,pn)^{13}N$, $^{14}N(p,pn)^{14}O$	^{13}N	9.96 min
O	$^{16}O(p,pn)^{15}O$, $^{16}O(p,3p3n)^{11}C$, $^{16}O(p,2p2n)^{13}N$, $^{16}O(p,p2n)^{14}O$, $^{16}O(p,3p4n)^{10}C$	^{14}O, ^{15}O	70.61 s, 122.24 s
P	$^{31}P(p,pn)^{30}P$	^{30}P	2.50 min
Ca	$^{40}Ca(p,2pn)^{38}K$	^{38}K	7.64 min

Table 2: Mean energy (E_{mean}), maximum energy (E_{max}), maximum range (R_{max}) and mean range (R_{mean}) of positrons, emitted by β^+isotopes induced during irradiation of water by therapeutic proton beams (presented in Table 1). Data from National Institute of Standards and Technology [35] and Brookhaven National Laboratory[36]. If the isotope obeys several β^+decays, only the most intensive is given.

ISOTOPE	E_{mean}(kev)	E_{max}(kev)	R_{mean}(mm)	R_{max}(mm)
^{10}C	814	1908	3.4	9.3
^{11}C	386	960	1.2	4.2
^{13}N	492	1199	1.7	5.4
^{14}O	771	1808	3.2	8.7
^{15}O	735	1732	3.0	8.3
^{30}P	1441	3210	6.8	16.2
^{38}K	2323	5022	11.5	25.6

Positrons obey the annihilation process after losing their energy. The most probable reaction channel is the creation of the para-positronium with an electron from the tissue. This state has a 125 ps mean lifetime and its leading decay is via two antiparallel 511 keV gammas. The competitive triplet state is an ortho-positronium with the mean lifetime in a vacuum equal to 142 ns. It decays predominantly by three gammas with a continuous energy spectrum. Ortho-positronium state is not registered in conventional PET imaging, where only 511 keV gammas are taken into consideration. It is known in the literature that PET reconstructed β^+activity profile could be correlated with the proton range [15, 37], as depicted in Figure 2.

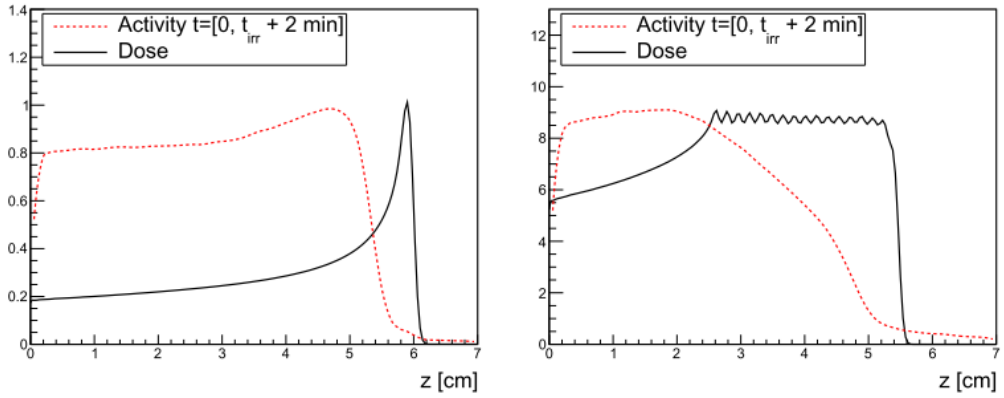

Figure 2: Relative depth dose distribution and β^+activity profiles produced in water by the parallel beam of 95 MeV protons, as calculated using Monte Carlo transport calculation using FLUKA code [38]. Units are arbitrary. Adapted from [37].

2.2 PROTON RADIOTHERAPY

The history of proton radiotherapy starts in 1905 with the Bragg and Kleemann publication [39]. They discovered that the energy deposition of the ions passing through the homogeneous material was inversely proportional to their square root velocity. The idea of ions based radiotherapy was proposed four decades later, shortly after World War II [40]. The first patients were treated with protons in Lawrence Berkeley Laboratory, US, in 1954 [41]. Currently, there are 102 particle therapy facilities in operation (February 2020), 37 under construction (December 2019) and 28 in the planning stage worldwide [42]. Most of them use protons.

Accelerators

For the production and acceleration of the therapeutic proton beams, synchrotrons, synchrocyclotrons and cyclotrons are used. Depending on the machine, the beam could be delivered quasi-continuously (cyclotron) or in patches - spills (synchrotron). Due to the time difference between the patches in the synchrotron [15], inter-spill range verification is possible. For the cyclotron, the quasi-continuously time structure means that the beam is also delivered in patches but in much shorter time-intervals [43].

This feature makes the inter-spill range monitoring impossible for cyclotrons as additional tagging devices have to be used to determine the actual beam status with ms precision. In such a short time, the produced activity would be so low that the counting statistic for PET registration would not be sufficient. In synchrotrons, ions are extracted at the required energy allowing the beam intensity to be set independently of their energy. Protons extracted from cyclotrons have constant energy and an energy degrader is used to decelerate the beam, reducing the beam intensity [4]. Currently available medical cyclotrons are typically dedicated to proton therapy facilities, whereas synchrotrons are frequently used to accelerate different ions, e.g. protons, oxygen and carbon ions.

Beam delivery system

Protons leaving the cyclotron pass through an energy degrader, which slows them down to the kinetic energy required by the treatment plan. The multiple proton interactions lead to a broadening of proton energy distribution [44]. Dipole magnets next reduce the variance of proton energy distribution with narrow momentum selection. The beam is delivered via vacuum ion-guide to the treatment room, passing through several forming elements (i.e. quadrupole and dipole magnets, collimators, slits, etc.). In order to deliver the beam from various angles and directions, a rotating gantry with a nozzle is applied. The nozzle is the last element of the system before the beam will be delivered to the patient. However, in some specific cases, i.e. eye melanoma treatment room, the gantry is useless and the horizontal fixed-beam eye-line is satisfactory, which is also beneficial from the economic perspective.

Beam formation could be realized in two regimes: passive scattering or active Pencil Beam Scanning (PBS). Scattering foil made out of high Z elements and dedicated aperture are used to obtain the required beam size for the passive approach. Additionally, a fast-rotating absorber (so-

called energy modulator) with varying absorber thickness is positioned in the beam path to cover the whole Spread-Out Bragg Peak (SOBP) within one rotation. The more recent technique is PBS, where two orthogonal scanning magnets tilt the beam to cover the entire slice of the tumour. Then, the energy of protons is decreased at the energy degrader and the next slice of the tumour is scanned. The beam leaving the nozzle has a specific shape and properties determined during the commissioning measurements. Such the beam model will be then used for the depth dose calculation in treatment plans and the resulting proton range [4].

Cyclotron Centre Bronowice

In Poland, a single proton therapy centre is currently under operation. The Cyclotron Centre Bronowice (CCB) is located at the Institute of Nuclear Physics Polish Academy of Science (IFJ PAN) in Cracow. CCB is equipped with two isochronous cyclotrons, AIC-144, developed at IFJ PAN and Proteus C-235 cyclotron (IBA, Belgium). AIC-144 was used for the proton therapy of eye melanoma. Since February 2011 up to January 2016, 128 patients were irradiated. Currently, it is used for research purposes, mainly for the high dose exposure of the electronics used in high energy physics detectors or space missions.

Proteus C-235 cyclotron delivers the proton beams to two rotating gantries with the PBS, one horizontal fixed-beam room for the eye melanoma irradiation with passive scattering technique and an experimental hall dedicated for physics experiments. The facility offers the beam in the energy range between 70 MeV and 226 MeV. Nowadays, about 20-25 patients are treated every day in CCB. Figure 3 shows the scheme of the CCB facility with the Proteus C-235 cyclotron, beam delivery system, treatment rooms and experimental hall.

Depth dose distribution

Dose is defined as an energy of radiation deposited in a matter to the mass of the matter. The unit of dose in the SI system is Gray [Gy = 1J/1kg].

For the monoenergetic beam, energy deposited by a broad beam of protons in tissue increases with the depth, reaches its maximum in the Bragg peak region and falls to zero just after the distal fall-off [46]. According to [47], the distal fall-off is the distance between 80% and 20% or between 90% and 10% of the maximum dose after the Bragg peak. The Bragg peak width of the monoenergetic broad proton beam is de-

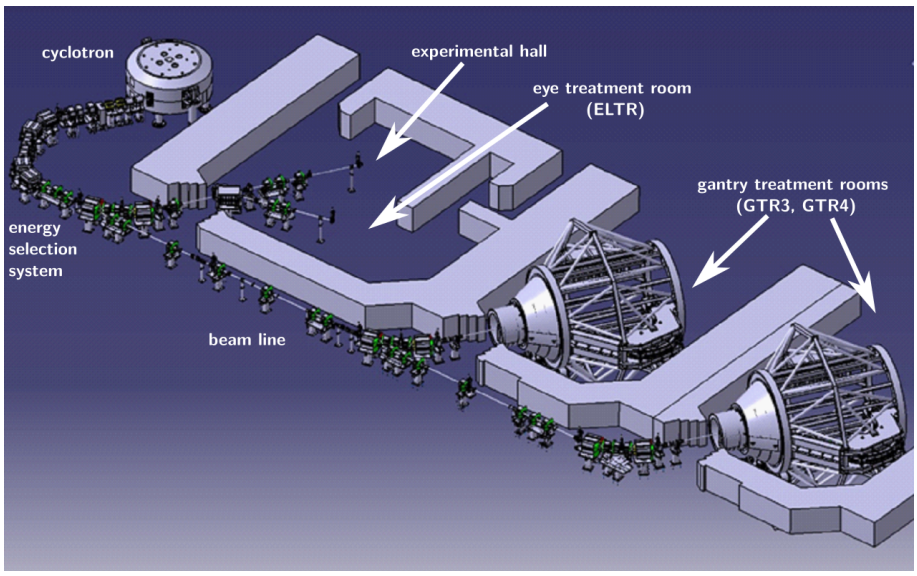

Figure 3: Scheme of the beamlines at the CCB facility. 230 MeV beam extracted from the Proteus C-235 cyclotron is transported via an energy selection system into the experimental hall and three treatment rooms. Figure adapted from [45].

termined by range straggling, observed due to the stochastic process of energy loss along their path. The depth dose distributions for ions and photons are presented in Figure 4. The difference between ions (protons and carbons) and photons profiles shows clear advantages of the ions radiotherapy over the photons, assuring better dose conformity.

2.3 RANGE OF THE PROTON BEAM

According to [48], the range R of a charged particle of a given type and energy in a given medium is the expectation value of the path length p that it follows until it comes to rest. A related quantity known as a Continuous Slowing Down Approximation (CSDA) range (R_{CSDA}) is defined as [48]:

$$R_{CSDA} = \int_0^{E_0} \left(\frac{dE}{\rho dx}\right)^{-1} dE \tag{2}$$

where E_0 is the initial kinetic energy of the particle, ρ is a material density and the $\frac{dE}{dx}$ term - stopping power. The R_{CSDA} is typically given in units $\frac{cm^2}{g}$. Range concept is depicted in Figure 5.

Therefore, for a broad parallel proton beam, it is practical to define the range as a distance at which the dose at the distal edge reaches 50% of the maximal value. Furthermore, this R_{50} range can be easily

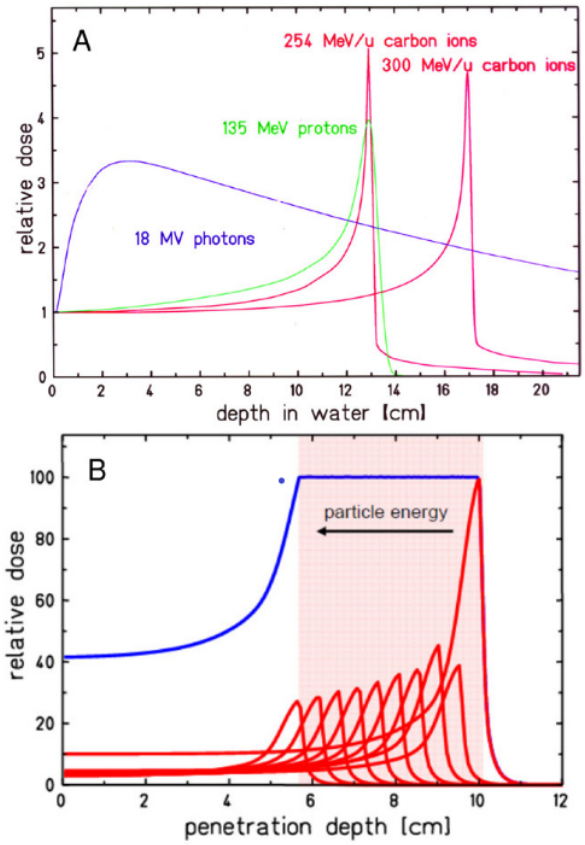

Figure 4: (A) Exemplary depth dose distributions of broad, parallel beam high-energy X-rays and monoenergetic ion beams (proton and carbon) constituting the so-called Bragg peak. (B) In order to cover the entire tumour volume, the Bragg peak is extended by overlapping different pristine beams at different intensities and energy, creating Spread-Out Bragg Peak (SOBP). Figure adapted from [33].

determined experimentally, e.g. by measurements in a water phantom using a plane–parallel ionization chamber.

Pencil Beam Scanning technology is preferably used in modern proton therapy, i.e. the patient is treated with a set of narrow pencil beams having different ranges and intensities. The depth dose distribution of the single pencil beam can be determined using a large diameter plane-parallel ionization chamber such as PTW Bragg Peak Chamber or IBA Stingray. These chambers can measure the primary beam and most of the scattered particles. Then the range of an individual pencil beam can be defined as the distance at 50% of distal fall–off of the Bragg peak.

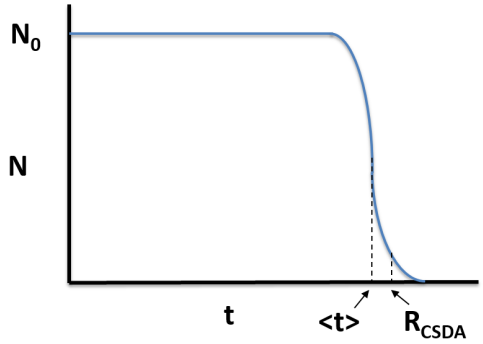

Figure 5: The number of monoenergetic charged particles (N) penetrating through a slab thickness t of absorbing material. $< t >$ is the projected range and (R_{CSDA}) is the continuous slowing down approximation range. Figure adapted from [48].

Range uncertainties

Accurate assessment of the depth of penetration is essential for proton radiotherapy and may significantly impact reducing an overdose of OAR or underdosing of the target volume. Faulty range assessment leads to an 'error' in dose distribution which might result in deposition of target dose in the distal edge of the SOBP, as depicted in Figure 6. There are several sources of the range uncertainty recognized in literature [49]. Currently, most Treatment Planning Systems rely on CT scans and corresponding calibration curves to calculate dose distribution. However, beam hardening (which occurs when an X-ray beam comprised of continuous wide energy spectrum passes through an object, resulting in selective attenuation of lower energy photons), reconstructed image noise and partial volume effect (tissues of widely different absorption are encompassed on the same CT voxel resulting in average attenuation value of these tissues) affect the range assessment directly, especially in case of metal implants presence.

Additionally, Hounsfield Unit (HU) from CT images must be converted to the relative proton stopping power. A stoichiometric calibration of the CT numbers with tissue parameters is widely known and established [50, 51]. As the HU depends on X-ray linear attenuation coefficients, the information about the material composition in the CT scan is missing, and actual conversion depends on the atomic composition of the material. It was reported that two different materials with the same HU value, could lead to differences in relative stopping power at the level of 1.1% for soft tissues, 1.8% for bones and 3% in general [49, 52]. Therefore, CT images imperfections and HU versus relative proton stopping power calibration are considered to have a systematic contri-

bution to the range uncertainty. For more information please refer to a more comprehensive description that could be found in [50, 51].

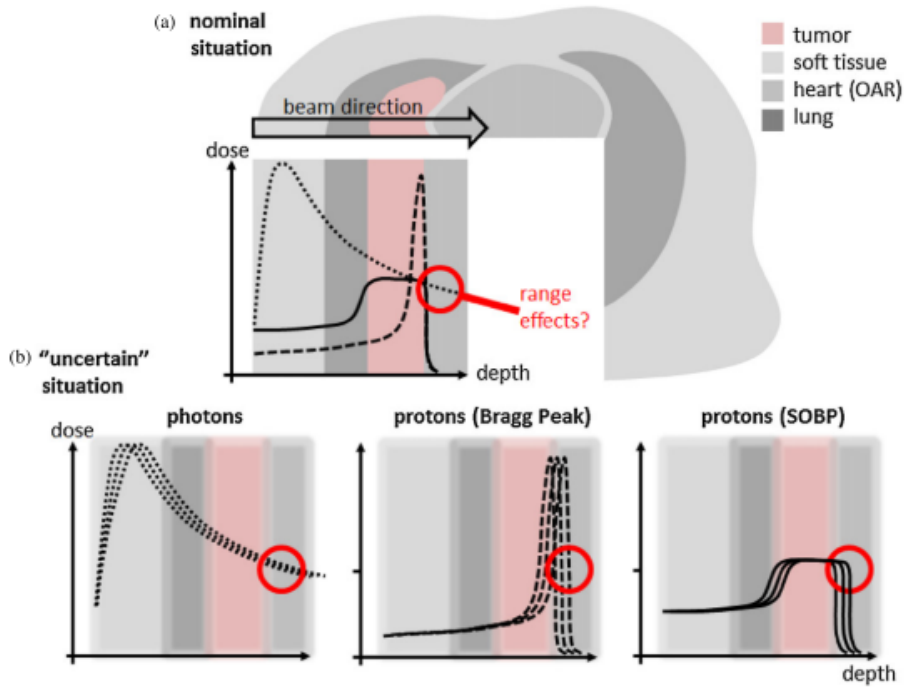

Figure 6: (a) Comparison between dose depth profiles for photons (dotted line), monoenergetic broad, parallel proton beams (dashed line) and proton-induced SOBP (full line). (b) Impact of the range uncertainties on the depth dose curves. Variations of density might have a significant impact on the range of proton beams. Figure by [49].

Additionally, two other sources of range uncertainty can be considered. The first one originates from proton energy distribution - the differences are typically less than 1%. At this stage of technology, there is not much room for further improvement [49]. Substantial contribution to the range uncertainty originates from variations of patient positioning with respect to the beam. The most prone for an error are situations when large density, heterogenic volumes are treated. Moreover, as the typical course of proton radiotherapy lasts over a few weeks, changes of patient anatomy might lead to overdosage in OAR or underdosage of the target volume. The tumour mass and volume changes, patient weight loss/gain, and daily changes in the filling of nasal cavities, bladder, rectum or bowel have to be considered. Some of these effects (tumour and patient weight-specific) might vary systematically across the whole treatment duration, whereas others (fillings in internal cavities) occur sporadically. All the reasons mentioned above emphasize the need for the development of precise *in-vivo* range monitoring methods.

2.4 MONTE CARLO METHODS FOR PARTICLE TRANSPORT

Monte Carlo algorithms were first proposed to solve differential equations [53]. A growing interest in nuclear physics coincided with the beginning of the computer era, which provided the necessary computing power to perform the calculations. The first researchers who used it extensively were Stanisław Ulam and John von Neuman from Los Alamos (USA), where the *Monte Carlo* name was given to the method. They used it for neutron transport calculations for the hydrogen bomb. As large statistics were needed to model stochastic processes adequately, the development of the first computers was necessary to improve the method in different disciplines.

In the Monte Carlo technique, a random number is sampled from a probability density function to simulate step-by-step interactions and transport of each particle. The random number generator has to demonstrate a long enough period not to repeat the random number during the simulation [4]. The probability density function should refer to a given particle's probability of a given type of interaction. The probability of particle interaction is modelled using both theoretical models and experimentally derived interaction cross-sections. For every single particle, all possible interactions are simulated, and all secondary particles are then tracked. Due to computational economy, the particle tracking is continued down to the predefined energy cut-off, i.e. the secondary particles produced with the energy below the cut-off threshold are stopped and their energy is deposited at the place of origin. This allows to speed up the simulation and adjust the simulation setup for specific needs. The method can be used to simulate proton interactions within the human body and radiation interactions within a detector, making it a powerful tool for both radiation treatment and diagnostics (PET, SPECT or CT) applications.

Several general-purpose Monte Carlo radiation transport toolkits are currently used for research purposes, such as FLUKA [38], Geant4 [54], Shield-HIT [55], GATE/Geant4 [56] or TOPAS [57]. Nowadays, computational capabilities have increased due to multiple CPUs for parallel computing or GPU cards. It shortened the calculation time enabling Monte Carlo based dose estimation to be incorporated into the clinical practice. GPU-based Monte Carlo gPMC code dedicated to proton therapy was recently developed and validated with patient data [58, 59]. Wan Chan Tseung and colleagues [60, 61] presented GPU-accelerated MC code pGPUMCD which had been already used for routine daily QA and dose calculation in a clinical TPS. Moreover, the FRED GPU-accelerated Monte Carlo code was developed in Rome by Schiavi and

colleagues [62] and was validated and commissioned for the CCB facility in Krakow [23, 63]. Recently, FRoG - GPU-accelerated platform for analytical pencil beam dose calculation has been developed for clinical investigations enabling the transport simulation of four ions (protons, helium, carbon and oxygen) [64–66].

Patient treatment plans are prepared with a Treatment Planning System (TPS). Most of them rely on analytical pencil beam models adjusted for a facility. The beam model aims to describe the variation of the beam range and the beam broadening in the distance from the isocenter [49]. The model is calculated and validated based on dosimetric measurements in a water phantom. Apart from analytical models, more accurate Monte Carlo based dose calculation algorithms [67] are of increasing interest in radiotherapy nowadays.

2.5 POSITRON EMISSION TOMOGRAPHY (PET)

PET is one of the most exploited molecular imaging techniques in diagnostics. The most widely used application of PET is a cancer diagnosis. For diagnostics purposes, patients are injected with the β^+radioligands (i.e. fluorodeoxyglucose with ^{18}F radiotracer) metabolized predominantly by cancer tumours. It is required that radiotracers bound to the ligands have a half-life time long enough to ensure sufficient counting statistics during the examination and short enough to protect the patients and other people from unnecessary radiation exposure after completing the scan. In addition, other radiotracers properties such as the energy spectrum of produced positrons, its mean range within the tissue, capabilities to cross the brain-blood barrier have also been taken into account. Essential radiotracers for diagnostics are ^{18}F, ^{15}O, ^{13}N and ^{11}C with half-life times at the level of 110 minutes, 2 minutes, 10 minutes and 20 minutes, respectively.

In the patient body, radiotracers obey β^+decay leading to the annihilation with electrons (see Section 2.1). In conventional PET scanners, only para-positronium states producing two gamma-rays are considered. Annihilation gamma-rays leaving the patient body are then registered in the detector ring where inorganic crystals such LSO, BGO or LYSO are typically used, as depicted in Figure 7. The line between two detectors which registers the signal is called Line of Response (LOR). In order to determine if the two signals registered by two separate detectors working in coincidence are originated from the same annihilation, two types of discrimination are applied:

1. Time threshold

   The coincidence is observed if the time difference between registered photons is lower than the applied threshold (about a few ns for commercially available scanners).

2. Energy threshold

   The coincidence is observed if both registered photons originated from the annihilation. Due to the intrinsic detector energy resolution (typically at the level of 10-15% [68]), the energy threshold is set from ~430 keV to ~600 keV. Thus, the energy threshold varies between scanner models.

In conventionally used PET scanners, during the reconstruction process, it is assumed that annihilation occurs at the whole LOR length with the same probability. It results in a low Signal to Noise Ratio (SNR) and overall poor image quality of the reconstructed PET images. In order to improve the PET image quality (increase the SNR), additional information about the Time-Of-Flight (TOF) is measured for each gamma detection. It enables more precise modelling of the annihilation point [69], as depicted in Figure 7. The accuracy of the annihilation point determination is limited by the accuracy of the time difference calculation related to the electronic time resolution. It is called TOF resolution. Nowadays, the PET imaging community works towards the TOF resolution at the level of 10 ps [70] introducing a quantum leap in PET imaging and quantification. The TOF at ten ps Full Width at Half Maximum (FWHM) automatically determines a direct representation of the estimated emission distribution of positrons with the mm accuracy. The time-consuming reconstruction will not be necessary anymore.

Another breakthrough improvement in PET imaging was introducing the total body imaging technology as the new EXPLORER scanner was approved for clinical studies [72]. It enables simultaneous measurement of the β^+activity within the whole patient. In traditional whole-body scanners, the patient has to be scanned in several positions. However, the cost of the scanner is expected to be at the level of $10 million [73]. Therefore, it makes it unreachable for most of the hospitals and research institutes.

2.5.1 *PET data organization*

The following parametrization of coincidences are used in PET imaging [74]:

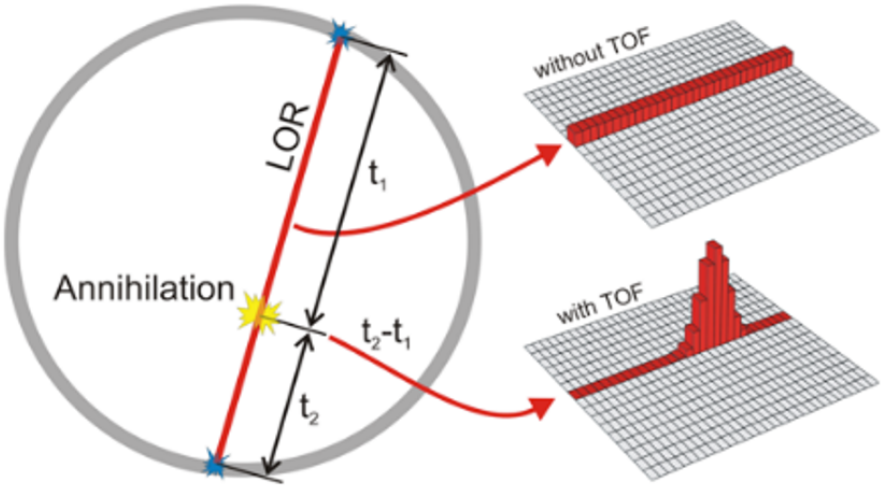

Figure 7: Principle of the PET signal detection with incorporated TOF information. Figure by [71].

1. List-mode

   In the sequential data stream all coincidence events are stored. It is of advantage when the total number of registered coincidences is lower than the number of all possible LORs. The reconstruction based on the list-mode acquisition does not suffer from LORs grouping.

2. Sinogram

   The coincidences are organized into sinograms format enabling neighbouring LORs grouping, reducing data storage and reconstruction time, and not significantly affecting the reconstructed spatial resolution. An explanation of the sinogram term is given below.

In order to find the true activity distribution within the imaging object denoted as a $f(x, y)$, all registered LORs are organized into a set of projections where each projection $p(s, \phi)$ is formed by integration along all s (parallel LORs) at a given angle ϕ, as depicted in Figure 8. All projections for $0 \leqslant \phi < 2\pi$ create a 2D function of s and ϕ which is known as a sinogram.

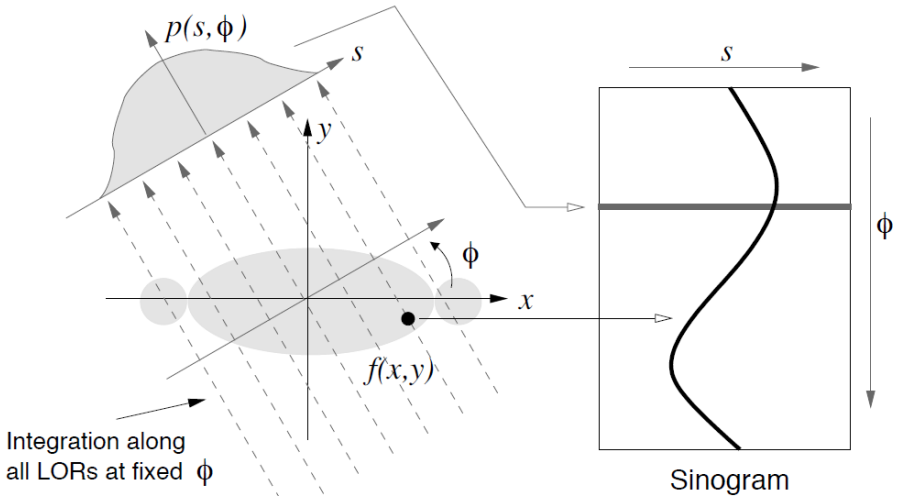

Figure 8: The schematic presentation shows how the $p(s, \phi)$ distribution and sinogram are calculated. The integration along all parallel LORs at a given angle ϕ forms projection $p(s, \phi)$. Each projection is represented as a single row of ϕ in the sinogram. Figure adapted from [75].

2.5.2 *PET data reconstruction*

In general, every imaging system could be represented by the linear relationship [75]:

$$p = Hf + n \tag{3}$$

where p is a vectorized version of all projections - $p(s, \phi)$, H is a system model also known as a system matrix, f is a vectorized version of the unknown activity distribution, i.e. the PET image and n is an error of observations.

As the reconstruction aim is to find the f, the solution of that problem could be delivered by the H matrix inversion [74]:

$$\widehat{f} = H^{-1}p \tag{4}$$

However, the inversion problem is ill-posed due to the stochastic nature of the measurement error and small perturbation of p caused by the measurement noise leading to a significant error of the reconstructed image $\widehat{f}$. Therefore, additional constraints have to be added in the reconstruction workflow [74].

There are two types of approaches for PET data reconstruction. The first group includes analytical approaches giving exact and direct solutions of the activity distribution reconstruction (f) based on known projections (p). This mathematical solution is fast and direct. The disadvantage is that those methods rely on an idealized system model,

and projection noise is neglected leading to lower image resolution and poor noise properties, observable as streaking artefacts [75, 76]. The most commonly used technique is Filtered Back Projection (FBP).

The second group of the reconstruction algorithms rely on the stochastic nature of the observations. They include physical phenomena like photons absorption and scattering and acquisition conditions as non-ideal photon detection processes. The estimation of the activity distribution is an iterative process, and every new image calculation is based on previous estimation [74]. As the mathematical model is more accurate than the analytical one and the improvements are made at every iteration, the images have better quality than FBP direct solutions but at the cost of reconstruction complexity and time [75, 76]. The most widely used iteration method for PET imaging is the MLEM algorithm and its faster version, Ordered Subset Expectation-Maximization (OSEM) .

2.5.2.1 *Filtered Back Projection (FBP)*

The basis of the FBP algorithm is a Radon transform which, in PET imaging context, maps the original activity image f into the set of projections p (sinogram) and is expressed as follows [74, 77]:

$$p(s,\phi) = \int_{-\infty}^{\infty} f(x, \phi x + s)\,dx \tag{5}$$

In order to find the activity distribution image, the inverse of the discrete Radon transform, which unfolds the original distribution by the projections, is used. The process is known as a Back Projection and transforms data from projection space ($p(s,\phi)$) to the image domain ($f(x,y)$) as follows:

$$f(x,y) = \int_{0}^{\pi} p(x\cos\phi + y\sin\phi, \phi)\,d\phi \tag{6}$$

FBP is dedicated to 2D reconstruction and is calculated in two steps [76]. First, the filtration of each projection of the sinograms in Fourier space is performed using a high pass filter (i.e. ramp filter with various windows) [74]:

$$\widehat{p} = \int_{-\infty}^{\infty} |\widehat{s}|\Big(\int_{-\infty}^{\infty} p(\widehat{s},\phi)e^{-j2\pi\widehat{s}v}\,d\widehat{s}\Big)e^{-j2\pi sv}\,ds \tag{7}$$

where $|\widehat{s}|$ is a ramp filter.

Secondly, the discretized Inverse Radon Transform is performed as follows:

$$\widehat{f}(x,y) = \int_{0}^{\pi} \widehat{p}(x\cos\phi + y\sin\phi, \phi)\,d\phi \tag{8}$$

2.5.2.2 *Maximum Likelihood Expectation-Maximization (MLEM)*

Due to the complexity of the stochastic approach, the iterative reconstruction algorithm includes five components [74]:

1. Image model

   The image representation specifies the image model. The methods typically used to discretize the image domain are pixels (2D image elements) or voxels (3D image elements). However, other methods such as spherical symmetry based 'blobs', bell-shaped radial profiles [78, 79] or polyhedrons [80] have also been proposed.

2. Data model

   In principle, data models characterize the statistical distribution of each measurement p_j with respect to its mean value $< p_j >$. Usually, PET coincidence data obey independent Poisson distribution. The probability (likelihood L function) of Poisson distributed photon counts (p) is a real photon count at a given emission rate f is expressed as:

   $$L(\vec{p}|f) = \prod_{j=1}^{N_{LOR}} \frac{exp(- < p_j >) < p_j >^{p_j}}{p_j!} \tag{9}$$

   The actual distribution of the PET data often differs from a 'pure' Poisson model due to various pre-processing methods and statistics. For example, suppose the registered coincidence number per bin is high. In that case, the data obey approximately Gaussian distribution (the variance σ_j^2 of each bin could be estimated based on pre-processing methods) as follows:

   $$L(\vec{p}|f) = \prod_{j=1}^{N_{LOR}} \frac{1}{\sqrt{2\pi}\sigma_j} exp(-\frac{(p_j - < p_j >)^2}{2\sigma_j^2}) \tag{10}$$

   Other models were also introduced, such as approximations of Poisson or shifted Poisson distributions to model pre-corrected data and for practical computation reasons [75].

3. System matrix

   System matrix H relates reconstructed image and measured data by storing information about the probability that emission from voxel i is detected in projection j as follows [74]:

   $$< p_j >= \sum_{i=1}^{P} H_{j,i} f_i \tag{11}$$

where $H_{j,i}$ is the element of the system matrix and f_i is an activity in the i voxel. System matrix H could model either only the geometrical mapping from the image to data or geometrical effects and other physical effects, such as detector properties (i.e. energy blurring, dead time, efficiency), attenuation, positron range, etc. [76]. Since the H matrix could be prohibitively large (especially for 3D PET), other approaches to make it manageable are introduced, i.e. on-the-fly calculation, symmetry and compression techniques or the most commonly used decomposition of the matrix H into individual, easy to store and calculate components [81].

4. Cost function

   The critical component of the iterative reconstruction algorithm is a cost (objective) function that links unknown image with the measured data and defines the 'best' image. The most common approach is the Maximum Likelihood method which chooses an $\widehat{f}$ image estimate with the greatest likelihood $L(\vec{p}|f)$ value.

5. Optimization algorithm

   The last component is an algorithm optimizing the cost function finding the 'best' image $\widehat{f}$ estimate. The most widely used approach is the Expectation-Maximization algorithm.

These all assumptions lead to the iterative equation describing the MLEM algorithm for sinogram data as follows:

$$\widehat{f}_i^{n+1} = \frac{\widehat{f}_i^{n}}{\sum_{j'=1}^{N} H_{j',i}} \sum_{j=1}^{N} H_{j,i} \frac{p_j}{\sum_{i'=1}^{P} H_{j,i'} f_{i'}^{n}} \quad i = 1, ..., P \tag{12}$$

The sum over i' is a forward projection. The sum over j in the numerator represents the backprojection of the ratio between measured and estimated data. The sum over j' in the denominator represents the sensitivity of the scanner for voxel i.

The sensitivity map determines the probability that emitted from a voxel i back-to-back 511 keV gamma quanta will be registered with J-PET scanner as the coincidence:

$$s_i = \frac{N_r}{N_c} \tag{13}$$

where N_r is the number of registered coincidences and N_c is the number of simulated coincidences.

The list-mode MLEM reconstruction formula slightly differs from the sinogram based reconstruction, converting summation over sinogram bins to the summation over events [82]. The formula is given as:

$$\widehat{f}_i^{n+1} = \frac{\widehat{f}_i^{n}}{\sum_{j'=1}^{N_{LOR}} H_{j',i}} \sum_{j=1}^{N_{LOR}} H_{j,i} \frac{1}{\sum_{i'=1}^{P} H_{j,i'} f_{i'}^{n}} \quad i = 1, ..., P \tag{14}$$

Additional TOF information in the list-mode MLEM algorithm is incorporated in the system matrix H:

$$\widehat{f}_i^{n+1} = \frac{\widehat{f}_i^{n}}{\sum_{j'=1}^{N_{LOR}} H_{j',i}} \sum_{j=1}^{N_{LOR}} H_{j,i}^{TOF} \frac{1}{\sum_{i'=1}^{P} H_{j,i'}^{TOF} f_{i'}^{n}} \quad i = 1, ..., P \tag{15}$$

where the $H_{j,i'}^{TOF}$ is the system matrix incorporating the TOF weighting kernel.

There are several open-source software tools for PET data reconstruction. The first one, and probably the most popular, is Software for Tomographic Image Reconstruction (STIR) [83, 84], offering a multiplatform, object-oriented framework for data manipulation and reconstruction in tomographic imaging, supporting PET, CT and SPECT modalities. The library allows users to successfully reconstruct and manipulate the data from existing scanners of leading vendors as well as layer-based geometry with recently implemented TOF-MLEM reconstruction[85].

A more generic approach is proposed in the Customizable and Advanced Software for Tomographic Reconstruction (CASToR) framework [86, 87]. The generic character of the software and flexibility in terms of the input data file format caused that all information needed for the reconstruction, such as data format (list-mode or histogram), normalization, attenuation correction, scatter correction, random correction, etc. has to be pre-computed and incorporated in the input data file by the user. CASToR, in general, does not estimate PET corrections like it is possible in STIR.

There are several other open-source software platforms available such as NiftyRec [88], Occiput.io [89], Open-source MATLAB Emission Tomography Software [90]. However, the first two are the most commonly used, validated, and have the biggest community and support of the developers.

2.5.3 *Quantitative corrections in PET*

During the PET examination, several unwanted effects are observed, leading to inaccurate PET image reconstruction. First, apart from true

coincidences, random and scattered coincidences are recorded, as depicted in Figure 9. Moreover, attenuation of the annihilation photons is influenced by the patient anatomy. Additionally, read-out electronics imperfections, detector efficiency, geometrical effect, etc., also have to be considered and included correctly in the system matrix H.

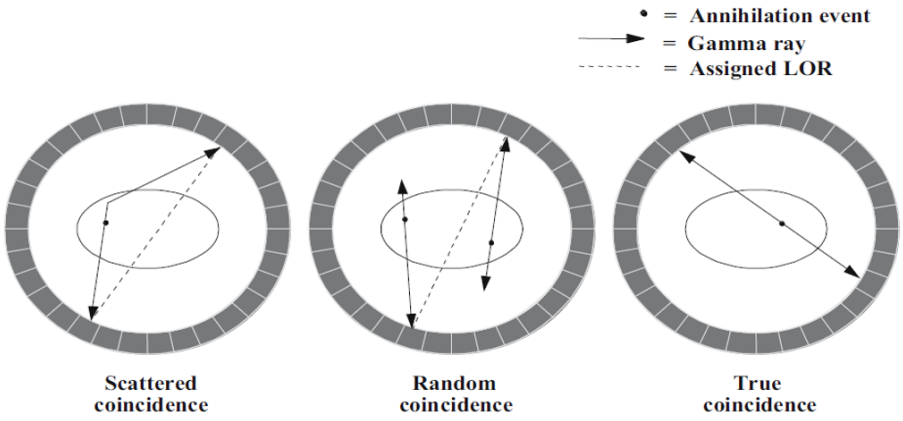

Figure 9: Types of coincidence events recorded by a PET scanner. Figure adapted from [74].

Therefore, in order to achieve fully quantitative PET images, several corrections have to be applied:

- Random coincidences correction(

  The finite width of the electronic time window creates the opportunity to detect and classify two uncorrelated single events as a true coincidence. Several techniques are used to estimate the random coincidences, i.e. estimation by the delayed coincidences. Lack of random correction resulted in increased reconstructed activity in the whole FOV region [74].

- Scatter coincidences correction

  As the most likely interaction of 511 keV photons in tissue is Compton scattering, there is a high chance that one or both annihilation gammas undergo scattering in the patient body or detector. The scattered fraction defined as a proportion of accepted coincidences that have undergone Compton scattering varied between 15% (2D scanners) and 40% (3D scanners). The scatter correction is the most challenging part of the PET data correction. Various techniques were introduced to calculate it, such as Monte Carlo calculations, convolution and deconvolution approaches or multiple energy window techniques. However, lack of scatter correction

results in increased reconstructed activity in the middle of FOV [74].

- Attenuation correction

  Photons originated from annihilation passing through the medium might be attenuated. Attenuation is quantified by linear attenuation coefficient (μ) specific for each material and photon energy. Several approaches were introduced to correct the attenuation, such as methods using coincidence emission data, singles transmission data or the most common CT-based correction where HU were converted to the attenuation coefficient μ using bi-linear conversion [91]. Lack of the attenuation correction resulted in increased reconstructed activity at the boundaries of the patient/phantom with significantly lower activity within the body/phantom [74].

- Normalization correction

  Normalization correction includes several components, i.e. geometric and solid angle effects, detector (crystal) efficiency, detector interference, detectors and electronics dead-time, etc. Component-based normalization is currently one of the most widely used approaches to model normalization [92].

The impact of each correction is described more extensively in [74].

As mentioned before, decomposition of the matrix H belongs to the standard procedure in modelling of the PET system:

$$H = ANX \tag{16}$$

where A and N are diagonal matrices of the attenuation and normalization factors for each LOR, respectively. X is a geometric projection matrix where each row represents an image of a line (LOR) through the Field Of View (FOV). Various projectors (ray tracing algorithms used to calculate geometric projection matrix) could be used, such as Siddon [93], Joseph [94] or others [95]. It is worth mentioning, that matrix X could be adapted to include TOF modelling. Other physical phenomena (i.e. photons depth of interaction in crystal) and system-specific properties (i.e. system resolution related convolution operation) could be modelled and also incorporated in the H matrix [92].

All elements of the H matrix have to be provided in the format where each correction is calculated for each LOR separately. Thus, the final generalized formula in the matrix-vector form (to prevent excess writing of

summations and subscripts) for the MLEM algorithm (Equation 12) is given as follows [81]:

$$\widehat{f}^{n+1} = \frac{\widehat{f}^{n}}{A^{T}N^{T}X^{T}} A^{T}N^{T}X^{T} \frac{p}{ANX\widehat{f}^{n} + s + r} \tag{17}$$

2.6 J-PET

J-PET is a new, affordable, cost-effective PET technology. Inorganic crystals (L(Y)SO, BGO), typically used in PET scanners, are replaced by plastic scintillators to detect annihilation photons. The replacement of tens of expensive crystals along the z-axis with one long plastic scintillator strip allows reducing significantly the cost of the whole scanner (the cost of the same volume of the plastic scintillator is about 80 times lower than for L(Y)SO [96]) and complexity of the read-out electronic system. It allows the construction of a scanner based on very long scintillators (even up to 2 metres) covering larger FOV than offered by conventional PET imaging systems. On the other hand, due to the differences in densities and atomic composition, the detection efficiency of the system based on plastic strips is significantly lower [21, 96, 97]. The reason for that is mainly due to the detector material density equal to 1.023 $\frac{g}{cm^3}$ and 7.2 $\frac{g}{cm^3}$ for plastic scintillators and LYSO crystals, respectively [98]. In order to compensate for crystal detection efficiency superiority over plastic scintillators, three strategies could be applied:

- increasing the number of layers
- increasing the thickness of the plastic scintillators
- applying longer scintillators in order to increase geometrical acceptance and cover greater FOV

Detailed studies of the differences in LYSO and plastic scintillator detectors in the context of medical imaging (detector efficiency and geometrical - solid angle - acceptance) are given in [96, 99].

Annihilation gamma-rays interact with plastic scintillators via Compton scattering and cause the emission of scintillation photons in the visible light spectrum. Typically, a single deposition within the plastic resulted in a few thousand scintillation photons emitted isotropically and propagated to the plastic strip ends. Then, the light is converted into an electronic signal by photomultipliers. Scintillator strips are covered with a reflective foil to avoid photon losses. Additionally, plastic polymers absorb much fewer scintillation photons than crystals (attenuation length of plastic polymers is about 400 cm compared to the order

of 20 cm for the crystals [96, 98]), which makes the usage of longer strips possible. The signal duration in plastic is also significantly shorter (~ 5 ns) than in commercially available crystals (~ 50 ns) [96, 98].

The idea of J-PET imaging is presented in Figure 10. Two steps procedure based on TOF information is applied to reconstruct the position of annihilation. First, the interaction point of the annihilation gamma-ray within the scintillator is calculated with two separate modules based on the time difference of collected signal arrival at both ends on the scintillator strip. Then, the annihilation point along the LOR is determined from the time difference between interactions in both strips.

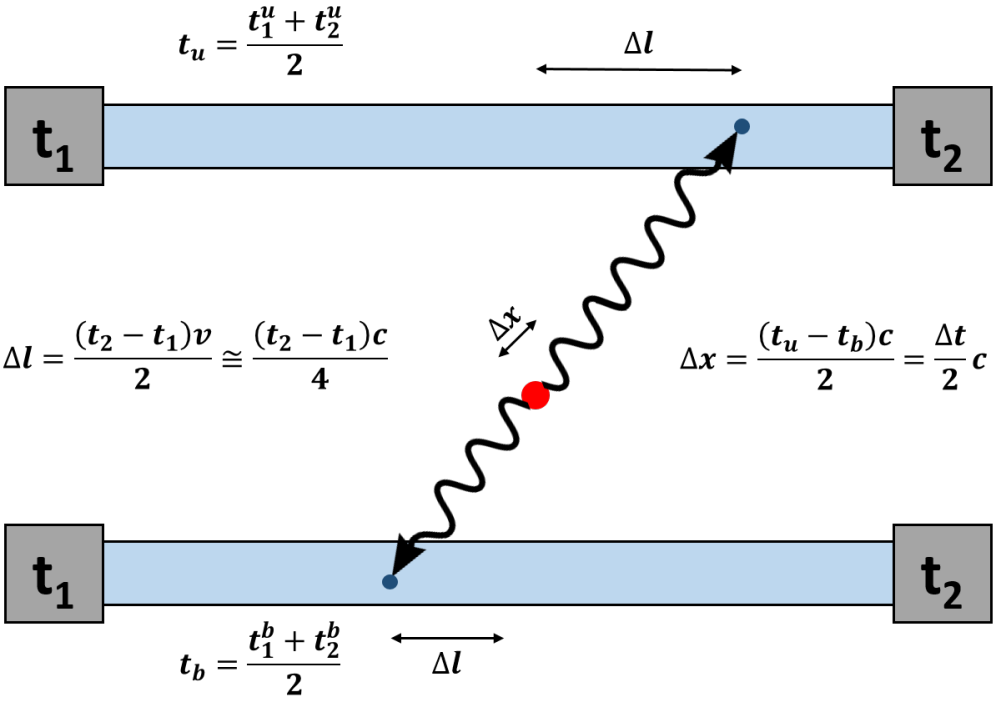

Figure 10: The principle of measurements with the J-PET modules. First, annihilation gamma interaction time with the strip is calculated as a mean of the time measured by the photomultipliers. t^u and t^b correspond to the interaction time in top and bottom strips, respectively. t_1^u and t_2^u denote measurement times by the left and the right photomultipliers, respectively. The position of the annihilation is determined from the difference between the interaction times in the two strips. Δl denotes a distance between the place of the interaction and the centre of the scintillator. v and c stand for an effective velocity of the light in a plastic strip and speed of light in a vacuum, respectively. Δx is a distance between the centre of the LOR and the annihilation position. Figure adapted from [98].

One of the first prototypes of the J-PET detector (constructed in 2016) is built out of three layers of EJ-230 plastic scintillator [100] strips (7x19x500

mm^3). The outermost layer consists of 96 strips, while the middle and innermost - 48 strips. All strips are wrapped up with the refractive and kapton foils to prevent scintillation photons emerge from the plastic. At both ends of each strip, the Hamamatsu R9800 vacuum tube photomultipliers are placed. Data is acquired by means of Time-to-Digital Converters (TDC) and Field Programmable Gate Array (FPGA) for read-out and data transmission [101–103]. As the data is collected in a triggerless mode, further analysis is performed by the dedicated software - J-PET Framework [104].

Currently, the next generation prototype of the modular (digital) J-PET is under construction and final validation. It consists of 24 modules. Each module is built out of 13 separate scintillator strips (6x24x500 mm^3). As in the prototype, the same cover foils for the strips are used. Each of the strips is connected to 8 silicon photomultipliers (4 at each side). Digital J-PET is designed to work as an independent scanner and could also be incorporated as a part of the three layer prototype creating the fourth (innermost) layer. Both prototypes are presented in Figure 11.

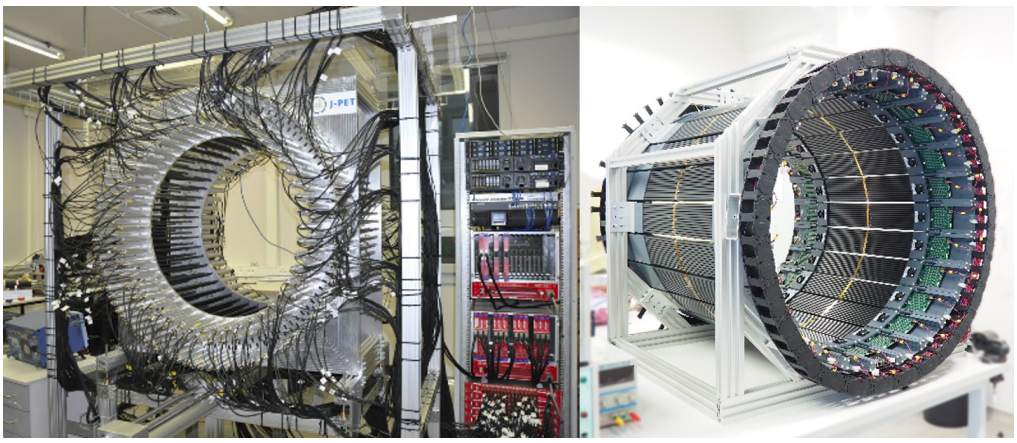

Figure 11: Two prototypes of the J-PET scanners: the 3-layers prototype (left) and the digital model of the new J-PET scanner (right). The latter one could be incorporated as a fourth, innermost layer to the 3-layers prototype. Figure by courtesy of the J-PET collaboration.

2.7 PROTON BEAM RANGE MONITORING

The two most widely explored approaches for range monitoring are based on prompt gamma and PET imaging. The distribution yields for the production of β^+emitters and prompt gammas per primary proton for 15 cm range in water are at the level of about 0.05 [8, 105]. However, additional effects of the attenuation have to be considered as only a fraction of emitted gammas will emerge from the patient body. Monte

Carlo simulation shows that the number of emerging prompt gammas is about ten times higher than annihilation gammas (assuming no isotopes wash-out or time correction). The ratio is reaching 50-90, assuming PET wash-out and time correction. However, due to the higher geometrical acceptance and much larger detection efficiency, in-room PET scanners gathered much greater statistics than prompt gamma range monitoring systems [106]. Prompt gammas enable real-time range monitoring as they are produced almost simultaneously (with a few ns delay) with the proton interaction [105]. Additionally, in proton therapy, 1D prompt gamma distal fall-off is closer to the dose depth Bragg peak than 1D PET fall-off. Prompt gamma fall-off is about 0.5-1.0 mm proximal to the dose depth Bragg peak and PET distal fall-off about 5-6 mm proximal with respect to the prompt gamma fall-off as presented in Figure 12 [106].

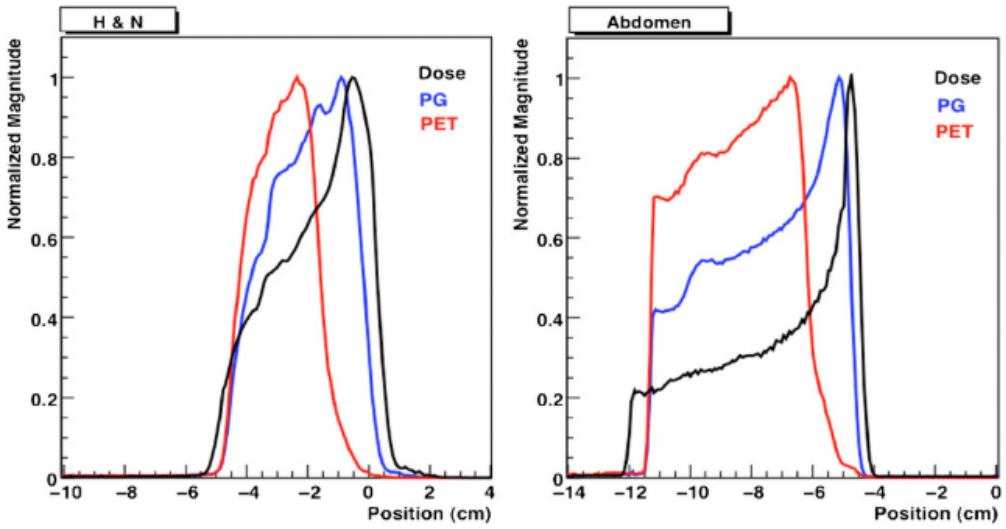

Figure 12: PET signal (red), prompt gamma PG (blue) and dose (black) simulated profiles along the beam direction for some exemplary head and neck (left) and abdomen (right) irradiation plans with PBT. Profiles are normalized for better visualisation. Figure by [106].

Besides the techniques mentioned above, several approaches of range monitoring use primary or secondary particles (protons or neutrons) or acoustic pressure waves [107, 108] generated by protons passing through the matter.

2.7.1 *PET range monitoring methods*

β^+activity distribution strongly depends on the elemental composition of the irradiated human tissue [109]. Due to that, several studies were

conducted to resolve the elemental composition of different tissues [49], which was needed to assess the activity distribution, especially in the case of inhomogeneous areas. Exemplary β^+activity distributions are depicted in Figure 13. In order to verify the treatment, the reconstructed PET signal is compared with the reference reconstructed PET image from the previous fraction. It helps to check the reproducibility of the patient irradiation [110]. In another approach, the accuracy of the activity distribution is checked with respect to the so-called true reference calculated using Monte Carlo simulations [16, 111] or less time consuming analytical approaches based on CT images and planned dose distributions [112, 113]. Recently, more sophisticated models calculating activity distribution have been introduced. They use additional tissue segmentation information from other imaging modalities - Dual-Energy Computed Tomography or Magnetic Resonance Imaging - and include wash-out effects [114, 115].

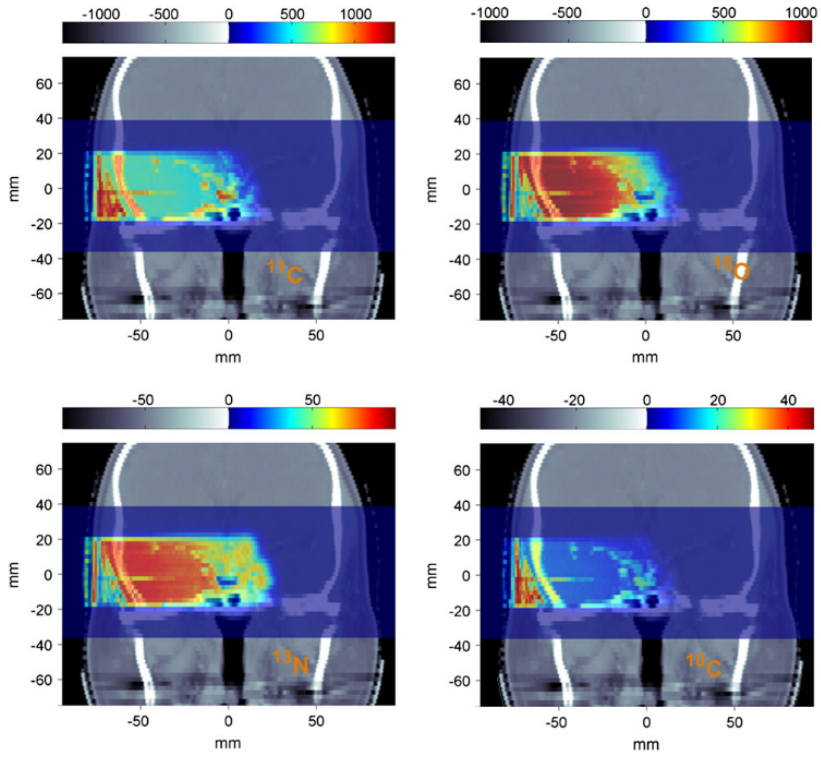

Figure 13: Example of the calculated spatial total β^+activity concentration produced during 1 Gy proton irradiation of a skull-base tumour. The most abundant β^+emitters: ^{11}C, ^{15}O, ^{13}N, and ^{10}C, contribute to this total activity. Isotopes concentrations are given in 10^3/ml (colour scale). CT images display in grayscale. Figure adapted from [109]

In analytical approaches, only the region that comprises the distal fall-off of the PET signal can be calculated and assessed with the convolutional filter functions [116]. This method is invertible and inverse filter functions could be used to deconvolute dose from the measured PET activity distribution. Some of them have been already validated experimentally [117, 118]. Other reconstruction methods based on machine learning or deconvolution struggle with wash-out effects and high image noise of the data acquired after the irradiation [119–121].

As the decay time of the most contributed β^+radioisotopes [122, 123] is in the order of minutes (Table 2) and various beam time structure is possible, four PET acquisition setups for range monitoring are considered [26, 124]:

1. In-room: Acquisition is performed just after the irradiation in the treatment room. The patient is transported from the irradiation gantry to the scanner located in the same room. Thus, relatively high counting statistics could be potentially collected.

2. Off-line: Acquisition is similar to the in-room approach. However the PET scan is performed in a different room. The time needed for patient transport and positioning leads to the lowest counting statistics.

3. Inter-spill: Acquisition is dedicated only for the synchrotron facilities, where the beam is delivered with the specific, modifiable time structure (described earlier within the text).

4. In-beam: Acquisition is performed during the patient's irradiation. It is characterized by high noise levels as all secondary particles could potentially contribute to the registered signal.

First off-line solutions for clinical application were tested at Hyogo Ion Beam Medical Center of Hyogo, Japan [125]. Next, the same method was tested and validated at the Massachusetts General Hospital (MGH) [111, 126–128], at the Heidelberg Ion-Beam Therapy Centre (HIT), Germany [129, 130] and the Proton Therapy Institute, University of Florida, Jacksonville, USA [131]. In all cases, commercially available PET or hybrid PET/CT scanners were used in measurements. All of them assured sufficient reproducibility and sensitivity [49], offering full ring coverage and high detection efficiency. Furthermore, additional information from CT images enabled proper co-registration between imaging and treatment patient position avoiding patient movement during the transport between treatment and imaging rooms.

The off-line imaging were improved by introducing the in-room approach, where the standalone PET scanner was situated in the treatment

room. PET scan was performed immediately after the irradiation, with the same treatment couch and patient immobilization if possible. It assured higher PET signal statistics and solved the co-registration problem (if the same couch and patient immobilization are used). On the other hand, as the duration of a patient's presence in the irradiation room increases, less number of patients could be potentially treated. This approach was tested at the MGH with the NeuroPET scanner [132, 133].

In-beam solutions was tested clinically so far at the GSI [16, 134], at the Heavy Ion Medical Accelerator in Chiba [135, 136], and the Kashiwa Center in Japan [110, 137]. Recently, at the Centro Nazionale di Adroterapia Oncologica (CNAO) in Italy [15, 138] PET detector, built within the INSIDE project framework, has been tested for inter-spill measurements. The differences between produced activities in two subsequent fractions have been investigated, showing reproducibility at the excellent submillimetre level. Detector setup and exemplary reconstructed PET images are depicted in Figure 14. Lastly, experiments with the DoPET system and various material phantoms were performed at the CCB [139, 140]. As the geometrical constraints of the beam, patient couch and additional medical equipment had to be considered, unconventional PET scanners configurations were simulated and proposed for the in-beam/inter-spill proton beam range verification such as dual-head scanners [15, 23, 138], axially shifted (single-ring OpenPET) or axially slanted full rings and dual ring [141–144] configurations. The differences between them are depicted in Figure 15.

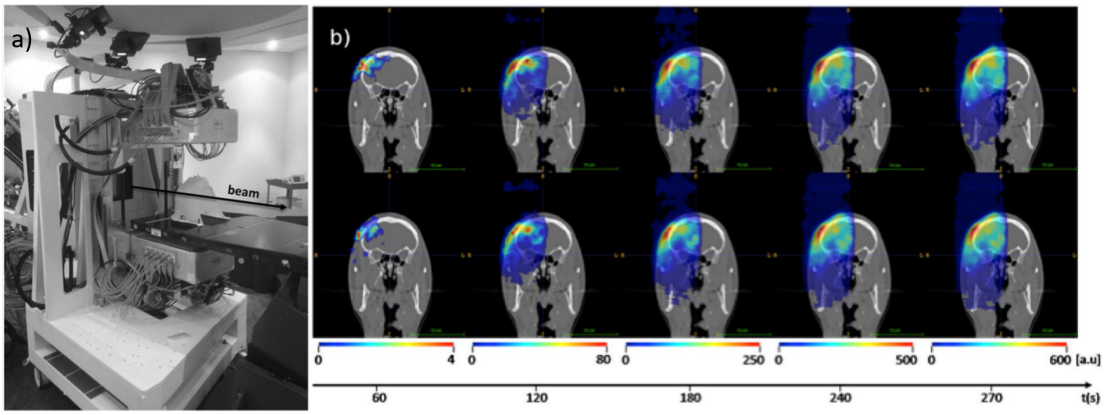

Figure 14: a) The prototype of the INSIDE PET detector developed at CNAO, Pavia. b) Reconstructed activities measured with the detector superimposed onto patient CT for two subsequent proton treatment fractions (top and bottom). Presented PET images were reconstructed every 60 seconds up to the final total activity, including 30 seconds post-irradiation acquisition. Figure adapted from [15]

In order to improve the in-beam approaches, TOF information could be used [23, 145]. Another promising milestone that can improve PET range verification and PET imaging, in general, is the community's ongoing efforts to bring ultra-fast detectors with TOF around ten ps, enabling real-time, reconstruction-less imaging and significantly reducing image artefacts, especially for unconventional configuration setups. Moreover, investigations towards quasi real-time imaging of the very short-lived β^+emitters (half-time in the millisecond range) such as ^{12}N are conducted [146].

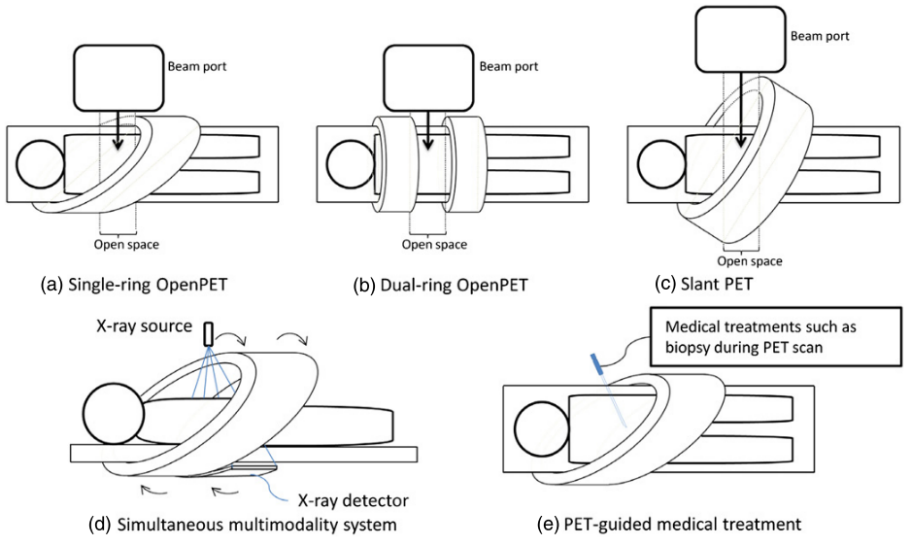

Figure 15: Conceptual illustrations of PET geometries with an open space accessible to the patient. The proposed single-ring OpenPET (a) has the shape of a cylinder cut at a slant angle and the beam port that can be placed near the patient bed, the same as in dual-ring OpenPET (b). Conventional cylinder PET can also provide an open space by placing it at a slant angle against the patient bed (c). Applications are shown as well for the single-ring OpenPET for PET-CT as a simultaneous multimodality system (d) and PET-guided biopsy as a PET-guided medical treatment (e). Figure adapted from [142]

More detailed information about the PET-based *in-vivo* range verification methods in hadron therapy can be found in [26, 49]. Generally, 1-5 mm range verification accuracy is expected for the PET range monitoring [7], unless co-registration of bony structures is applied where 1-2 mm accuracy is achievable [49, 111].

Range assessment methods

Several algorithms were proposed for the range verification. Knopf et al. [126] investigated the so-called 'Beam's Eye-View' method (BEV), considering the entire distal fall-off distributions at every (x,y)-coordinate. All activity profiles (in beam direction) are normalized to their maximum, shifted against each other and the profile difference is calculated only in the region between the last local maximum (z_{min}) and the end (z_{max}) of the activity profile. The shift is introduced to find the minimum difference between the activity profiles. The method's weakness is the problem with an identification of the last distal maximum in PET images where several local maxima are observed (see Figure 16). To overcome that issue, a most-likely-shift method was proposed [147]. It finds the optimal position z_{min} as the lowest difference between the activity profiles.

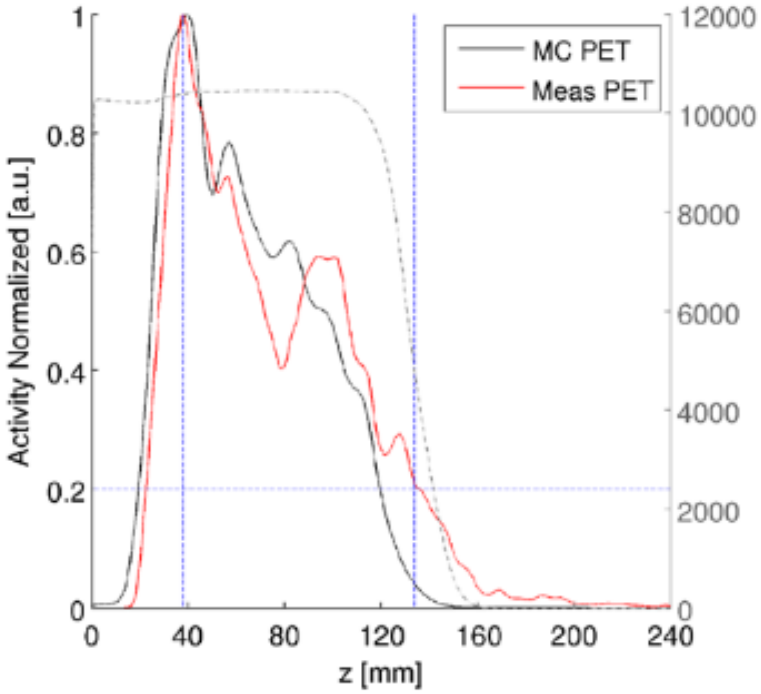

Figure 16: Normalized β^+-activity profiles (solid lines) obtained by Monte Carlo simulation (MC PET) and in-beam PET measurement (Meas PET), as well as the corresponding dose profile (dashed line). The blue (dashed straight) lines denote the location of the activity maximum, the 50% dose fall-off (vertically, left to right) and the 20% activity limit (horizontally). Figure adapted from [147].

Min et al. [133] introduced an analysis where the middle point was calculated as a mean of 50% and 25% fall-off depth positions. The difference between the middle points of two activity profiles is calculated and defined as a range difference.

Recently, Ferrero et al. [15] have introduced two methods for comparison of the activity distributions. First, the Overall View (OV) method has been derived, which is the extension of BEV where the range differences are calculated. Then, the Region Of Interest (ROI) is calculated considering every possible 3D direction to find the minimum Euclidean distance between contours. In the second method, PCC is calculated in a ROI including the activity distal fall-off. Another method developed by this group was presented in [138]. Here, an activity range distribution along the beam direction was calculated. Then, the difference between a set of activity range distributions was used to compare between two PET images. Due to the complexity of the method, more details could be found in the original publication [138].

Another PCC-based method for range assessment was introduced by Kuess and colleagues [148] to assure that rotational and translational shifts could be recognised.

In order to determine the difference between Monte Carlo calculated β^+production profile and the reconstructed PET data profile for the single proton beam in the PMMA phantom, Kraan and colleagues [149, 150] proposed to fit the error function to the proximal rise and distal fall-off of the reconstructed activity. Then, the difference between 50% rise and 50% fall-off position was calculated to verify the range assessment.

2.7.2 *Prompt gamma range monitoring methods*

The idea of using prompt gamma for range monitoring was presented for the first time in 2003 [151] and the first feasibility studies were performed three years later using a single detector with parallel slit geometry placed behind a collimator [152]. In general, prompt gamma devices could be classified into imaging and non-imaging systems. Imaging systems can be divided into mechanical and electronic collimation based apparatus. Non-imaging devices could be classified into prompt gamma timing (PGT), prompt gamma peak integral (PGPI) and prompt gamma spectroscopy (PGS) as they use information about the timing and/or photon energy [8].

Two main concepts are introduced in the literature for mechanical collimation: parallel multislit and knife edge cameras (pinhole cameras). Both approaches aim to build the system to detect prompt gamma orthogonally to the beam axis [153]. For the first method, position-

sensitive or multiple detectors are required, positioned behind the collimators. Several Monte Carlo studies were performed to optimise the geometry of the system [154], gathering the signal emitted from the whole beam path [155] and exploiting additional TOF information [153]. The first results showed promising results for the PMMA phantom, indicating the precision of the range retrieval at the level of 1–2 mm [156].

In contrast to the multislit solution, the knife edge approach has just one slit that allows obtaining 2D images. For proton therapy, a 1D profile along the beam direction is sufficient. The first approach of the pinhole camera was introduced by Kim et al. [157]. Next, the collaboration of IBA and Politecnico Milano built the prototype based on LYSO crystals and a standard HiCam system [158]. Feasibility tests with 100 MeV and 160 MeV protons impinged PMMA phantom revealed a 1-2 mm standard deviation in the range assessment. Further work to improve the first prototype (i.e. silicon photomultipliers were installed to read out the signal from the LYSO crystals) was performed [159]. The results up to 2 mm standard deviation of the range assessment in inhomogeneous targets with tissue equivalent inserts [160] and standard deviation smaller than 4 mm under close-to-clinical conditions (phantom head irradiation) were reported [161]. Moreover, shifts in the proton range on the 2-5 mm order could be distinguishable [162]. So far, it is the first prompt gamma solution used in clinical application [7, 163, 164]. The first results reported 2 mm inter-fractional global range variations (in agreement with CT information) [163]. The described system is depicted in Figure 17.

The idea behind the Compton camera is to use segmented detectors capable of registering two or more successive gamma-ray interactions. Coordinates of the interaction point link deposited energy with Compton scattering equations. It is possible to represent gamma-ray trajectory as cones with the vertices placed in the interaction points. The superposition of multiple cones is a gamma-ray production position. In principle, 3D imaging of the gamma rays is possible. Moreover, Compton cameras are very well adapted for prompt gamma imaging as Compton scattering is the dominant process for the gammas with energy on the order of a few MeV. In the Compton camera, electronic discrimination is applied, assuring higher detection efficiency [8]. Currently, Compton cameras are the subject of intensive research and many solutions are available. The solutions could be distinguished by different detector types: scintillators [165, 166], semiconductors [167, 168], a combination of scintillators and semiconductors [169, 170] or gaseous [171, 172]. Based on the reported assessment results, the system proposed by Polf and colleagues [167] utilizing room-temperature semiconductor

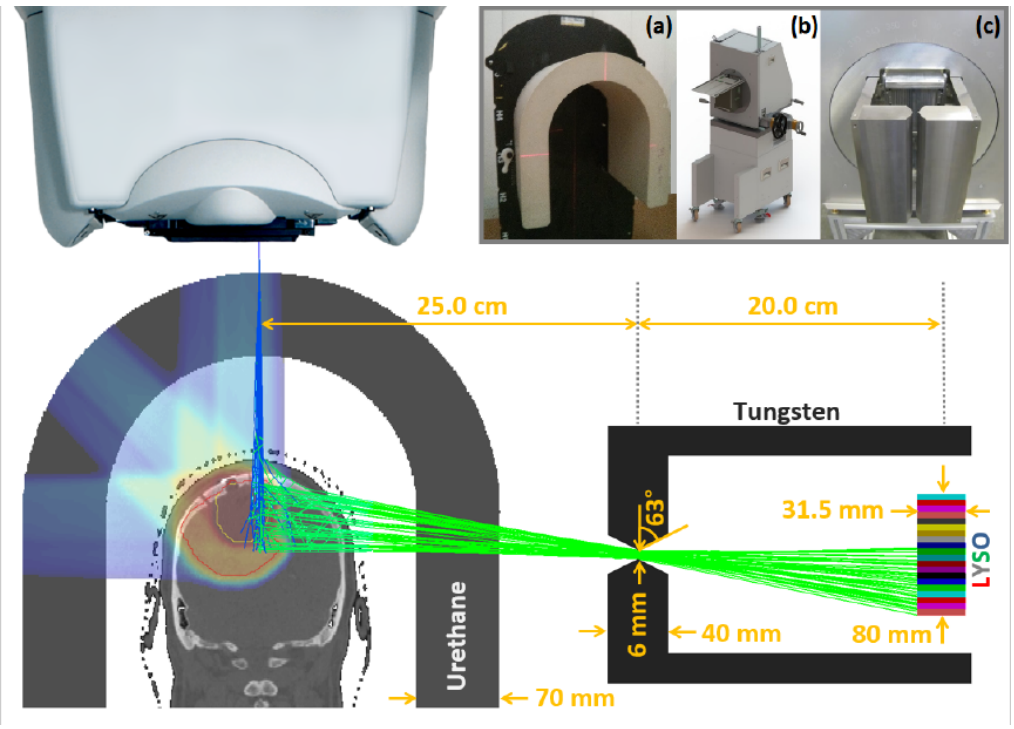

Figure 17: Scheme of the pinhole system for prompt gamma imaging. The gamma rays produced by primary protons (blue lines) pass through the aperture (green lines). The upper right inset presents a table-mounted U-shaped range shifter (a), camera trolley positioning system (b) and camera knife-edge slit collimator (c). Figure by [164].

detectors fully embedded in the treatment couch is worth mentioning. Recent experimental studies show the system's capability to reconstruct 3D images of the prompt gamma distribution and ability to determine range shifts on the order of 3 mm in phantoms [173].

Both PGT and PGPI methods rely on TOF information registered with the scintillator detectors. The transit time of protons with the therapeutic energy range is in the order of a few ns and depends on the proton path length. This phenomenon leads to the differences in the width of the prompt gamma TOF distributions for various energies (Figure 18). The mean value in the TOF spectrum will change with the target position changes. Furthermore, the broadening of the TOF distribution is observed as the primary beam energy increases and the thickness of the target is enlarged [174]. Recently, an experiment [175] with the clinical beam currents in the PBT scheme has been performed. It was shown that the uncertainties of 10.3 mm and 1.0 mm for spot (2.7×10^8 primary protons) and layer (3.8×10^{10} primary protons) are expected, respectively. For the lower statistics (single PBS spot with 1.0×10^8 primary protons), the uncertainty range was even higher (16.0 - 27.6 mm) proving that the

statistics was a major problem for PGT range verification. The peak integral of the prompt gammas TOF distributions (PGPI approach) was also investigated for the range verification by Krimmer and colleagues [176]. Measurements with PMMA phantom and 65 MeV protons revealed 3 mm range deviation in the proton range assessment for the 10^8 primary protons statistics.

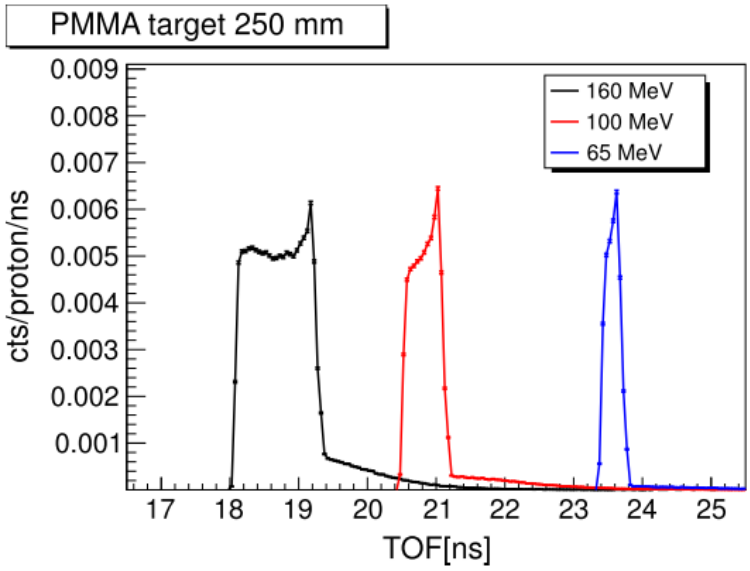

Figure 18: TOF prompt gamma distributions emerging from the PMMA phantom, produced by totally stopped 65 MeV (blue line), 100 MeV (red line) and 160 MeV (black line) proton beams. Figure by [8].

PGS is an alternative method for indirect range monitoring. It relies on the identification of specific prompt gamma-ray lines and their relative contribution. Time-resolved spectroscopic information with respect to the radiofrequency signal of the accelerator is used to extract information about characteristic emission lines from the background radiation [177, 178]. Recently, significant improvements in hardware for the new clinical prototype have been introduced and extensive test measurements with phantoms have been performed [179]. A millimetre range assessment precision and submillimetre accuracy at the level of summing neighbouring pencil beams to increase statistics have been reported. The scheme of the prototype is illustrated in Figure 19. Currently, preparation and recruitment for clinical trials at MGH are in progress [7]. An extended description of prompt gamma range verification methods can be found in [8].

The accuracy of the prompt gamma range verification method is associated with the performance of the gamma detector used. Since the development of an optimal detector is an ongoing research project, no

definite statement about achievable range verification accuracy can be made. However, considering recent developments, submillimetre precision in range measurement seems feasible [7, 49].

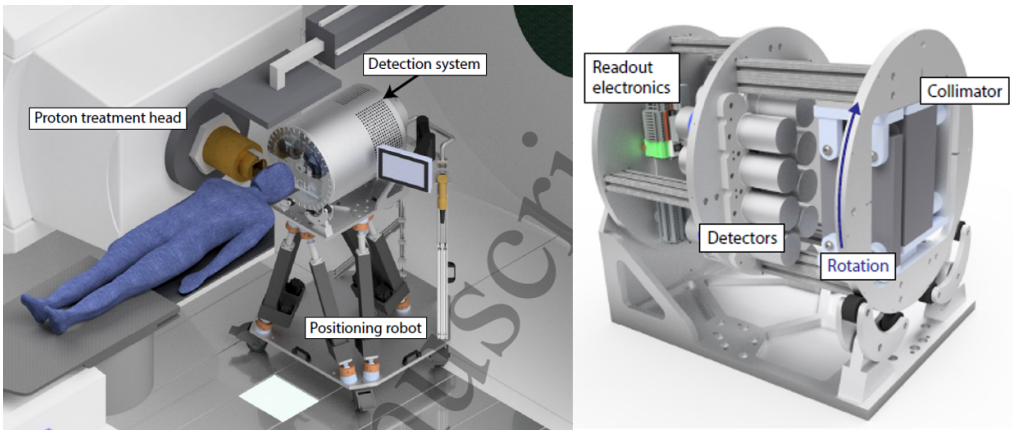

Figure 19: Left: Visualisation of the clinical prototype of the range verification system installed in the MGH treatment room. Detector of the system is mounted on a positioning robot and placed on a platform on wheels allowing unlimited movement. Right: The clinical prototype consists of a tungsten collimator, eight scintillation detectors and read-out electronics. The detector frame is feasible to adjust (rotate) to the gantry angle. Figure adapted from [179].

2.7.3 *Other range monitoring methods*

Next to the already described PET system [15], the Dose Profiler is being developed as a part of the INSIDE project [9, 180, 181] for the carbon beam range monitoring. It opens the possibility to monitor scattered secondary fragments with the energy enough to emerge from the patient. It consist of 7 layers of scintillating fibre trackers where charged fragments deposit energy in each layer, enabling reconstruction (back-tracking) of the trajectory. The detection principle with the Dose Profiler is shown in Figure 20. The first clinical-like experiment with an anthropomorphic phantom [9] shows that the Dose Profiler can perform fragment tracking at the design rate and back-tracking resolution of 7 mm at 50 cm from the patient. Currently, the preparation for the operation during the clinical trial phase is ongoing.

A similar approach to the Dose Profiler concept was presented by Bashkirov and colleagues [12] with the proton CT (pCT) dedicated detector [182]. The proof-of-principle experiment at the Northwestern Medicine Chicago Proton Center and Monte Carlo simulations were performed with the water phantom and pediatric head phantom. The pCT scanner

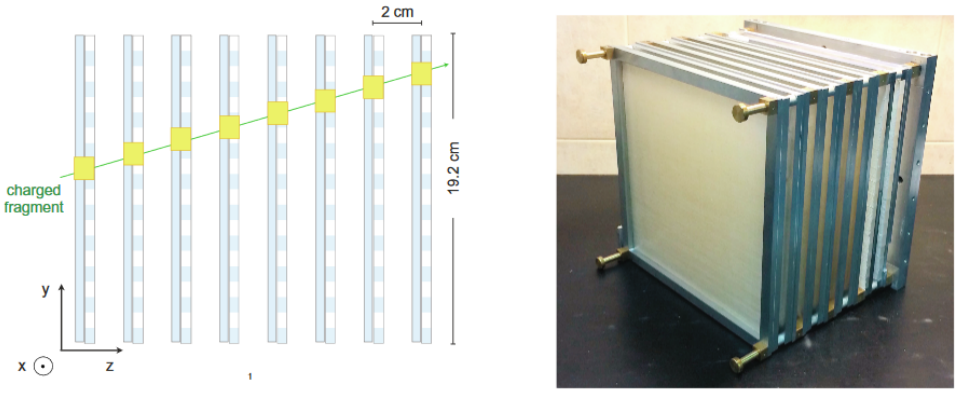

Figure 20: Left: Schematic view of the Dose Profiler, depicted with the detection principle based on the measuring of secondary fragments. Yellow squares indicate the place where the energy deposition occurs in the fibre (blue). The particle trajectory is shown in green. Right: Dose Profiler layers during the assembly. Figure adapted from [9].

was positioned at 90 degrees with respect to the proton beam axis in order to measure primary particles scattered at large angles during the irradiation. The first experimental and simulation results are promising. However, additional experiments and further improvements in data analysis are needed to fully exploit the feasibility of proton beam range monitoring with the pCT scanner.

MONDO project aims to develop of the tracking detector for the precise measurements of the secondary ultra-fast neutron flux, energy spectrum and angular distributions in the energy range of 20-400 MeV [11, 183]. The tracker consists of 800 layers of scintillating plastic fibres arranged in x-y oriented planes, orthogonal to each other. The operation principle of the detector is based on double elastic neutron scattering reactions. In a single elastic scattering reaction, a recoil proton is produced via (n, p) reaction (neutron interacts with a hydrogenated target) and proton momentum is correlated with the primary momentum of the neutron. Both recoil protons (from two consecutive elastic neutron scattering) are then detected with the same principle as in the case of the Dose Profiler. Thus, knowing the energy and direction of the recoil protons and incident neutrons, the energy and direction of incoming neutrons can be determined. The detector has not been validated in clinical-like conditions or phantom studies yet. Only Monte Carlo simulations and experiments with proton beams and cosmic rays have been performed [184].

The last but not least group of methods extracts the beam range from the thermoacoustic emissions resulting from the volume heated by the radiation-induced energy deposition. Waves' properties: amplitude, fre-

quency and shape strictly depend on the material and deposited energy. Two characteristic pressure waves could be generated [185]. The first one (α-wave) is produced in the pre-peak Bragg region and has a cylindrical shape. The second one (γ-wave) is emitted by the Bragg peak region and has spherical shape. TOF information about γ-wave arrival (τ^{γ}) is used to calculate the distance (l) between the Bragg peak and the detector assuming that speed of the acoustic wave (v) is known, using a simple rule: $l = v \cdot \tau^{\gamma}$. Submillimetre precision has been already presented in proof-of-principle experiments with water phantom and proton beams with clinically used energies [107, 108]. An additional simulation study with patient data reported accuracy better than 1.6 mm [186].

3

THE APPROACH

The first part of the chapter introduces the concept of using the J-PET technology for proton beam range monitoring. Considerations on the detection efficiency are given, along with the description of the investigated geometrical configurations based on plastic scintillators.

In the second part, the complexity of the problem explored in the thesis is explained. Proton beam irradiation, origin of β^+signal in the patient, J-PET detector response, PET data acquisition, corrections and reconstruction, range assessment method and the comparison between the investigated geometrical configurations are described.

Lastly, the rationale for software selection is given. Requirements for the Monte Carlo simulations and PET data reconstruction toolkits with the considered software are presented. Furthermore, the rationale for using the GATE and CASToR toolkits with their short overviews is given. Additionally, the toolkits functionalities and PET data reconstruction workflow used in the thesis are explained.

3.1 CONCEPT OF THE J-PET SCANNER TECHNOLOGY FOR PROTON RANGE MONITORING

Requirements for the PET-based range monitoring protocol depend on geometrical configuration of the detector. For off-line and in-room modes, one of the limitations is the room size. It is critical to ensure that the scanner fits into the room enabling unrestricted rotation of the proton gantry and treatment couch between the irradiation of consecutive treatment fields, when the patient is positioned on the couch. For in-beam and inter-spill scenarios, integrating the PET scanner in the treatment position is not trivial. The patient is typically irradiated from various directions and the gantry nozzle has to rotate around the patient. In addition, couch has to move freely between the irradiation fields and the PET scanner components cannot overshadowed the beam. Therefore, the PET scanner for in-beam and inter-spill acquisition modes is differently shaped from the cylindrical PET scanners conventionally used for diagnostic imaging. Axially shifted, axially slanted and dual-head configurations were depicted in Figure 15.

A crucial aspect that has to be considered in the context of the proton beam range monitoring is the quality of the PET signal related to the

number of registered coincidences. The fraction of coincidences that are used for image reconstruction does not exceed 1 % [96] for 2-mm-thick LYSO crystals (for 20 cm diameter water phantom with uniformly distributed activity) and is even lower for the plastic scintillator used in J-PET [98]. One solution for the crystal-based system to improve the PET signal quality is to increase the crystal's thickness leading to significantly higher price of the detection system [96]. As the plastic strips of the J-PET are relatively cheap and have the photomultipliers at their ends, three options for improving the PET signal quality could be considered:

- increase of the plastic thickness (as in the case of crystal scintillators),
- adding subsequent layers of the plastic strips/modules,
- increase the length of the scintillators to enlarge the FOV.

It also raises the cost of the system, but the price difference is not as substantial as in the case of crystals [96]. In this work, six configurations of PET scanners based on J-PET technology are investigated (Figure 21). All of them are built out of J-PET modules. The first three configurations have a cylindrical (barrel) shape with one, two or three layers of modules, whereas the three others are built as dual-heads. Single, double and triple layer barrels are built out of 24, 48 and 72 modules, respectively. Each layer of the multi-layer system consists of the same number of modules. For dual-head configurations - 12, 24 and 24 modules are simulated for single, double and triple layer setups. The exact number of modules (24) is also modelled for the single layer barrel. Studies with those configurations could be experimentally validated since a modular J-PET prototype with one layer consisting of 24 modules has already been built at the Jagiellonian University.

One of the aims of the Monte Carlo simulations conducted in the frame of this thesis was to determine an optimal setup configuration for in-room range monitoring of the therapeutic proton beam. The J-PET scanner geometry based on modules was simplified with respect to the actual prototype and is depicted in Figure 22. In particular, the covers at the strip ends, kapton and reflective foils were not simulated [17]. Moreover, simulations of the optical photon propagation within the plastic scintillators were also skipped. This was a reasonable assumption because the application of kapton and reflective foils caused the propagation efficiency of light in the plastics reach almost 100% [17, 97, 98]. The radius of the barrel, defined as a distance between the isocenter and centre of the innermost strip in the module, was set to 381.86 mm as

it is in the modular J-PET prototype. The distance from the isocenter to the detector surface is equal to 312.25 mm for the dual-head setups. It corresponds to the distance of 300 mm from the isocenter to the face of the plastic scintillator. 300 mm distance is a compromise between a reasonable geometrical acceptance, and the patient's comfort during the irradiation and PET signal acquisition. It also assures sufficient space to avoid collision with the treatment couch. A gap between layers is fixed for all setups and equals 44 mm (the distance between opposed strip surfaces from contiguous layers). The modules in the barrels are positioned parallel to the z-axis. In contrast, the modules in dual-head configurations are positioned perpendicular to the z-axis. It is motivated by the potential improvement of the PET detector resolution, which in this configuration is determined by the scintillator width equal 6 mm [23, 187].

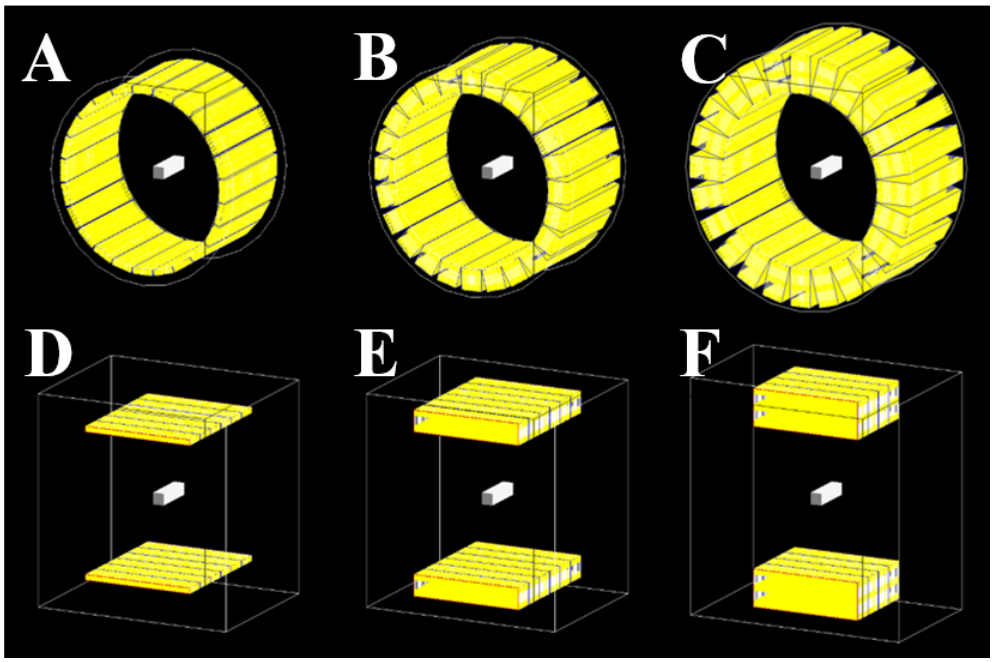

Figure 21: J-PET panel configurations considered in this work for Monte Carlo simulations: single layer barrel (A), double layer barrel (B), triple layer barrel (C), single layer dual-head (D), double layer dual-head (E), triple layer dual-head (F) with an isocentrically positioned PMMA phantom.

A brief summary of the J-PET module configurations is presented in Table 3. Schematic visualization is depicted in Figure 22.

One of the parameters characterizing the construction of the scanner is the geometrical acceptance (ω). For all barrel configurations, geomet-

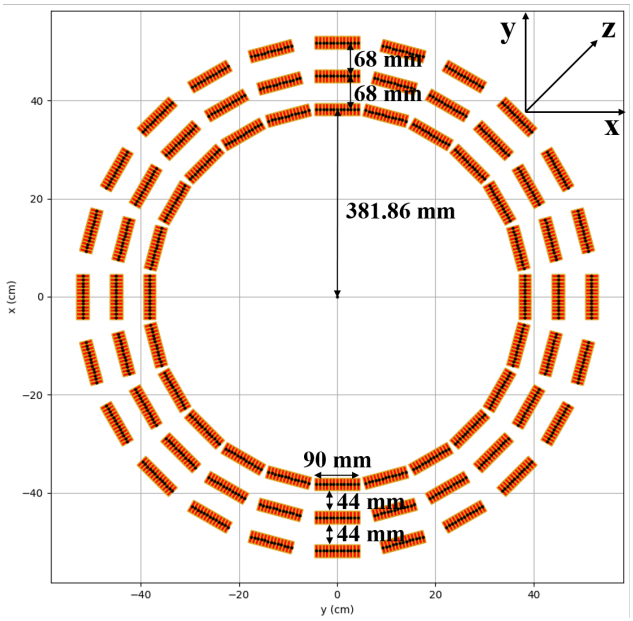

(a) Setup: triple layer barrel

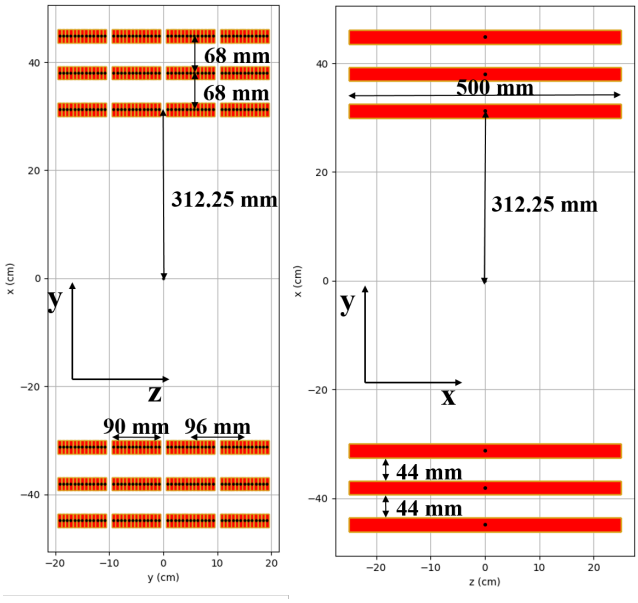

(b) Setup: triple layer dual-head

Figure 22: A schematic sketch of the triple layer barrel (top - transaxial view) and triple layer dual-head (bottom - axial view on the left and transaxial view on the right) scanners. For the double and single layer configurations, one and two outermost layers are removed, respectively. For the single and double layer dual-head configurations, two additional outermost modules in each layer are added. Additionally, the coordinate system used in the thesis is presented.

rical acceptance (ω) is the same and could be determined by the coverage of the solid angle by the first layer:

$$\omega_{barrel} = \frac{\alpha}{\frac{\pi}{2}} = \frac{\arctan\frac{l}{R}}{\frac{\pi}{2}} \approx 0.38 \tag{18}$$

where R is a first layer barrel radius and l is a half the length of the plastic scintillator strip. A schematic view and the description of the parameters of the calculation is depicted in Figure 23. The above calculations are performed for the centre of the scanner and do not consider gaps between the adjacent modules.

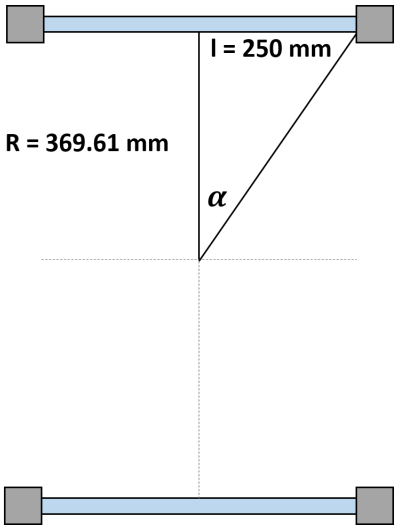

Figure 23: Schematic presentation of the geometrical acceptance. The dimensions are given for barrel setups.

The geometrical acceptance of the dual-head configuration is depicted in Figure 24 [188] and can be calculated as:

$$\omega_{dual-head} = \frac{8 \cdot \arctan\omega}{4\pi} = \frac{8 \cdot \arctan\frac{ab}{h\sqrt{a^2+b^2+h^2}}}{4\pi} \tag{19}$$

where a is a half-length of the head along the y-direction (237 mm for single and double layer dual-head setups and 189 mm for triple layer dual-head configuration), b is a half-length of the plastic scintillator strip (250 mm) and h is a distance between isocenter and first layer plastic scintillator surface (300 mm).

The values of geometrical acceptance for all the configurations are given in Table 3. They vary between 0.22 and 0.38. In addition, in order

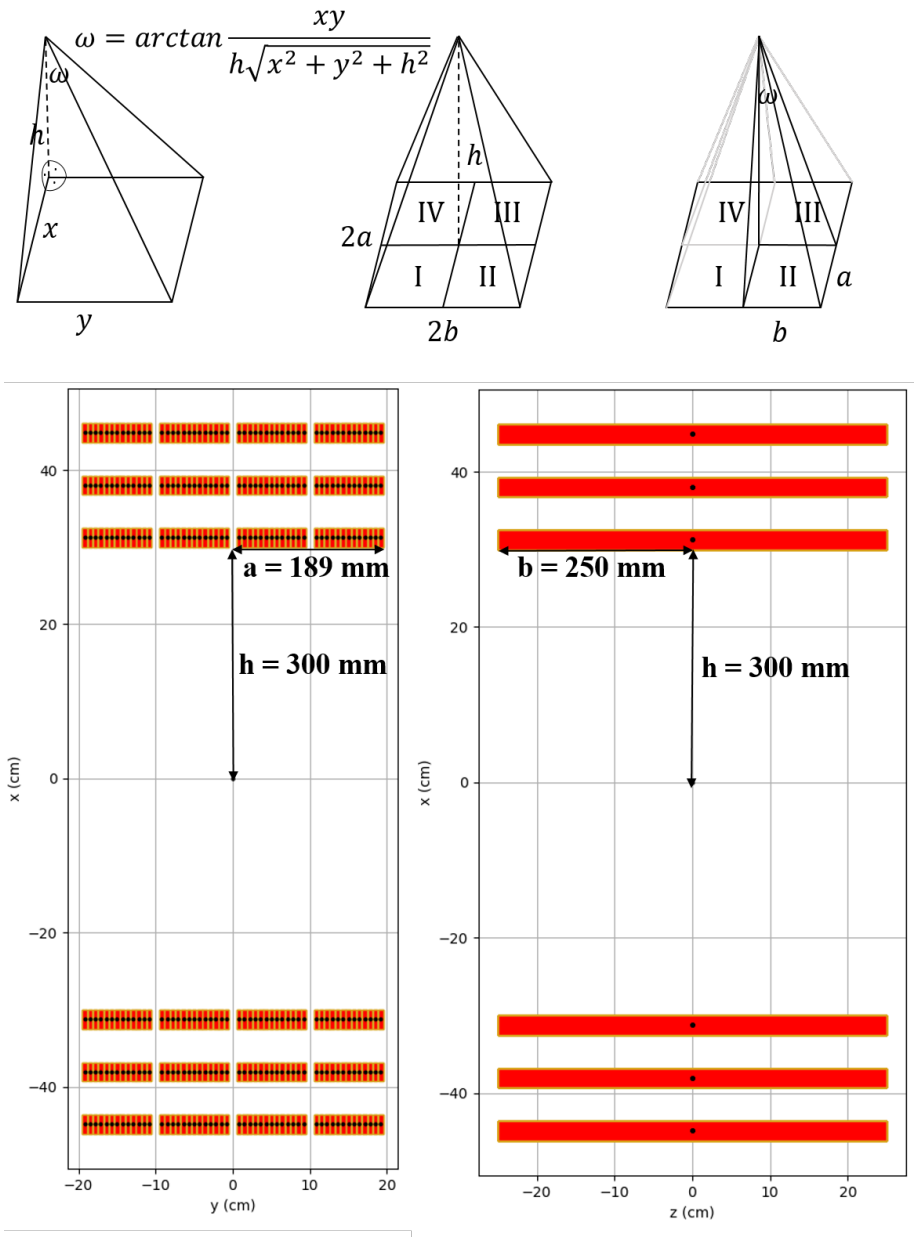

Figure 24: Scheme for calculation of the geometrical acceptance of the triple layer dual-head configuration. The top row explains the procedure of the calculation. The equation for ω is used to calculate the solid angle for the rectangular pyramid where one of the edges is also the pyramid height (top left). As the geometrical acceptance is calculated for the middle point of the scanner, $\omega_{dual-head}$ could be calculated as a sum of 4 identical ω calculated for the rectangular pyramid (8 considering two heads) - top middle. The calculation of the single ω is shown in the top right picture with the corresponding values depicted in the bottom row. Corresponding values of a, b and h for triple layer dual-head are given.

to compare different geometrical configurations, the efficiency factor (η) has been calculated as:

$$\eta = \frac{N_c}{N_p} \tag{20}$$

where N_c is a number of registered coincidences and N_p is a number of simulated back-to-back gamma pairs (Chapter 4) or primary protons (Chapter 5 and Chapter 6).

Table 3: Geometrical acceptance of the detectors in different geometrical configurations.

SETUP	NUMBER OF MODULES	NUMBER OF MODULES PER HEAD	NUMBER OF MODULES PER LAYER (IN HEAD)	GEOMETRICAL ACCEPTANCE
Single layer barrel	24	n/a	24	0.38
Double layer barrel	48	n/a	24	0.38
Triple layer barrel	72	n/a	24	0.38
Single layer dual-head	12	6	6	0.26
Double layer dual-head	24	12	6	0.26
Triple layer dual-head	24	12	4	0.22

3.2 THE GENERAL WORKFLOW TO SIMULATE THE RESPONSE OF THE J-PET SYSTEMS FOR RANGE MONITORING IN PROTON THERAPY

In this section a general workflow is described, to simulate the response of the PET system, based on the novel J-PET detectors, to measure the β^+activity induced by scanning proton beams and in consequence to monitor the range of the beam. The workflow proposed in the thesis could be divided into five main components.

In the preparation phase (pre-processing), the data on the irradiation conditions is to be collected. In particular, the treatment plan with all the contributing pencil beams has to be prepared. The beam model should be available for each individual pencil beam in order to prepare input for Monte Carlo transport calculation. In addition, the Computed Tomography (CT) scans should be available to prepare the treatment plan and to assess the attenuation of annihilation photons, emitted from the proton induced β^+activity.

In the first stage, the simulation of the β^+distribution activity induced during proton beam irradiation is calculated. The distribution depends on the above mentioned beam properties (beam model), CT image of patient or phantom, and CT calibration (converting the HU into atomic composition and relative stopping power). As a result of these calculations, the emission map of photons, originating primarily from the annihilations is produced.

In the next step, the performance of the investigated PET scanner built out of the J-PET detection modules is assessed. First, the acquisition of the coincidences based on the signal detected within the detectors is modelled. The coincidences list is scored in a Monte Carlo routine to collect information on geometrical positions of all β^+radioactive emissions induced by the proton beam. The PET activity distribution in phantom and patient varies between different possible acquisition modes. In the off-line mode, detector response cannot be affected by secondaries produced by the proton beam. In this thesis only the in-room mode was investigated.

In the following stage of the modelling, the reconstruction of the PET imaging is performed. The reconstruction is an iterative process, which should be optimized with regard to the optimization time and the image quality. One of the approaches to derive the optimal number of iterations is the application of the Maximum-Likelihood Expectation-Maximization (MLEM) reconstruction algorithm. PET images are also prone to various correction factors [68] (see Section 2.5.3). Some corrections are impossible to incorporate depending on the acquisition mode, e.g. scatter correction techniques are challenging to implement in real-time. It is impossible to incorporate scatter information during in-beam or inter-spill acquisition [15]. In this thesis attenuation and sensitivity corrections were applied.

Finally, the analysis of the PET images is performed to improve the quality of images and to derive information needed for the assessment of the proton range. The range calculation analysis is needed to compare quantitatively and qualitatively between the geometrical configurations of the PET scanners and to find the accuracy of the beam range assessment. The choice of the range assessment method will depend on the acquisition mode. More sophisticated methods might be used for the off-line or in-room applications where the analysis is performed after the irradiation followed by the PET image acquisition. On the other hand, simple approaches will be appropriate for in-beam and inter-spill modes as the analysed result must be given during the patient treatment (see Section 2.7.1).

The complexity of the problem described in the thesis: proton beam irradiation, proton beam induced β^+signal in phantom and patients, the study of the properties of various J-PET modules, geometrical configurations, expected performance and relative difference, require complex toolkits to handle all these aspects. Analytical approaches (if they exist) are not so sophisticated and typically cover just one part such as proton beam induced β^+activity (Section 2.7.1). Therefore, more comprehensive solutions have to be considered. In this work, Monte Carlo simulations were used to mimic reality with the required accuracy.

3.3 RATIONALE FOR SOFTWARE SELECTION

Simulation software should calculate proton transport in the patient, production of the β^+activity in nuclear reactions induced by proton beam and the corresponding PET imaging of the induced β^+activity. Ideally, the calculations should be relatively fast (GPU or multi-threading support) and the output of the simulations (coincidences list) should be compatible with the software used for the reconstruction. Two simulation software toolkits were considered for the purpose of Monte Catlo simulations performed in this thesis: FLUKA [38, 189] and GATE [56]. Recent developments of FLUKA [189] enable the entire working pipeline starting from the simulation of proton irradiation throughout the PET reconstruction. However, lack of the attenuation correction and time-of-flight modelling in FLUKA restrict the potential availability of this software for the purpose of this thesis to Monte Carlo simulations only. Therefore, an alternative tool, GATE software, is dedicated for the Monte Carlo simulations having the same functionalities as FLUKA in terms of proton irradiation and more comprehensive tools for simulations of the PET imaging, e.g. coincidence sorter capabilities. Moreover, open-source PET reconstruction toolkits offer automatic conversion of the coincidences list from GATE to the file format specific for this software. Taking into consideration all pros and cons, Monte Carlo simulations were performed in GATE software.

In order to exploit the feasibility of the J-PET technology for the proton beam range monitoring, reconstruction of PET data simulated in GATE is necessary. There are three aspects of the J-PET technology which the reconstruction software should address: 1) multi-layer configurations 2) TOF modelling along the LOR and 3) TOF modelling along the plastic scintillator strip (see details in Section 2.6). Due to the specific design of the J-PET scanner, none of the existing PET reconstruction software toolkits does offer a solution for modelling the TOF along the strip. Some of the projects support multi-layer reconstruction (e.g. STIR [83], CASToR

[86], PRESTO [80]). Among several available open-source solutions (described in Section 2.5.2.2), two were considered: CASToR and STIR as the ones with the greatest capabilities, community and developers support. However, at the time when the decision was made, STIR did not support TOF modelling and CASToR software was selected.

All the scripts for both GATE Monte Carlo simulations and PET CASToR data correction, processing and reconstruction used and/or newly developed for the purpose of the thesis are open-source, available to download from the Github repository of the author of this thesis (`https://github.com/jawka`).

3.3.1 *Monte Carlo simulation framework and proton beam modelling*

GATE software was developed within the OpenGATE collaboration. GATE exploits Geant4 features (validated physics models, sophisticated geometry description, powerful visualization and 3D rendering tools) with tools dedicated to emission tomography and ion radiotherapy (GATE-RTion). Software is also dedicated to users who prefer the more straightforward interface and simulation process preparation than the C++ coding required to use Geant4. Due to the open-source character of the GATE project, the developers are welcome to propose new applications and software solutions.

Among all GATE functionalities, a few were used in the thesis and enumerated below:

- built-in sets (lists) of physics models embedding various interactions types characterized by specific production cut-offs dedicated for clinical applications, e.g. nuclear medicine or proton and ion radiotherapy,
- tools for the geometry handling offer the user define setups or support for CT images, which are crucial for simulations of the therapy treatment planning and PET imaging,
- actors - scoring tools that interact with the simulation kernel in order to save specific information needed by the user, e.g. PhaseSpace actor scores secondary particles or particles which enter/leave the given volume; Dose actor stores information about deposited energy/dose in a given volume,
- radiation sources with the support of dedicated software import and export tools; treatment plan optimized in the clinical TPS can be simulated on the CT grid of the patient using proton beam model,

- digitizer and coincidence sorter needed for PET imaging enabling to model energy and spatial resolutions of the detector, electronics characteristic (digitizer), combined coincidence windows - prompt and delay - and multiple coincidences handling,
- a list of coincidences is stored in a ROOT file format, which is easy to automatically convert to the file format required by PET reconstruction software tools.

In this thesis, all the simulations were performed with the GATE software version 8.2 equipped with Geant4 version 10.4.2.

The simulation scenarios presented in the thesis require individual geometry, radiation source definitions, scoring settings and sets of physics models. For this reason, scenario-specific simulation parameters are described separately for each experiment in the Materials and Methods sections of the subsequent chapters. However, the parameters common to all simulation scenarios are listed below:

- Deposited energy of both coincidence photons has to be in the range of 200-380 keV. The coincidence is reported if the time difference between registered photons is lower than three ns.
- GATE coincidence sorter is used to analyze and process coincidences lists. A default GATE multicoincidences policy was chosen (GATE flag: keepIfAllAreGoods) - multicoincidences are discriminated. A more detailed explanation could be found in reference [190].
- Since CASToR reconstruction software does not support TOF modelling along the J-PET strip, the 50 cm long strips were artificially discretized into 100 0.6x2.4x0.5 cm^3 crystals. The strip discretization into 5 mm crystals is performed because the TOF resolution along the strip is expected to be at the level of σ=5 mm [191].

3.3.1.1 *GATE Monte Carlo simulations of the proton beam used in CCB*

In order to perform simulation studies of phantom irradiation with proton beams, parameters characterizing the CCB proton beam characteristic were implemented in the GATE simulation framework. This part of the work was based on the previous studies of Jan Gajewski with GPU-accelerated FRED Monte Carlo software [62] and measurements in the collaboration with the CCB Dosimetry and Quality Control Section. For the purpose of these simulations, the proton beam model for one of the CCB gantry rooms was derived.

Phase space of parameters constitutes the beam model, characterising a proton pencil beam. The beam is typically modelled at the nozzle exit [192]. All the simulations presented within the thesis were performed with the GATE software [56] and the beam model described by nine parameters for each measured nominal beam energy [44]:

- two energy parameters: mean energy ($\widehat{E}$) and energy spread(σ_E),
- six optical parameters of the beam: spot size in mm (σ_x and σ_y), beam divergence in rad (σ_θ and σ_ϕ) and beam emittance (M_x and M_y) in mm $\cdot$ rad; each in x- and y-directions,
- one dosimetric parameter, i.e.calibration factor ($q_{N/MU}$): number of primary protons per monitor unit [$p+/MU$].

Exemplary spot sizes (σ_x and σ_y) for the CCB modelled with FRED software along the beam direction is shown in Figure 25.

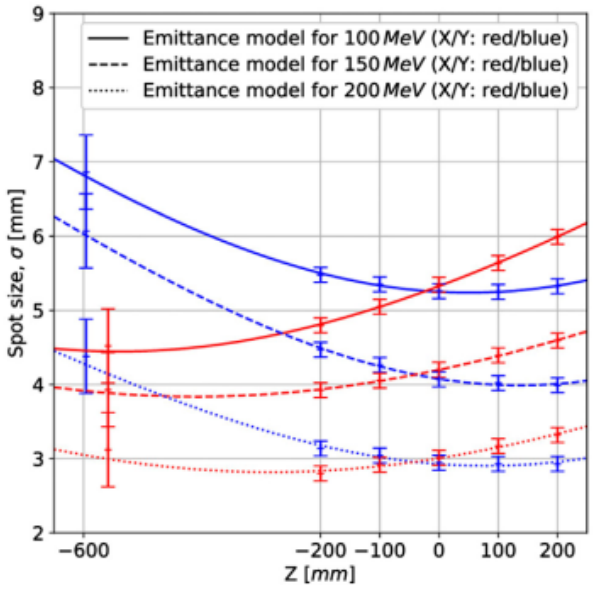

Figure 25: The spot size of the pencil beam in air, as measured at CCB. Figure adapted from [63].

Additionally, information about the distances between nozzle exit to the isocenter (1680 mm) and dipole magnets to the isocenter (2215 mm and 1846 mm for scanning magnet in x and y direction, respectively) had to be specified. As the beam model preparation itself is out of the scope of this thesis, more detailed explanations of the beam model parametrization, preparation and experimental validation may be found in [44, 192, 193].

For the commissioning of the Eclipse TPS, the measurements of proton pencil beam parameters in air and in a water phantom were performed

by the CCB Dosimetry and Quality Control Section for the nominal energies from 70 MeV to 226 MeV in 10 MeV steps. Twiss parameters[194], describing the lateral propagation of the beam for 17 distinct nominal energies, were then modelled by Jan Gajewski using GPU-accelerated FRED Monte Carlo software [62] to speed up the parameter optimization process (GATE does not support GPU). Then, to meet the GATE software requirements the results were interpolated by the author to the whole energy spectrum using polynomial equations as required by GATE format and described in [190]. The beam model parameters and fitted polynomials are depicted in Figure 26.

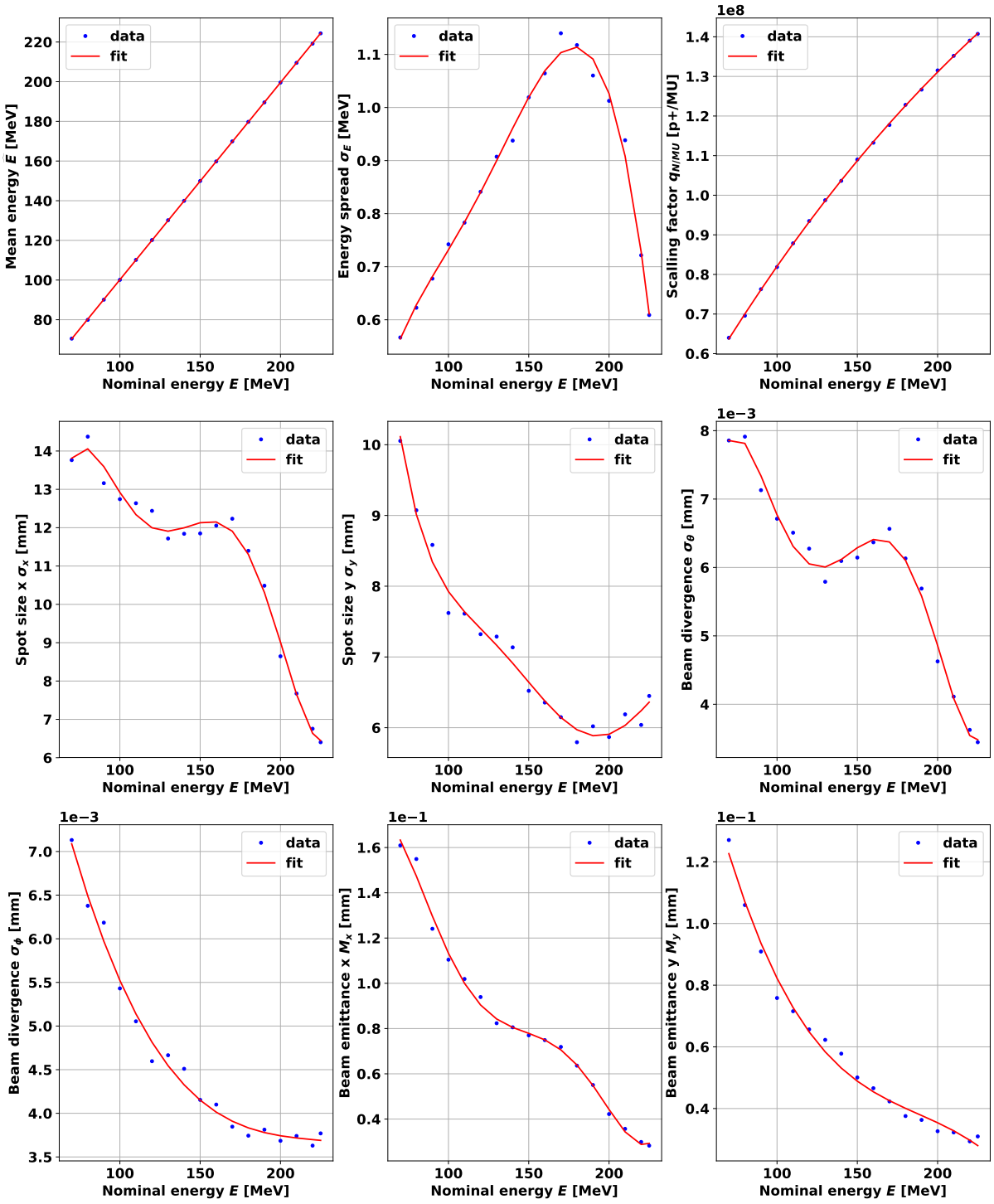

Figure 26: Energy-dependent parameters of beam model for the Pencil Scanning Beam model at the gantry 1 (GTR3) at the CCB.

3.3.2 *PET image reconstruction framework*

CASToR is an open-source project dedicated to 4D transmission (CT) and emission (PET and SPECT) tomographic reconstruction. The CASToR project aims to provide a user-friendly framework that offers basic image reconstruction features for non-expert users and more advanced tools for the reconstruction specialists and developers. New reconstruction algorithms, projectors, dynamic data modelling, kinetic models and others could be implemented in the framework of the CASToR. The generic character of the CASToR software and flexibility in the selection of the input data file format caused that all information needed for the reconstruction: list-mode or histogram data format, normalization, attenuation correction, scatter correction, random correction, etc. has to be pre-computed and incorporated in the input data file by the user. One of the advantages of CASToR is that it can be executed in multi-thread and multi-computer modes. CASToR ver. 2.0.3 was used in this dissertation.

A schematic workflow of the PET data reconstruction with CASToR is depicted in Figure 27. Coincidence data could be provided in both list-mode or sinograms format. In Monte Carlo simulations with GATE, developers provide the converter of the coincidence list from GATE in ROOT file format to the CASToR format. However, corrections factors (attenuation, normalization, sensitivity, scatter coincidences, random coincidences) for the PET reconstruction have to be calculated by the user. Ideally, all the corrections should be given for each LOR independently [195]. There is no option, in official release of the CASToR ver.2.0.3, to provide the sensitivity and attenuation corrections as a map with the values given for each voxel at the same time. CASToR will not calculate corresponding correction factors for each LOR [195]. In the presented workflow, sensitivity maps represents the voxel-vise probability that emitted back-to-back 511 keV gamma quanta will be registered with the J-PET scanner as the coincidence. If the sensitivity map is provided, there is no possibility for the attenuation correction map to be incorporated in the reconstruction. If the attenuation correction map is provided, the scanner sensitivity map is calculated internally by the CASToR software considering only the geometrical acceptance. In crystal scintillators such as LSO, BGO, where gamma quanta detection efficiency is high, the calculation is correct. However, for the J-PET based scanners, the sensitivity map calculation using CASToR is not valid. Plastic scintillators are long and for very oblique planes the possible path of the interaction within the strip is longer. As a result, the probability of the energy deposition increases significantly [97] with respect to the direct

planes. To overcome this J-PET-specific issue, CASToR developers shared with the thesis author dedicated CASToR functionality (-opti SENS). It enables merging the attenuation correction map with sensitivity correction information delivered in the list-mode format into a single map containing both attenuation and sensitivity corrections. As the full characteristic of the digital J-PET system was not achievable at the moment of the thesis preparation, normalization correction (as described in Section 2.5.3) was impossible to include in reconstruction. However, the sensitivity correction concept replaced it. For the list-mode reconstruction, only the MLEM and TOF-MLEM reconstruction algorithms are available in CASToR and were used in the thesis.

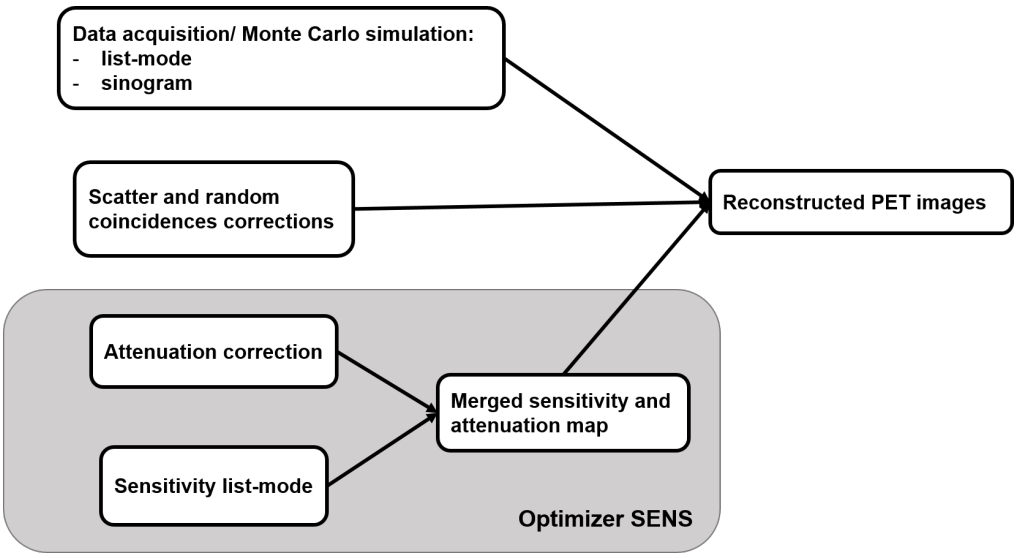

Figure 27: The workflow to reconstruct the PET images with the CASToR software.

In order to reconstruct the PET data, the merged sensitivity and attenuation map is forward projected by CASToR. The resulting system matrix H is than used for the image reconstruction. Scatter and random corrections were not investigated and incorporated in the reconstruction framework presented in this work.

Preliminary experimental tests of the digital J-PET system show that expected TOF resolution along the LOR is about 500 ps and this value was used for the reconstruction. The reconstruction was performed using true and scatter coincidences unless mentioned otherwise. All the data were reconstructed with the list-mode TOF-MLEM algorithm with the Siddon projector [93]. Reconstruction FOV was equal to 400x400x400 mm^3 for triple layer dual-head and 400x400x500 mm^3 for other geometrical configurations. The voxel size was fixed for all configurations: 2.5x2.5x2.5 mm^3. Both attenuation, and merged sensitivity and attenu-

ation maps had the same voxel size as the reconstruction FOV. MLEM cost function does not use any prior converging to the image that fits the "best" to the data. However, in case of low statistics or data fitting too closely (more iterations were used than optimal), the ill-conditioned problem leads to the high frequency "checkerboard-like" artefacts [74]. One of the solutions is the usage of analytical algorithms such as FBP. Another approach that was used in this thesis is post-reconstruction image filtering. Typically a 3D Gaussian filter is used with the FWHM related to the spatial resolution [74]. Post-reconstruction 3D Gaussian smoothing (σ equal to 2 voxels in transaxial and axial directions) was applied unless mentioned otherwise.

4

PET DATA RECONSTRUCTION

This chapter introduces PET data reconstruction performed in this thesis with the CASToR toolkit. The work started with Monte Carlo simulations performed with GATE code. Then, in the validation of the workflow, the cuboid phantom with uniformly distributed activity was applied.

In the next step, PET data correction for sensitivity and attenuation (correction maps) were computed and applied to all reconstructed PET images. Finally, the procedure of the merged sensitivity and attenuation correction map calibration is presented. These correction maps improve the quality of the reconstructed images as described in Section 2.5.3.

Random and scatter corrections were not considered in the thesis. Our Monte Carlo simulation setup was not designed to record the random coincidences (Chapter 4 and Chapter 6) or its sensitivity was relatively low (Chapter 5). Lack of the scatter correction leads to higher activity reconstructed in the center of the phantom with respect to the borders of the phantom. Implementation of the scatter correction is challenging, as discussed in Section 2.5.3 and is out of the scope of this thesis.

4.1 MATERIALS AND METHODS

4.1.1 *Reconstruction workflow*

A cuboid water phantom (25x25x30 cm^3) with the uniformly distributed activity source was simulated as depicted in Figure 28. The phantom was positioned isocentrically in the FOV of the J-PET detector. The activity source was defined as a total number of 10^9 back-to-back 511 keV gamma quanta propagated isotropically in all directions. For GATE simulations, emlivermore_polar physics list [17] was used to enable electromagnetic interactions of the gamma-rays with J-PET. In addition, to avoid random coincidences, back-to-back gammas from subsequent events were generated at 1 μs time intervals, while the acquisition time was set to 1000 seconds. Finally, the simulation results were used in order to validate the PET data correction and reconstruction workflow.

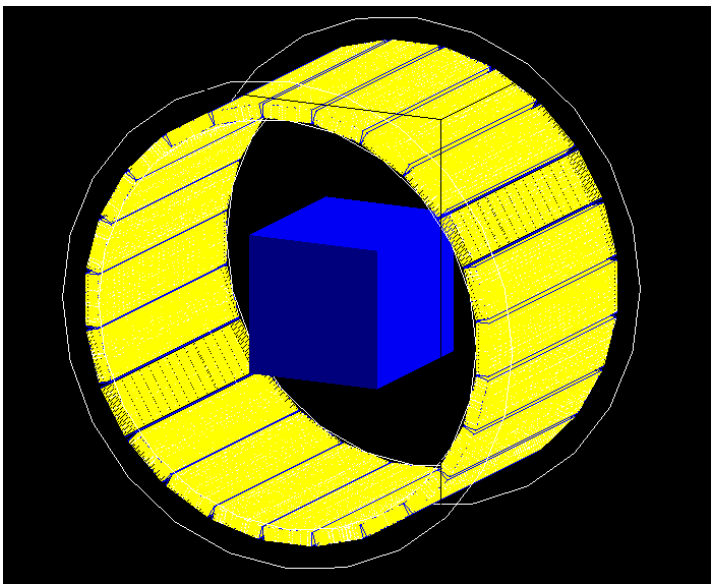

Figure 28: The setup for Monte Carlo simulation used for validation of the reconstruction workflow. Here, a single layer barrel configuration with the isocentrically positioned water phantom was visualized in GATE software.

4.1.1.1 *Sensitivity correction*

The sensitivity correction requires an additional Monte Carlo simulation to obtain sensitivity list-mode. Sensitivity list-mode is a list of true coincidences typically acquired from a water phantom registered from the whole FOV. Scattered and random coincidences are not considered as the scanner's sensitivity does not depend on the imaged object. However, since plastic scintillators used in J-PET show low efficiency for the detection of Compton scattering events (for 24 mm thick scintillator and 200 keV photon energy threshold, the efficiency is equal to 0.1 [97]), Monte Carlo simulations demand high statistics of the primary particles to register all possible LORs. For this reason, an alternative approach was presented.

Conventionally, to obtain sensitivity list-mode, simulations are performed in the water phantom to increase the number of true coincidences and shorten the simulation time. Here, the water phantom was replaced by the air phantom. The cuboid air phantom was covering $\frac{1}{8}$ of the whole FOV. The phantom was filled with a uniformly distributed 10^{11} back-to-back 511 keV gamma quanta events, as is presented in Figure 29. The cuboid air phantom is limited to $\frac{1}{8}$ of the whole FOV because $\frac{7}{8}$ rest of the FOV can be obtained by symmetric transformation. The simulation statistics was 10^{11} for all six setup configurations. PLGrid Infrastructure and Prometheus clusters were used to speed up the sim-

ulation. In order to avoid random coincidences, back-to-back gamma from subsequent events were generated in time intervals of 10 ns.

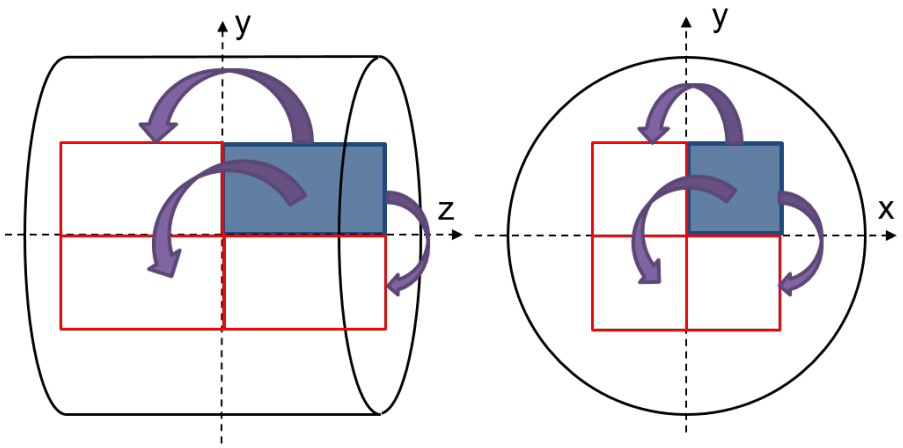

Figure 29: A scheme illustrating the processing of the LORs required to obtain sensitivity list-mode. Blue rectangles show air phantom covering $\frac{1}{8}$ FOV. Red rectangles indicate the areas of FOV to which the original LORs were transformed, as indicated by violet arrows.

Simulation results were subsequently processed as schematically indicated in Figure 29. First, each true coincidence was transformed into seven new positions based on geometrical symmetries of the J-PET system. Then, for each LOR, new annihilation positions were calculated and new coordinates of the detectors which registered the coincidences were assigned. The resulting sensitivity coincidence list was used afterwards as the input for calculating the phantom/patient-specific sensitivity map that merged sensitivity and attenuation corrections (so-called merged sensitivity and attenuation map) (see Figure 27).

4.1.1.2 *Attenuation correction*

Attenuation correction of the simulated air and water phantoms depends on the attenuation coefficient μ. μ is equal to 0.0005 cm^{-1} and 0.1 cm^{-1} for photons of energy 511 keV for air and water, respectively [196]. Resulted attenuation μ map for the water phantom is presented in Figure 30. The map was prepared by the author of the thesis.

4.1.1.3 *Merged sensitivity and attenuation map*

In order to merge sensitivity and attenuation maps, dedicated SENS optimizer reconstruction algorithm has to be used. The optimizer is not a part of the official release of the CASToR project yet, but the developers kindly shared it with the J-PET collaboration. It was initially devel-

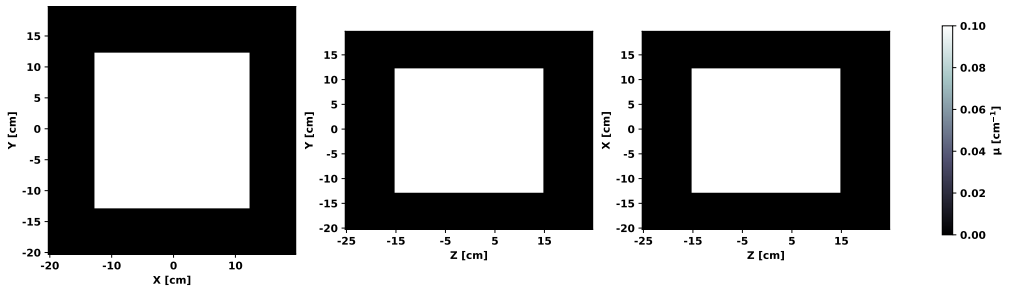

Figure 30: Attenuation map of the water phantom in axial (left), sagittal (centre) and coronal (right) views.

oped to compute a sensitivity map from an acquisition of the phantom with the uniformly distributed activity, such as a uniform cylinder/cubic/cuboid covering the whole FOV. However, it works also with non-uniform phantoms and patient attenuation μ maps. SENS optimizer is used for the reconstruction with one iteration and no TOF information is used for the reconstruction. The resulting map needs to be calibrated.

Merged sensitivity and attenuation map is calculated whenever the attenuation map changes, i.e. for each new object scanned. Sensitivity list-mode is always the same for each J-PET scanner configuration.

Since many coincidences have to be processed (as indicated in Table 4), the reconstruction is very time-consuming. It takes about 10 minutes for a high-performance PC station using 40 cores for a single layer barrel configuration.

Calibration factor of the merged sensitivity and attenuation map

The reconstructed merged sensitivity and attenuation map has to be calibrated. Activity values observed in the non-calibrated merged sensitivity and attenuation map are relatively high (if the number of registered coincidences is large, voxel values are also large, i.e. on the order of 10^6). The resulting map is then forward projected and used in the delimiter of the MLEM algorithm (see Equation 17) in the reconstruction (Figure 27). It resulted in very low voxel values in the reconstructed PET images (i.e. the order of 10^{-11}).

To avoid this, correction of the merged sensitivity and attenuation map has to be applied. The easiest approach to calculate the voxel-wise calibration factor is to perform simulations and reconstruct an image of a phantom with uniformly distributed known activity. The calibration factor is then calculated as the ratio of the mean activity of the reconstructed PET image and the known simulated activity, both within the same ROI. For calibration factor calculation, the whole phantom region was used as a ROI. As the simulated activity was 10^9 back-to-back

quanta and the number of voxels equal to $1.2 \cdot 10^6$, the known simulated activity was equal to $\frac{10^9}{1.2 \cdot 10^6}$=833 back-to-back quanta per voxel. Then, the voxel-wise calibration factor is applied for the merged sensitivity and attenuation map. The calibration procedure has to be performed for each J-PET setup configuration but does not have to be repeated whenever the new attenuation map is applied.

4.1.2 *PET image reconstruction*

PET data reconstruction using the MLEM algorithm (3 iterations) with TOF equal 500 ps and voxel size 2.5x2.5x2.5 mm^3 was performed with CASToR. Attenuation and sensitivity correction were included. Post-reconstruction 3D Gaussian filter with σ equal to 2 voxels in transaxial and axial directions was applied to smooth the results.

An additional procedure was performed to validate the PET data reconstruction performed with the CASToR. Particular attention was given to activity reconstructed in the middle of the phantom. The enhanced activity was associated with the effect of scatter coincidences [196]. Thus, scattered and true fractions were reconstructed separately.

4.2 RESULTS AND DISCUSSION

4.2.1 *Sensitivity maps*

The number of true coincidences registered from a phantom filled uniformly with $8{\cdot}10^{11}$ primary back-to-back gamma quanta covering the whole FOV (after post-processing; see Figure 29) and the corresponding η are presented in Table 4.

The highest number of coincidences was registered by the triple layer barrel ($8.13{\cdot}10^9$) configuration, while the lowest for the single layer dual-head ($1.37{\cdot}10^9$). This occurs because the geometrical acceptance of the barrel configurations is higher and additional layers increase the configuration efficiency for the coincidence registration. A comparison between the geometrical configurations with the same number of modules (24) revealed that the increased number of layers resulted in more registered coincidences. The triple layer dual-head was the setup with the highest number of registered coincidences ($4.00{\cdot}10^9$), while the single layer barrel with the lowest number of registered coincidences ($1.88{\cdot}10^9$).

In order to visualize the sensitivity list-mode, the sensitivity maps were plotted and depicted in Figure 31 for barrel and in Figure 32 for dual-head based setup configuration.

Table 4: The number of true coincidences and efficiency factor η obtained from sensitivity simulations extended to cover the whole FOV ($8{\cdot}10^{11}$ primary back-to-back gamma quanta) for each J-PET setup configuration.

SETUP	COINCIDENCES [$\times 10^9$]	η
Single layer barrel	1.88	$2.4{\cdot}10^{-3}$
Double layer barrel	4.90	$6.1{\cdot}10^{-3}$
Triple layer barrel	8.13	$1.0{\cdot}10^{-2}$
Single layer dual-head	1.37	$1.7{\cdot}10^{-3}$
Double layer dual-head	3.42	$4.3{\cdot}10^{-3}$
Triple layer dual-head	4.00	$5.0{\cdot}10^{-3}$

Sensitivity maps for the barrel configurations from Figure 31 show the maximum sensitivity (in separate voxels) of 0.04, 0.1 and 0.16 for single, double and triple layer setups. The regular ring shapes visible in transaxial views are due to the gaps between subsequent modules within the layer. For the single layer configuration, gaps between modules within the layer are relatively small. Each subsequent layer will have bigger gaps as the number of modules is the same but the layer's radius is growing. In general, voxel sensitivity is increasing with the number of layers. However, due to the increasing gaps between adjacent modules within the layer, so-called ring effects in the sensitivity map in the middle of the scanner are observed They are more pronounced in configurations with a greater number of layers.

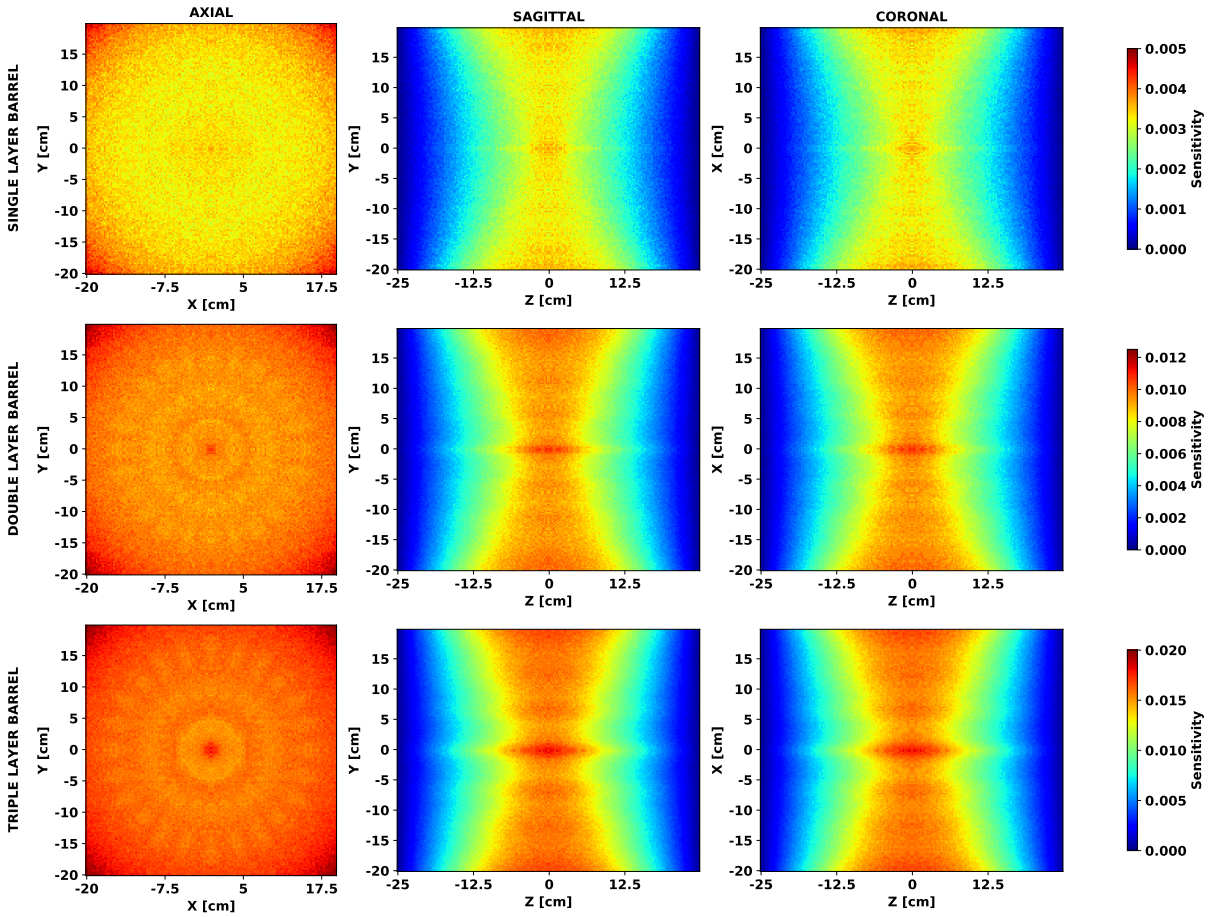

Figure 31: Sensitivity maps for single layer barrel (top), double layer barrel (middle) and triple layer barrel (bottom) configurations in axial (left), sagittal (centre) and coronal (right) views. All presented planes are passing through the centre point of the proposed scanners.

Sensitivity maps for the dual-head configurations from Figure 32 show the maximum sensitivity (in separate voxels) of 0.04, 0.1 and 0.105 for single, double and triple layer setups. Vertical lines observed in coronal view for single layer configuration are due to the gaps between the adjacent modules. This effect is reduced when subsequent layers of modules are added. As a result, they register photons emerging from the imaged object at the angles not covered by the innermost detector layer.

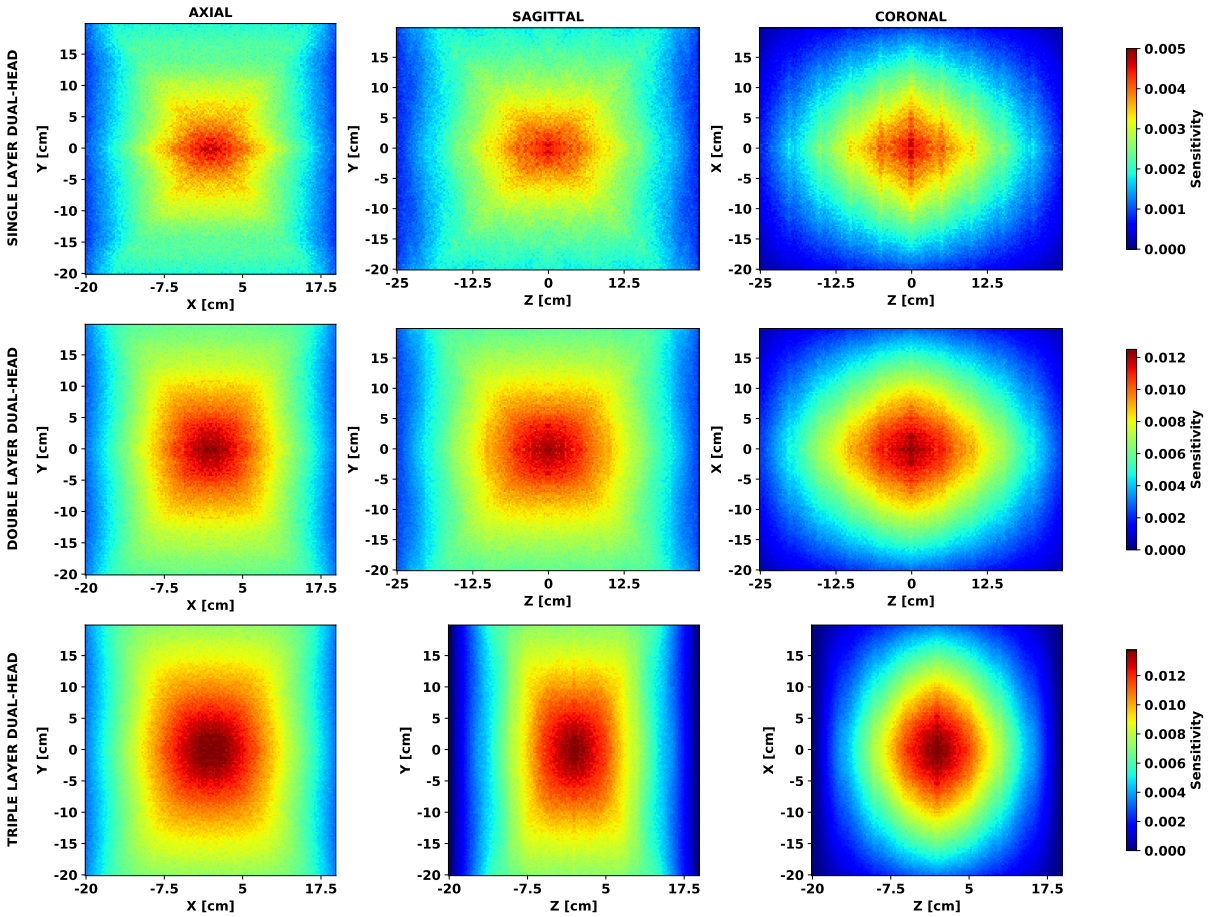

Figure 32: Sensitivity maps obtained for single layer dual-head (top), double layer dual-head (middle) and triple layer dual-head (bottom) configurations in axial (left), sagittal (centre) and coronal (right) views. All presented planes are passing through the centre point of the proposed scanners.

4.2.2 *Merged sensitivity and attenuation map*

An example of the calculated, non-calibrated merged sensitivity and attenuation map is depicted in Figure 33. The calibration factor of the merged sensitivity and attenuation map is given in Table 5.

Very high voxel values of the non-calibrated merged sensitivity and attenuation map are shown in Figure 33 cannot be treated as the sensitivity map in the context of the definition given in Section 2.5.2.2. These maps have to be calibrated as discussed in Section 4.1.1.3. In Table 5, calibration factors calculated according to the procedure given in the Section 4.1.1.3 are presented.

All other merged sensitivity and attenuation maps presented in the thesis include the relevant calibration factor given in Table 5.

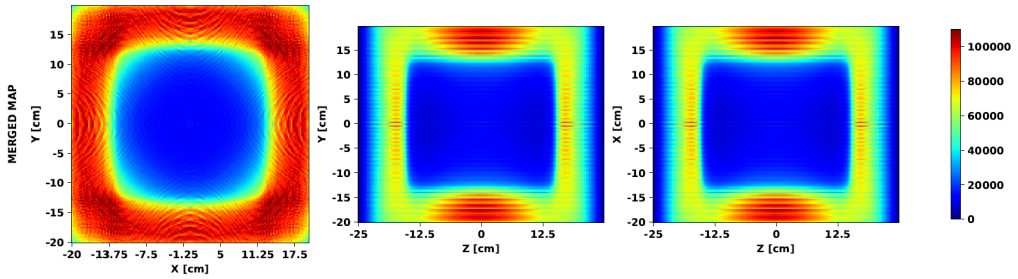

Figure 33: Non-calibrated merged sensitivity and attenuation map of the water phantom for single layer barrel configuration in axial (left), sagittal (centre) and coronal (right) view.

Table 5: The calibration factor of the merged sensitivity and attenuation map for each J-PET setup configuration.

SETUP	CALIBRATION FACTOR
Single layer barrel	$1.32 \cdot 10^{-8}$
Double layer barrel	$1.48 \cdot 10^{-8}$
Triple layer barrel	$1.50 \cdot 10^{-8}$
Single layer dual-head	$0.84 \cdot 10^{-9}$
Double layer dual-head	$1.02 \cdot 10^{-8}$
Triple layer dual-head	$7.00 \cdot 10^{-9}$

Attenuation and sensitivity maps and processed merged sensitivity and attenuation maps for single layer barrel and single layer dual-head setup configurations are depicted in Figure 34 and Figure 35, respectively. The same type of figures are presented in Appendix A and cover double layer and triple layer geometrical configurations.

Ring shapes for barrel configurations (Figure 34) observed in sensitivity maps are also observed in merged sensitivity and attenuation maps. In addition, vertical lines visible in the sensitivity map of the single layer dual-head (Figure 35) are also propagated in merged sensitivity and attenuation maps.

Greater voxel values in merged sensitivity and attenuation maps outside of the phantom than inside the phantom result from lower linear attenuation coefficient of air than water. The process of merging attenuation and sensitivity correction is time-consuming. For example, a reconstruction of the merged sensitivity and attenuation maps for the single layer barrel setup lasts 10 minutes with a high-performance computer

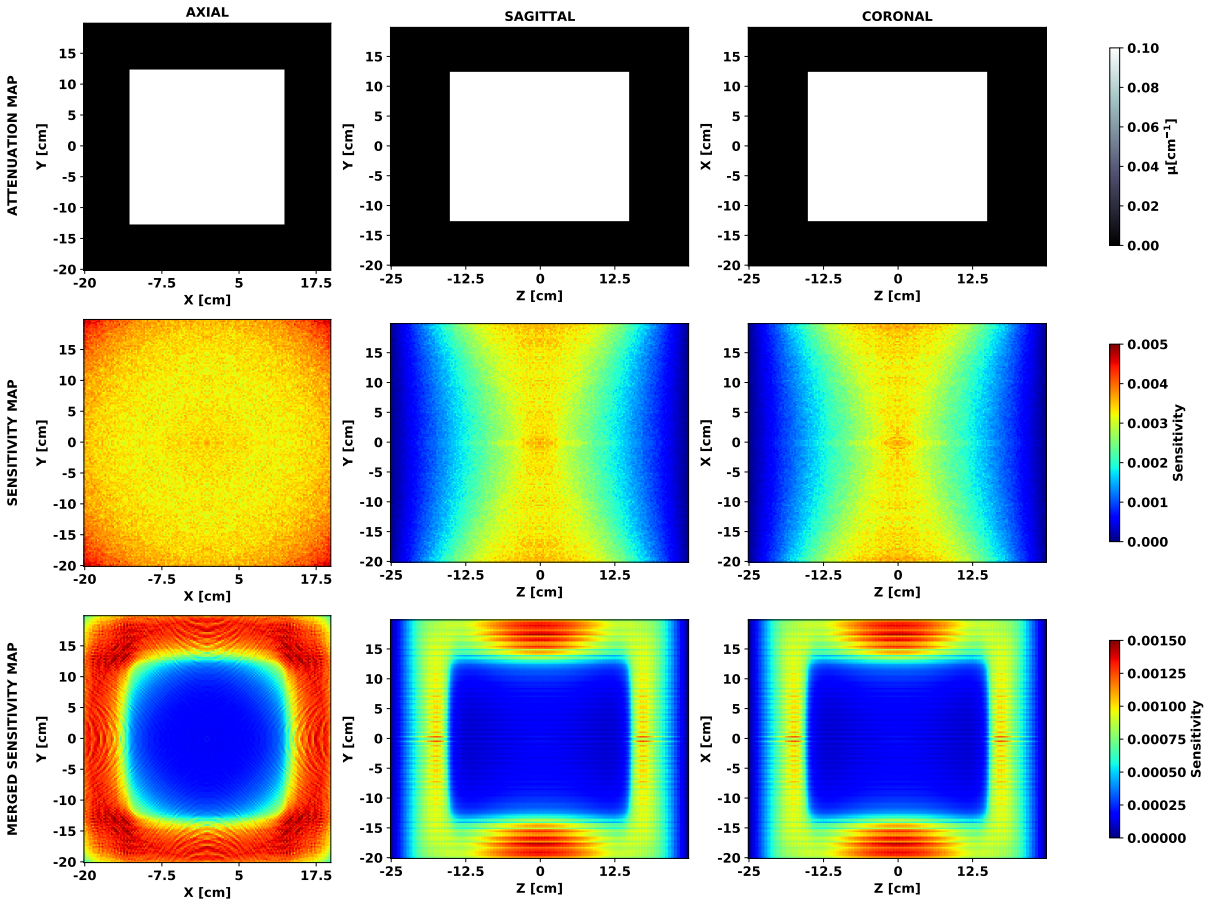

Figure 34: Attenuation correction (top), sensitivity (middle) and merged sensitivity and attenuation (bottom) maps of the water phantom for single layer barrel configuration in axial (left), sagittal (centre) and coronal (right) view.

station equipped with 40 cores working simultaneously. One approach to reducing the reconstruction time is reconstructing the map with reduced statistics or to use/develop software uses both (not merged) attenuation and sensitivity correction maps.

In order to apply the merged sensitivity and attenuation maps for the reconstruction of the actual PET images, they have to be calibrated as discussed in Section 4.1.1.3.

4.2.3 *PET reconstructed images*

Resulted number of coincidences and the corresponding efficiency factor η from water phantom PET acquisition are presented in Table 6.

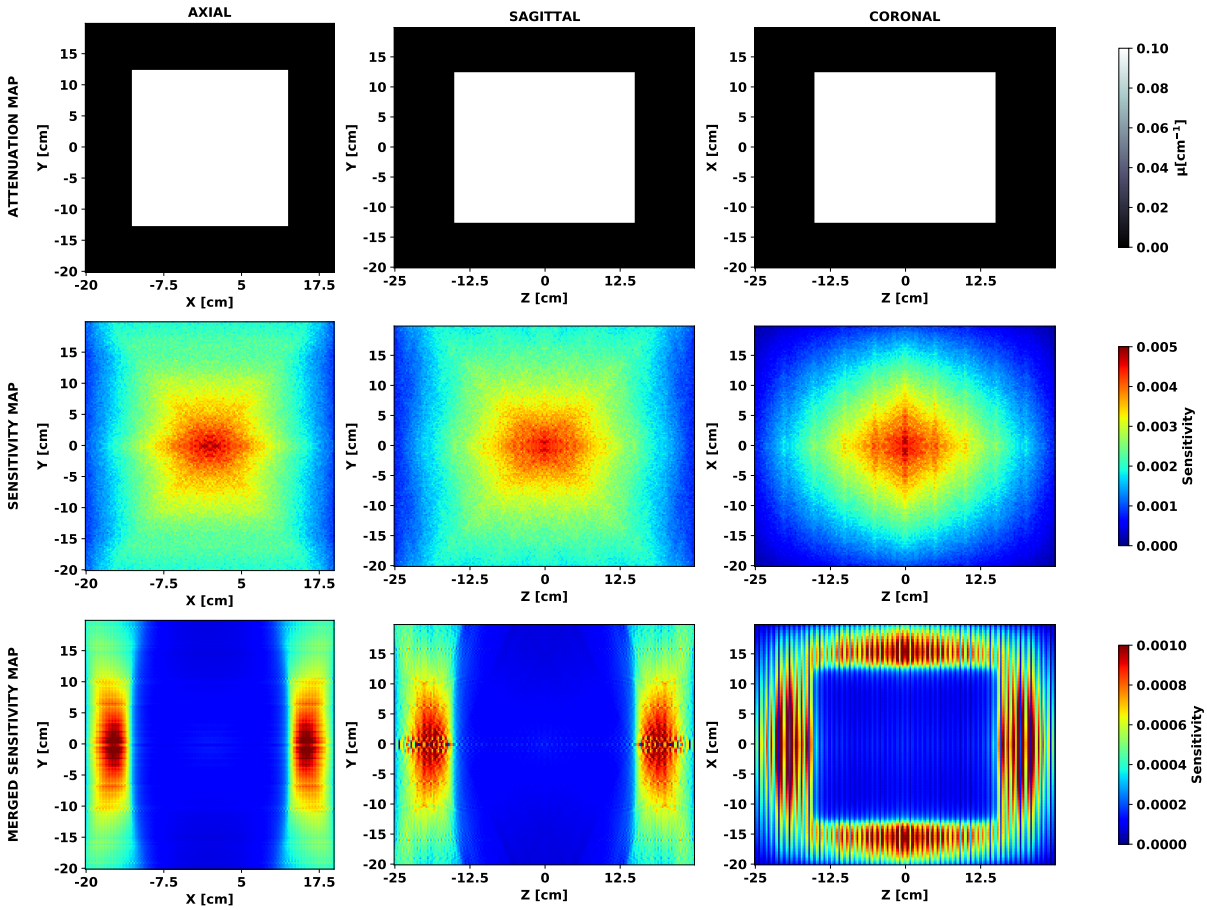

Figure 35: Attenuation correction (top), sensitivity (middle) and merged sensitivity and attenuation (bottom) maps of the water phantom for single layer dual-head configuration in axial (left), sagittal (centre) and coronal (right) view.

Reconstructed PET images of the water phantom uniformly filled with activity for barrel and dual-head setup configurations are presented in Figure 36 and Figure 37, respectively.

For a phantom of the same material, the same dimensions and filled with the same activity, the highest number of coincidences was registered in the triple layer barrel configuration ($3.2{\cdot}10^6$), while the lowest for the single layer dual-head ($2.6{\cdot}10^5$). Double layer dual-head setup is the most efficient 24 module setup in terms of the efficiency for detection of coincidences. It registered $7.7{\cdot}10^5$ coincidences, while single layer barrel and triple layer dual-head $6.6{\cdot}10^5$ and $7.2{\cdot}10^5$, respectively. This result is different to the sensitivity simulations where the activity was positioned in air and triple layer dual-head registered the highest number of coincidences. The bigger the imaged object is, the greater the number of photons is scattered in imaged object (scatter fraction in-

Table 6: The number of coincidences and efficiency factor η computed for different J-PET setup configurations. True and scatter fractions are distinguished.

SETUP	COINCIDENCES [x10^5]			η
	ALL	TRUE	SCATTER	
Single layer barrel	6.6	3.2	3.4	$6.6 \cdot 10^{-4}$
Double layer barrel	19.2	9.4	9.8	$1.9 \cdot 10^{-3}$
Triple layer barrel	32.2	16.1	16.1	$3.2 \cdot 10^{-3}$
Single layer dual-head	2.6	1.4	1.2	$2.6 \cdot 10^{-4}$
Double layer dual-head	7.7	4.0	3.7	$7.7 \cdot 10^{-4}$
Triple layer dual-head	7.2	3.7	3.5	$7.2 \cdot 10^{-4}$

creases) but with the lower mean energy. Subsequently, the maximum energy deposit in the plastic will be lower than in the case of 511 keV photons and the probability of the energy deposition above the detection energy threshold (200 keV) is lower. Therefore, the number of coincidences detected by double layer dual-head is greater than the triple layer dual-head configuration consisting off the same number of modules. Please note that the triple layer setup has the geometrical acceptance $\frac{1}{5}$ times smaller with respect to the double layer. In conclusion, the geometrical acceptance of the detector plays a dominant role with respect to the number of layers used to build the detector, particularly for large phantoms/patients.

Table 6 shows that the true fraction of coincidences is bigger for dual-head based configurations than for the barrel based setups consisting of the same number of modules. The difference comes from the geometrical properties of the setups. Photon path length through the plastic scintillator (especially for the most oblique LORs) is longer for the dual-head configurations because the modules within the head are positioned parallel to the coronal plane. In contrast, modules in barrel based setups are facing the proton beam axis. Therefore, the longer the possible interaction path of the annihilation photon, the higher probability of the energy deposition above the detection threshold.

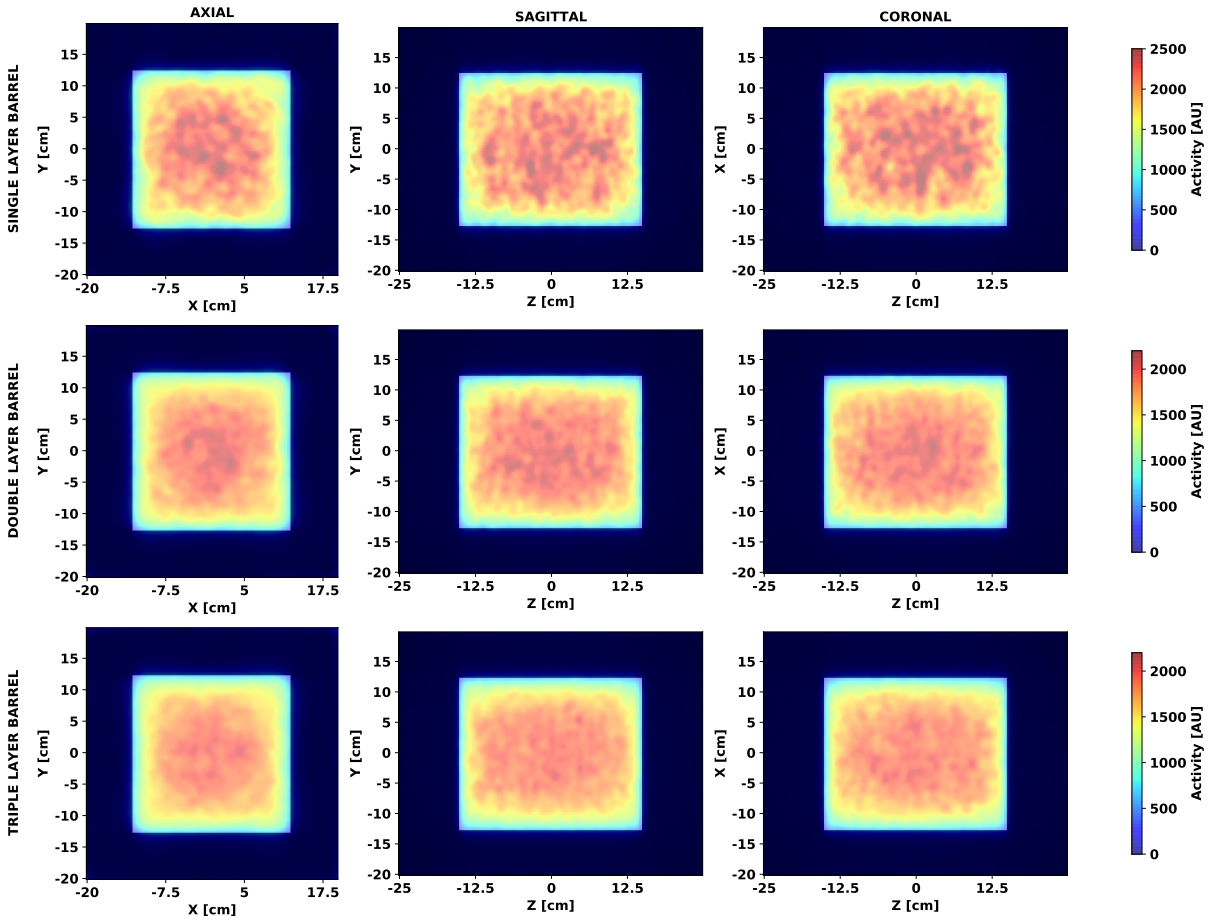

Figure 36: Reconstructed PET images of the uniform phantom for single layer barrel (top), double layer barrel (middle) and triple layer barrel (bottom) configurations in axial (left), sagittal (centre) and coronal (right). PET images are superimposed on CT images of the phantom.

The reconstructed PET images are noisy due to the low number of coincidences. A characteristic elongated rectangular activity distribution visible along the y-direction for dual-head configurations (Figure 37) is due to the scanner geometry (position of the heads). LORs are collected only by two opposite heads and the geometry does not imitate the cylinder. The coincidences which might reduce that effect are not registered as no additional detectors are included in the plane perpendicular to the existing heads.

For all the reconstructed PET images, higher activity is observed in the centre of the phantom with respect to its edges. This is because both the scattered and true coincidences were used for the reconstruction. This effect is known in the literature [196]. The scatter fraction of coincidences significantly contributed to the increased activity in the centre of the phantom. To address that issue, the scatter correction should be

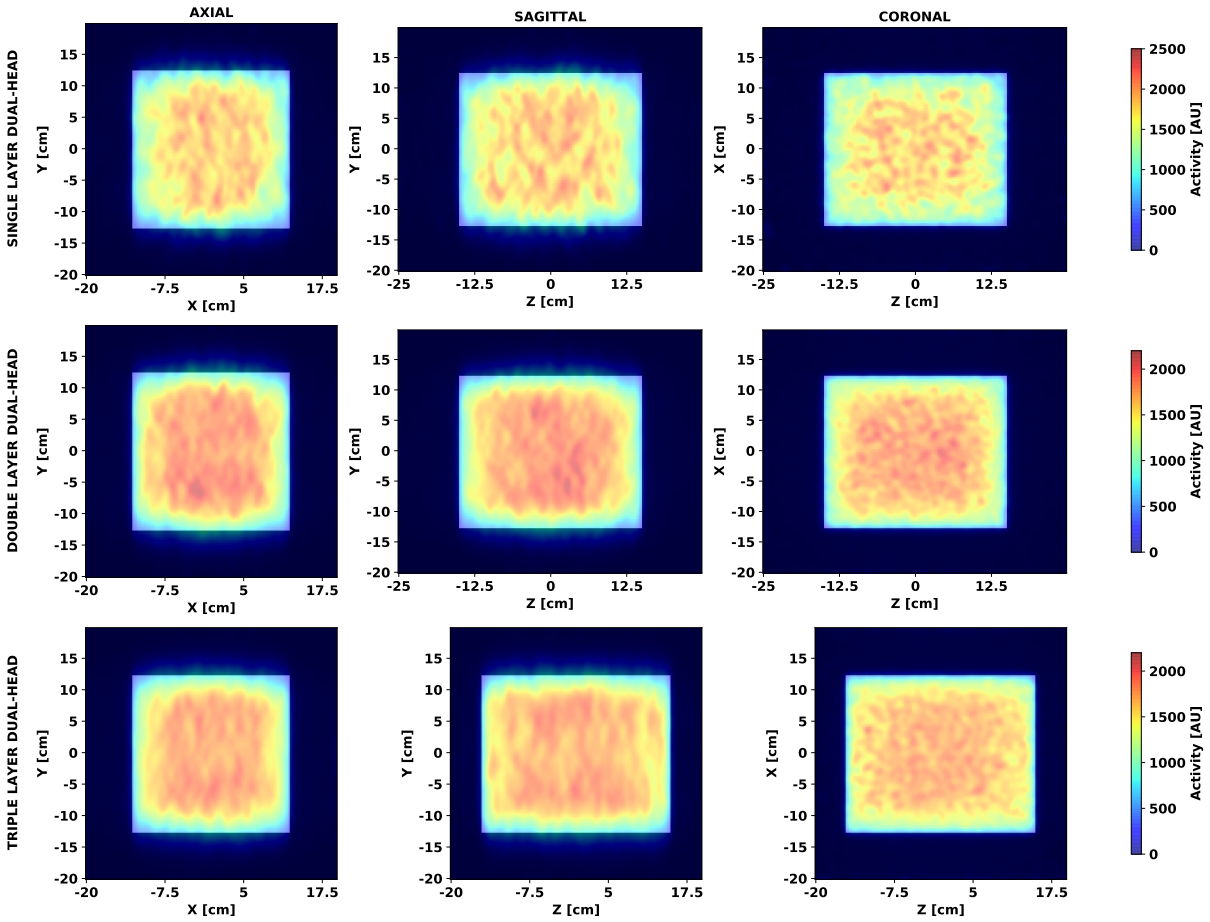

Figure 37: Reconstructed PET images of the uniform phantom for single layer dual-head (top), double layer dual-head (middle) and triple layer dual-head (bottom) configurations in axial (left), sagittal (centre) and coronal (right). PET images are superimposed on CT images of the phantom.

applied as it was discussed in Section 2.5.3. The simulated activity value per voxel was equal to 833.(3). Reconstructed PET images show the voxel values of about 1500-2000 AU in the middle of the phantom (lower at boundaries). Considering that sensitivity is calculated only for true coincidences, scatter fraction states about 50% of all coincidences (Table 6) and scatter correction is missing. Therefore, two times higher activity of the reconstructed PET images is expected.

The true and scatter fractions reconstructed separately for the single layer barrel and the single layer dual-head configurations are depicted in Figure 38 and Figure 39, respectively. PET images reconstructed using only true coincidences show uniform distribution within the phantom (considering low statistics and noisy images), In contrast, on images reconstructed using only scattered coincidences the activity is focused in

the centre of the phantom. Thus, the reconstructed activity of the phantom with true coincidences is similar to the simulated value. The same effect is observed for all geometrical configurations. As the number of registered coincidences is relatively low, the high and low activity spots are observed in the reconstructed images.

As discussed above, reconstructed PET images proved that the reconstruction workflow for all geometrical configurations was validated and worked correctly.

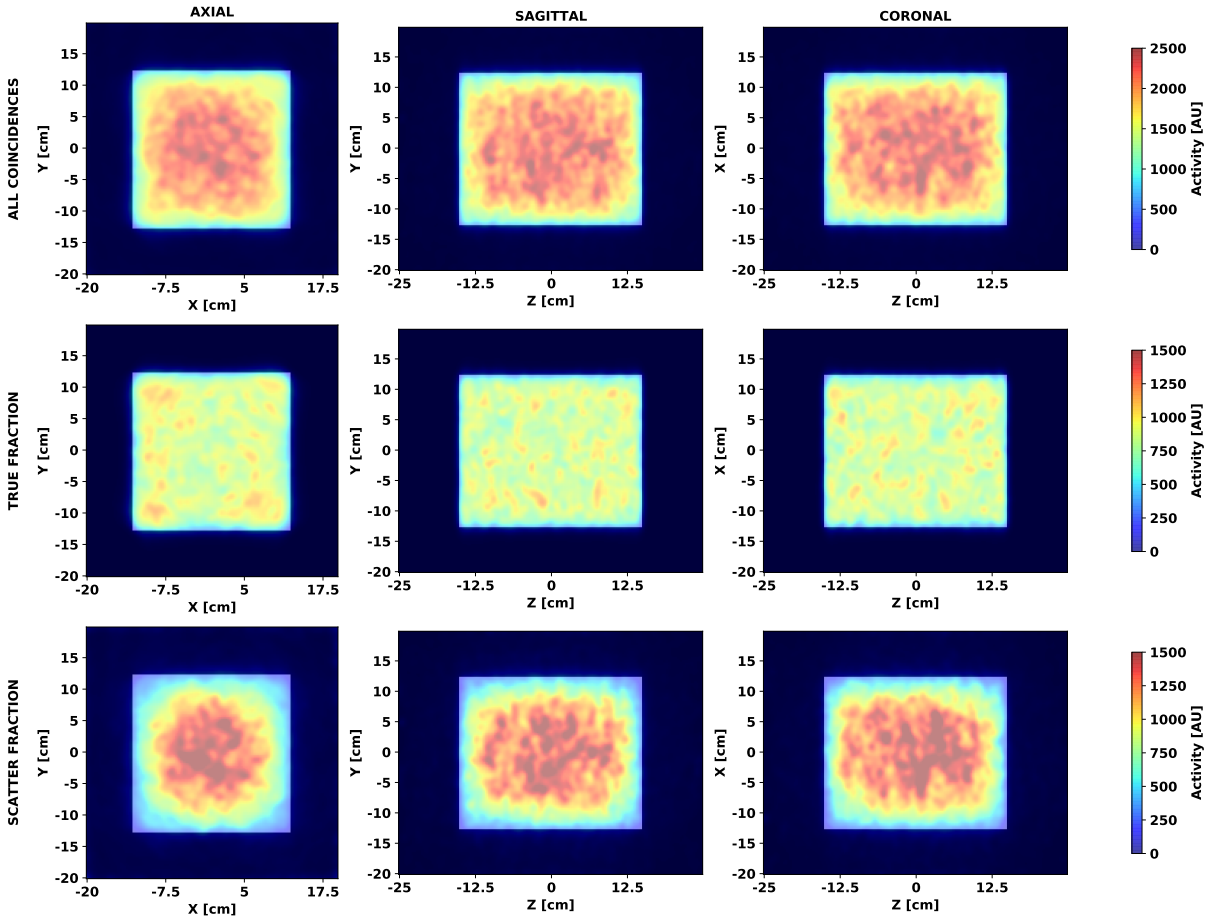

Figure 38: Reconstructed PET images with all (top), true (middle) and scatter (bottom) coincidences for the single layer barrel configuration in axial (left), sagittal (centre) and coronal (right) views superimposed on CT images.

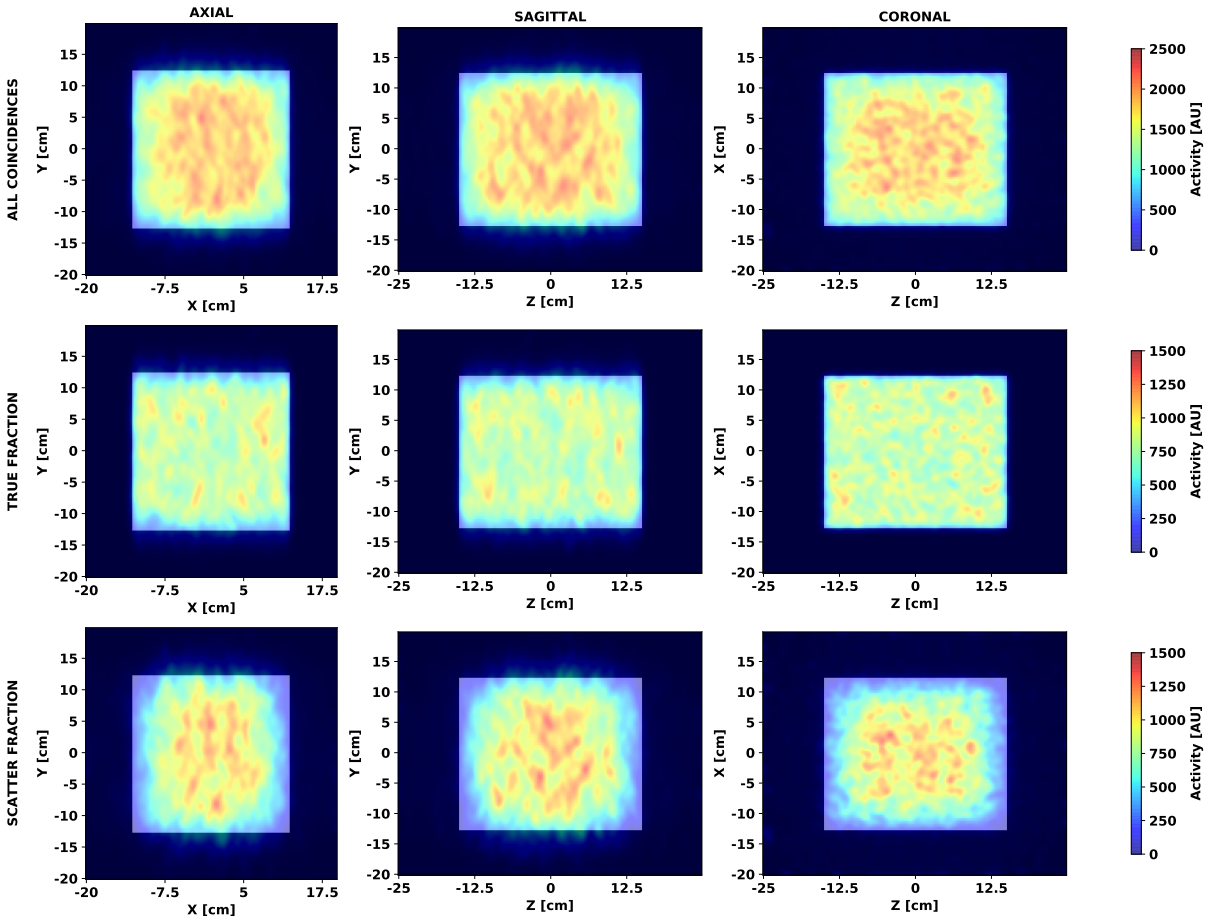

Figure 39: Reconstructed PET images with all (top), true (middle) and scatter (bottom) coincidences for the single layer dual-head configuration in axial (left), sagittal (centre) and coronal (right) views superimposed on CT images.

5

SIMULATION OF PROTON RANGE VERIFICATION IN THE PMMA PHANTOM

The main aim of the analysis described in this Chapter is to determine the accuracy of the activity-based assessment of the proton beam range for the PMMA phantom irradiation for all the investigated J-PET scanner configurations. Three studies are presented to investigate the precision of proton-induced β^+activity imaging:

(a) Study 1: Feasibility of activity imaging induced by proton beams

The number of the coincidences with distinguished types (true/scatter/random) is calculated along with the efficiency factor η for all the geometrical setup configurations.

(b) Study 2: Investigation of the precision of β^+activity distal fall-off point identification

The simulation was performed for 150 MeV protons (10^8 primary protons) and repeated 50 times for each geometry setup. As a result, the mean and standard deviation of the difference between the middle points calculated from the reconstructed and true 1D activity profiles were obtained. The middle point is calculated as a means of 50% fall-off depth position. In addition 1D activity profiles and reconstructed PET images from 50 merged simulations were presented (primary protons number: $5{\cdot}10^9$). Furthermore, to compare the geometrical configurations, the number of coincidences and the η are given for the merged simulations.

(c) Study 3: Estimation of the J-PET system sensitivity to detect proton beam range

The study investigated the sensitivity of the J-PET system to estimate the proton beam range. It was addressed by measuring the activity distal fall-off from the reconstructed PET images and comparing them to the induced β^+activity from the emission map simulated in GATE. It was performed for 150 MeV proton beam and six proton energies leading to ranges which differ from the nominal range by -3, -2, -1, 1, 2 and 3 mm. The energies and ranges are presented in Table 7 and the median range is referred to as a reference.

Table 7: Proton beam energies used for the detection of differences in range.

BEAM ENERGY [MEV]	BEAM RANGE [MM]	DIFFERENCE FROM THE REFERENCE [MM]
149.94	158.69	-3.0
150.47	159.69	-2.0
151.00	160.69	-1.0
151.53	161.69	—
152.06	162.69	1.0
152.59	163.69	2.0
153.12	164.69	3.0

5.1 MATERIALS AND METHODS

5.1.1 *Simulation workflow*

Isocentrically positioned PMMA phantom (5x5x20 cm^3) with ionisation potential of PMMA set to 80 eV was impinged with the proton beam. The *QGSP_BIC_HP_EMY* [197] physics list with an additional *Radioactive Decay* model was used for the simulations. In addition, several production cuts to increase the time performance of simulation (gamma quanta, electrons and positrons produced within the phantom - 0.1 mm - and outside of it - 1.0 mm) were used.

The beam source was positioned 70 cm upstream from the gantry room isocenter (60 cm upstream from the PMMA phantom surface). The proton beam model was initially prepared by Jan Gajewski from Department of Proton Therapy and Radiation Research based on gantry commissioning measurements and adapted to the Monte Carlo GATE in the frame of this thesis. A more detailed explanation of this procedure is given in Section 3.3.1.1. The PhaseSpace actor [190] was used to score the emission map (true production β^+activity map) [198]. Its role was to score events on particles produced within the patient body, i.e. production position, production time, particle type, particle energy, etc., of each secondary particle. The emission map for given energy was simulated in the phantom only once using the phantom grid with the 0.5x0.5x0.5 mm^3 voxel size.

In order to check the response characteristic of the J-PET detectors organized in presented geometrical configurations, two simulations were performed:

(a) Simulation 1

The simulation of 150 MeV protons was performed and repeated 50 times for each J-PET geometrical configuration. 10^8 primary protons were simulated. For the purpose of the analysis separated simulations and all merged 50 simulations as one were used for the analysis.

(b) Simulation 2

Interaction of seven proton beams with initial energies differing in the proton range by 1 mm each were simulated in the PMMA phantom and scored in the six geometrical PET configurations. The energies and ranges are presented in Table 8. The number of primary protons for each simulation was set to 10^8.

In order to find the linear attenuation coefficient (μ) of the PMMA phantom, a CT scan of the phantom was acquired with the Siemens Somaton CT scanner located at CCB with the acquisition parameters typically used for the patient diagnostics imaging. The mean Hounsfield Units (HU) value of the phantom was calculated within the cylindrical ROI of 5cm radius and 5 cm height and transformed as described in [91] to the linear attenuation coefficient. The resulted μ = 0.104 cm^{-1} was assigned to the PMMA phantom for the consecutive PET reconstructions [91].

The coincidence sorter was used to obtain the list of coincidences as described in Section 3.3.1. For the image reconstruction, the integrated (in-beam and off-beam phases) coincidences of all types (true, scattered and random) were used. The optimal number of iterations for the reconstruction was chosen based on the Normalized Root Mean Square Deviation (NRMSD) [199] given as follows:

$$\mathrm{NRMSD} = \sqrt{\frac{\sum_{i=1}^{I}(x(i)-\hat{x}(i))^2}{\sum_{i=1}^{I}\hat{x}(i)^2}} \tag{21}$$

where I is the total number of voxels, while x and $\hat{x}$ are reconstructed images and emission map, respectively.

The optimal number of iterations for the MLEM reconstruction algorithm is defined as the one for which the NRMSD reaches the minimum. Only the voxels of the phantom (or the patient body in the next Chapter), neglecting the air background were considered for the calculation. The optimal number of iterations computed from Equation 21 was 2, 3 or 4, depending on the analyzed reconstruction activity profile. Finally, three iterations were arbitrarily used to reconstruct PET images of proton beam-induced activity in the PMMA phantom.

5.1.2 *Analysis methods*

The 1D emission profiles and reconstructed activity profiles were calculated along the beam direction within the PMMA phantom and normalized to the maximum value. Then, the sigmoid function was fitted to the distal fall-off of the activity profile according to the following formula:

$$y = \frac{a}{1 + e^{-c(x-b)}} \tag{22}$$

where y and x are the data points and a, b and c are fitting parameters.

The middle point at 50% of the maximum value of the 1D profile fall-off was calculated for each profile (b parameter from Equation 22). The difference between the middle points of the emission and reconstructed β^+activity profiles were calculated to assess the sensitivity of all geometrical configurations for the proton beam range changes at the level of 1 mm. A graphical interpretation of the middle points and their difference calculation is depicted in Figure 40.

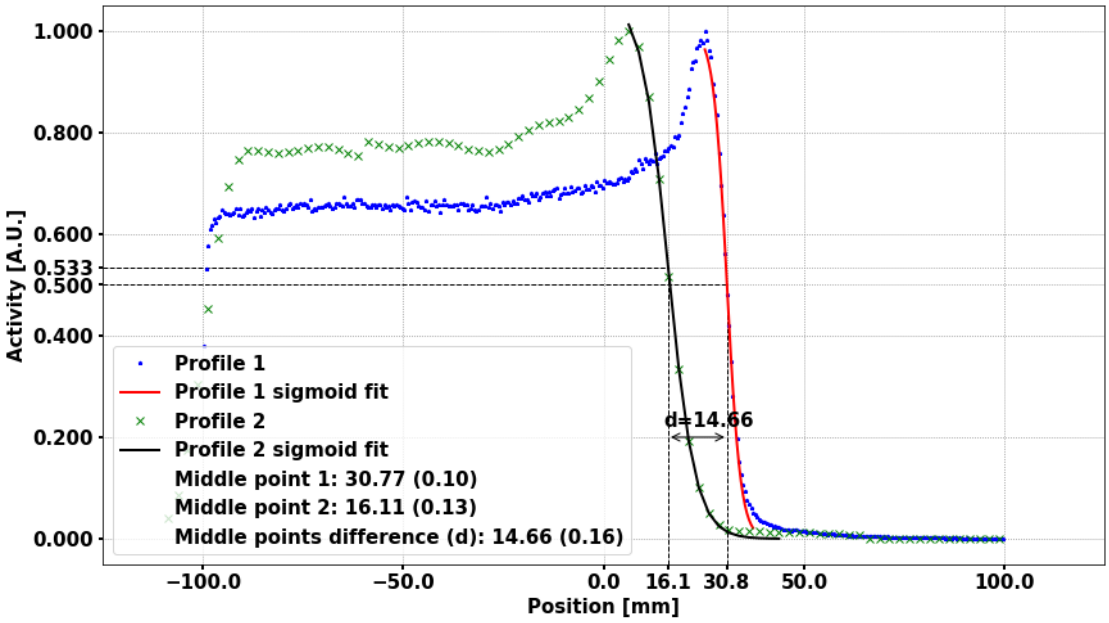

Figure 40: Example of two activity profiles (profile 1 - blue and profile 2 - green) with corresponding sigmoid fits (red and black solid lines) to the distal fall-offs based on Equation 22. The middle points (position along the beam axis) are calculated as the values where half of the maximum of the sigmoid function is calculated (dashed grey lines). Finally, the difference between middle points (d) is given.

For investigation of the precision of β^+activity distal fall-off point identification (study 2), the stability of the J-PET system was assessed.

Stability is defined as a standard deviation of the difference between reconstructed and emission profiles. In this work, stability was calculated from 50 simulations.

The particular category of the setups consisting of 24 modules is investigated and compared in 3 feasibility and precision studies as they would be investigated experimentally in the near future.

5.2 RESULTS

5.2.1 *PET reconstructed images*

Reconstructed PET images of β^+activity produced by a single pencil beam of 150 MeV protons in a homogeneous PMMA with the dose and true production activity (emission) distributions are shown in Figures 41-44. Images corresponding to the lower number of primary protons (10^8) are presented in Figure 41 and Figure 42 for barrel and dual-head based configurations, respectively. The images obtained from merging 50 simulations ($5{\cdot}10^9$) for each J-PET scanner geometry from study 2 are shown in Figure 43 and Figure 44 for barrel and dual-head based configurations, respectively. It could be noticed, that the β^+activity range is shorter than the dose distribution range, as discussed and explained in Section 2.7. Additionally, merged sensitivity and attenuation maps are presented in Appendix B.

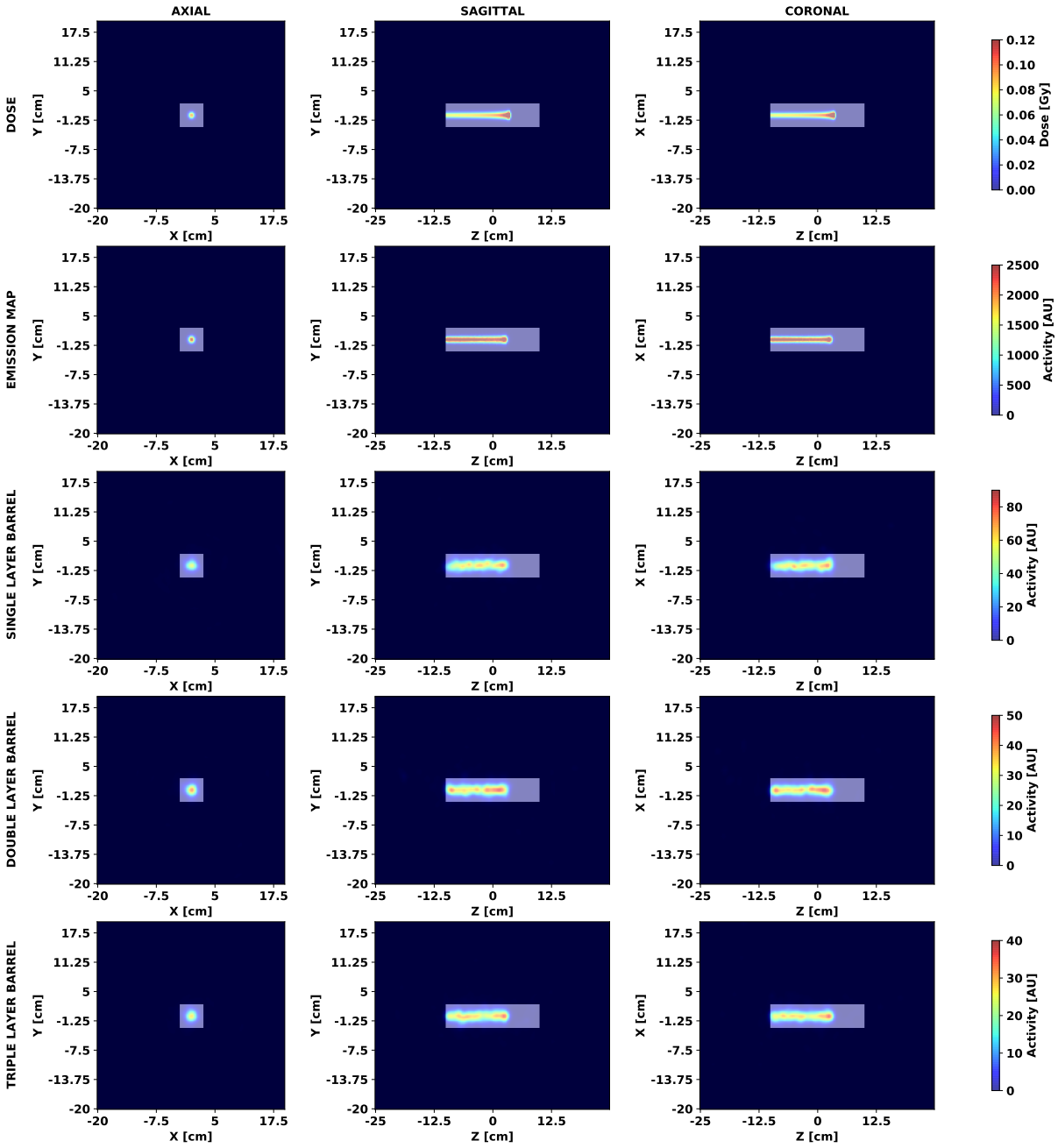

Figure 41: Dose distributions (top row) and emission maps (second row) in the PMMA phantom (5x5x20 cm^3) after irradiation with a single proton pencil beam of 150 MeV. The corresponding reconstructed PET images for single layer barrel (third row), double layer barrel (fourth row) and triple layer barrel (bottom row) in axial (left), sagittal (centre) and coronal (right) views are superimposed on CT images. Presented images were obtained from the simulation of 10^8 primary protons.

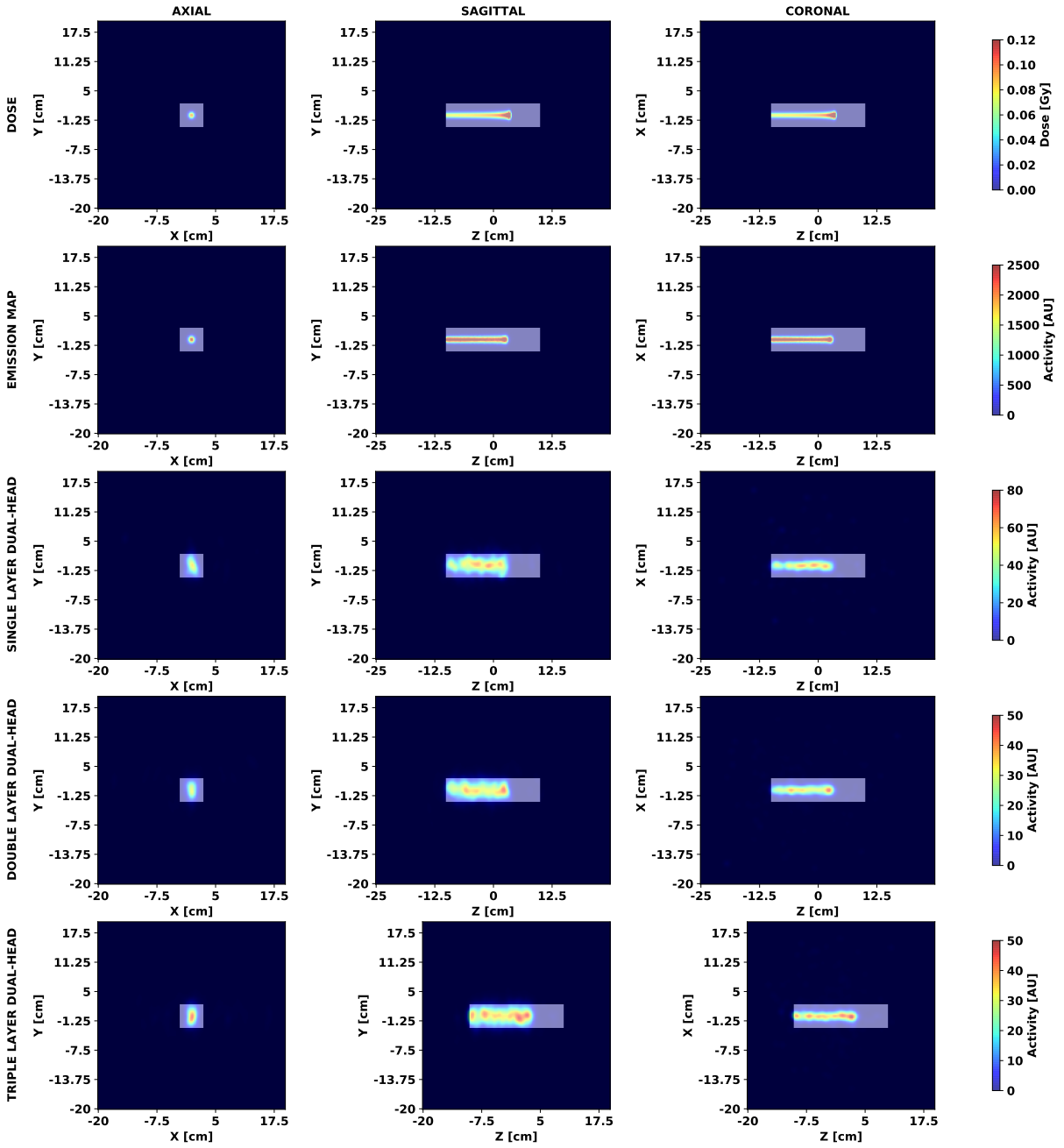

Figure 42: Dose distributions (top row) and emission maps (second row) in the PMMA phantom (5x5x20 cm^3) after irradiation with a single proton pencil beam of 150 MeV. The corresponding reconstructed PET images for single layer dual-head (third row), double layer dual-head (fourth row) and triple layer dual-head (bottom row) in axial (left), sagittal (centre) and coronal (right) views are superimposed on CT images. Presented images were obtained from the simulation of 10^8 primary protons.

Barrel and dual-head setups show qualitatively different results. The elongated shape visible as an activity distribution spread in phantom along the y-direction (Figure 42) is observed for dual-head configurations. The reason for that is that the LORs are collected only by two opposing heads and the geometry is not cylindrical. The effect is also observed in the previous study (see Section 4.2.3) and more detailed explanation could be found in Section 4.2.3. Reconstructed activity distributions are noisy due to the low statistics of the coincidence events that was listed in Table 8. The small number of registered events caused a non-regular shape (the activity with gaps along the profile) of the reconstructed activity distribution.

Figure 43 and Figure 44 illustrate the results of calculation of dose, emission map and PET images in the same way as images shown in Figure 41 and Figure 42 but with fifty times higher statistics, i.e. $5{\cdot}10^9$ protons.

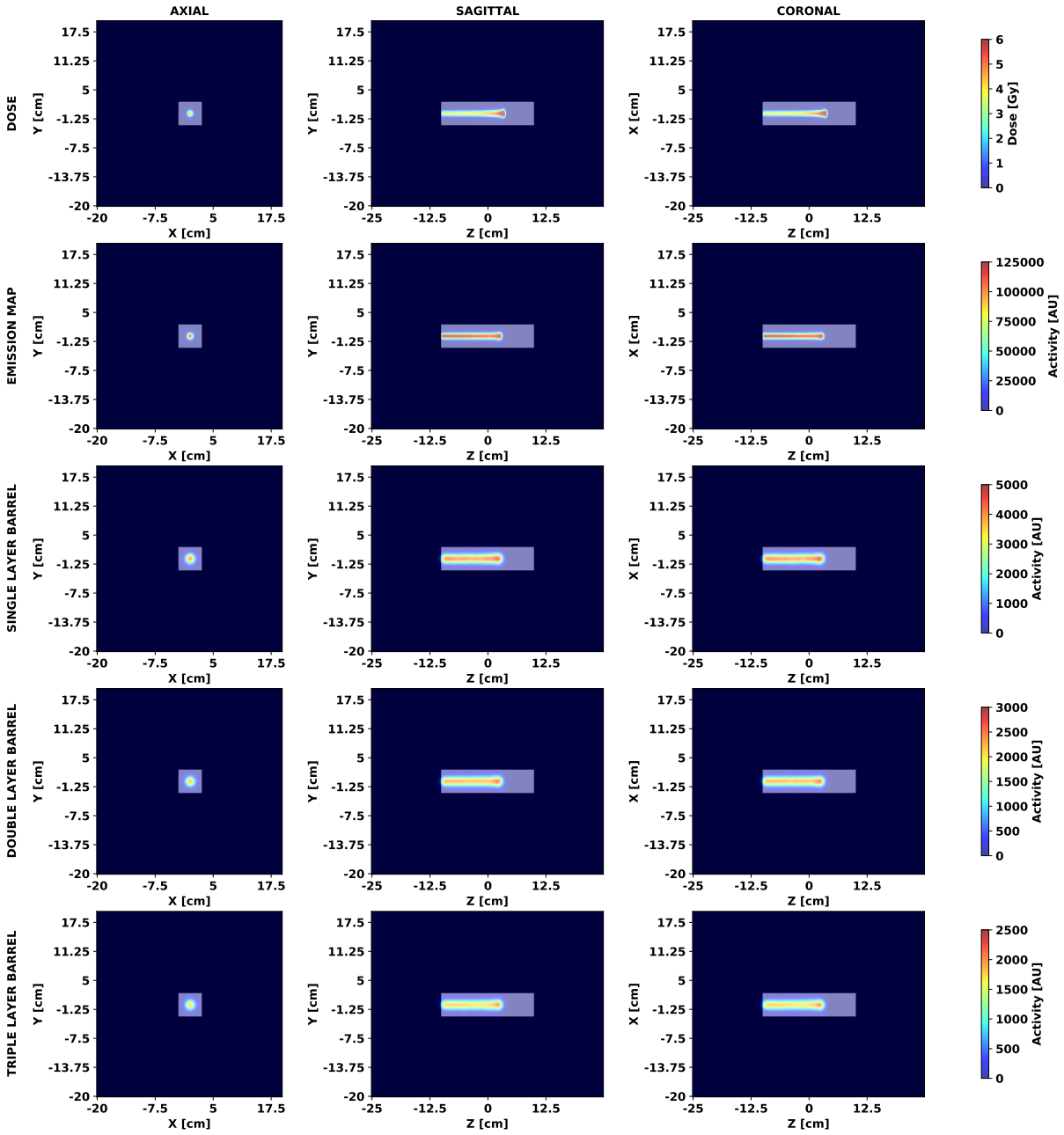

Figure 43: The image of the dose (top row) and emission maps (second row) after 150 MeV proton pencil beam interacting in a homogeneous PMMA phantom. The reconstructed PET images for single layer barrel (third row), double layer barrel (fourth row) and triple layer barrel (bottom row) J-PET setup configurations in axial (left), sagittal (centre) and coronal (right) views are superimposed on CT images. Presented images were obtained from the simulation of $5{\cdot}10^9$ primary protons.

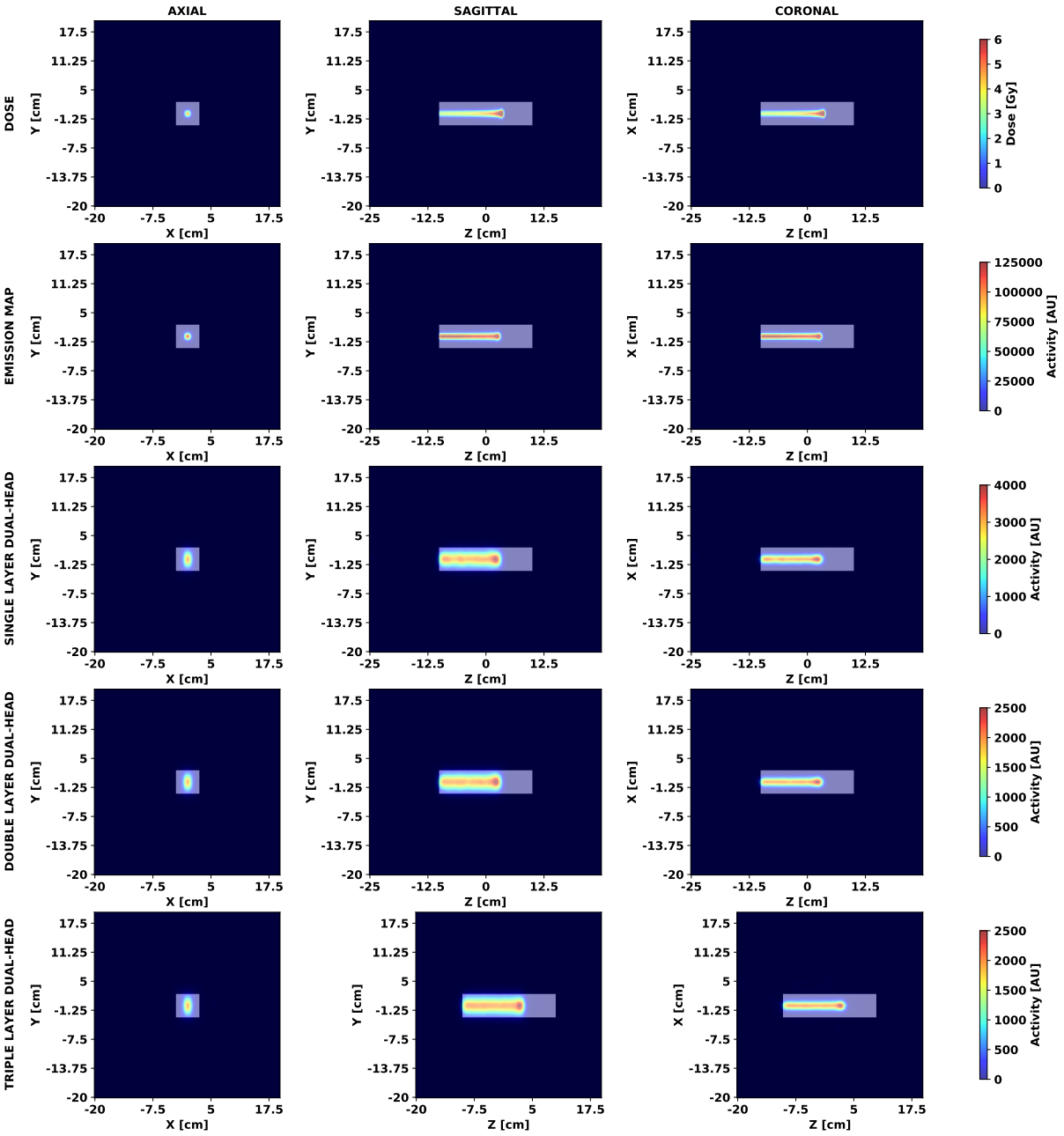

Figure 44: The image of the dose (top row) and emission maps (second row) after 150 MeV proton pencil beam interacting in a homogeneous PMMA phantom. The reconstructed PET images for single layer dual-head (third row), double layer dual-head (fourth row) and triple layer dual-head (bottom row) J-PET setup configurations in axial (left), sagittal (centre) and coronal (right) views are superimposed on CT images. Presented images were obtained from the simulation of $5{\cdot}10^9$ primary protons.

This result confirmed that better statistics led to visually improved quality of the reconstructed images.

The reconstructed activity distributions visually well approximate the emission distribution. This is achieved due to the relatively small annihilation of attenuation photons (with respect to the phantom presented in Chapter 4). Also, the small phantom size is the reason for the relatively small scatter fraction described (along with true and random fractions) in more detail later in the text.

5.2.2 *Feasibility of activity imaging induced by proton beams*

The number of coincidences, efficiency factor η and fraction of scatter and random events contribution are shown in Table 8 and Table 9.

Table 8: The number of registered coincidences are distinguished into true, scatter and random fractions and efficiency factor η for all geometrical configurations for a single pencil beam of 150 MeV and $5{\cdot}10^9$ primary protons. Setups consisting of 24 modules are marked with $\star$.

SETUP	COINCIDENCES [x10^4]				η
	ALL	TRUE	SCATTER	RANDOM	
$\star$ Single layer barrel	3.00	2.28	0.51	0.21	$6.0{\cdot}10^{-6}$
Double layer barrel	5.80	4.55	1.00	0.26	$1.2{\cdot}10^{-5}$
Triple layer barrel	8.09	6.42	1.36	0.30	$1.6{\cdot}10^{-5}$
Single layer dual-head	2.42	1.93	0.38	0.11	$4.8{\cdot}10^{-6}$
$\star$ Double layer dual-head	4.56	3.68	0.76	0.13	$9.1{\cdot}10^{-6}$
$\star$ Triple layer dual-head	5.25	4.33	0.78	0.13	$1.0{\cdot}10^{-5}$

Table 9: True, scatter and random fractions for all geometrical configurations. Setups consisting of 24 modules are marked with ⋆.

SETUP	FRACTION [%]		
	TRUE	SCATTER	RANDOM
⋆ Single layer barrel	75.8	17.0	7.1
Double layer barrel	78.3	17.2	4.5
Triple layer barrel	79.4	16.9	3.7
Single layer dual-head	79.8	15.9	4.3
⋆ Double layer dual-head	80.6	16.6	2.8
⋆ Triple layer dual-head	82.6	14.9	2.5

Note that the presented results are not affected significantly by the scatter fraction, as presented in Table 8 and Table 9. As the PMMA phantom is significantly smaller with respect to the water phantom presented in the previous chapter (see Figure 34), fewer photons emerging from the phantom are scattered as they are attenuated. Assuming that the phantom is relatively small, the impact of additional layers on the number of registered coincidences is predominant over the detector's geometrical acceptance, resulting in a true fraction increase as the number of layers grows. Moreover, a greater true fraction for dual-head configurations than barrel setups is observed due to greater photon path length through the plastic scintillator, as discussed in Section 4.2.3. The effect mentioned above causes the scatter fraction for the dual-head configurations to be slightly lower than for the barrel setups.

The number of random coincidences increased with the number of layers. Furthermore, a greater number of random coincidences for barrel configurations over dual-head based setups is observed. This is because the PET data was integrated over time. The greater number of random coincidences in barrel configurations is due to their larger geometrical acceptance. Effect of the greater path length in the plastic scintillator (as in the case of scatter and true fraction) is no longer significant as the energy of the prompt gammas are of the order of MeV and the probability of the interaction within the plastic is lower than for annihilation quanta.

5.2.3 *Investigation of the precision of β^+activity distal fall-off point identification*

Examples of the reconstructed and emission profiles for single layer barrel and triple layer dual-head configurations (with 10^8 primary protons impinged PMMA phantom) are presented in Figure 45. The same profiles for $5{\cdot}10^9$ primary protons are depicted in Appendix C. The effect of the low number of coincidences (activity fluctuations along the beam direction) is also observed.

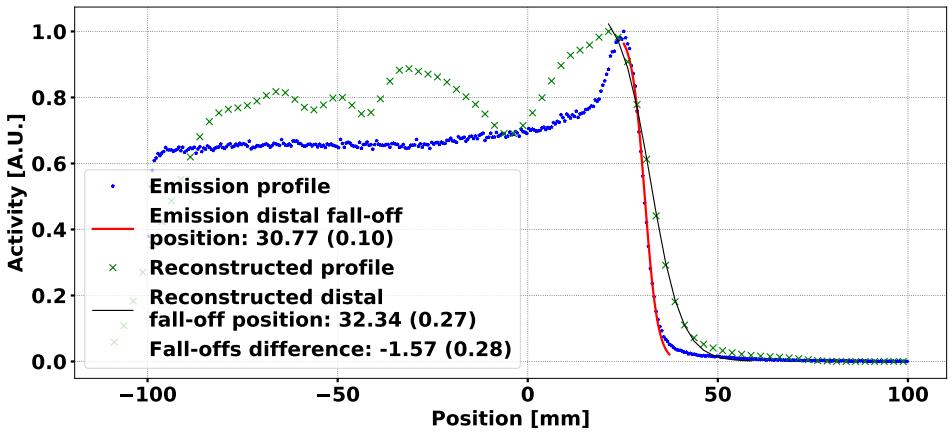

(a) Single layer barrel

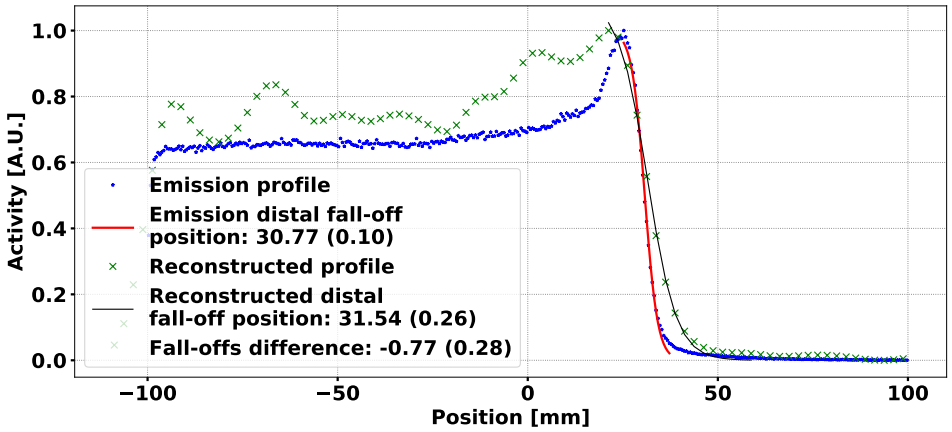

(b) Triple layer dual-head

Figure 45: Normalized emission and reconstructed activity profiles for the single layer barrel and the triple layer dual-head. The distal part of the emission profile and the reconstructed activity were fitted with sigmoid functions. Data originated from simulations with 10^8 primary protons.

The histograms of the difference between reconstructed and emission profile middle points for all geometrical configurations are depicted in Figure 46.

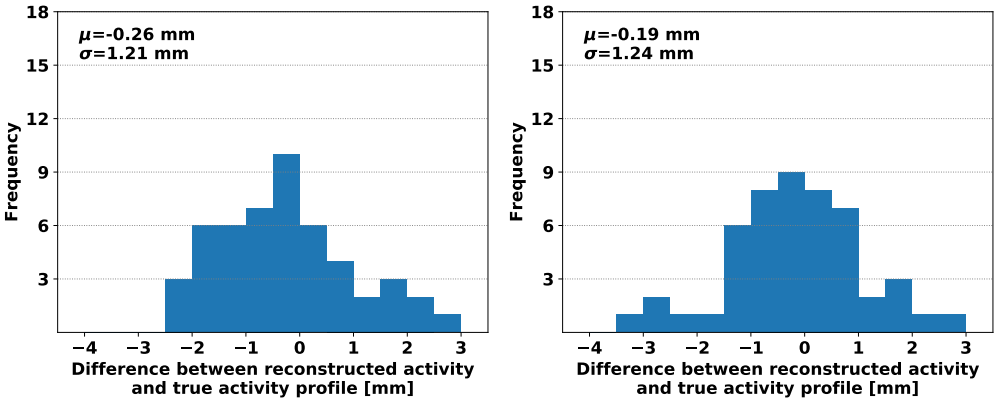

(a) Single layer barrel

(b) Single layer dual-head

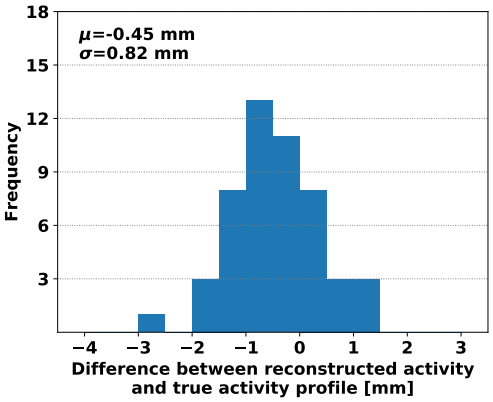

(c) Double layer barrel

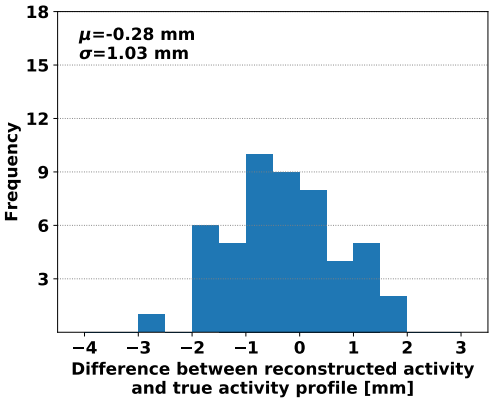

(d) Double layer dual-head

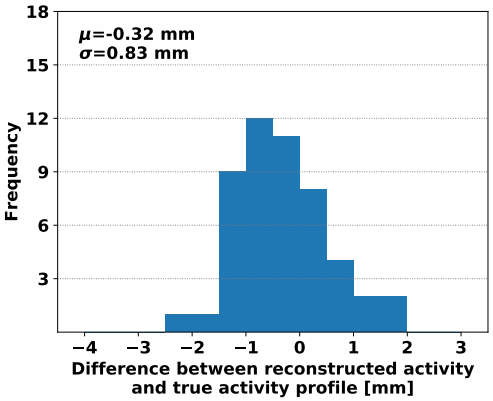

(e) Triple layer barrel

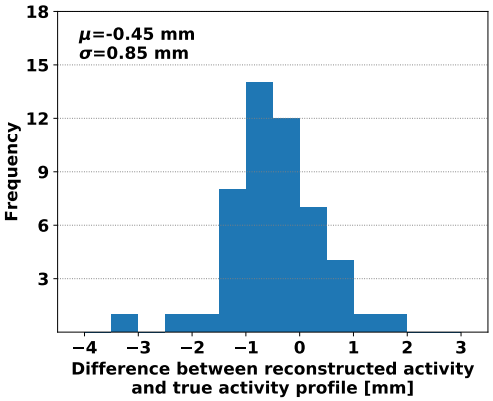

(f) Triple layer dual-head

Figure 46: Histograms of the difference between reconstructed and emission activity profiles for various geometrical configurations.The standard deviation is considered as a measure of the precision of the range determination.

The mean difference between the reconstructed and emission profiles range from -0.19 mm for single layer dual-head to -0.45 for double layer barrel and triple layer dual-head. In general, it shows a very good agreement between the reconstructed and emission activity range. Furthermore, considering the standard deviations, ranges calculated from the emission profiles are in agreement in 1σ with ranges calculated from the reconstructed profiles.

It is found that dual-head J-PET systems equipped with additional layers increase the mean difference and decrease the standard deviation. For the double and triple layer barrels, the standard deviation of the differences (0.82 mm and 0.83 mm, respectively) between profiles are at the same level and are better than for a single layer barrel. Adding a third layer to the barrel setup does not improve the result in terms of stability (standard deviation) over all double layer configurations.

5.2.4 *Estimation of the J-PET system sensitivity to detect proton beam range*

In this study, the 150 MeV proton pencil beam and the beams with neighbouring energies corresponding to range variation of $\pm$1,2,3 mm were simulated (see Table 7). This was performed to investigate the sensitivity of different setup configurations to detect these variations based on β^+activity produced by protons in homogeneous PMMA phantom. The emission and reconstructed activity profiles which were used to calculate 1D activity profiles along the beam direction are shown in Appendix D.

The differences between the positions of the distal fall-off middle points are gathered in Table 10. The differences in Table 10 are given for the beam with the median range of 161.69 mm.

5.3 DISCUSSION

In conclusion, the results presented in the former chapter demonstrate that the accuracy of the range assessment using the J-PET technology for solid phantom should not exceed 1.5-2 mm. What is important, the mean differences between middle points are smaller than the expected J-PET resolution, which is at the level of a few mm [17, 98]. Therefore, it can be concluded that after the experimental verification, in principle, all six configurations could be considered for practical application for proton range monitoring.

Standard deviation (SD) of the difference between reconstructed and emission activity profiles was used to measure precision of the range determination. It was found that additional detector layers improve the

Table 10: Difference between reconstructed activity distal fall-off middle point positions.

	BEAM						
	1	2	3	4	5	6	7
BEAM ENERGY [MEV]	149.94	150.47	151.00	151.53	152.06	152.59	153.12
BEAM RANGE [MM]	158.69	159.69	160.69	161.69	162.69	163.69	164.69
CONFIGURATION	ACTIVITY FALL-OFFS DIFFERENCE [MM]						
Single layer barrel	-1.66	-3.10	-1.18	—	-0.08	0.45	1.44
Double layer barrel	-4.17	-1.06	-1.03	—	0.83	0.93	3.96
Triple layer barrel	-1.77	-2.14	0.05	—	0.97	1.71	3.15
Single layer dual-head	-1.90	-1.66	-0.84	—	3.30	5.86	6.17
Double layer dual-head	-3.41	-1.91	0.56	—	1.12	4.05	2.39
Triple layer dual-head	-1.60	-2.05	-1.61	—	-0.19	2.25	2.59

precision by decreasing the SD for both barrel and dual-head systems. Among the geometrical configurations consisting of 24 modules, the lowest difference is found for single layer barrel, whereas the biggest for triple layer dual-head. As expected, the lowest SD is found in triple (0.83 mm) and double layer barrel (0.82 mm) and the highest for single layer barrel(1.21 mm) and single layer dual-head (1.24 mm). Thus, presented values are smaller than the planning treatment volume PTV treatment planning margins which are applied, i.a., to account for proton range uncertainty, and are at the level of a few mm up to 1 cm [4]. Therefore, the PET-based range monitoring application with the J-PET scanner could potentially reduce the safety margins and, consequently, the deposited dose in surrounding healthy tissue or OAR.

Direct comparison with other PET-based range monitoring systems is not straightforward because of the differences in the setups, e.g., PMMA phantom size and irradiation geometry.

Recently, the mobile PET system called DoPET developed in Italy at the Pisa University [139, 140] has been tested in CCB. Kraan and colleagues irradiated various phantoms and acquired PET signals immediately after the irradiation for 5 minutes mimicking the in-room range monitoring approach. Their experiments and Monte Carlo simulations with FLUKA revealed that the efficiency factor is at the level of η=2.85·10^{-5} compared to η in the range from 4.8·10^{-6} to 1.6·10^{-5} achievable with the J-PET scanner, as found in the frame of this thesis. The number of coincidences expected to be registered with the triple layer dual-head (the best among the scanners with 24 modules) is of the same order equal to η=1.6·10^{-5} (see Table 8). It has to be considered that in the case of the simulations presented within the thesis, the signal was integrated over time. Due to the differences mentioned above, a direct comparison of both systems is impossible. However, it might be concluded that the registered signal for the optimized J-PET scanner geometry (number of layers and modules, distance between heads, barrel radius) and DoPET equipment might be similar for the in-room/off-line applications.

Other experimental studies were performed at the Massachusetts General Hospital with a cylindrical slab PMMA phantom [126]. Measured PET activity distributions were compared to the Monte Carlo FLUKA and Geant4 codes. Three phantom setups were prepared. Two layers of PMMA were separated with air, lung or bone equivalent tissue slabs. The authors found range differences up to 2.6 mm, 1.5 mm and 1.7 mm between two measurements for PMMA-Lung-PMMA, PMMA-Air-PMMA and PMMA-Bone-PMMA slabs, respectively.

PET measurements with the PMMA phantoms were also performed with a whole-body dual ring Open-PET for the in-beam scenario with ^{11}C and ^{10}C radioactive beams [141]. The authors claimed that the beam position could be measured with a precision of 2 mm. In another Monte Carlo simulation study [136], a 150 mm spherical PMMA phantom mimicking a human head was exposed to a ^{10}C beam. The study revealed that the range could be verified with an accuracy of 0.6 mm. It is worth enhancing that the β^+signal registered from the irradiations with ^{11}C and ^{10}C ions is greater than from the ^{12}C ions beam. The ^{11}C and ^{10}C are also decaying to positrons, leading to better statistics and improved image quality.

The range uncertainties calculated in the thesis are expressed in Section 5.2.3 as the standard deviations of differences between the reconstructed and emission profiles. As discussed in the previous section, PET reconstructed activities (from experiments or simulations) are typically compared with the β^+emission distributions calculated with Monte

Carlo transport simulations of proton beams. The uncertainty of the range assessment originated from the uncertainties of Monte Carlo transport calculations, PET system properties and the PET acquisition statistics.

Monte Carlo transport calculations with various interaction cross-sections applied [34, 200] show that the activity range differences below 1 mm are found when a 5 minutes PET acquisition just after the treatment (in-room scenario) is considered. The difference increases up to 5 mm for a 30 minutes acquisition with 15 minutes delay after the treatment (off-line scenario). Unfortunately, no experimental verification with the J-PET scanners was possible at the time of the thesis preparation. However, the first feasibility studies performed at the lab of the Jagiellonian University indicate that the uncertainty of the position of the photon interaction place along the 50-cm long plastic strip of the J-PET module is at the level of 7 cm (FWHM) [98].

The activity range uncertainties calculated for all considered geometrical configurations are below 2 mm. This number is an order of magnitude lower than the precision of the 2nd generation J-PET system to localise the coincidence hit along the plastic strip. In the approach presented in the thesis an idealistic performance of the J-PET scanner is assumed that is expected to be achieved with the next generation J-PET detector equipped with wave-length shifters to increase the accuracy of localisation of the hit in the plastic. If this idealistic performance is not assumed, the activity range uncertainty would grow. Incorporation of that effect which is, however, out of the scope of the thesis, needs further investigation.

6

SIMULATION OF INDUCED ACTIVITY IMAGING ON PATIENT DATA

In the frame of this chapter, the feasibility of the simulation of the proton treatment plan, activity production and emission, along with the PET signal detection in six J-PET geometrical configurations, was performed. The number of coincidences of each type (true/scatter) is calculated along with the efficiency factor (η). Additionally, a qualitative comparison between reconstructed and emission β^+profiles is presented.

In the second step, optimization of two imaging parameters, i.e. reconstruction iteration number for a MLEM algorithm and post-reconstruction image smoothing, was performed. Two imaging parameters were optimized. First, the optimal number of iterations is calculated for each J-PET geometrical configuration using the NRMSD metric. Then, optimal post-reconstruction filter is proposed to assure the best match between reconstructed and true production activity distribution. Two types of filters are investigated: Gaussian (standard PET smoothing approach [68]) and median (as proposed by [15]).

6.1 MATERIALS AND METHODS

6.1.1 *The treatment and imaging protocol*

Spatial distribution of nuclear interactions leading to the production of β^+radioisotopes was calculated using GATE for a treatment plan of the patient treated at CCB. For the calculation, the in-room PET acquisition scenario was assumed.

The patient was diagnosed with glioblastoma located above the sella region. Planning Treatment Volume (PTV) was equal to 25.44 cm^3. The plan included two opposite irradiation fields (angles of the irradiation fields: 90°and 270°). The patient couch was positioned perpendicular to the beam axis and no rotation of the couch between the irradiation fields was needed. This allowed to simulate the entire treatment plan in one process as the GATE did not manage the couch rotation. If the user wants to include the rotation, the simulations must be divided into several smaller simulation scenarios with the manually rotating couch and then merge the results. The treatment plan consists of 1380 pencil

beams. The total number of $1.5 \cdot 10^{10}$ primary protons were simulated in GATE for both fields.

The treatment and imaging scenario protocol presented in the thesis assumes that the PET scanner is located in the proton therapy treatment room. The protocol assumes 10 minutes of continuous irradiation and 1 minute of the post-irradiation preparation of the patient for the PET scan. During this time, the patient is moved on the couch from the irradiation nozzle to the PET gantry. The position of the isocenter in the treatment plan is overlapped with the isocenter of the PET scan. The protocol is simplified with respect to the clinical treatment protocol. Several events, e.g. time needed for a technician to enter the treatment room, the time needed to rotate the gantry between fields, were not incorporated.

The PET signal is collected for 5 minutes with the same patient immobilization used in the treatment. PET data acquisition starts 1 minute after the irradiation. It assures registration of the signal originating from both rapidly decaying ^{15}O ($T_{1/2}$=122.24 seconds) as well as slower decaying ^{11}C ($T_{1/2}$=20.33 minutes). The advantage of the assumed protocol with respect to the off-line acquisition is an increase of the detected PET signal. For the off-line PET, the time needed for a patient transport causes a decrease of the β^+signal originating from ^{15}O.

6.1.2 *The simulation workflow*

The simulation workflow requires four steps (Pre-processing, I stage simulation, II stage simulation, PET reconstruction) presented schematically in Figure 47 and described in details below.

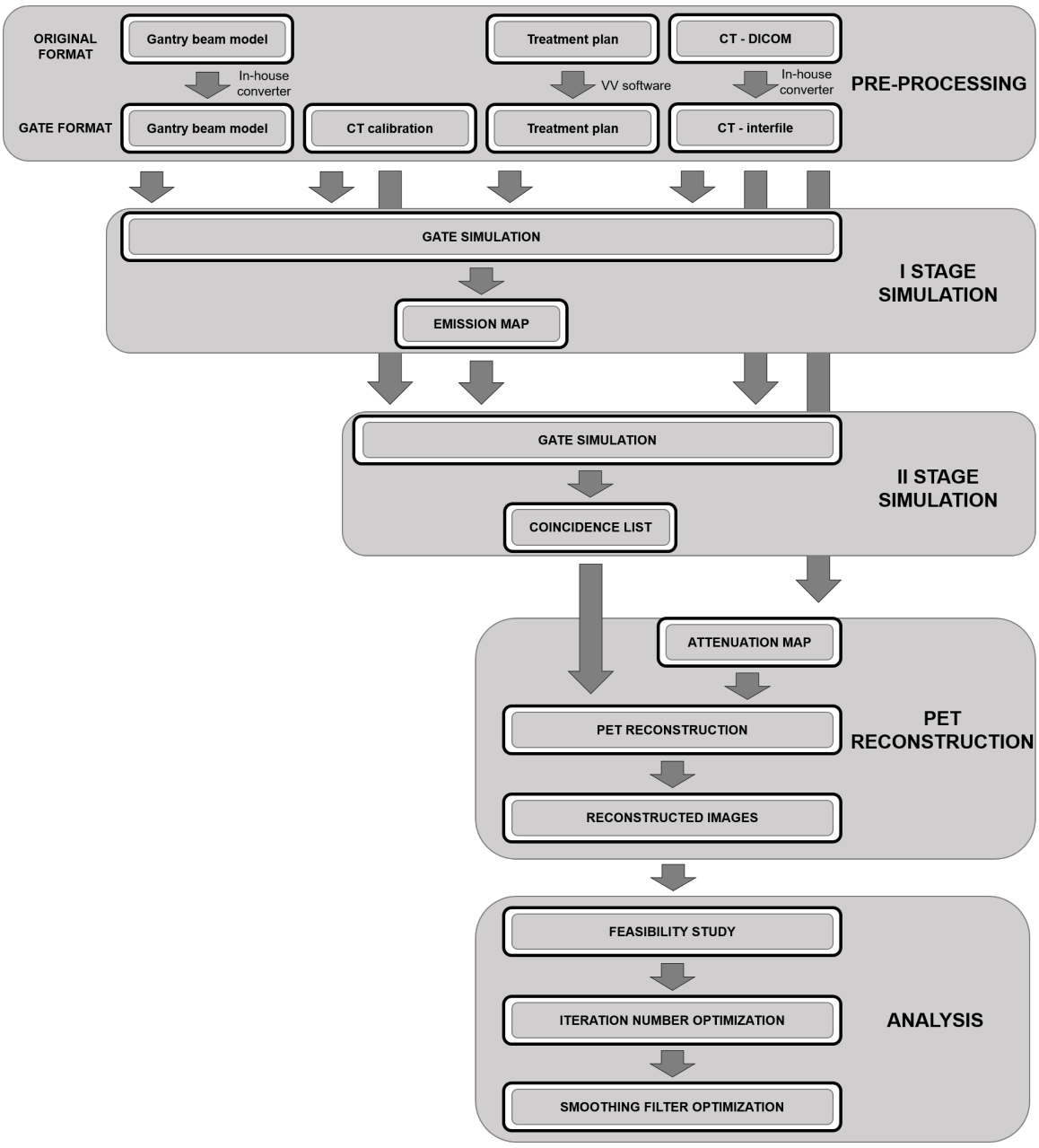

Figure 47: Scheme of the data preparation (pre-processing), I and II stage of the GATE Monte Carlo simulations, PET reconstruction and analysis.

6.1.2.1 *Pre-processing*

Before starting the work, several preparatory steps were necessary.

For Monte Carlo beam transport calculation, two data sets were required: the beam model as described in Section 3.3.1.1 and CT-based Hounsfield Units (acsHU) conversion to the body-tissue material composition [51, 201]. The calibration has been done by Gabriela Foltyńska from the Treatment Planning Section at CCB.

Additionally, the treatment plan was converted from Digital Imaging and COmmunications in Medicine (DICOM) format to the format of the GATE input file using open-source VV software [202]. This software is an open-source platform image viewer for fast and simple visualization of spatio-temporal images. It also offer tools for qualitative evaluation of image registration and deformation field visualization. Among other functionalities, it also enables the conversion of radiotherapy plans saved in the DICOM format to the GATE format.

The CT image of the patient was anonymized for the simulation. The applied CT image resolution was 0.69x0.69x1.2 mm^3. DICOM CT images were converted to the interfile format [203] compatible with GATE using the in-house developed script.

6.1.2.2 *I and II stage simulations*

For this study, a two-stage simulation approach was performed. In the first stage, the true β^+production activity distribution map (emission map) in the patient was simulated. Then, the resulting map was used for the PET simulation of the proposed six geometrical setups. This approach enables the production of the β^+emission map once for all six geometry configurations. Furthermore, this map could also be used for other geometries if needed. The second stage of the simulation includes only electromagnetic effects of the photons, whereas the first one also includes nuclei interactions. Therefore, this approach is computationally more efficient than a simulation of both steps for each geometrical configuration, assuring data redundancy. The workflow of both steps is as follows:

I stage: β^+activity simulation

The irradiation with multiple pencil beams in the geometry defined by the CT image was defined by the treatment plan. The *QGSP_BIC_HP_EMY* physics list the *Radioactive Decay* model was used in GATE for the simulations. PhaseSpace actor [198] (a more detailed explanation of the actor is given in Section 5.1.1) was attached to the patient CT. The output of

this step was the emission map, calculated from the information saved in the PhaseSpace actor. Production coordinates of all positrons produced during the in-beam phase constituted the emission map in the CT image grid. Here, for simplicity, the positron range was neglected. Calculations were performed using the Prometheus computational cluster [204]. The simulation was split into 5000 jobs simulated with $3{\cdot}10^6$ primary protons each. Each job was started with a different random number generator and took about 10 hours.

II stage: PET simulation

Separate simulations for each geometrical configurations of the J-PET scanner were performed. The simulation setup included the patient CT, emission map produced in the I stage and the J-PET scanner. The *emliver-more_polar* physics list was used in GATE software. Back-to-back gamma sources of monoenergetic 511 keV gamma quanta with the spatial distribution described in the emission map were simulated. Photons emerging from the patient were then detected with the J-PET scanners. As an output of the stage, the list of coincidences was produced by the GATE software.

6.1.2.3 *PET image reconstruction*

For PET image reconstruction, CASToR requires as an input the attenuation map in the same grid as the reconstructed PET image. Therefore, after the CT image conversion to the map of attenuation coefficients (μ) [91], the final attenuation map was resampled to the voxel grid of the PET reconstruction grid.

The coincidences list (output from stage II) was then used for the PET image reconstruction as described in Section 3.3.2.

6.1.3 *Analysis methods*

In the frame of the analysis, the feasibility study and two imaging parameters optimization (the number of iterations and the post-reconstruction smoothing filter) were performed. For the analysis, in-house developed Python scripts were used. All the scripts are open-source, available to download from the Github repository of the author of this thesis (`https://github.com/jawka`).

6.1.3.1 *Feasibility study: produced and reconstructed activity in the patient*

In order to investigate the feasibility of the simulation of the proton treatment plan, activity production and emission number of coincidences of each type (true/scatter) were calculated with the efficiency factor (η) following the procedure described in previous Chapters. Additionally, the dose, emission and reconstructed activity of 1D profiles across the isocenter were presented for a qualitative assessment.

The Normalized Root Mean Square Deviation (NRMSD) (Equation 21) was used to calculate the optimal number of iterations for the MLEM reconstruction algorithm following a strategy presented in detail in Section 5.1.1.

6.1.3.2 *Optimization of imaging parameters*

PET reconstructed images with the optimal number of iterations were used for finding an optimal post-reconstruction filtering to assure the best match between reconstructed and emission distribution images. Two post-reconstruction filters were tested: median and Gaussian. Four 3D filters (1x1x1 - non-smoothed images, 3x3x3, 5x5x5, 7x7x7 voxel sizes) were investigated for the median filter. For the Gaussian smoothing, five isotropic 3D filters of voxel size from 1x1x1 to 5x5x5 were used, where the numbers indicate the 1σ kernel size (i.e. for 3x3x3 kernel: 1σ = three voxels in all three dimensions). Reconstructed and smoothed PET images and emission maps were normalized prior to the subsequent analysis. The similarity between images was assessed within two ROIs (described below) with the PCC formula given as:

$$PCC = \frac{\sum_{i=1}^{I}(x_i - x_m)(y_i - y_m)}{\sqrt{\sum_{i=1}^{I}(x_i - x_m)^2 \sum_{i=1}^{I}(y_i - y_m)^2}} \tag{23}$$

where I is the total number of voxels, x_m is the mean intensity of the normalized emission image, y_m is the mean intensity of the normalized reconstructed activity image, x_i is the intensity of the i^{th} pixel in the normalized emission image and y_i is the intensity of the i^{th} pixel in the reconstructed activity image.

For the PCC analysis, two binary image masks based on CT grid were computed:

- PTV

  The mask considers only the PTV, which covers the tumour region with a few mm margin. Therefore, only voxels with the mask value equal to 1 are taken for the PCC calculation and the others are neglected.

- ACTIVITY

  The mask includes the region where the true production activity distribution is observed. First, all voxels with activity values greater than 10% of the maximum true production activity distribution were chosen. Then, subsequent morphological, image processing operations of dilation and erosion were applied to improve the uniformity of the mask (eliminate the gaps) [205].

The resulting masks were prepared using CT images and additional interpolation with the linear function was applied to transform masks to the PET reconstruction grid. Masks contours overlayed on dose distribution are shown in Figure 48 (top row). The threshold of 0.5 was applied to the masks with the PET reconstruction grid to binarize the interpolated masks.

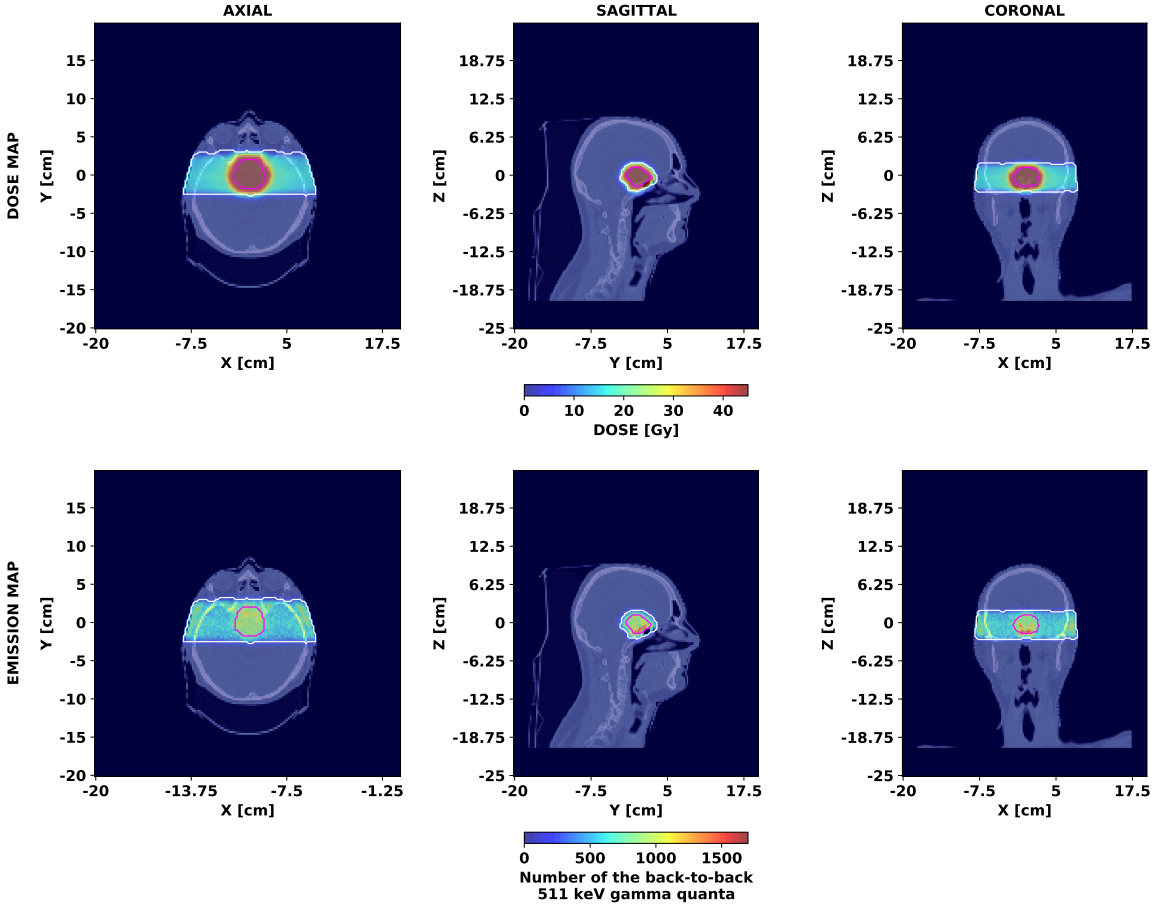

Figure 48: Dose distributions (top) and emission maps (bottom) with PTV ROI (red contour) and ACTIVITY ROI (white contour) used for the PCC calculation.

6.2 RESULTS

6.2.1 *Feasibility study: production and reconstructed activity in patient*

6.2.1.1 *Emission map*

The overall number of produced positrons for the presented in-room simulation scenario was $1.30 \cdot 10^7$.The true production activity distribution calculated for the described above in-room scenario is presented in Figure 48 (bottom row). The activity peak visible in the middle of the PTV ROI comes from overlapping of two activity distributions produced by two opposing treatment fields.

The distribution is shorter as compared to the depth of the corresponding dose distribution. This is because the observed PET distal fall-offs of proton-induced activities are about 6-7 mm proximal with respect to the dose fall-off, as presented in Figure 12.

6.2.1.2 *Reconstructed PET images*

Merged sensitivity and attenuation maps for all geometrical configurations are presented in Appendix E. The procedure was described in detail in Section 4.1.1. Examples of PET images reconstructed with 3D isotropic Gaussian smoothing (σ=2.5 mm - 1 voxel) applied post-reconstruction are shown in Figure 49 and Figure 50. Images were reconstructed with the optimal number of iterations as given in Table 13. More details on optimal number of iterations are presented later in the text (see Section 6.2.2.1).

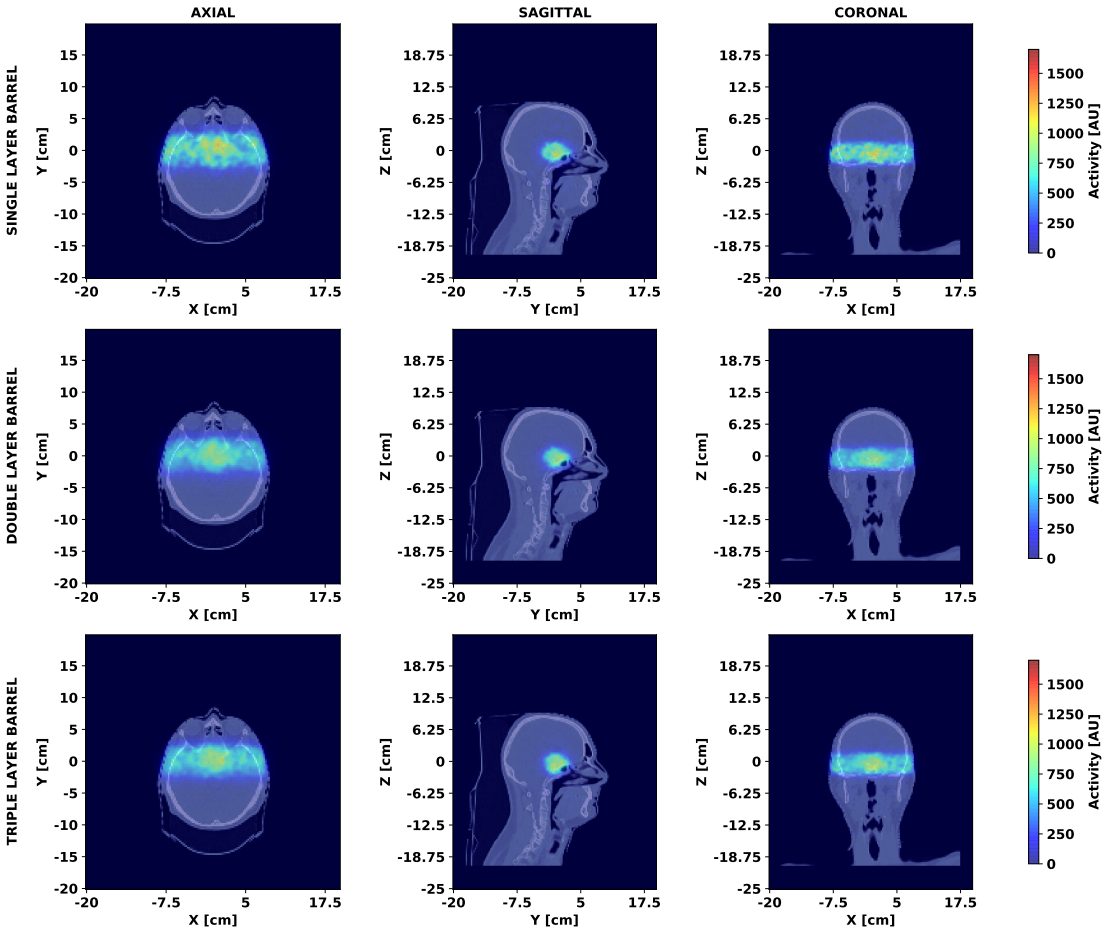

Figure 49: Reconstructed PET images superimposed on CT images for single layer barrel (top), double layer barrel (middle) and triple layer barrel (bottom) configurations in axial (left), sagittal (centre) and coronal (right) views.

The dose, emission and reconstructed activity 1D profiles across the isocenter are presented in Figure 51 and Figure 52 for barrel and dual-head based setups, respectively.

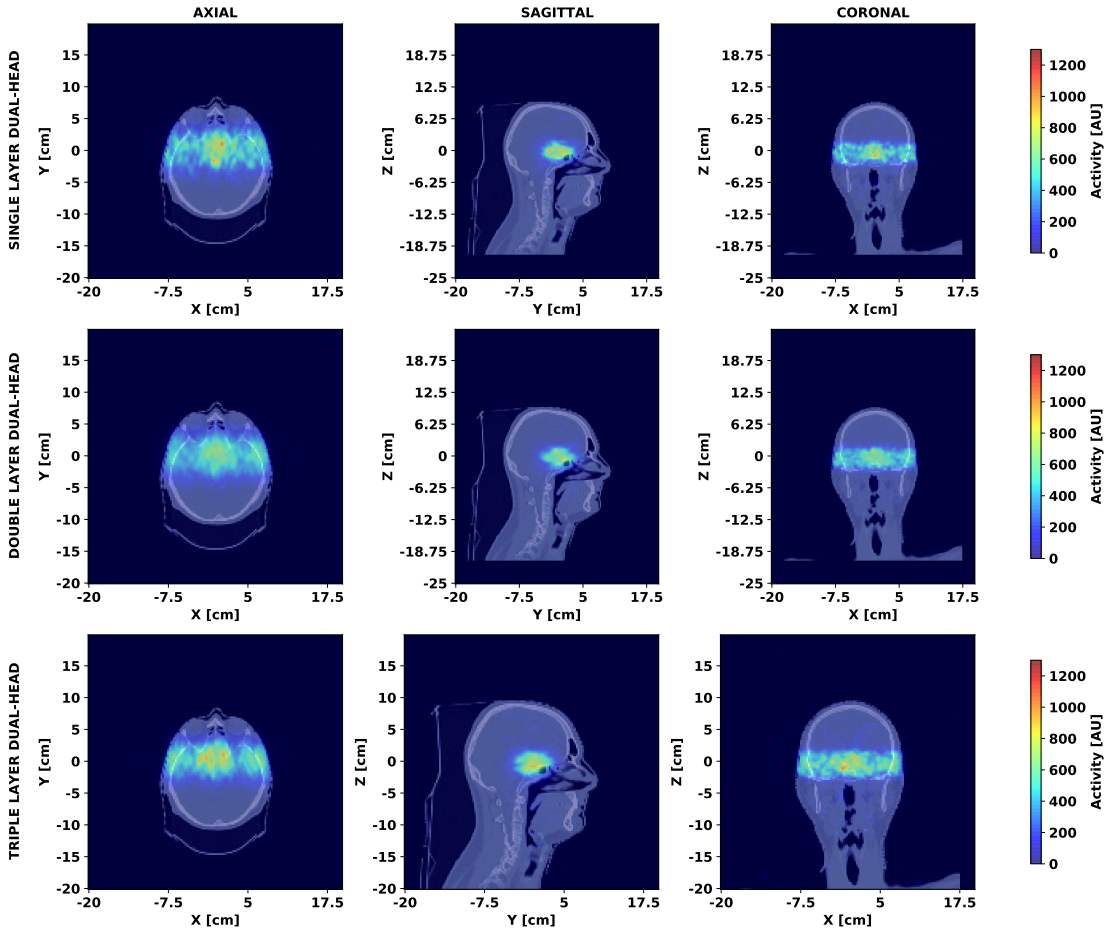

Figure 50: Reconstructed PET images superimposed on CT images for single layer dual-head (top), double layer dual-head (middle) and triple layer dual-head (bottom) configurations in axial (left), sagittal (centre) and coronal (right) views.

Presented PET images prove that the established workflow for the Monte Carlo simulations with GATE and PET reconstruction with CASToR is valid. As it is expected (and stated in previous Chapters), the elongated shape of the activity for dual-head setups is observed. Additionally, qualitative analysis of the dose, emission and reconstructed activity, presented in profiles in Figure 51 and Figure 52, overlap with themselves. Enhanced activity in the tumour region is observed for all three profiles and the increased activity in emission and PET reconstructed images is found. It proves the feasibility of the simulation of proton treatment plan and activity production as well as PET data reconstruction.

The number of produced coincidences, efficiency factor for all geometrical configurations (η) and true/scatter fraction contributions are shown in Table 11 and Table 12.

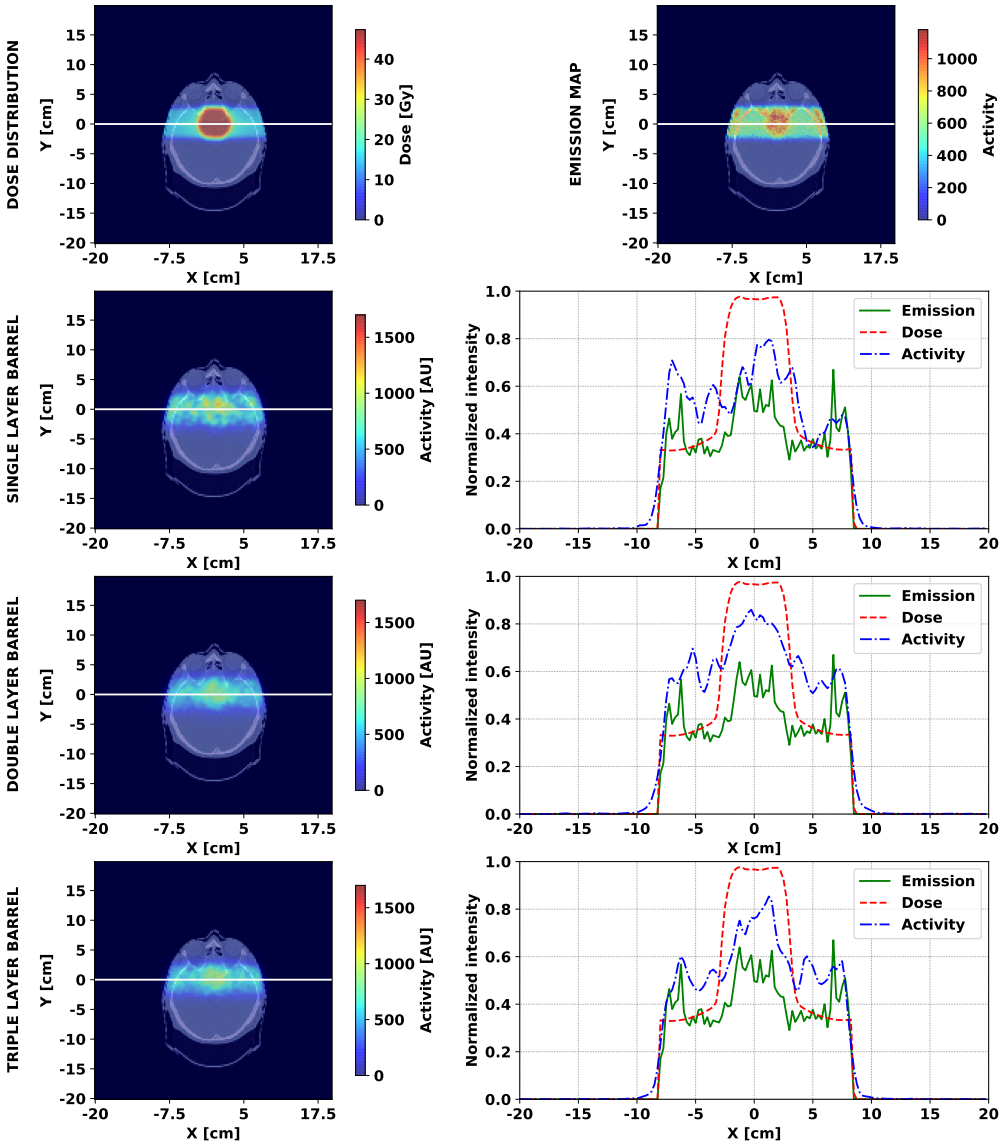

Figure 51: Reconstructed PET images of the activity collected during the in-room scenario (left column) with the corresponding dose, emission and reconstructed image profiles (right column). The results are presented for a single layer barrel (second row), double layer barrel (third row) and triple layer barrel (bottom row) J-PET setup configurations. The white line shows the profile position. Prior to the profiles drawing, reconstructed PET images were smoothed with a Gaussian filter with σ=1x1x1 voxels and then all images were normalized to the maximum intensity in the image. Dose and emission maps are shown (top row) as a reference.

The greatest number of registered coincidences is found for the triple layer barrel ($6.52 \cdot 10^4$) and the lowest for the single layer dual-head ($0.72 \cdot 10^4$), as expected. This is because the triple layer barrel has the

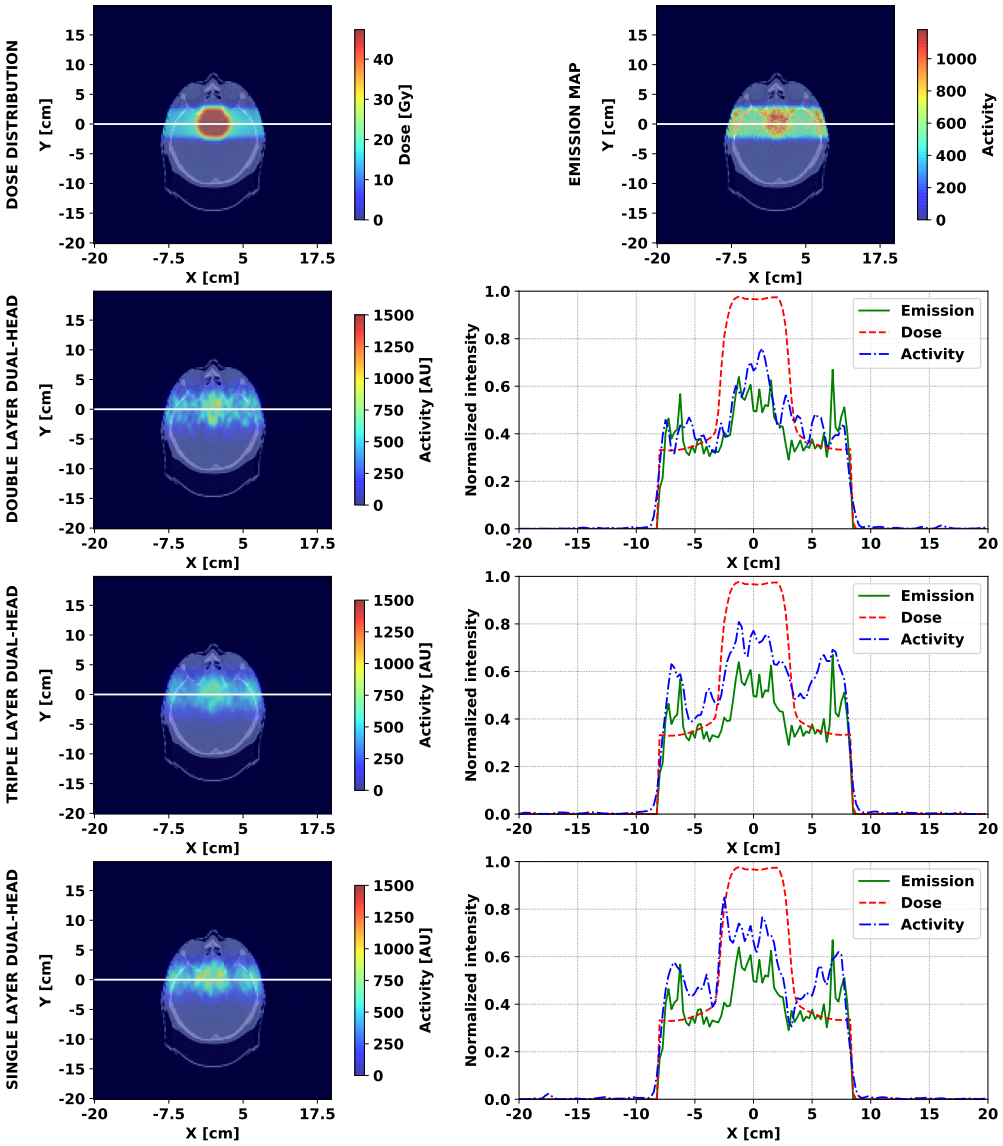

Figure 52: Reconstructed PET images of the activity collected during the in-room scenario (left column) with the corresponding dose, emission and reconstructed image profiles (right column). The results are presented for a single layer dual-head (second row), double layer dual-head (third row) and triple layer dual-head (bottom row) J-PET setup configurations. The white line shows the profile position. Prior to the profiles drawing, reconstructed PET images were smoothed with a Gaussian filter with σ=1x1x1 voxels and then all images were normalized to the maximum intensity in the image.

greatest geometrical acceptance and three layers of detectors. The single layer dual-head setup consists of the smallest number of detectors (12). The greatest η among the configurations consisting of 24 modules is observed in triple layer dual-head ($\eta=1.57\cdot10^{-6}$) and the lowest for

Table 11: The number of all registered coincidences, true and scatter numbers and efficiency factor presented for all geometrical configurations. Setups consisting of 24 modules are marked with ⋆.

SETUP	COINCIDENCES [x10^4]			η
	ALL	TRUE	SCATTER	
⋆ Single layer barrel	1.35	0.75	0.61	$0.90 \cdot 10^{-6}$
Double layer barrel	3.89	2.15	1.74	$2.60 \cdot 10^{-6}$
Triple layer barrel	6.52	3.66	2.86	$4.34 \cdot 10^{-6}$
Single layer dual-head	0.72	0.42	0.30	$0.48 \cdot 10^{-6}$
⋆ Double layer dual-head	2.10	1.20	0.90	$1.40 \cdot 10^{-6}$
⋆ Triple layer dual-head	2.36	1.43	0.93	$1.57 \cdot 10^{-6}$

Table 12: True and scatter fractions of registered coincidences for all geometrical configurations. Setups consisting of 24 modules are marked with ⋆.

SETUP	FRACTION [%]	
	TRUE	SCATTER
⋆ Single layer barrel	55.2%	44.8%
Double layer barrel	55.3%	44.7%
Triple layer barrel	56.1%	43.9%
Single layer dual-head	58.5%	41.5%
⋆ Double layer dual-head	57.1%	42.9%
⋆ Triple layer dual-head	60.7%	39.3%

single layer barrel (η=$0.90 \cdot 10^{-6}$). As the patient size is smaller than the water phantom presented in Chapter 4 and greater than the PMMA phantom presented in Chapter 5, the scatter fraction is at the level of about 40%, between values for the water phantom (~ 50%), and the PMMA phantom (~15%). Due to the patient size, the impact of additional layers on the number of registered coincidences is predominant over the geometrical acceptance. Therefore, the resulting true fraction increases as the number of layers grows for both barrel and dual-head based geometrical configurations. The scatter fraction for dual-head based setups

is slightly lower than for barrel based configurations. Due to the low number of simulated back-to-back gamma quanta (in-room scenario: $1.30 \cdot 10^7$) and the fact that they were simulated in equal time intervals (1 μs), no random coincidences are observed.

6.2.2 *Optimization of imaging parameters*

6.2.2.1 *Optimal iterations number*

The NRMSD values calculated for the each geometrical configuration in the first ten iterations are presented in Figure 53. The optimal iteration number used for reconstructed PET images presented in the Chapter are gathered for each setup in Table 13.

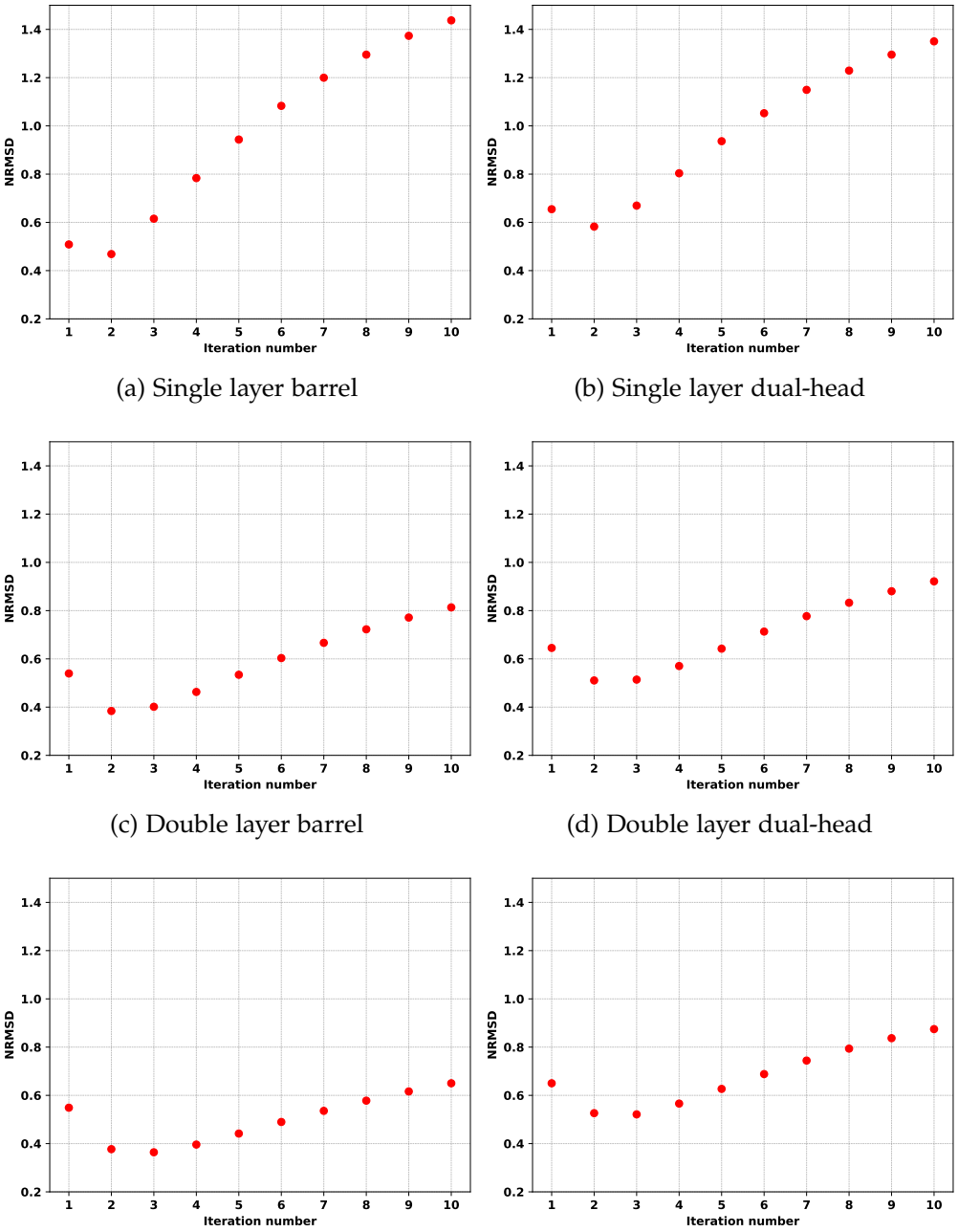

(a) Single layer barrel

(b) Single layer dual-head

(c) Double layer barrel

(d) Double layer dual-head

(e) Triple layer barrel

(f) Triple layer dual-head

Figure 53: The Normalized Root Mean Square Deviation (NRMSD) calculated for the selection of the optimal number of iterations for the reconstruction. The optimal number of iterations for the MLEM reconstruction algorithm is defined as the one for which the NRMSD reaches the minimum.

Table 13: The optimal number of iterations for all investigated J-PET setup configurations.

SETUP	OPTIMAL ITERATIONS NUMBER OF MLEM
Single layer barrel	2
Double layer barrel	2
Triple layer barrel	3
Single layer dual-head	2
Double layer dual-head	2
Triple layer dual-head	3

Optimal numbers of iterations are relatively small (2 or 3). This is the consequence of a low number of registered coincidences. The lower the number of coincidences, the faster the MLEM algorithm converges to the optimum. Images obtained with a number of iterations greater than optimal start to be noisier. A more detailed explanation could be found in Section 3.3.2 and [196].

6.2.2.2 *Analysis of Pearson Correlation Coefficient for the reconstructed PET images*

The best smoothing filter for the reconstructed PET images was found by comparing emission and reconstructed activity in PCC analysis. The numerical value of the PCC is a measure of the agreement between reconstructed and emission activities. Graphical presentation of the PCC in the form of so-called heatmaps for a given filter and each geometrical configuration for both PTV and ACTIVITY ROIs is given in Figure 54.

For the same applied filters, PCC values increase as the number of coincidences grows. In general, the greater the PET signal statistics, the better is the image quality. Overall, PCC values are greater for the ACTIVITY ROI than for PTV ROI. The PTV ROI is smaller than the ACTIVITY ROI and relatively smaller differences in the activity distributions within the ACTIVITY ROI with respect to the true production activity distribution are observed. This is indicated by the lower value of the PCC (Equation 23).

Examples of the PET images reconstructed with various smoothing filters for the single layer barrel and the triple layer dual-head setup are shown in Figure 55 and Figure 56, respectively.

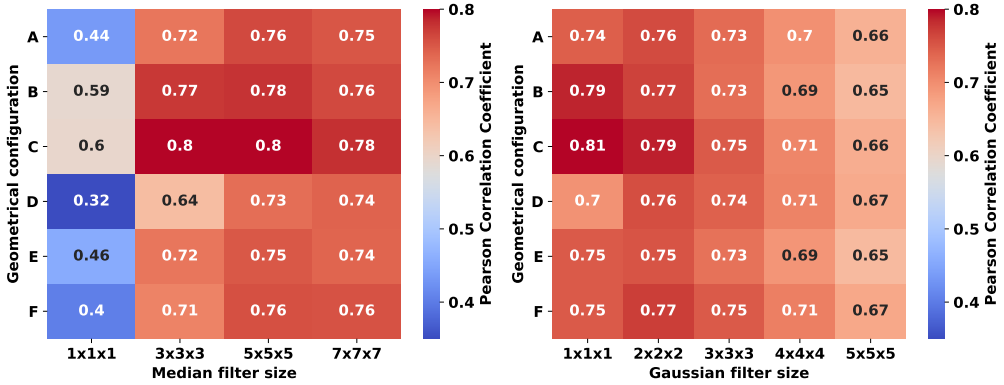

(a) ROI: ACTIVITY; filter: median

(b) ROI: ACTIVITY; filter: Gaussian

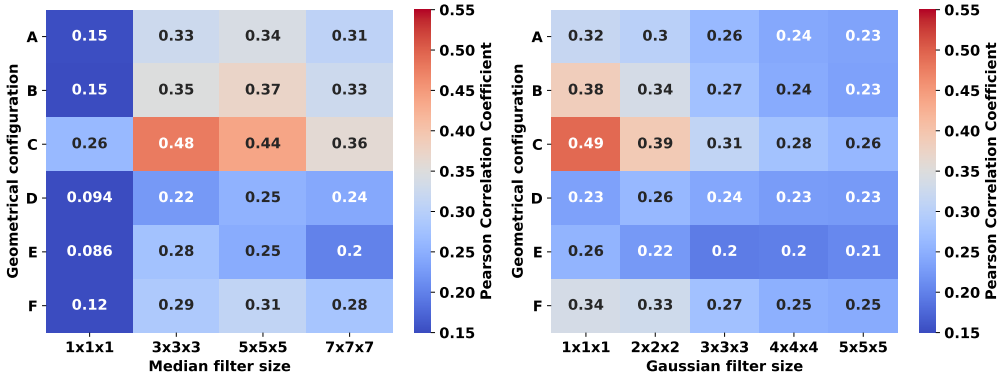

(c) ROI: PTV; filter: median

(d) ROI: PTV; filter: Gaussian

Figure 54: Graphical presentation of the Person Correlation Coefficients (PCC) (heatmaps) calculated for the ACTIVITY ROI and PTV ROI. 3D post-reconstruction filters of various sizes (median filter) and sigma (Gaussian filter) were applied. Capital letters A, B, C, D, E, F correspond to single layer barrel, double layer barrel, triple layer barrel, single layer dual-head, double layer dual-head and triple layer dual-head J-PET configuration, respectively.

The most accurate smoothing approach for the Gaussian filter is the one with kernel sizes: 1x1x1 and 3x3x3. The exception is observed for the single layer dual-head where filters 3x3x3 and 5x5x5 kernels seem to be optimal, but this setup is not suitable for PET imaging due to its low efficiency. The emission and reconstructed images are qualitatively comparable for both ROIs. Various kernel sizes show the best results for the median filtering approach depending on the geometrical configuration and considered ROI. However, for all cases, non-smoothed PET images (median filter with 1x1x1 kernel) show the worst results. Additionally, the best results between Gaussian and median filters are at the same level for both ROIs. Therefore, considering quantitative (PCC value)

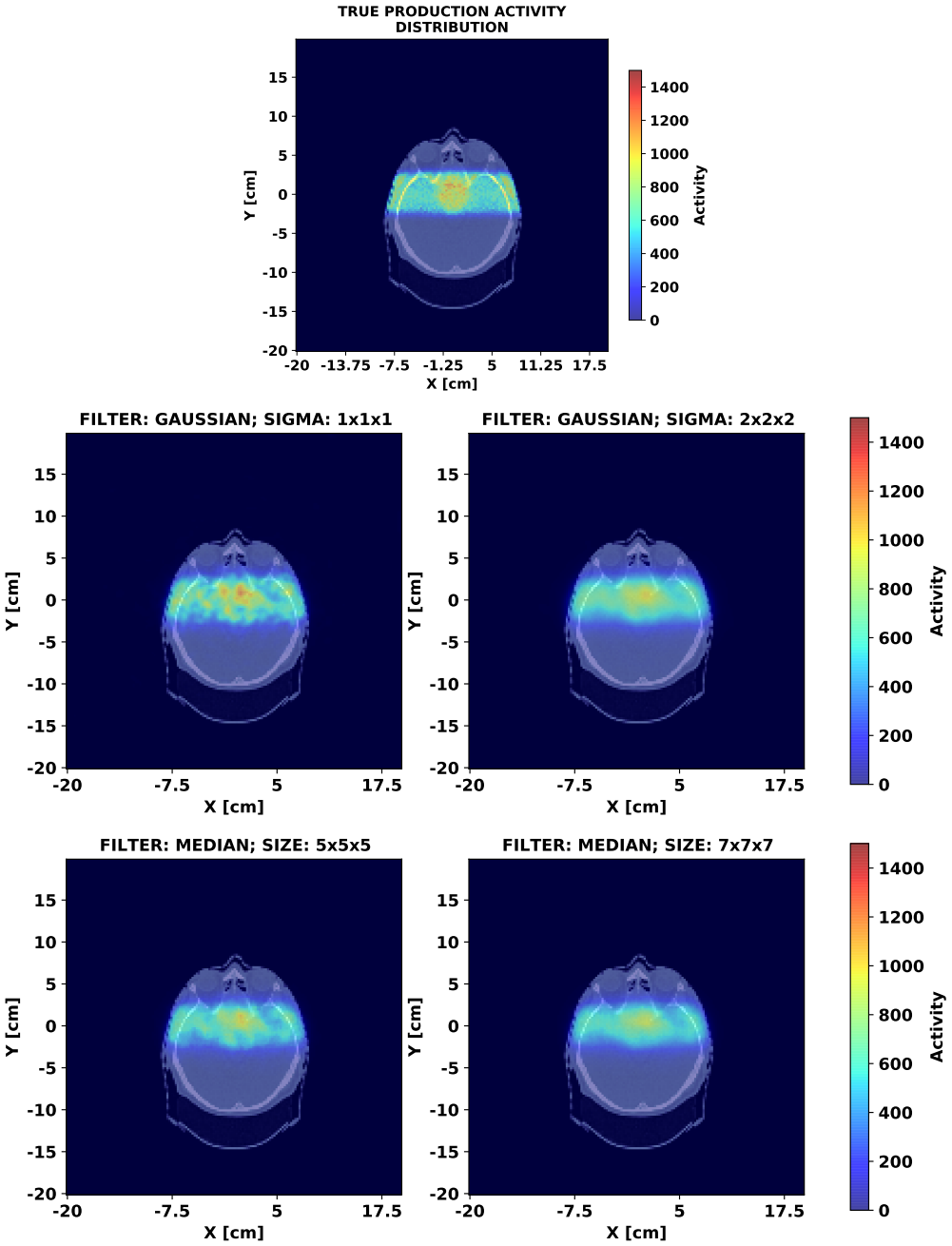

Figure 55: True production activity distribution (top) and PET images reconstructed for single layer barrel using the Gaussian (centre row) and median (bottom row) filters. The size of the filter applied is given at the top of each image.

and qualitative (reconstructed images) results, Gaussian filtering with a 1x1x1 kernel size tends to offer the optimal solution.

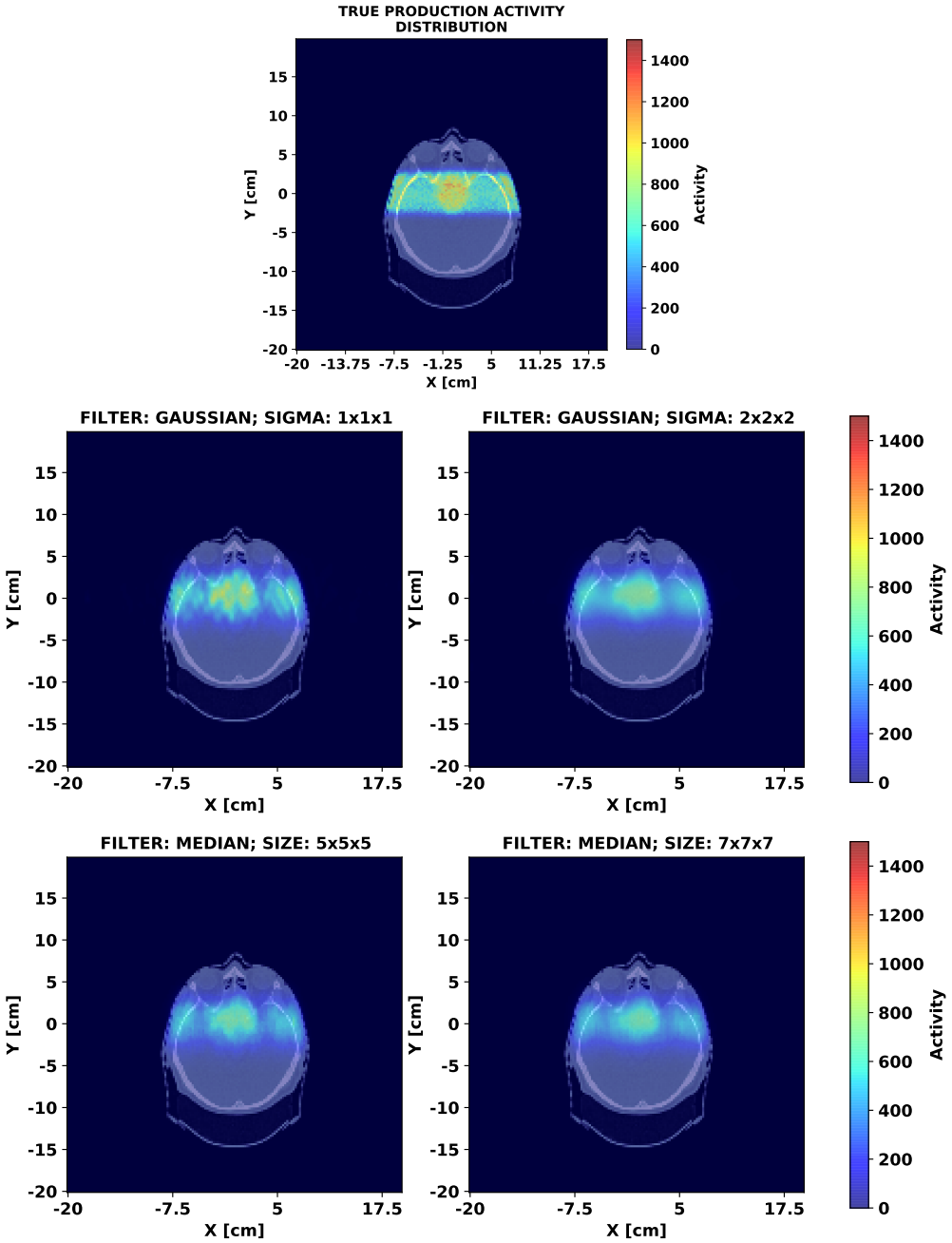

Figure 56: True production activity distribution (top) and PET images reconstructed for triple layer dual-head using the Gaussian (centre row) and median (bottom row) filters. The size of the filter applied is given at the top of each image.

Reconstructed images for all geometrical configurations in three anatomical orientations considering the best smoothing approaches are given in Appendix F.

6.3 DISCUSSION

In this chapter, quantitative and qualitative analyses have been performed to investigate the feasibility of the PET acquisition and reconstruction with the J-PET β^+signal originating from the patient irradiation. The analysis of the reconstructed PET images presented in Section 6.2 suggests that all presented geometrical configurations are feasible to collect sufficient signal for the in-room acquisition enabling the qualitative assessment of the proton-induced β^+activity in the patient. The reconstructed 3D activity distributions and 1D activity profiles well overlap with the emission and dose profiles. The PET image acquisition protocol investigated in this study assumed 10 minutes of continuous irradiation and 1 minute of the post-irradiation preparation of the patient for the PET scan. Firstly, the limitation of this simplified protocol is that the time needed for a technician to enter the treatment room to rotate the gantry between treatment fields was not taken into account. Additionally, the gantry rotation time with a speed of about $\sim 3°/s$ could also be incorporated in the future protocol for simulation of the J-PET imaging for proton therapy range monitoring.

The number of coincidences and the true/scatter fraction are highly dependent on the patient anatomy, treatment plan, tumour size and location, and on number of primary protons used for the treatment. The number of primary protons used in the treatment plan presented in this section is relatively small and consists of $1.5 \cdot 10^{10}$ primary protons. The number of protons used for irradiation of the tumour target with the typical dose of 2Gy is about 10^{11}. It leads to higher statistics for PET examination with respect to the presented patient case, even by a factor of 10, which will improve the quality of the reconstructed activity image for the in-room imaging scenario.

The optimization of the number of iterations in the MLEM reconstruction algorithm and post-reconstruction smoothing filter was presented in the former subchapter. Qualitative analysis reveals that the Gaussian filter approach with the specific kernel size 1x1x1 better match the reconstructed and true production activity distributions than PET images without any post-reconstruction image smoothing. The reason is that the reconstructed activity with a low number of coincidences is rugged, whereas true production activity distribution is obtained with higher statistics. The applied smoothing procedure improves the reconstructed image as it was demonstrated using PCC analysis. For lower true production activity and decreased registered coincidence statistics, the true and reconstructed images would be more rugged. The choice

of an optimal smoothing parameter would depend on detector setup configurations and imaging protocols.

A visual comparison suggests that the Gaussian filter with the kernel size 1x1x1 (σ= one voxel in three directions) offers best-reconstructed image quality for all J-PET geometrical configurations. However, this analysis was performed only for one patient with a relatively small number of primary protons. Therefore, further investigation for treatment plans with various primary protons and tumour localization is needed to generalize the present findings.

It is essential to compare the predicted performance of the setups based on the J-PET technology with the existing PET-based range monitoring systems, in which conventional crystal detectors are applied. One of the first range verification studies with patients was performed at the Massachusetts General Hospital, Boston, US [111]. PET-based reconstructed activity profiles were compared with the Monte Carlo simulations of the emission profiles. In addition, 50 distal fall-offs positions were used to compare emission and measured profiles using the off-line approach. The experiments revealed up to 2 mm range differences between Monte Carlo and reconstructed activities for patients with cranial base, spine, orbit and eye regions irradiation.

Nischwitz and colleagues [129] performed the analysis with an off-line scenario in the HIT facility using the most-likely-shift method [147]. They analyzed 20 patients that underwent proton irradiation followed by the PET/CT examination. Range assessment was performed between the two measurements, and between PET measurements performed, one early and one late during the radiation treatment, and Monte Carlo simulated predictions. For the first case, the ranges between the consecutive measurements deviated by 0.7 mm (±0.7 mm). The comparison showed that the mean range deviation between simulations and measurements was at the level of 3.3 mm (±2.2mm). Lower differences were observed for patients irradiated with ^{12}C. The same group also assessed the inter-fractional range variations with an off-line PET/CT scanner. They deduced from both PET measurements and Monte Carlo simulations that range shifts at the level of 3.0 mm could be distinguished, which offers the possibility to monitor range of proton beams and eventually reduce PTV safety margins.

A further study performed at the Proton Therapy Institute, Jacksonville, US, developed a PET-based range verification method for prostate irradiation. 50 PET/CT post-treatment imaging examinations were performed for ten prostate cancer patients (four to six scans per patient along the whole treatment course) [131]. PET-defined beam path was compared with a marker-defined path (calculated by the centroid of implanted

markers). An average displacement between paths from 0.6 mm up to 4.6 mm was observed depending on the resulting path discordance. It was found that the PET range verification method can derive additional information on the inter-fractional prostate motion. The authors claimed that the method might be used for patient-specific PTV margins calculation.

A combined study based on patient data from MGH and HIT for in-room PET and off-line PET/CT scenarios respectively were performed by Frey and colleagues [147]. Data from 15 patients was analyzed. The reconstructed PET activity distribution from the day of the treatment was compared with the PET images acquired after previous treatment fractions and Monte Carlo simulations. The range shifts of 2-3 mm at the 50% and 35% activity distal fall-offs were found. The authors claimed that this method demonstrates sufficient accuracy of PET-based range monitoring to be incorporated for clinical routine.

The NeuroPET scanner [132] was also used in MGH as an in-room PET scanner for treatment verification [133]. Data from 9 patients was analyzed. PET reconstructed activity was compared with Monte Carlo predictions using the middle points technique [133] also used in this thesis. The average differences between the middle points were smaller than 5 mm with the root mean square deviations from 4 to 11 mm. It was also reported that co-registration errors between PET and CT images lead to approximately 2 mm errors in estimation of the proton range. The study also showed no gain in the range assessment when the PET scan took 20 instead of 5 minutes.

Kuess et al. investigated both in-room and in-beam acquisition scenarios [148] using Monte Carlo simulations for the ^{12}C irradiation plans. The authors simulated the activity distributions. Based on the efficiency of the PET system, they predicted the shape of the reconstructed PET activity profiles. Based on the PCC analysis they claimed that for patients with head and neck tumours, identifying of 4 mm shifts was possible for the in-beam scenario and shifts greater than 4 mm for in-room acquisition.

A comprehensive simulation study with the in-beam scenario was conducted at GSI, Darmstadt, Germany [134]. A quantitative analysis was performed to assess the accuracy of the dual-head in-beam PET system [16] to detect range deviations between planned and applied treatment. Monte Carlo simulations were used as described in [206]. A comparison between simulated and reconstructed activity profiles was performed. Two activity distributions with modified ranges were delivered for each treatment plan: one with proton beam range reduced by 6 mm and the second with 6 mm overrange. The last simulation did not

introduce any modification to the range and was used as a reference. Then, all the images were compared by six experienced observers. The results show that the observers correctly recognized 6 mm range deviations in 70% of cases. For the task defined as detecting the presence of overrange, the sensitivity, specificity and efficiency at the levels of (91 ±3)%, (96 ±2)% and 94% were found, respectively. When the task was to detect the reduced range, the numbers were (92 ±3)%, (96 ±2)% and 95%.

Experiments with a dual-head PET detector in an inter-spill scenario were conducted at CNAO, Pavia, in the frame of the Instituto Nazionale di Fisica Nucleare (INFN) INSIDE project [15, 138]. A quantitative analysis was performed in the first study for data from a patient irradiated during two consecutive treatment sessions [15]. The PCC between measured activity maps at the level of 0.9 after 2 minutes of PET data acquisition was reported. An additional analysis with BEV and OV methods showed the range agreement below 1 mm between the treatment sessions. In the second study, Fiorina and colleagues [138] showed the feasibility of the method to determine the treatment compliance when morphological changes are present. The method could potentially help clinicians to detect variations of proton range that occurred during the patient treatment. An average activity range difference and compliance map analysis techniques were used in this study. More technical details about the analysis could be found in the paper [138].

The results presented in the thesis show similar precision obtained for the J-PET technology as compared to the other discussed PET-based range monitoring systems. The advantage of the J-PET technology is greater FOV with respect to other systems. Typical scanners have axial FOV at the level of 20-25 cm. The image quality obtained with J-PET is also similar to the PET images registered with other systems. Furthermore, due to the properties of the plastic scintillators (density is seven times lower than for conventional crystals, e.g. LSO), the J-PET system is much lighter, which matters when the detectors are to be mechanically connected to the treatment nozzle. Moreover, the number of needed photomultipliers and electronic parts is lower as the readout is done at the ends of the scintillator strips. The minimized number of photomultipliers, simplified electronic read-out and the lower price of plastic scintillators make the J-PET technology cost-effective, and therefore a very attractive and promising system for proton beam range monitoring in hadrontherapy.

7

SUMMARY

Proton therapy is one of the most advanced and precise radiation therapy techniques. The main advantage of the technique is excellent dose conformity leading to lower doses to Organs at Risk (OAR), increasing dose to target volume and reducing late side effects compared to the conventional photon therapy. The reason for that is the steep distal dose fall-off at the end of the Bragg peak. However, it is also a source of uncertainty of proton range in a patient, which may lead to significant underexposure of target volume or overexposure of an OAR, limiting the accuracy of proton radiotherapy. Therefore, the uncertainties of proton range during the patient treatment are considered one of the main disadvantages of proton therapy. To reduce this drawback, it is proposed to monitor the actual range of the proton beam during the treatment by different means. Protons interacting with human tissue produce β^+radioisotopes, which could be detected with a PET camera (scanner) and used to assess the range of the beam.

The aim of the work was to investigate the feasibility of the application of the novel type of PET system based on the organic scintillator modules, developed at the Jagiellonian University by the J-PET collaboration, for range monitoring of therapeutic scanning proton beams.

For this purpose, it was proposed to investigate six geometrical configurations of PET scanners based on 24, 48 and 72 J-PET modules. The modules were arranged in barrels and dual-heads. An advanced workflow was proposed to simulate the activity produced by the therapeutic proton beams in phantoms and in a patient and to reconstruct the PET signal registered by the proposed PET scanners. The data workflow started from the Monte Carlo transport calculations performed with the GATE for β^+activity originating either from the PMMA phantom or the patient. Then, the signal was propagated to six individual J-PET configurations, where it was collected, analysed and converted internally by GATE into the list of coincidences. The η factor (efficiency factor) was calculated based on the number of registered coincidences to assess the efficiency of each scanner for a particular simulation setup. PET images were reconstructed with CASToR software. Attenuation and sensitivity corrections were taken into account. List-mode MLEM algorithm with TOF modelling was used for the reconstruction. Finally, the analysis of the uncertainty of the range detection and the optimization of the reconstruction parameters were performed.

The reconstruction methodology was validated for a phantom with uniformly distributed activity, placed isocentrically in six different geometrical configurations. Prior to the reconstruction, each scanner was calibrated. The number of coincidences, η value, reconstructed PET images quality and impact of the scatter fraction were reported and discussed for each setup.

The developed methodology of the PET signal reconstruction was tested for range determination of proton pencil beams impinging on a PMMA phantom. Monte Carlo simulations of single beam irradiations were performed using the clinical beam model used for patient treatment at the Cyclotron Centre Bronowice CCB proton therapy centre. Monte Carlo studies of PET activity variations in phantom due to variation of proton beam energy revealed that the accuracy for a range assessment of the single proton pencil beam is at the level of 0.82 - 1.25 mm. The best sensitivity and stability of the proton range estimation was found for double and triple layer barrel configurations. An acceptable compromise of PET image quality, range estimation precision versus the number of J-PET modules and the ability to integrate the detector in the proton therapy treatment room were found for the double layer dual-head configuration. The images of the reconstructed activity distribution for all geometrical configurations show the feasibility of the CASToR software to reconstruct the coincidences signal induced by the proton beam and collected with the tested J-PET scanners. Furthermore, it was demonstrated that the accuracy of the β^+activity range detection at the level of 1.5-2mm is achievable. However, an experimental validation of the results is needed.

The final step of the work was to reconstruct the PET signal from the radioactivity induced in a patient treated at the CCB. In Monte Carlo simulations, in addition to the proton beam model of CCB, the CT calibration was applied to simulate PET activity distribution in the CT scan of the patient. The in-room PET acquisition scenario for the proton beam range monitoring was considered and presented in this work. Optimization of two data processing parameters (number of iterations and post-reconstruction smoothing filter) was performed. For optimization of the number of iterations, the Normalized Root Mean Square Deviation (NRMSD) value was used as a metric. For each scanner, an optimal number of iterations was found. Then the images reconstructed with an optimal number of iterations were used to optimize the post-reconstruction filtering. To do that, the Pearson Correlation Coefficient (PCC) was calculated between reconstructed and Monte Carlo simulated emission maps. The quantitative (PCC value) and qualitative (reconstructed images) results indicate that Gaussian filtering with 1x1x1 kernel size was found

as the optimal smoothing approach. The information about the lower level of PCC than expected could be potentially used if the anatomical changes in the patient body occur (tumour shrinking/growing, mucus in sinuses, etc.). Calculated PCC for PET images from subsequent treatment fractions lower than the set threshold might indicate the necessity of the treatment plan verification.

Developed methodology and simulation studies that were performed in the frame of this thesis proved that PET scanners based on J-PET technology are feasible to perform the in-room range monitoring of the proton beam in a patient. As expected and discussed in previous chapters, the quality of PET images obtained with J-PET scanners is better for barrels than for dual-head based setups. The comparison of the geometrical configurations built out of 24 modules shows that the highest statistics is collected with a triple layer dual-head setup. However, the image quality suggests an advantage of the single layer barrel configuration because the reconstructed activity is more similar to the emission distribution. The elongated shape of the reconstructed activity distribution along the y-axis is observed for dual-head setups due to the scanner geometry which is not cylindrical (two heads). The great advantage of the dual-head system is the ability to place the scanner in the treatment position and start PET signal acquisition immediately after the end of irradiation, increasing the beta+ signal originating from the decay of ^{15}O isotopes of short, 2 minutes half-life time.

In the thesis framework, GATE Monte Carlo simulations of the β^+signal originated from the patient, registered with the J-PET scanner and reconstructed with CASToR software are presented for the first time. The results show the feasibility of the J-PET technology for the in-room range monitoring for proton radiotherapy. Futhermore, the system with a larger FOV, lighter weight, fewer electronic parts and lower price makes the J-PET technology cost-effective, and a promising system for proton beam range monitoring in hadrontherapy.

APPENDIX A

Attenuation correction, sensitivity and merged sensitivity and attenuation maps of the water 20 x 20 x 25 cm^3 phantom for different geometrical configurations of the J-PET detectors.

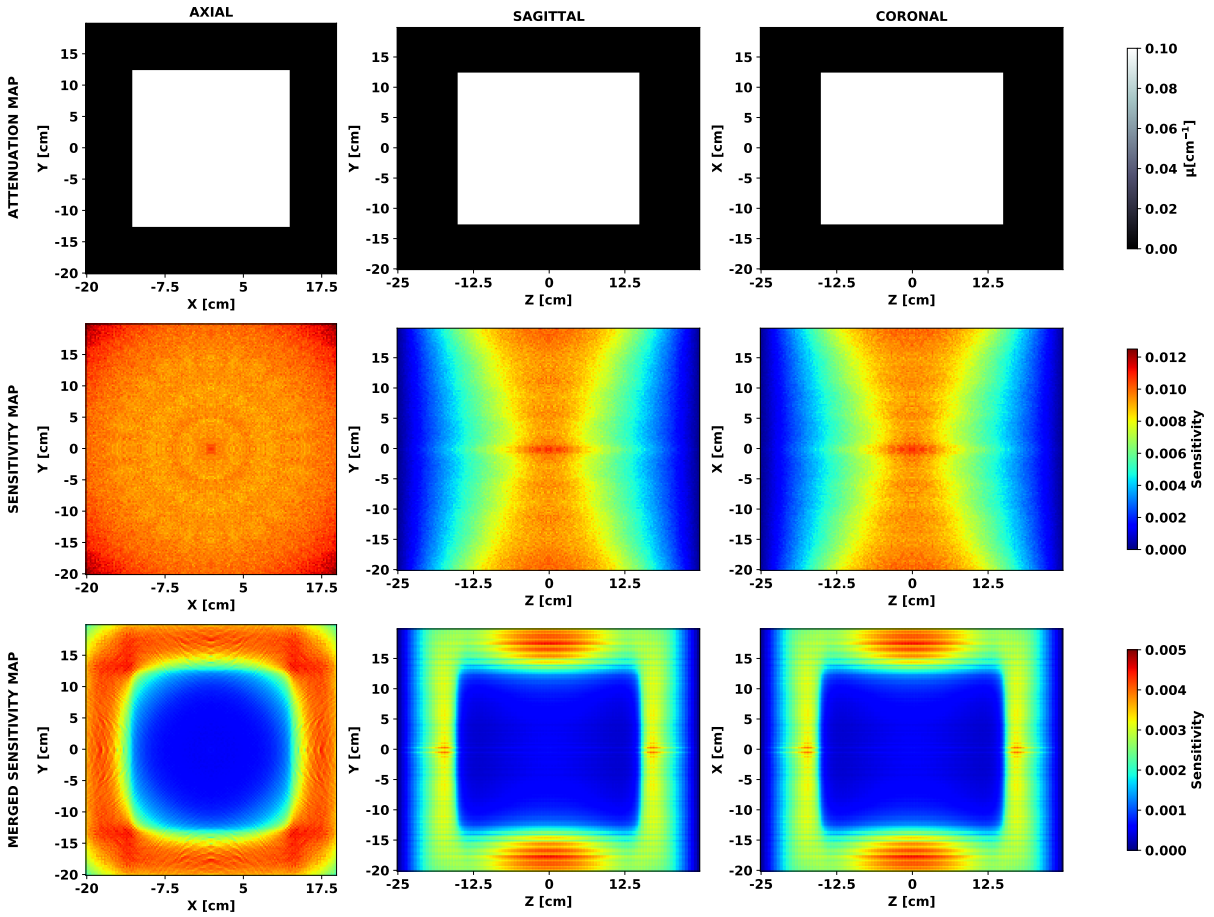

Figure 57: Attenuation correction (top), sensitivity (middle) and merged sensitivity and attenuation - merged sensitivity map (bottom) maps of the water phantom for double layer barrel configuration in axial (left), sagittal (centre) and coronal (right) view.

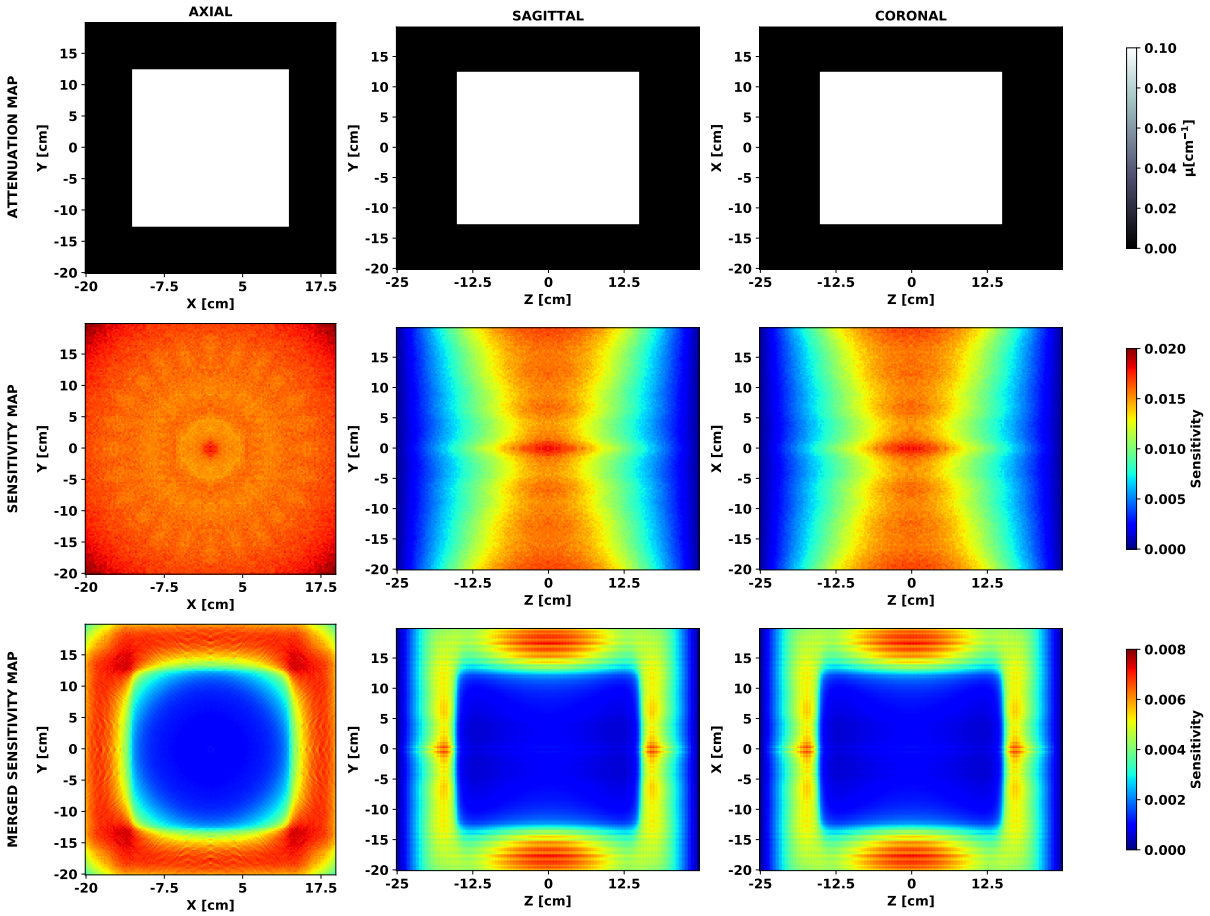

Figure 58: Attenuation correction (top), sensitivity (middle) and merged sensitivity and attenuation - merged sensitivity map (bottom) maps of the water phantom for triple layer barrel configuration in axial (left), sagittal (centre) and coronal (right) view.

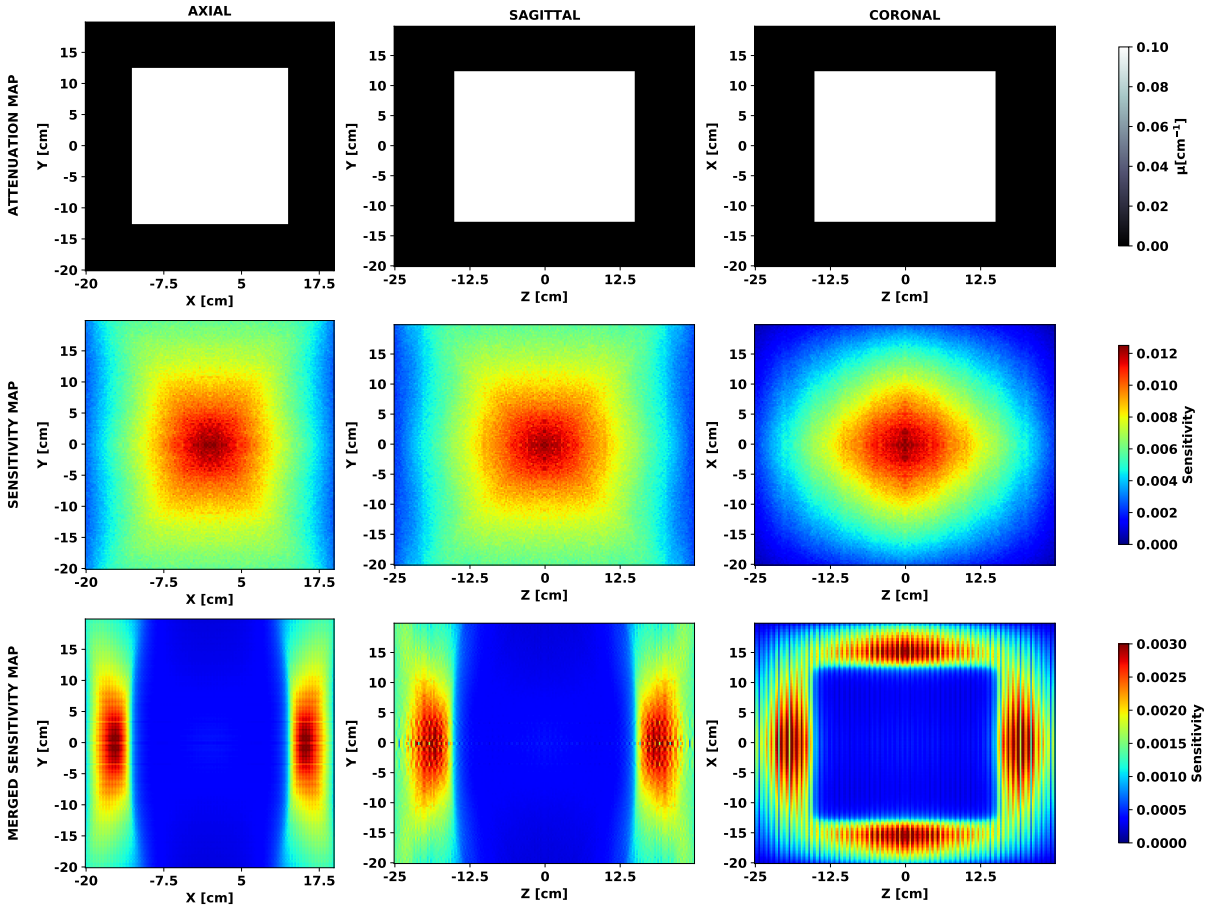

Figure 59: Attenuation correction (top), sensitivity (middle) and merged sensitivity and attenuation - merged sensitivity map (bottom) maps of the water phantom for double layer dual-head configuration in axial (left), sagittal (centre) and coronal (right) view.

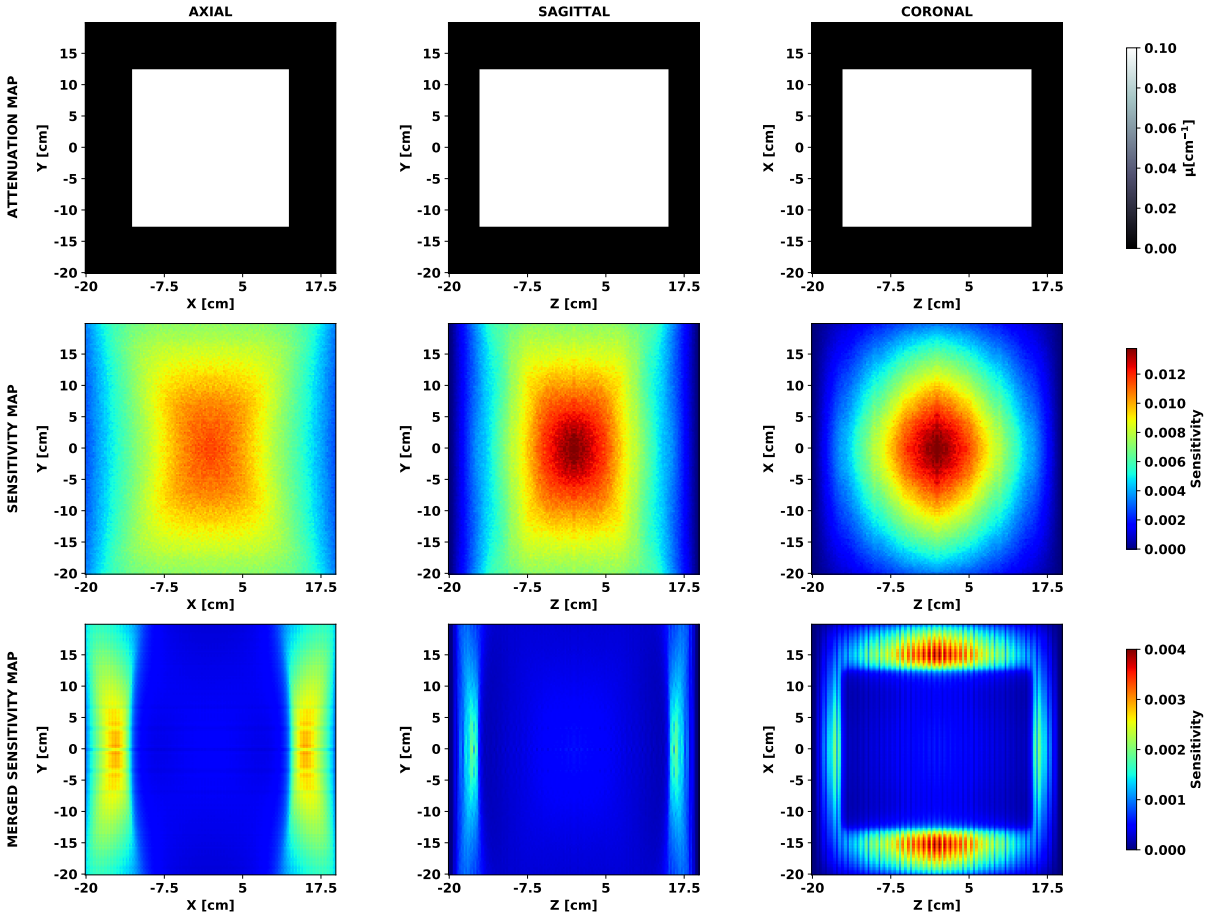

Figure 60: Attenuation correction (top), sensitivity (middle) and merged sensitivity and attenuation - merged sensitivity map (bottom) maps of the water phantom for triple layer dual-head configuration in axial (left), sagittal (centre) and coronal (right) view.

B

APPENDIX B

Attenuation correction, sensitivity and merged sensitivity and attenuation maps for the 5 x 5 x 20 cm^3 PMMA phantom and different configurations of the J-PET detectors.

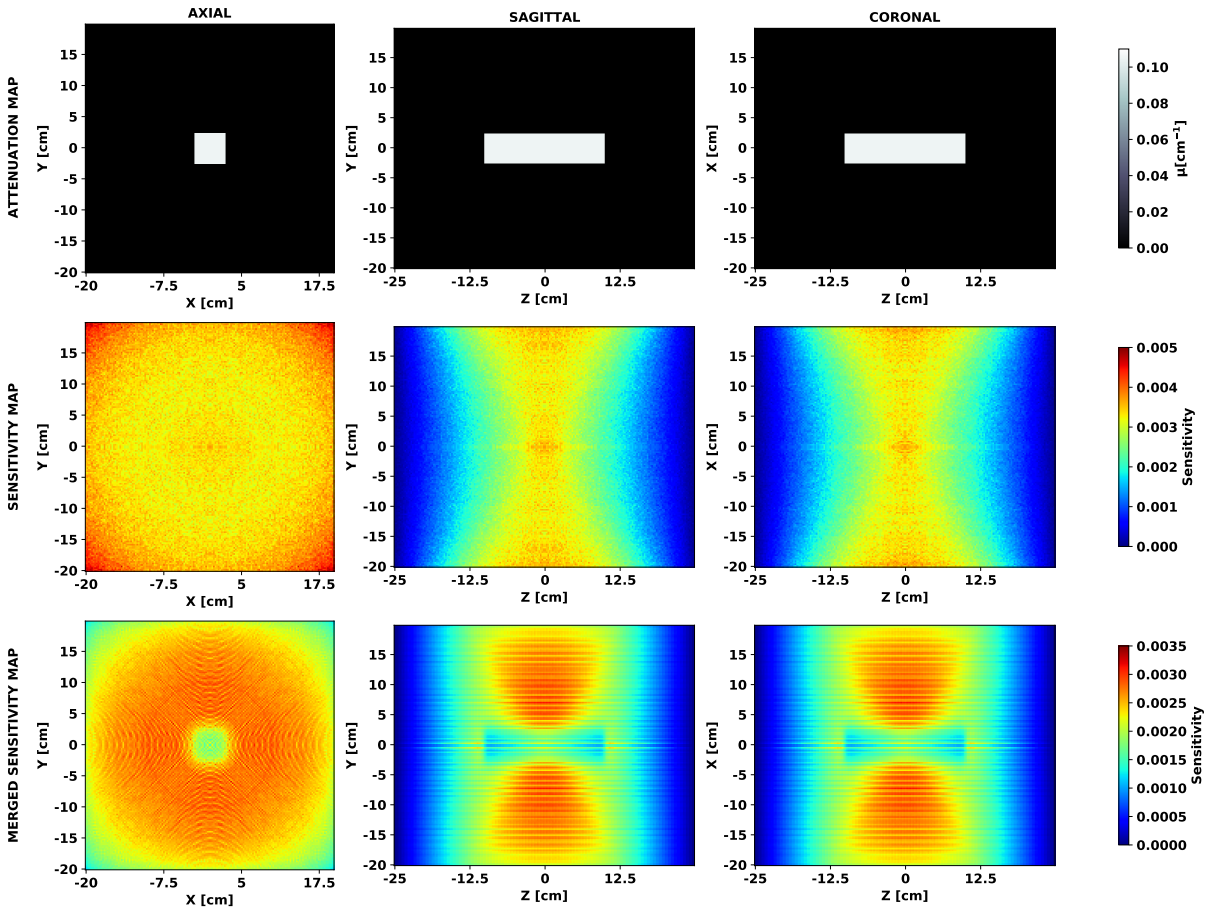

Figure 61: Attenuation correction (top), sensitivity (middle) and merged sensitivity and attenuation - merged sensitivity map (bottom) maps of the PMMA phantom for single layer barrel configuration in axial (left), sagittal (centre) and coronal (right) view.

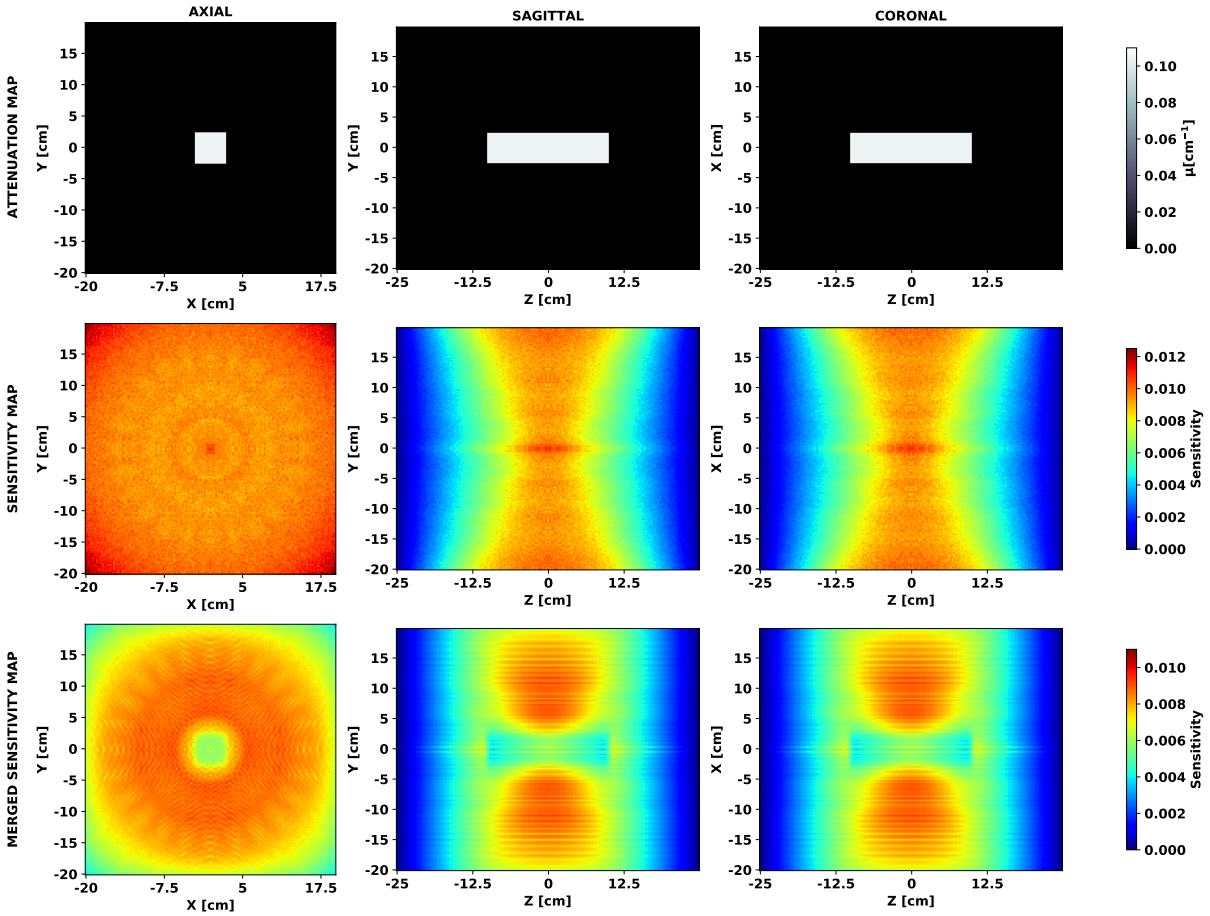

Figure 62: Attenuation correction (top), sensitivity (middle) and merged sensitivity and attenuation - merged sensitivity map (bottom) maps of the PMMA phantom for double layer barrel configuration in axial (left), sagittal (centre) and coronal (right) view.

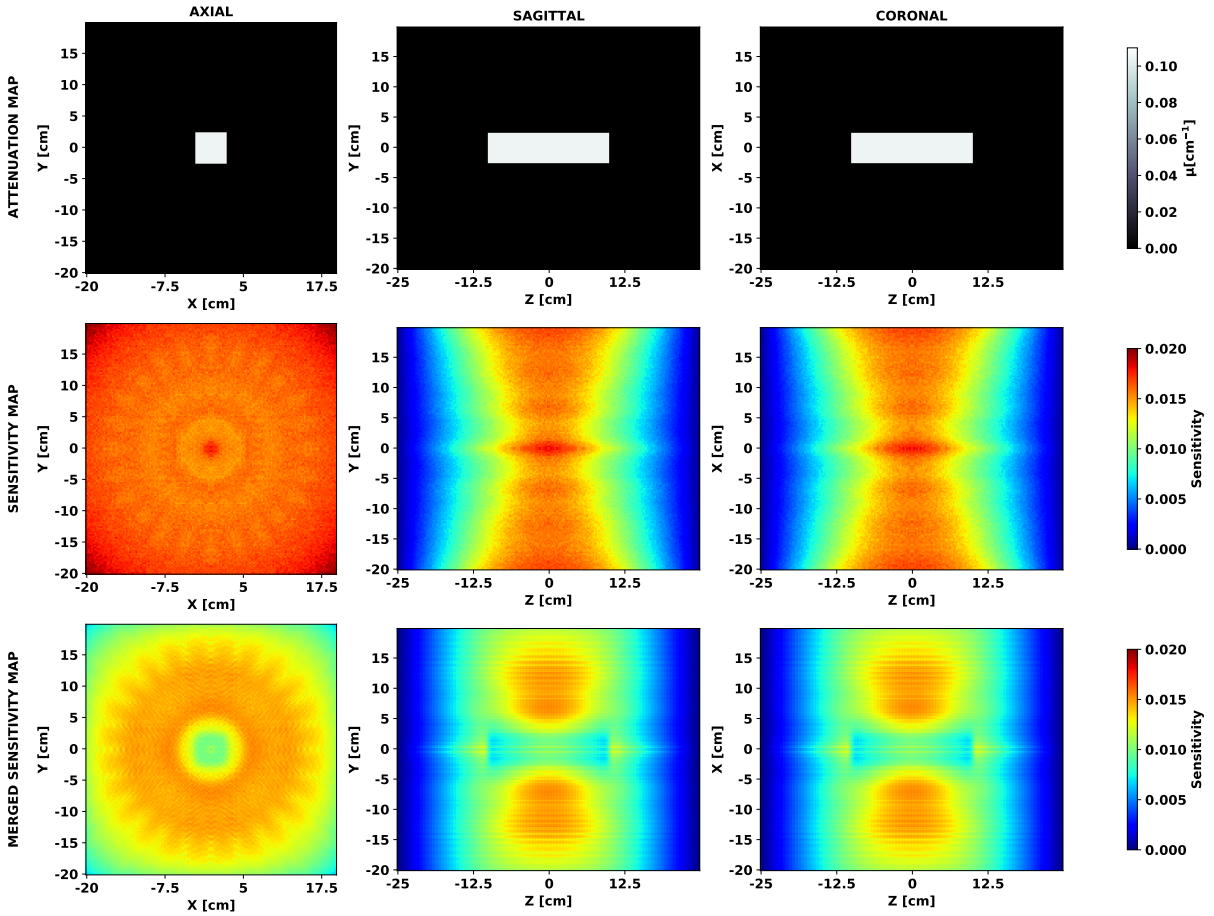

Figure 63: Attenuation correction (top), sensitivity (middle) and merged sensitivity and attenuation - merged sensitivity map (bottom) maps of the PMMA phantom for triple layer barrel configuration in axial (left), sagittal (centre) and coronal (right) view.

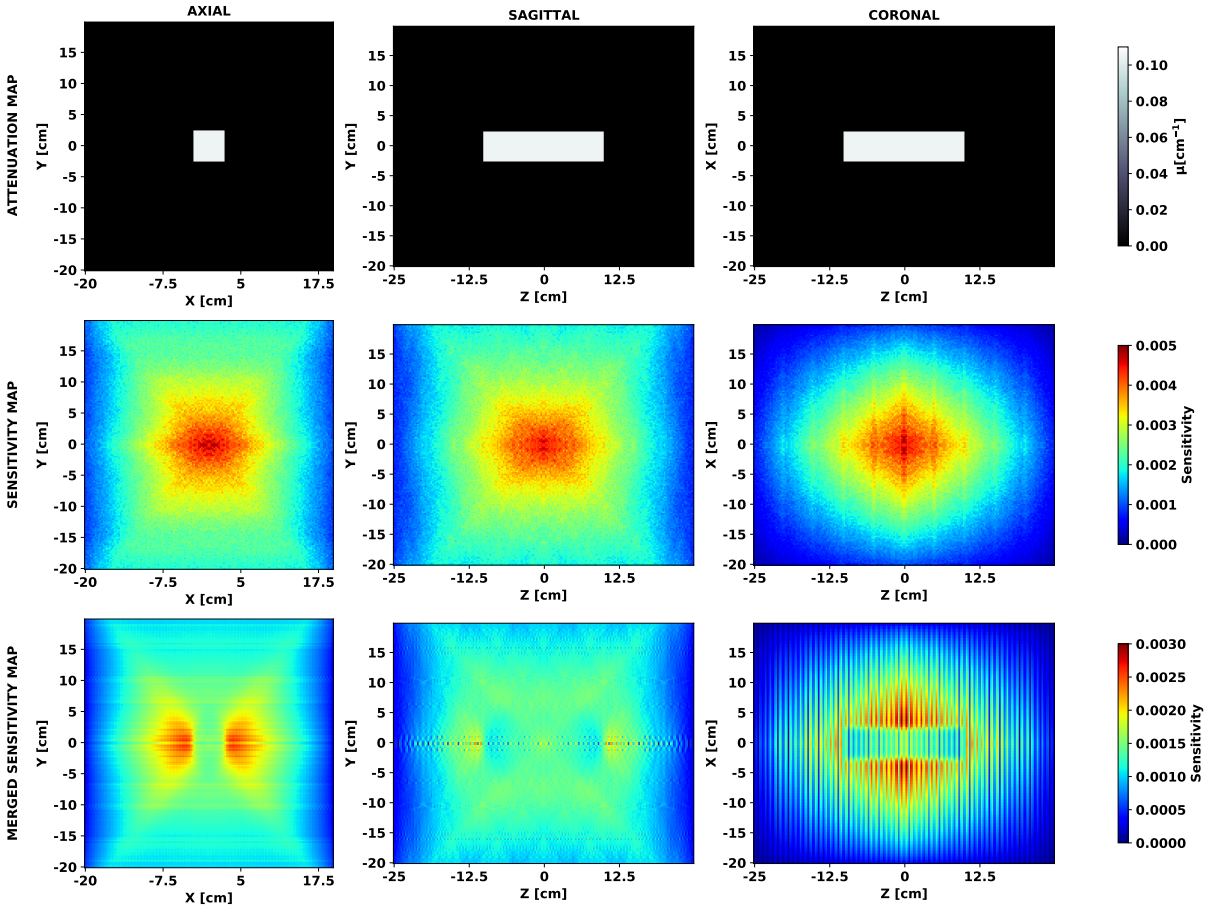

Figure 64: Attenuation correction (top), sensitivity (middle) and merged sensitivity and attenuation - merged sensitivity map (bottom) maps of the PMMA phantom for single layer dual-head configuration in axial (left), sagittal (centre) and coronal (right) view.

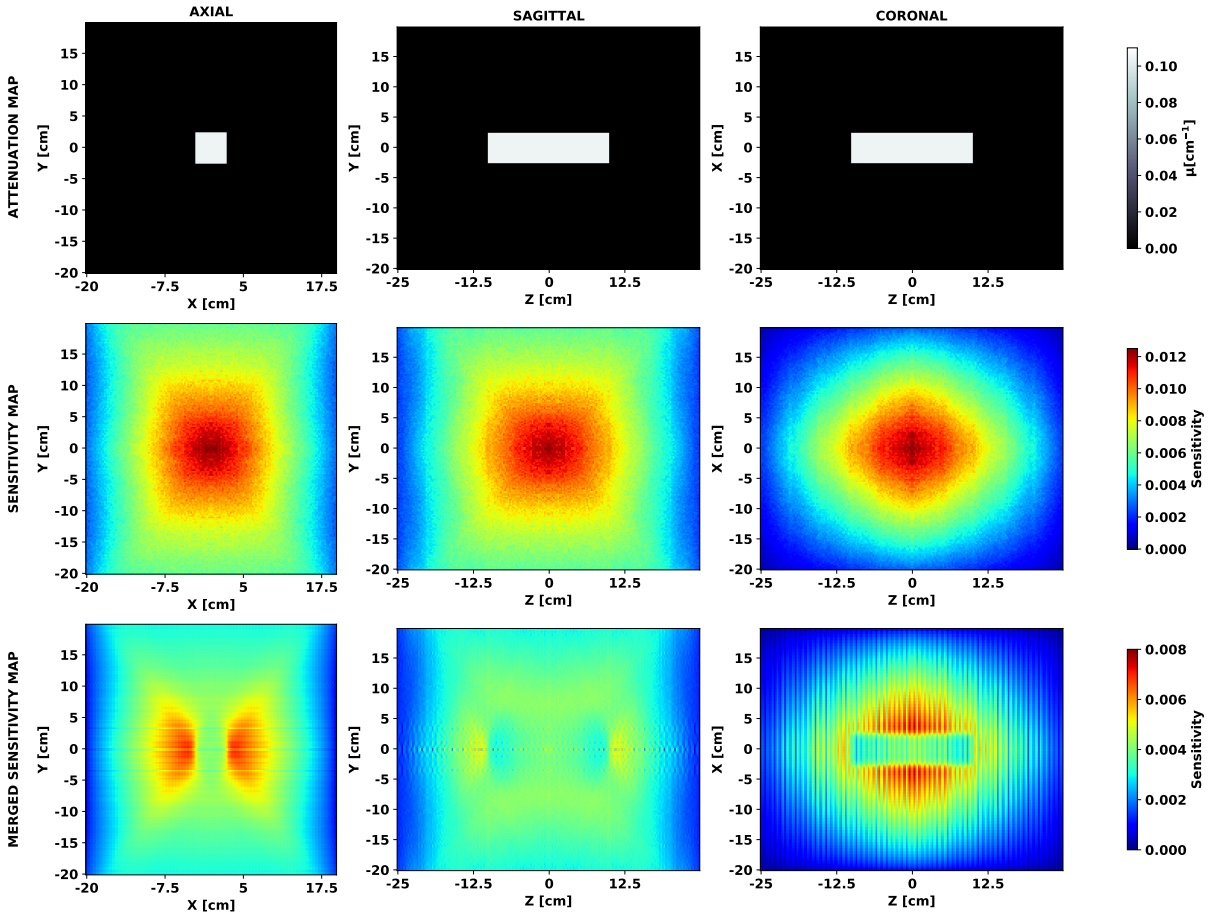

Figure 65: Attenuation correction (top), sensitivity (middle) and merged sensitivity and attenuation - merged sensitivity map (bottom) maps of the PMMA phantom for double layer dual-head configuration in axial (left), sagittal (centre) and coronal (right) view.

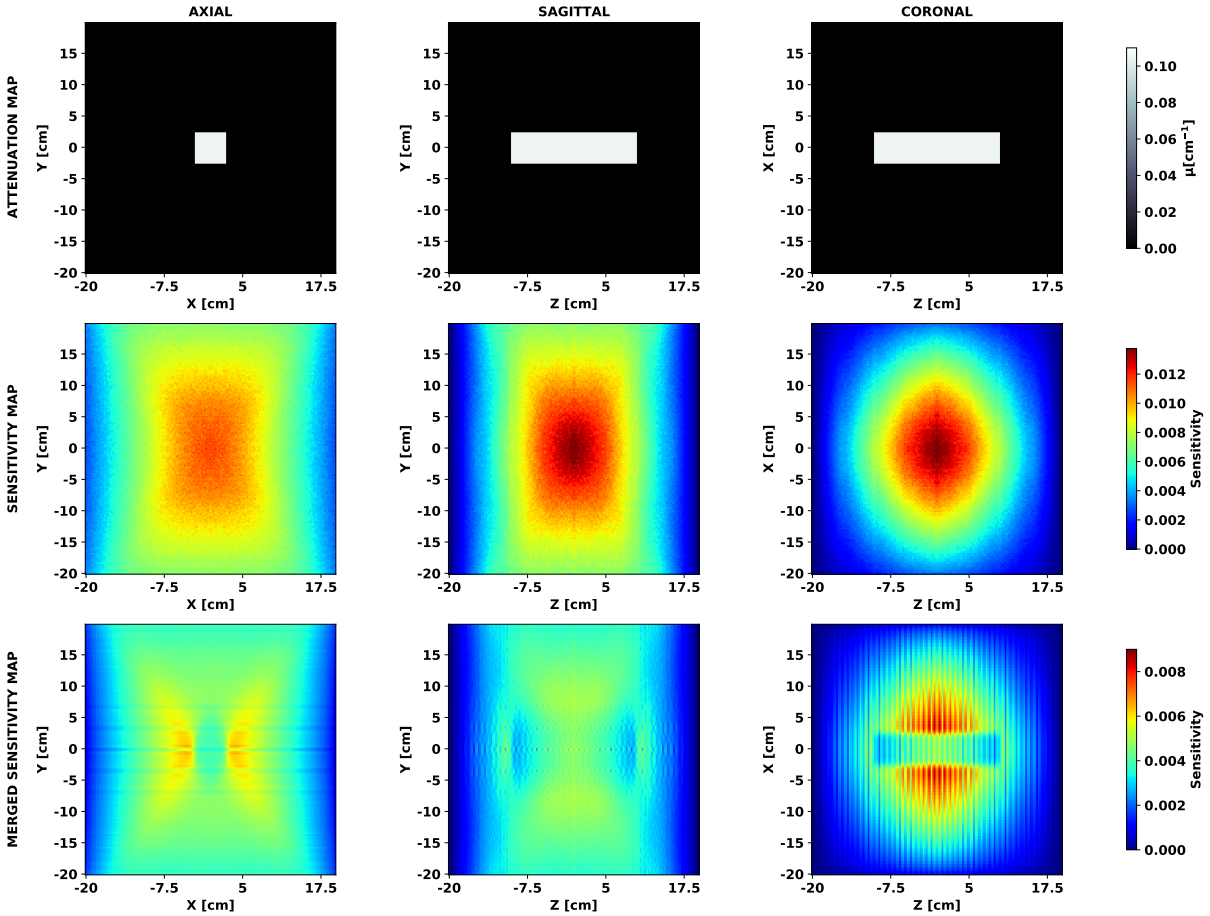

Figure 66: Attenuation correction (top), sensitivity (middle) and merged sensitivity and attenuation - merged sensitivity map (bottom) maps of the PMMA phantom for triple layer dual-head configuration in axial (left), sagittal (centre) and coronal (right) view.

C

APPENDIX C

Normalized emission and reconstructed activity profiles after irradiation with a proton pencil beam.

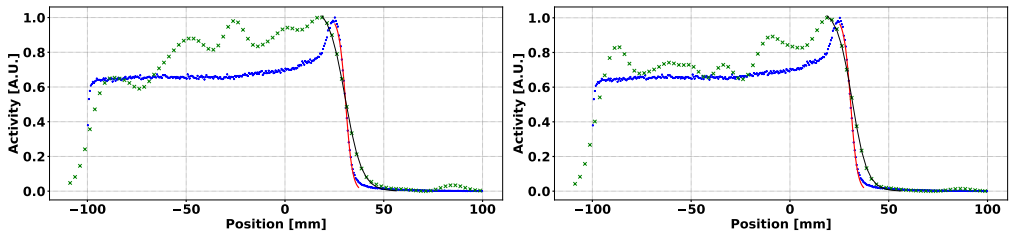

(a) Single layer dual-head

(b) Double layer barrel

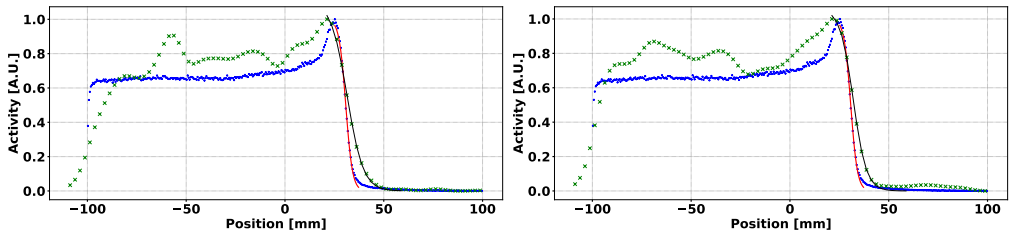

(c) Double layer dual-head

(d) Triple layer barrel

Figure 67: Normalized emission (blue dots) and reconstructed (green x markers) activity profiles with sigmoid function fitted (red and black lines) for various geometrical configurations. Results originate from simulations with 10^8 primary protons. Energy of the proton beam was 150 MeV.

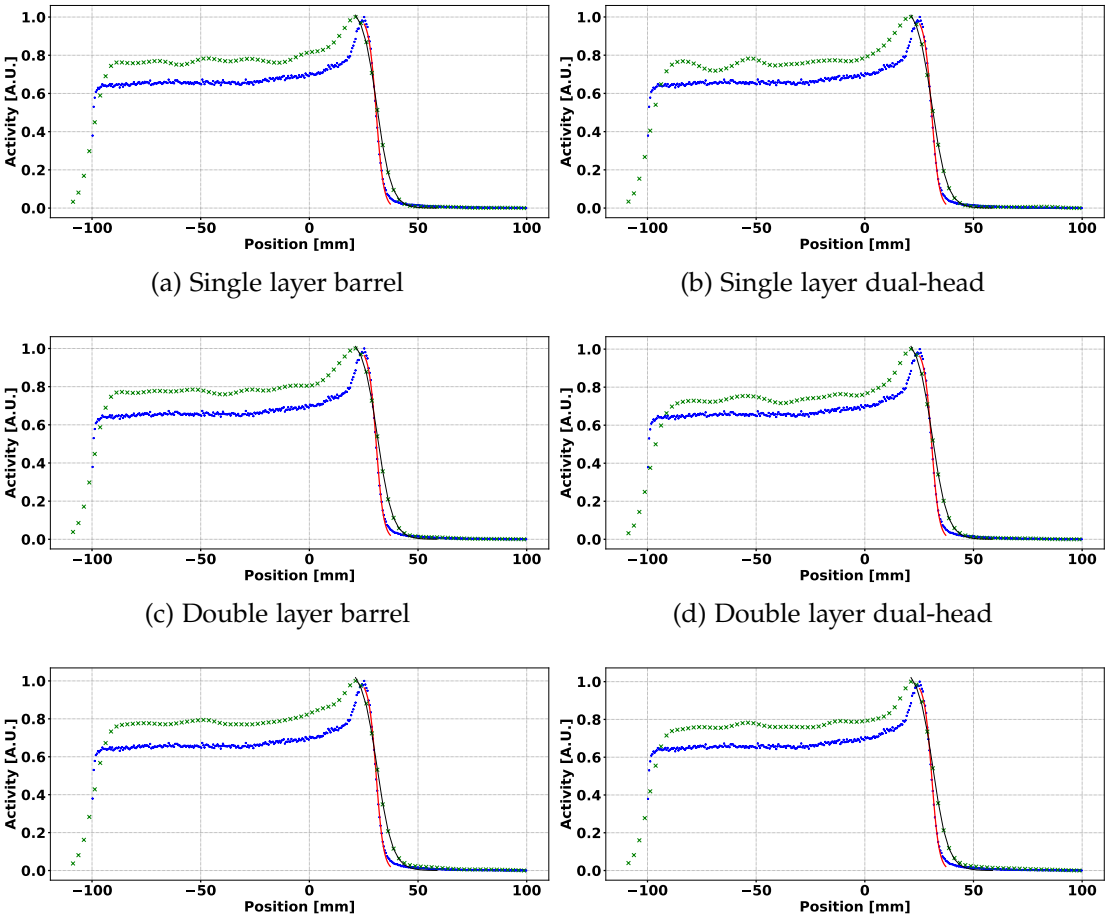

(a) Single layer barrel

(b) Single layer dual-head

(c) Double layer barrel

(d) Double layer dual-head

(e) Triple layer barrel

(f) Triple layer dual-head

Figure 68: Normalized emission (blue dots) and reconstructed (green x markers) activity profiles with sigmoid function fitted (red and black lines) for various geometrical configurations. Data is originated from the simulations with $5{\cdot}10^9$ primary positrons. Energy of the proton beam was 150 MeV.

D

APPENDIX D

Normalized true and reconstructed activity profiles after irradiation with pencil proton beams.

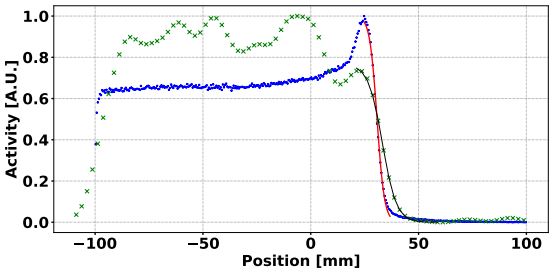

(a) Proton beam energy: 149.94 MeV

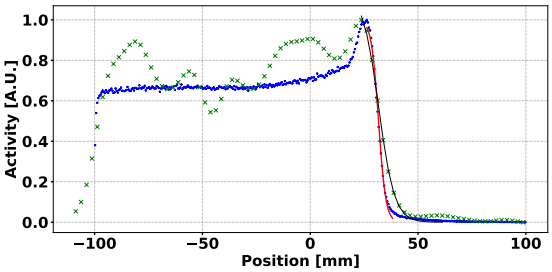

(b) Proton beam energy: 150.47 MeV

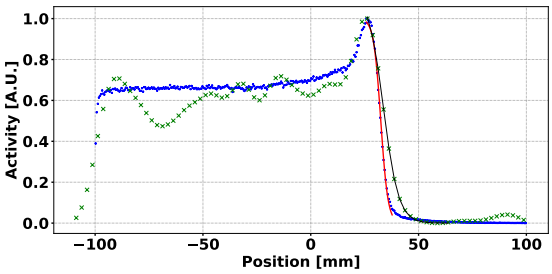

(c) Proton beam energy: 151.00 MeV

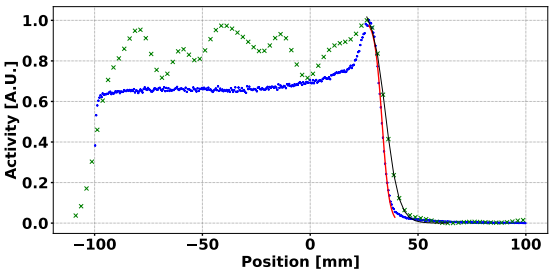

(d) Proton beam energy: 151.53 MeV

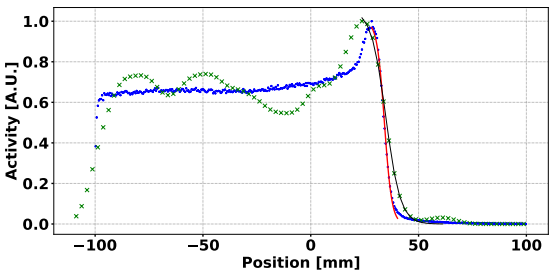

(e) Proton beam energy: 152.06 MeV

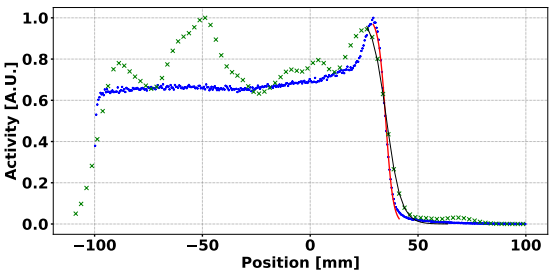

(f) Proton beam energy: 152.59 MeV

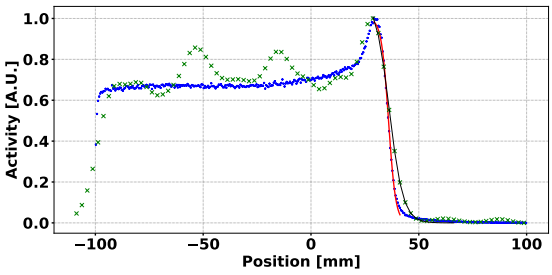

(g) Proton beam energy: 153.12 MeV

Figure 69: Normalized emission (blue dots) and reconstructed (green x markers) activity profiles fitted by sigmoid function (red and black lines) for various primary protons energies simulated. The profiles are plotted for single layer barrel configuration.

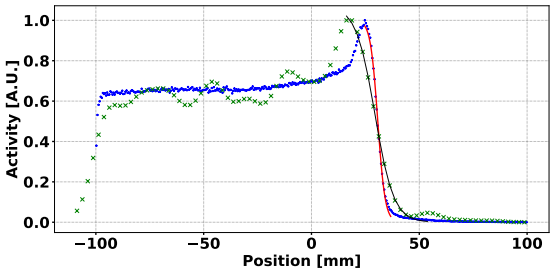

(a) Proton beam energy: 149.94 MeV

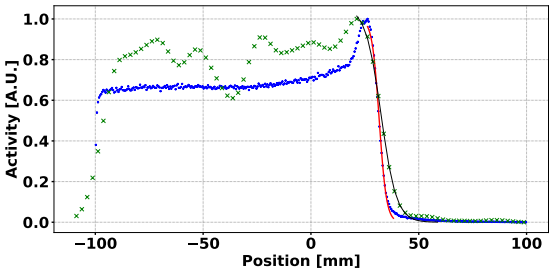

(b) Proton beam energy: 150.47 MeV

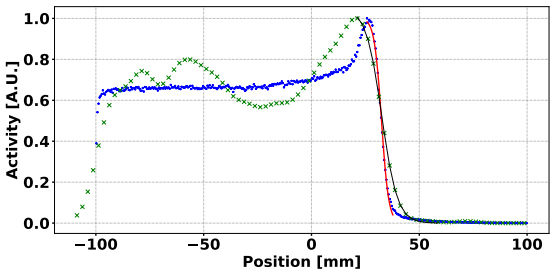

(c) Proton beam energy: 151.00 MeV

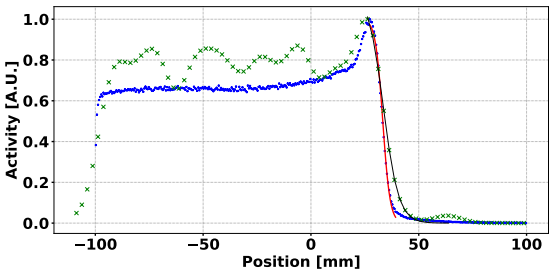

(d) Proton beam energy: 151.53 MeV

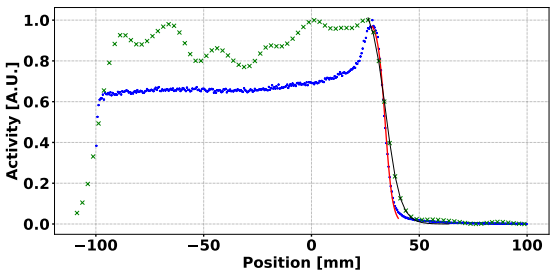

(e) Proton beam energy: 152.06 MeV

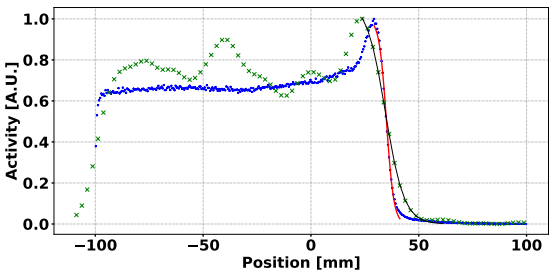

(f) Proton beam energy: 152.59 MeV

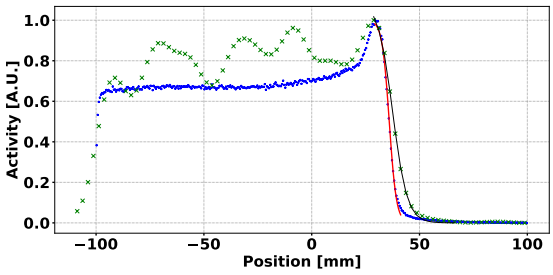

(g) Proton beam energy: 153.12 MeV

Figure 70: Normalized emission (blue dots) and reconstructed (green x markers) activity profiles fitted by sigmoid function (red and black lines) for various primary protons energies simulated. The profiles are plotted for double layer barrel configuration.

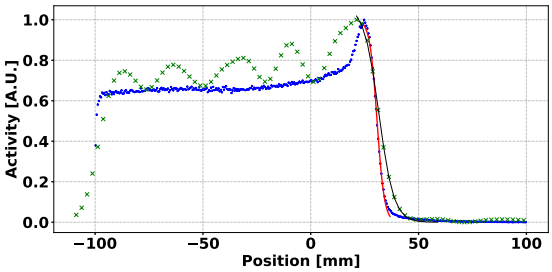

(a) Proton beam energy: 149.94 MeV

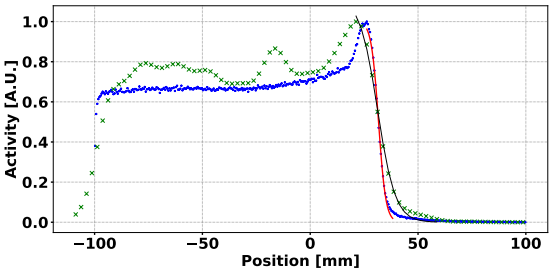

(b) Proton beam energy: 150.47 MeV

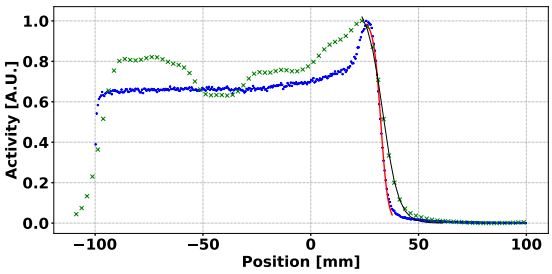

(c) Proton beam energy: 151.00 MeV

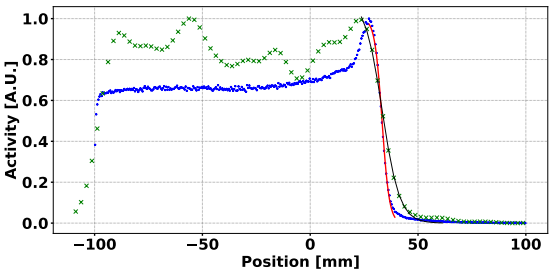

(d) Proton beam energy: 151.53 MeV

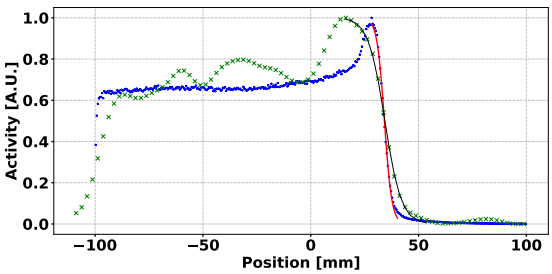

(e) Proton beam energy: 152.06 MeV

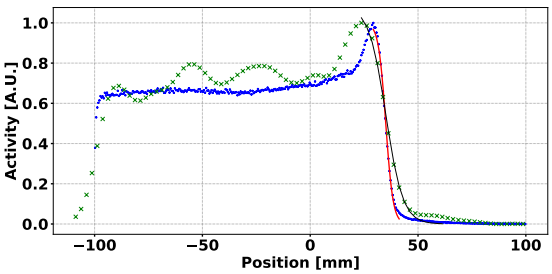

(f) Proton beam energy: 152.59 MeV

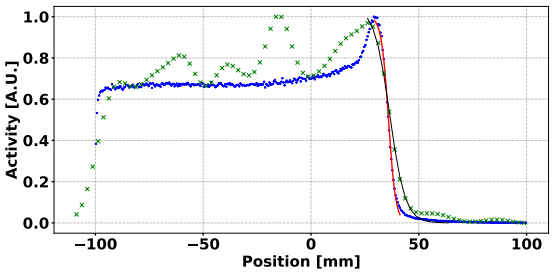

(g) Proton beam energy: 153.12 MeV

Figure 71: Normalized emission (blue dots) and reconstructed (green x markers) activity profiles fitted by sigmoid function (red and black lines) for various primary protons energies simulated. The profiles are plotted for triple layer barrel configuration.

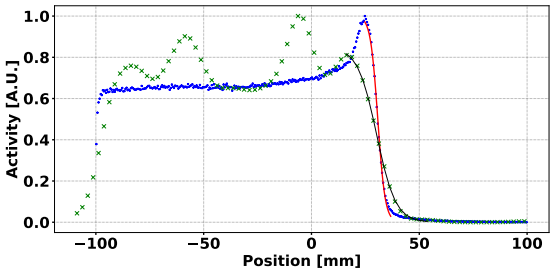

(a) Proton beam energy: 149.94 MeV

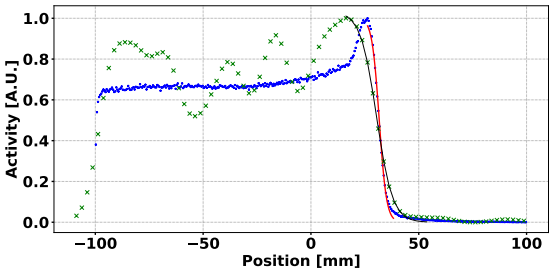

(b) Proton beam energy: 150.47 MeV

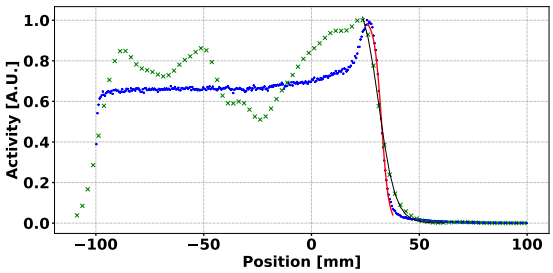

(c) Proton beam energy: 151.00 MeV

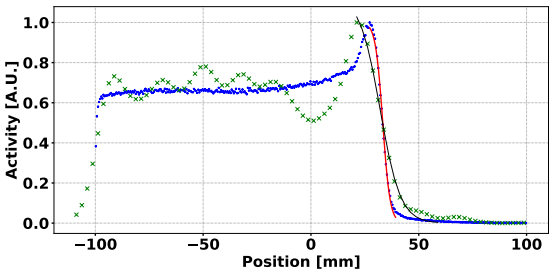

(d) Proton beam energy: 151.53 MeV

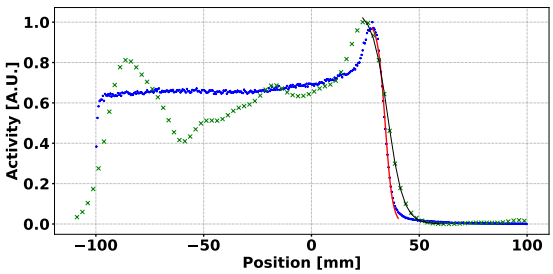

(e) Proton beam energy: 152.06 MeV

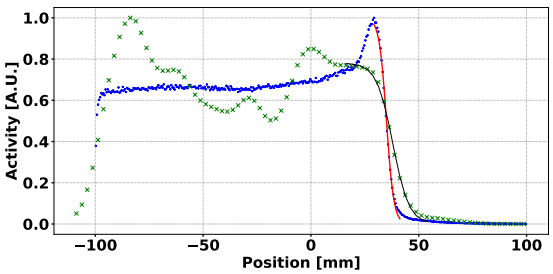

(f) Proton beam energy: 152.59 MeV

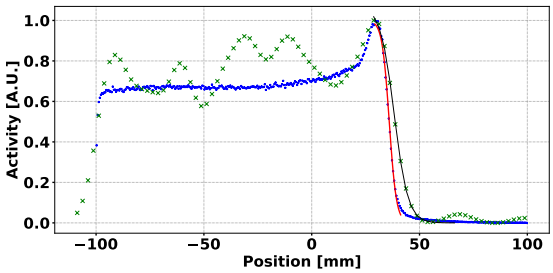

(g) Proton beam energy: 153.12 MeV

Figure 72: Normalized emission (blue dots) and reconstructed (green x markers) activity profiles fitted by sigmoid function (red and black lines) for various primary protons energies simulated. The profiles are plotted for single layer dual-head geometrical configuration.

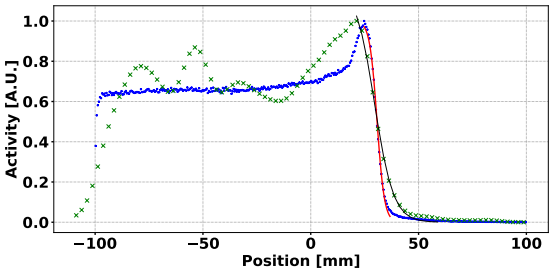

(a) Proton beam energy: 149.94 MeV

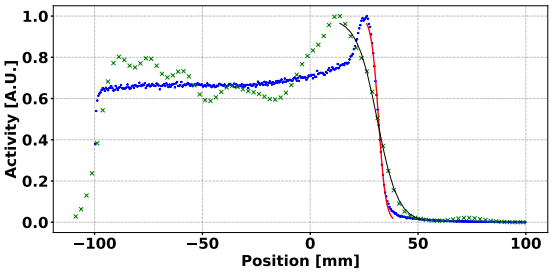

(b) Proton beam energy: 150.47 MeV

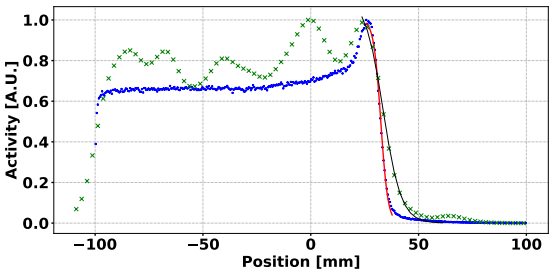

(c) Proton beam energy: 151.00 MeV

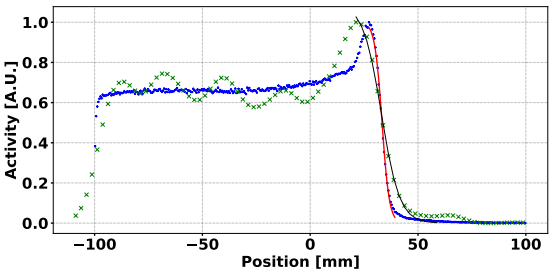

(d) Proton beam energy: 151.53 MeV

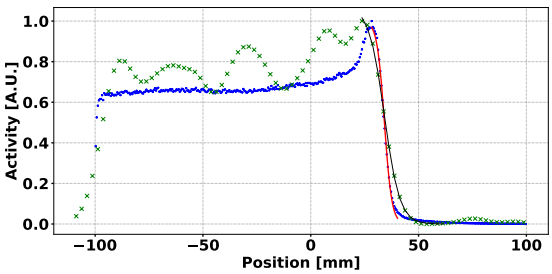

(e) Proton beam energy: 152.06 MeV

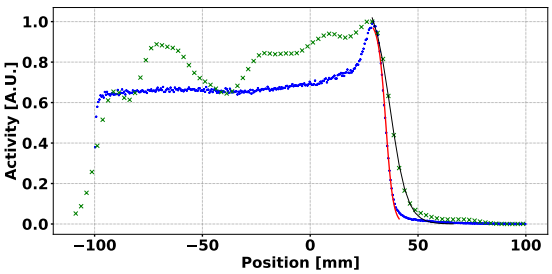

(f) Proton beam energy: 152.59 MeV

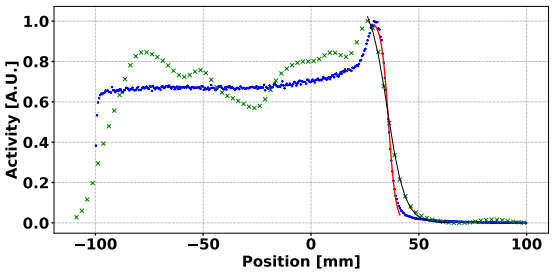

(g) Proton beam energy: 153.12 MeV

Figure 73: Normalized emission (blue dots) and reconstructed (green x markers) activity profiles fitted by sigmoid function (red and black lines) for various primary protons energies simulated. The profiles are plotted for double layer dual-head geometrical configuration.

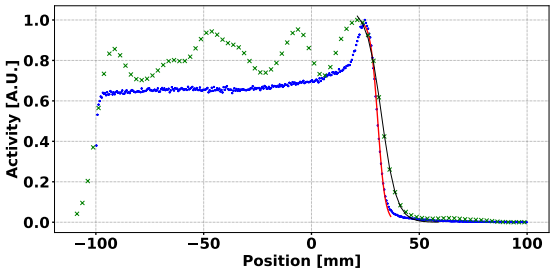

(a) Proton beam energy: 149.94 MeV

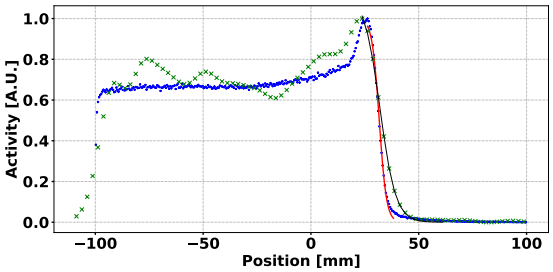

(b) Proton beam energy: 150.47 MeV

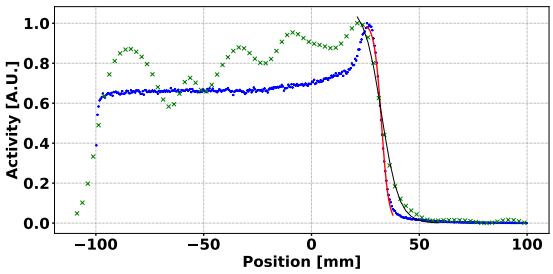

(c) Proton beam energy: 151.00 MeV

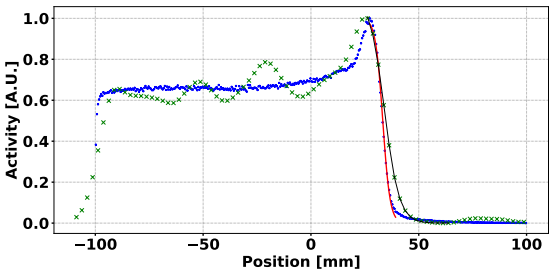

(d) Proton beam energy: 151.53 MeV

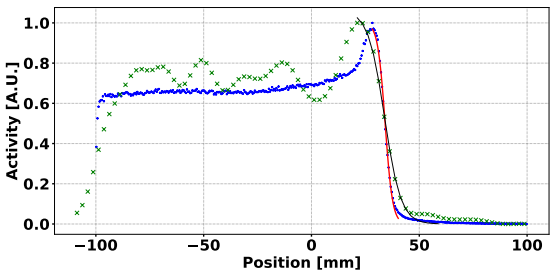

(e) Proton beam energy: 152.06 MeV

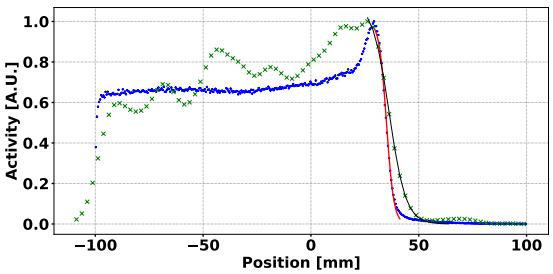

(f) Proton beam energy: 152.59 MeV

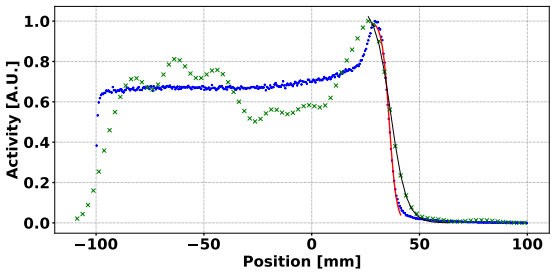

(g) Proton beam energy: 153.12 MeV

Figure 74: Normalized emission (blue dots) and reconstructed (green x markers) activity profiles fitted by sigmoid function (red and black lines) for various primary protons energies simulated. The profiles are plotted for triple layer dual-head geometrical configuration.

APPENDIX E

Attenuation correction, sensitivity and merged sensitivity and attenuation maps of the patient for different geometrical configurations of the J-PET modules.

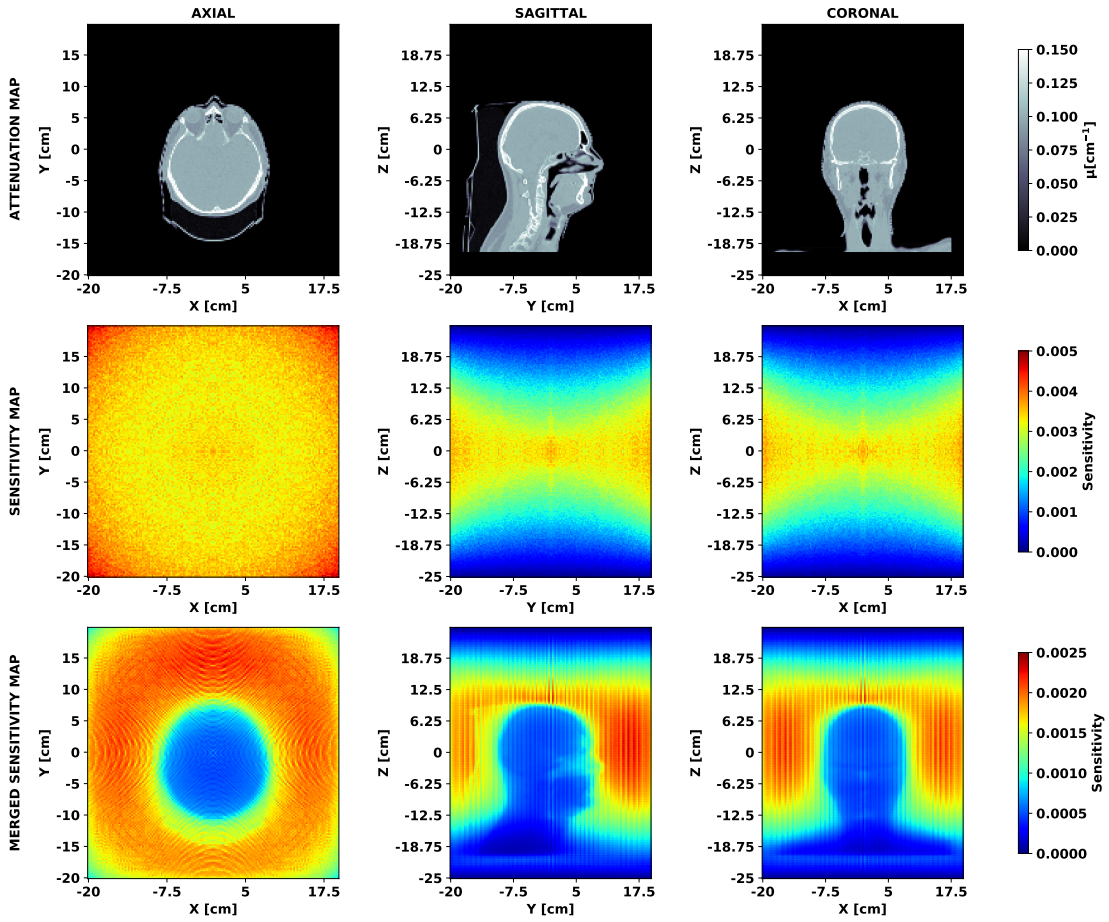

Figure 75: Attenuation correction (top), sensitivity (middle) and merged sensitivity and attenuation - merged sensitivity map (bottom) maps of the patient for single layer barrel configuration in axial (left), sagittal (centre) and coronal (right) view.

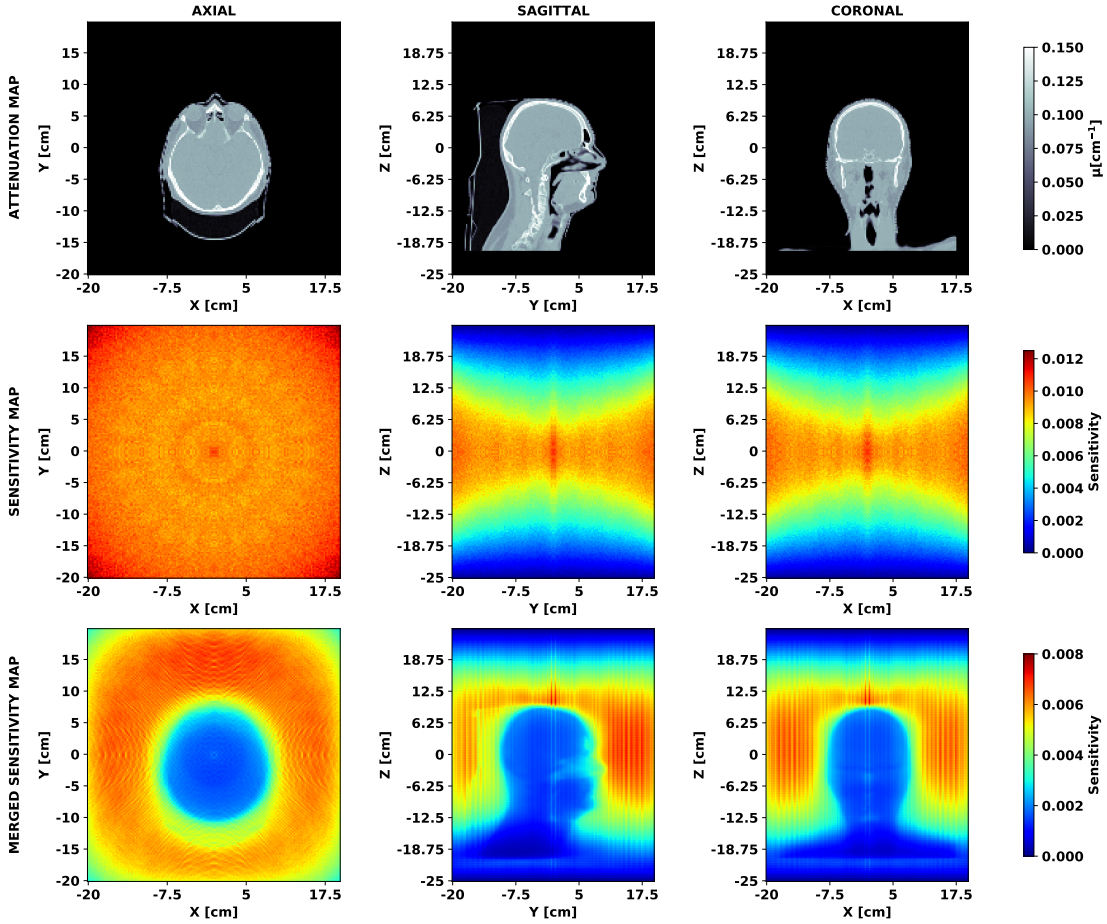

Figure 76: Attenuation correction (top), sensitivity (middle) and merged sensitivity and attenuation - merged sensitivity map (bottom) maps of the patient for double layer barrel configuration in axial (left), sagittal (centre) and coronal (right) view.

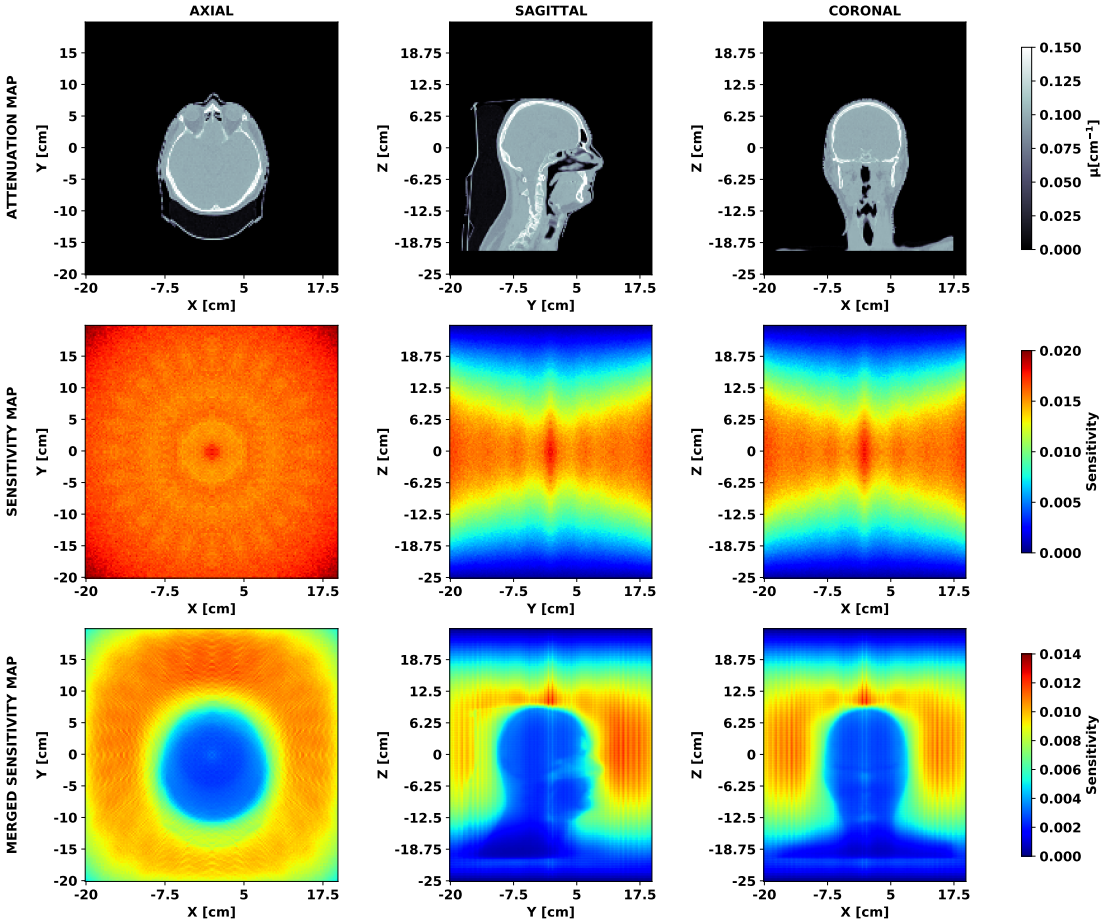

Figure 77: Attenuation correction (top), sensitivity (middle) and merged sensitivity and attenuation - merged sensitivity map (bottom) maps of the patient for triple layer barrel configuration in axial (left), sagittal (centre) and coronal (right) view.

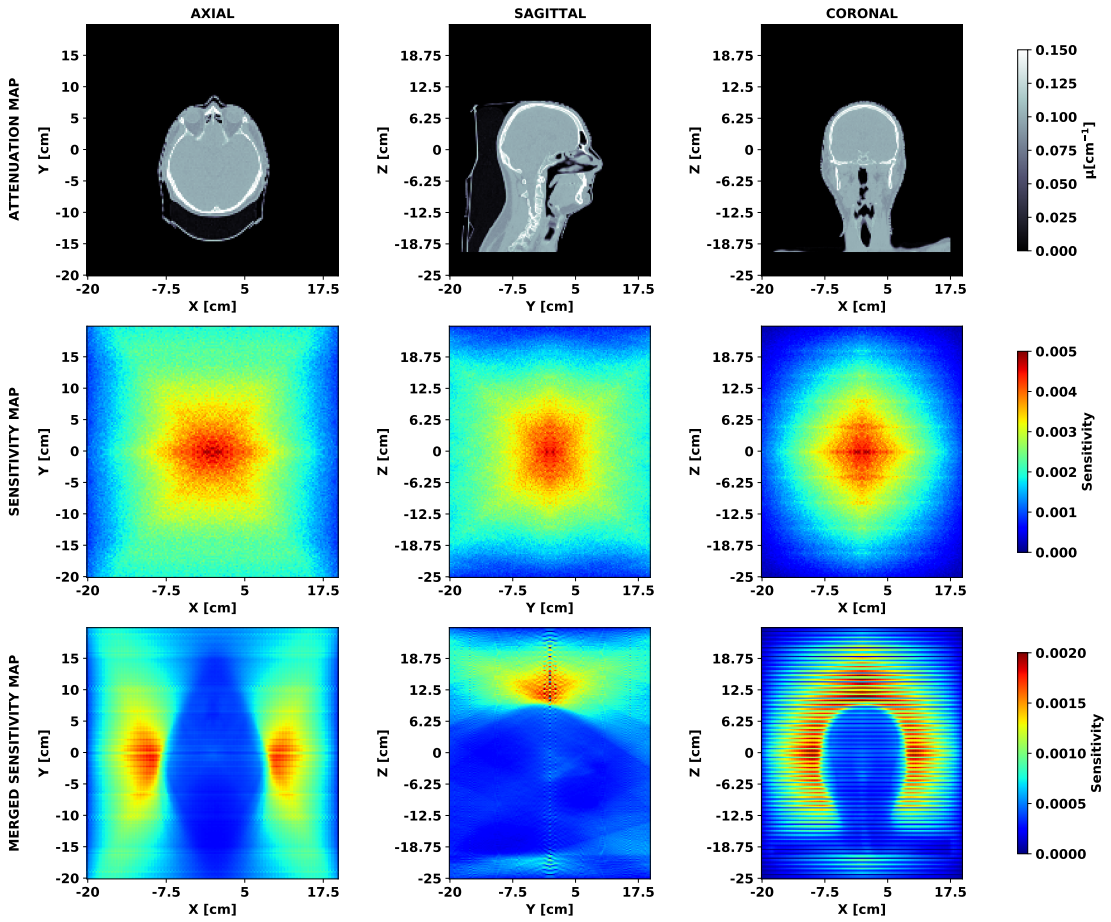

Figure 78: Attenuation correction (top), sensitivity (middle) and merged sensitivity and attenuation - merged sensitivity map (bottom) maps of the patient for single layer dual-head configuration in axial (left), sagittal (centre) and coronal (right) view.

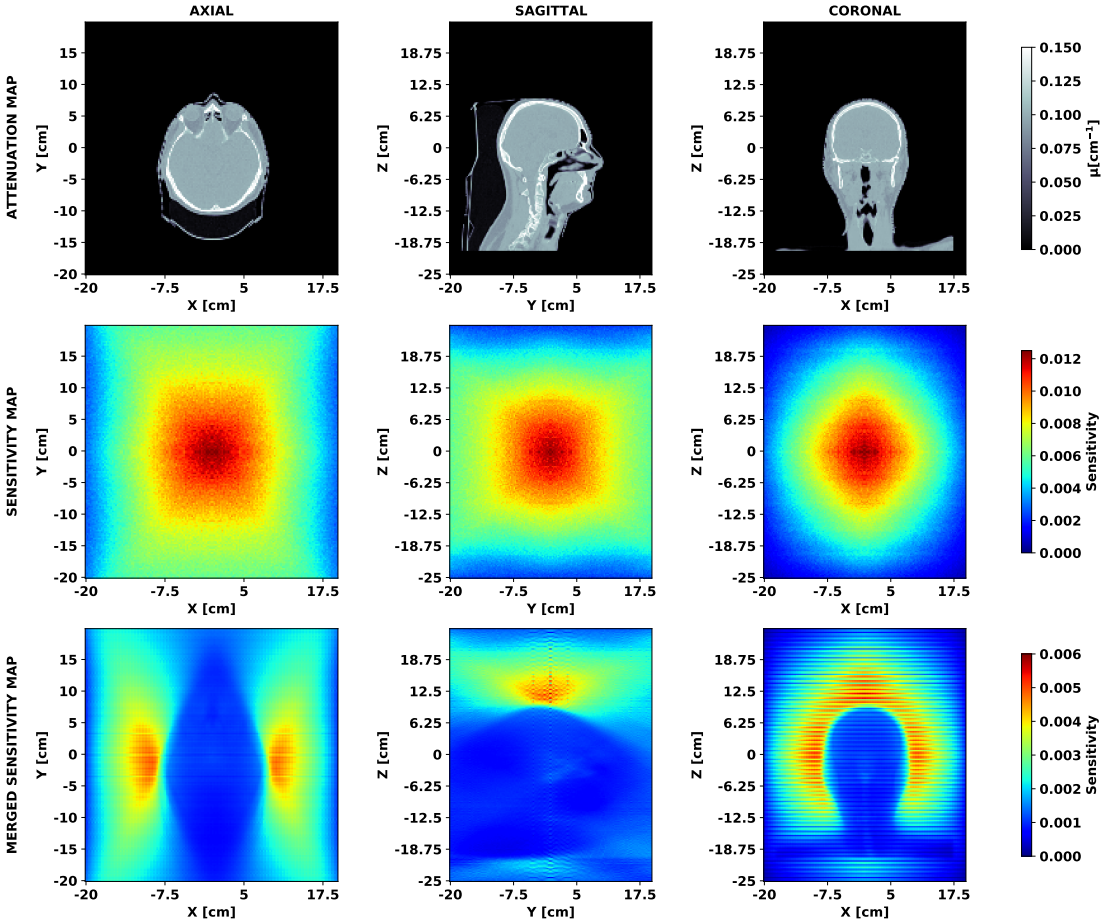

Figure 79: Attenuation correction (top), sensitivity (middle) and merged sensitivity and attenuation - merged sensitivity map (bottom) maps of the patient for double layer dual-head configuration in axial (left), sagittal (centre) and coronal (right) view.

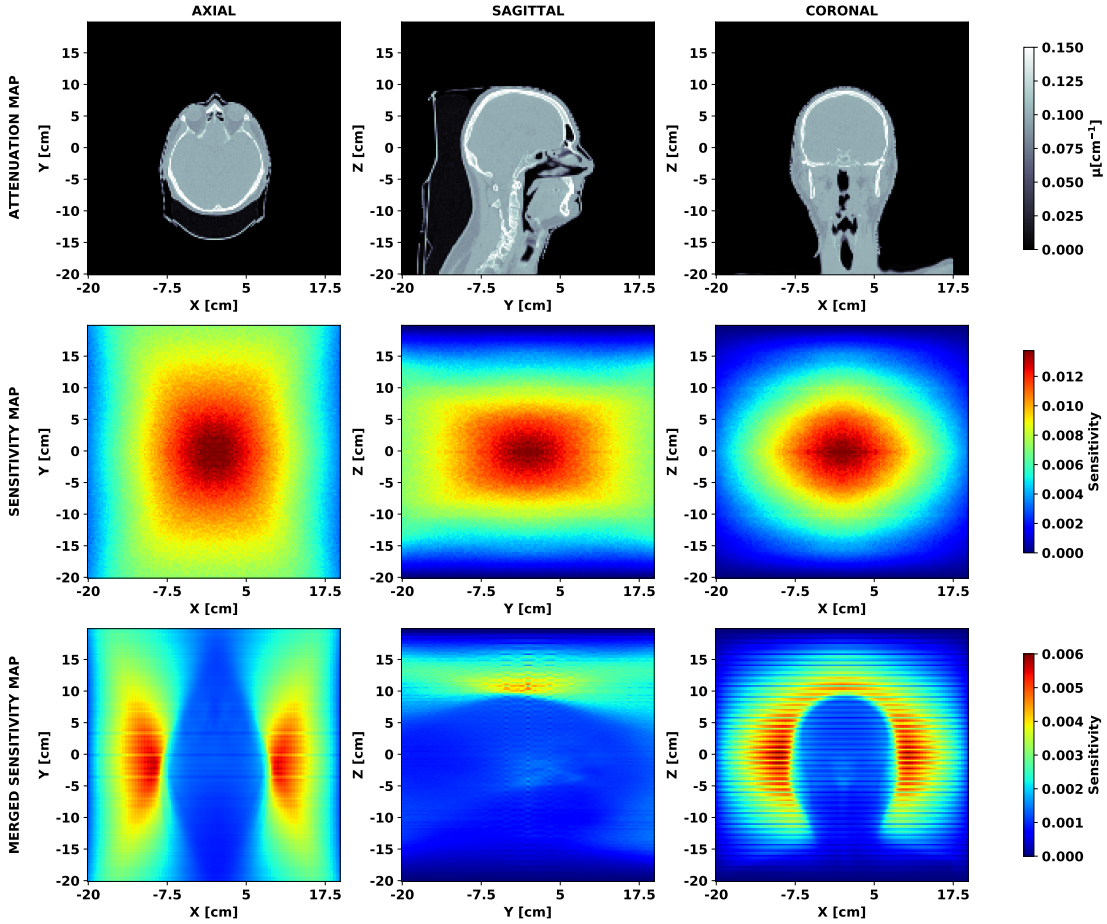

Figure 80: Attenuation correction (top), sensitivity (middle) and merged sensitivity and attenuation - merged sensitivity map (bottom) maps of the patient for triple layer dual-head configuration in axial (left), sagittal (centre) and coronal (right) view.

APPENDIX F

True production activity distribution and reconstructed PET images for different configurations of the J-PET modules.

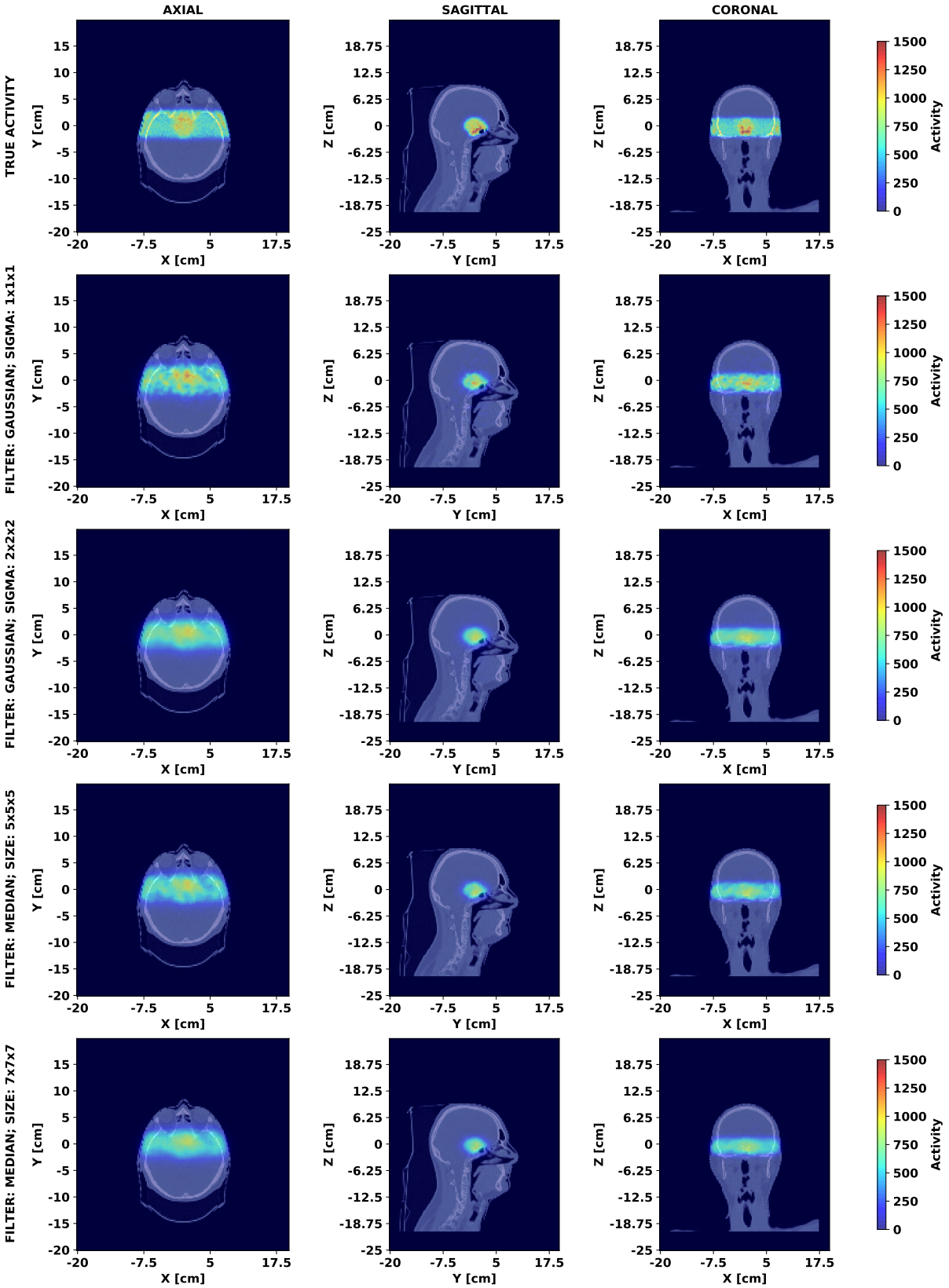

Figure 81: True production activity distribution and reconstructed PET images with the highest PCC for single layer barrel configuration in axial (left), sagittal (centre) and coronal (right) views superimposed on CT images. The calculation was performed for the simulated in-room PET acquisition scenario.

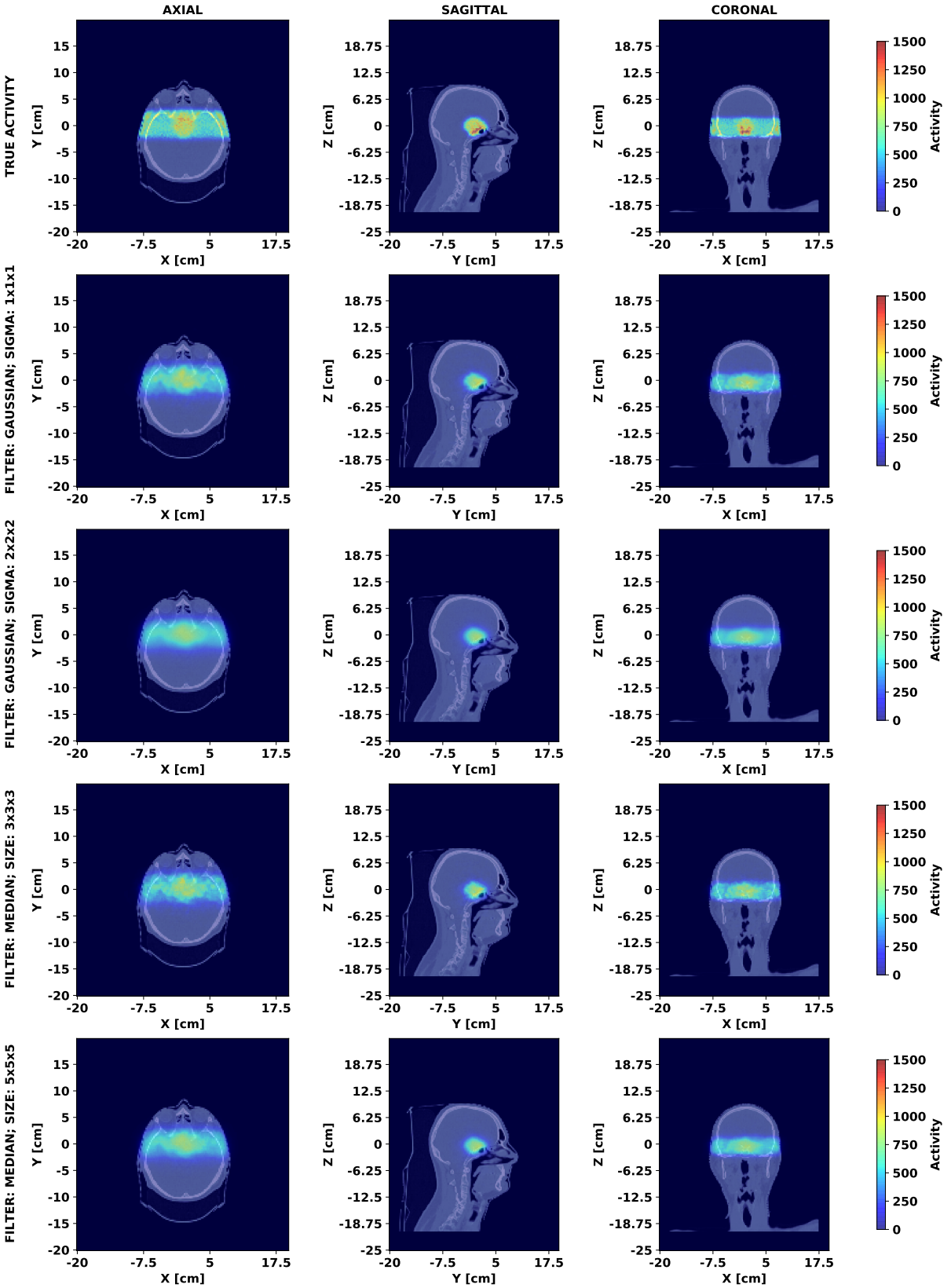

Figure 82: True production activity distribution and reconstructed PET images with the highest PCC for double layer barrel configuration in axial (left), sagittal (centre) and coronal (right) views superimposed on CT images. The calculation was performed for the simulated in-room PET acquisition scenario.

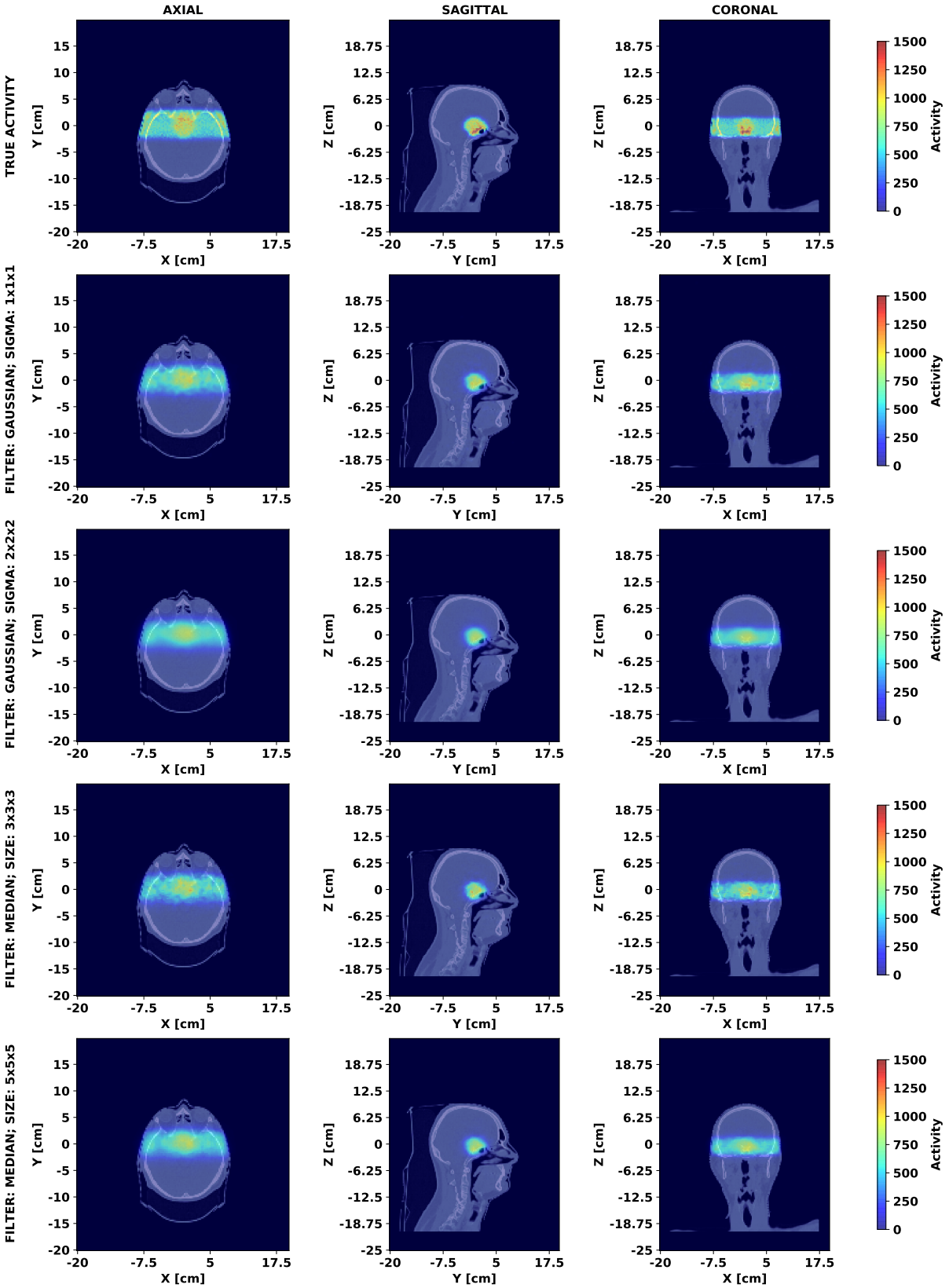

Figure 83: True production activity distribution and reconstructed PET images with the highest PCC for triple layer barrel configuration in axial (left), sagittal (centre) and coronal (right) views superimposed on CT images. The calculation was performed for the simulated in-room PET acquisition scenario.

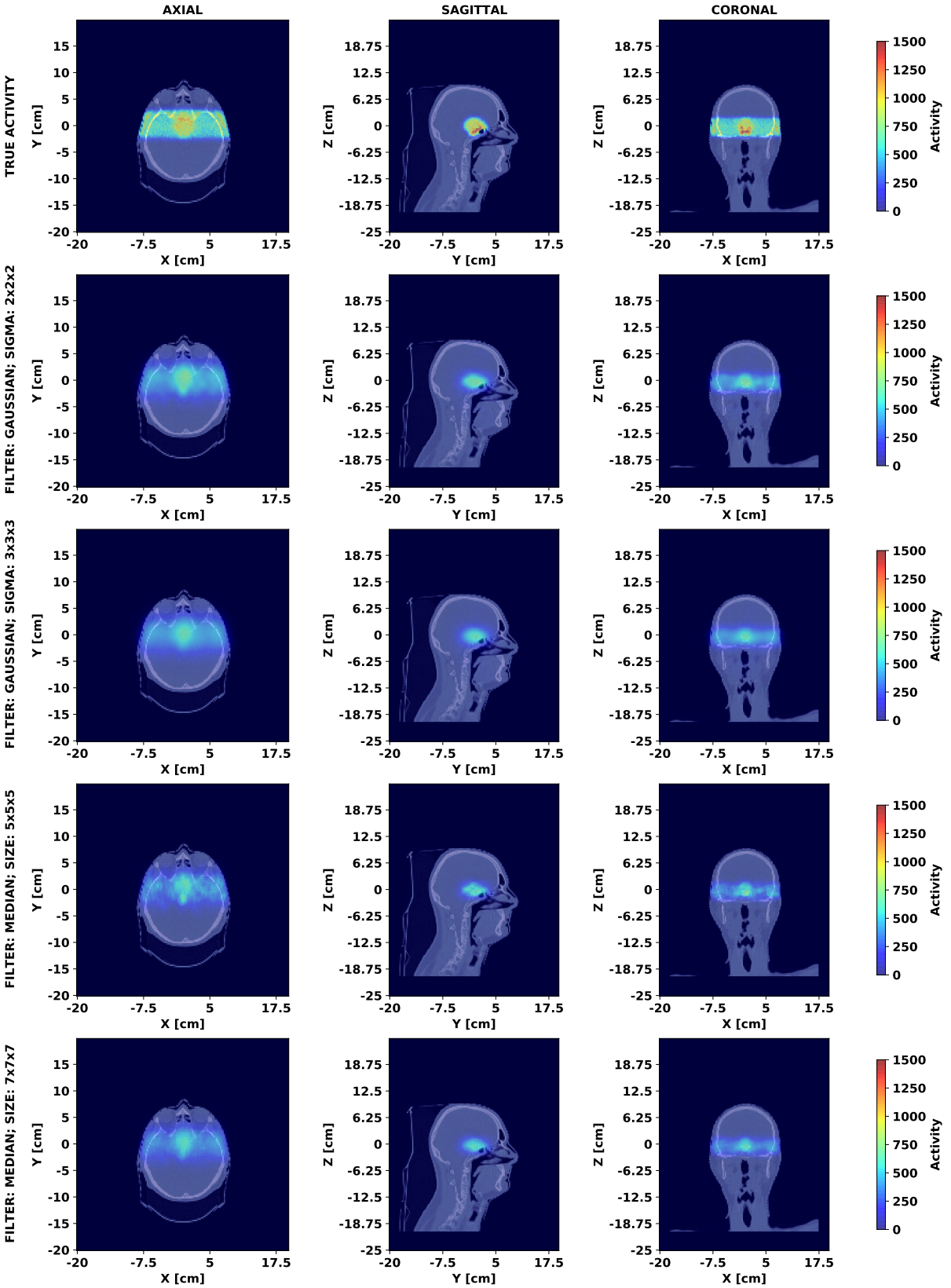

Figure 84: True production activity distribution and reconstructed PET images with the highest PCC for single layer dual-head configuration in axial (left), sagittal (centre) and coronal (right) views superimposed on CT images. The calculation was performed for the simulated in-room PET acquisition scenario.

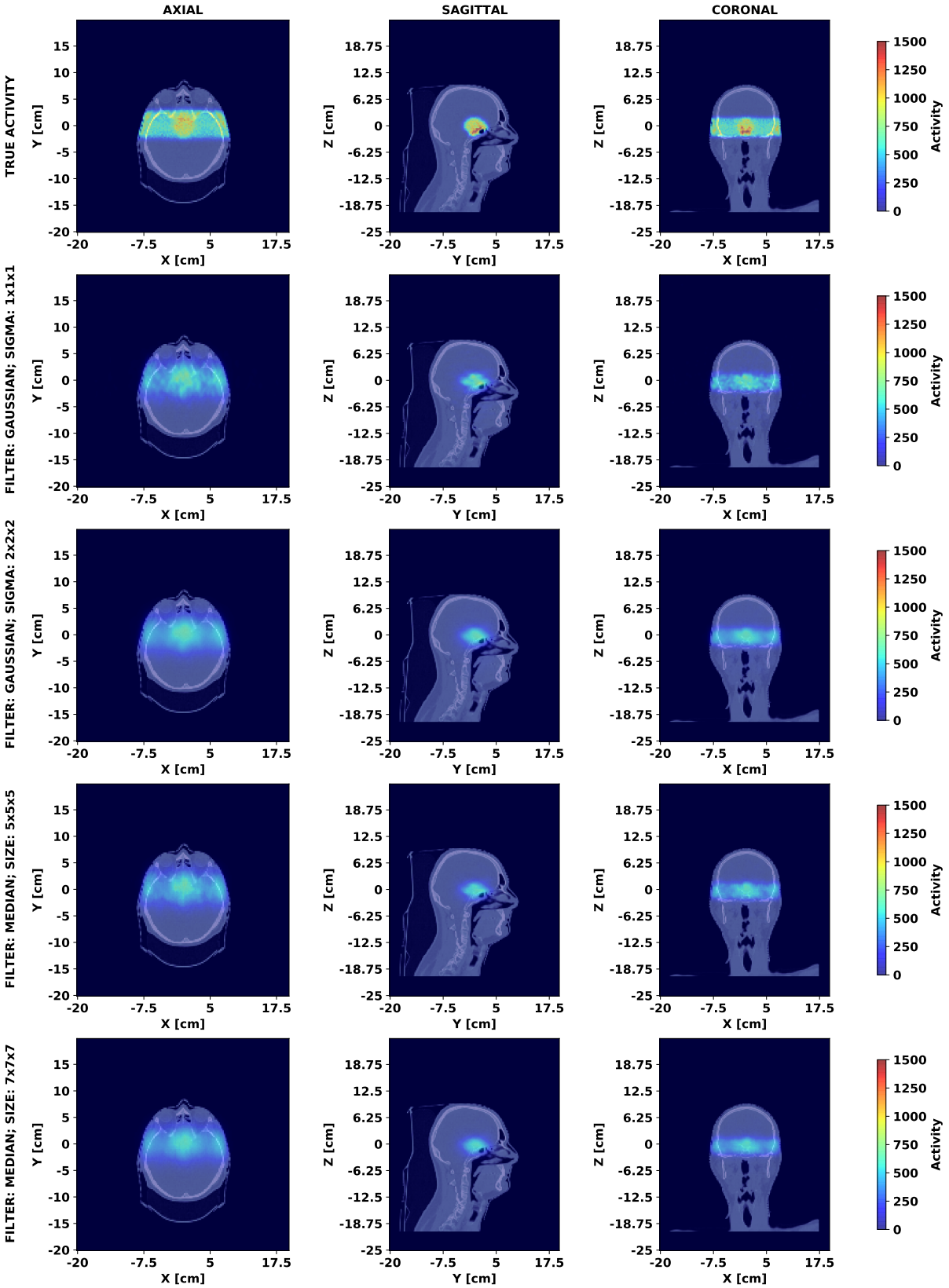

Figure 85: True production activity distribution and reconstructed PET images with the highest PCC for double layer dual-head configuration in axial (left), sagittal (centre) and coronal (right) views superimposed on CT images. The calculation was performed for the simulated in-room PET acquisition scenario.

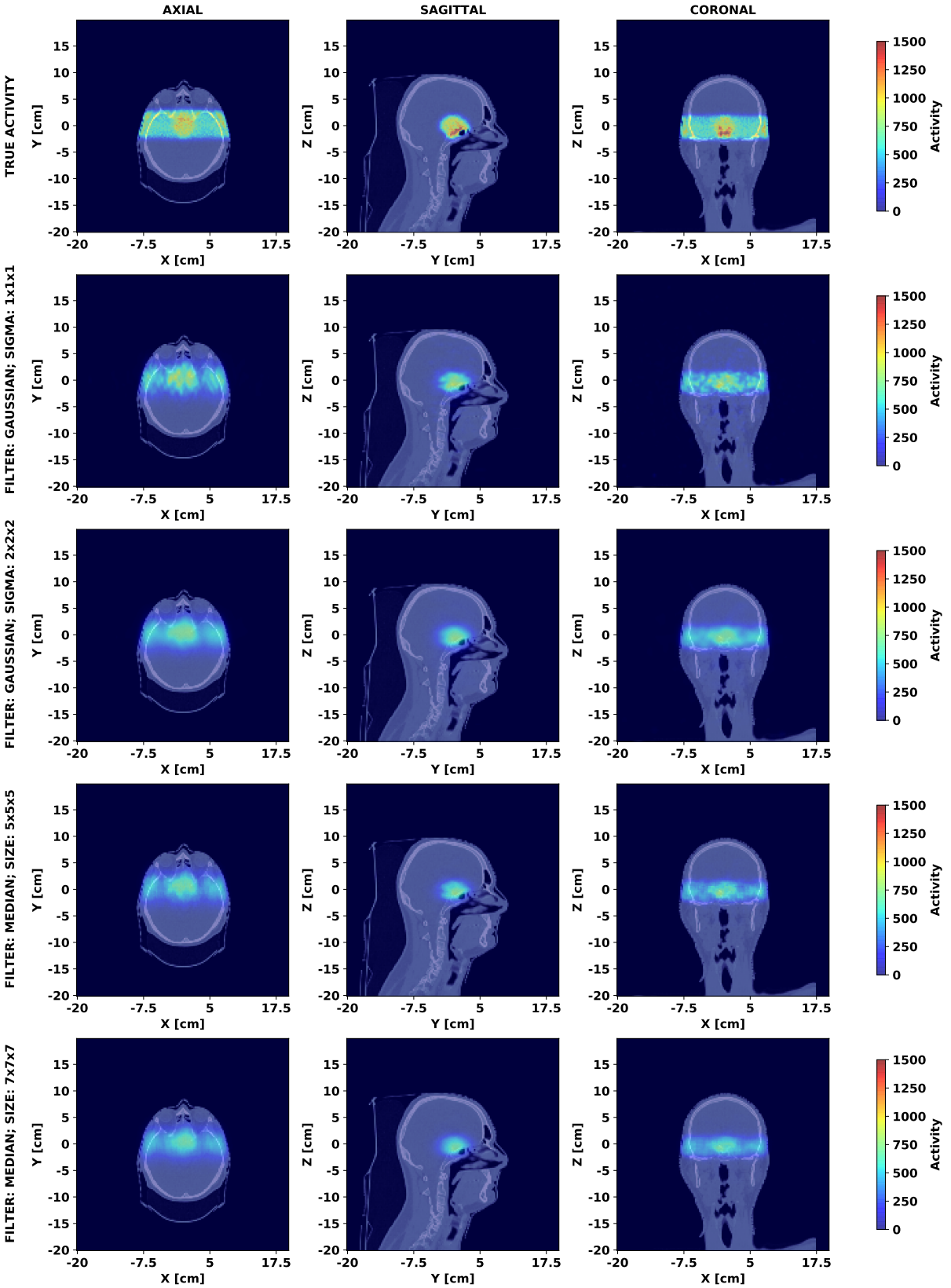

Figure 86: True production activity distribution and reconstructed PET images with the highest PCC for triple layer dual-head configuration in axial (left), sagittal (centre) and coronal (right) views superimposed on CT images. The calculation was performed for the simulated in-room PET acquisition scenario.

BIBLIOGRAPHY

[1] BWKP Stewart, CP Wild, et al. "World cancer report 2014." In: (2014).

[2] F Bray, J Ferlay, I Soerjomataram, et al. "Global cancer statistics 2018: GLOBOCAN estimates of incidence and mortality worldwide for 36 cancers in 185 countries." In: *CA: a cancer journal for clinicians* 68.6 (2018), pp. 394–424.

[3] *Raporty: Krajowy Rejestr Nowotworów [PL]*. http://onkologia.org.pl/raporty/. Accessed: 2020-03-15.

[4] H Paganetti. *Proton Therapy Physics*. Ed. by JG Webster, S Tabakov, and KH Ng. Vol. 103. Boston, USA: CRC Press Taylor & Francis Group, 2012, p. 690. ISBN: 1439836442. DOI: 10.1097/HP.0b013e31824e7040.

[5] H Nystrom, MF Jensen, and PW Nystrom. "Treatment planning for proton therapy: what is needed in the next 10 years?" In: *The British Journal of Radiology* 93.1107 (2020), p. 20190304.

[6] M Durante, R Orecchia, and JS Loeffler. "Charged-particle therapy in cancer: clinical uses and future perspectives." In: *Nature Reviews Clinical Oncology* 14.8 (2017), p. 483.

[7] K Parodi. "Latest developments in in-vivo imaging for proton therapy." In: *The British Journal of Radiology* 93.1107 (2020), p. 20190787.

[8] J Krimmer, D Dauvergne, JM Létang, and É Testa. "Prompt-gamma monitoring in hadrontherapy: A review." In: *Nuclear Instruments and Methods in Physics Research Section A: Accelerators, Spectrometers, Detectors and Associated Equipment* 878 (2018), pp. 58–73.

[9] G Traini, I Mattei, G Battistoni, et al. "Review and performance of the Dose Profiler, a particle therapy treatments online monitor." In: *Physica Medica* 65 (2019), pp. 84–93.

[10] G. Battistoni et al. "Measurement of charged particle yields from therapeutic beams in view of the design of an innovative hadrontherapy dose monitor." In: *Journal of Instrumentation* 10.2 (2015). ISSN: 17480221. DOI: 10.1088/1748-0221/10/02/C02032.

[11] M Marafini, L Gasparini, R Mirabelli, et al. "MONDO: a neutron tracker for particle therapy secondary emission characterisation." In: *Physics in Medicine & Biology* 62.8 (2017), p. 3299.

[12] VA Bashkirov, RW Schulte, RP Johnson, and Pankuch M. "In-Beam Range Verification with Scattered Particles Registered with a Particle CT Scanner." In: *59th AAPM meeting, Denver*. 2017.

[13] J Bauer et al. "Implementation and initial clinical experience of offline PET/CT-based verification of scanned carbon ion treatment." In: *Radiotherapy and Oncology* 107.2 (2013), pp. 218–226. ISSN: 01678140. DOI: 10.1016/j.radonc.2013.02.018. URL: http://dx.doi.org/10.1016/j.radonc.2013.02.018.

[14] MG Bisogni et al. "INSIDE in-beam positron emission tomography system for particle range monitoring in hadrontherapy." In: *Journal of Medical Imaging* 4.1 (2016), p. 011005. ISSN: 2329-4302. DOI: 10.1117/1.JMI.4.1.011005. URL: https://doi.org/10.1117/1.JMI.4.1.011005.

[15] V Ferrero, E Fiorina, M Morrocchi, et al. "Online proton therapy monitoring: clinical test of a Silicon-photodetector-based in-beam PET." In: *Scientific Reports* 8.1 (2018), p. 4100. ISSN: 2045-2322. DOI: 10.1038/s41598-018-22325-6. URL: http://www.nature.com/articles/s41598-018-22325-6.

[16] W Enghardt, P Crespo, F Fiedler, et al. "Charged hadron tumour therapy monitoring by means of PET." In: *Nuclear Instruments and Methods in Physics Research Section A: Accelerators, Spectrometers, Detectors and Associated Equipment* 525.1-2 (2004), pp. 284–288.

[17] P Kowalski, W Wiślicki, RY Shopa, et al. "Estimating the NEMA characteristics of the J-PET tomograph using the GATE package." In: *Physics in Medicine & Biology* 63.16 (2018), p. 165008.

[18] P Moskal, B Jasińska, E Skupień, and SD Bass. "Positronium in medicine and biology." In: *Nature Reviews Physics* 1.9 (2019), pp. 527–529.

[19] BC Hiesmayr and P Moskal. "Genuine multipartite entanglement in the 3-photon decay of positronium." In: *Scientific Reports* 7.1 (2017), pp. 1–9.

[20] BC Hiesmayr and P Moskal. "Witnessing entanglement in compton scattering processes via mutually unbiased bases." In: *Scientific reports* 9.1 (2019), pp. 1–14.

[21] D. Kamińska et al. "A feasibility study of ortho-positronium decays measurement with the J-PET scanner based on plastic scintillators." In: *Eur. Phys. J. C* 76 (2016), p. 445.

[22] P Moskal, N Krawczyk, BC Hiesmayr, et al. "Feasibility studies of the polarization of photons beyond the optical wavelength regime with the J-PET detector." In: *The European Physical Journal C* 78.11 (2018), p. 970.

[23] A Rucinski, J Baran, G Battistoni, et al. "Investigations on physical and biological range uncertainties in Krakow proton beam therapy centre." In: *arXiv preprint arXiv:1910.11943* (2019).

[24] HA Bethe, ME Rose, and LP Smith. "The multiple scattering of electrons." In: *Proceedings of the American Philosophical Society* (1938), pp. 573–585.

[25] F Bloch. "Bremsvermögen von Atomen mit mehreren Elektronen." In: *Zeitschrift für Physik* 81.5-6 (1933), pp. 363–376.

[26] AC Kraan. "Range verification methods in particle therapy: underlying physics and Monte Carlo modeling." In: *Frontiers in oncology* 5 (2015), p. 150.

[27] J Lindhard and M Scharff. "Energy dissipation by ions in the keV region." In: *Physical Review* 124.1 (1961), p. 128.

[28] J Lindhard, M Scharff, and HE Schiøtt. *Range concepts and heavy ion ranges*. Munksgaard Copenhagen, 1963.

[29] JF Ziegler. "Stopping of energetic light ions in elemental matter." In: *Journal of applied physics* 85.3 (1999), pp. 1249–1272.

[30] CC Juan, M Crispin-Ortuzar, and M Aslaninejad. "Depth-dose distribution of proton beams using inelastic-collision cross sections of liquid water." In: *Nuclear Instruments and Methods in Physics Research Section B: Beam Interactions with Materials and Atoms* 269.2 (2011), pp. 189–196.

[31] AJ Lomax. "Charged particle therapy: the physics of interaction." In: *The Cancer Journal* 15.4 (2009), pp. 285–291.

[32] HA Bethe. "Moliere's theory of multiple scattering." In: *Physical review* 89.6 (1953), p. 1256.

[33] M Durante and H Paganetti. "Nuclear physics in particle therapy: a review." In: *Reports on Progress in Physics* 79.9 (2016), p. 096702.

[34] S España, X Zhu, J Daartz, et al. "The reliability of proton-nuclear interaction cross-section data to predict proton-induced PET images in proton therapy." In: *Physics in Medicine & Biology* 56.9 (2011), p. 2687.

[35] *National Institute of Standards and Technology*. http://www.nist.gov/. Accessed: 2020-04-17.

[36] *Brookhaven National Laboratory*. www.nndc.bnl.gov/nndc/nudat. Accessed: 2020-04-17.

[37] AC Kraan, G Battistoni, N Belcari, et al. "First tests for an online treatment monitoring system with in-beam PET for proton therapy." In: *arXiv preprint arXiv:1411.7174* (2014).

[38] G Battistoni, T Boehlen, F Cerutti, et al. "Overview of the FLUKA code." In: *Annals of Nuclear Energy* 82 (2015), pp. 10–18.

[39] WH Bragg and R Kleeman. "XXXIX. On the α particles of radium, and their loss of range in passing through various atoms and molecules." In: *The London, Edinburgh, and Dublin Philosophical Magazine and Journal of Science* 10.57 (1905), pp. 318–340.

[40] RR Wilson. "Radiological use of fast protons." In: *Radiology* 47.5 (1946), pp. 487–491.

[41] CA Tobias, JH Lawrence, JL Born, et al. "Pituitary irradiation with high-energy proton beams a preliminary report." In: *Cancer research* 18.2 (1958), pp. 121–134.

[42] *Particle Therapy Co-Operative Group website*. https://www.ptcog.ch/. Accessed: 2020-03-30.

[43] Jan Gajewski. "Rozwój dwuwymiarowego, termoluminescencyjnego systemu dozymetrycznego dla zapewnienia jakości w jonoterapii nowotworów." PhD thesis. Institue of Nuclear Physics Polish Academy of Science, 2016 [In Polish].

[44] E Almhagen, DJ Boersma, H Nyström, and A Ahnesjö. "A beam model for focused proton pencil beams." In: *Physica Medica* 52 (2018), pp. 27–32.

[45] Magdalena Kłodowska. "Application of Monte Carlo methods in transport modelling of the therapeutic proton beam." PhD thesis. Institue of Nuclear Physics Polish Academy of Science, 2018.

[46] WD Newhauser and R Zhang. "The physics of proton therapy." In: *Physics in Medicine & Biology* 60.8 (2015), R155.

[47] ICRU78. *Prescribing, recording, and reporting proton-beam therapy. Technical Report ICRU Report 78*. Tech. rep. 2007.

[48] Frank Herbert Attix. *Introduction to radiological physics and radiation dosimetry*. John Wiley & Sons, 2008.

[49] AC Knopf and A Lomax. "In vivo proton range verification: a review." In: *Physics in Medicine & Biology* 58.15 (2013), R131.

[50] U Schneider, E Pedroni, and A Lomax. "The calibration of CT Hounsfield units for radiotherapy treatment planning." In: *Physics in Medicine & Biology* 41.1 (1996), p. 111.

[51] W Schneider, T Bortfeld, and W Schlegel. "Correlation between CT numbers and tissue parameters needed for Monte Carlo simulations of clinical dose distributions." In: *Physics in Medicine & Biology* 45.2 (2000), p. 459.

[52] MF Moyers, DW Miller, DA Bush, and JD Slater. "Methodologies and tools for proton beam design for lung tumors." In: *International Journal of Radiation Oncology* Biology* Physics* 49.5 (2001), pp. 1429–1438.

[53] Philip Mayles, Alan Nahum, and Jean-Claude Rosenwald. *Handbook of radiotherapy physics: theory and practice*. CRC Press, 2007.

[54] CZ Jarlskog and H Paganetti. "Physics settings for using the Geant4 toolkit in proton therapy." In: *IEEE Transactions on nuclear science* 55.3 (2008), pp. 1018–1025.

[55] K Henkner, N Sobolevsky, O Jäkel, and H Paganetti. "Test of the nuclear interaction model in SHIELD-HIT and comparison to energy distributions from GEANT4." In: *Physics in Medicine & Biology* 54.22 (2009), N509.

[56] D Sarrut, M Bardiès, N Boussion, et al. "A review of the use and potential of the GATE Monte Carlo simulation code for radiation therapy and dosimetry applications." In: *Medical physics* 41.6Part1 (2014).

[57] M Testa, J Schümann, H-M Lu, et al. "Experimental validation of the TOPAS Monte Carlo system for passive scattering proton therapy." In: *Medical physics* 40.12 (2013), p. 121719.

[58] D Giantsoudi, J Schuemann, X Jia, et al. "Validation of a GPU-based Monte Carlo code (gPMC) for proton radiation therapy: clinical cases study." In: *Physics in Medicine & Biology* 60.6 (2015), p. 2257.

[59] N Qin, P Botas, D Giantsoudi, et al. "Recent developments and comprehensive evaluations of a GPU-based Monte Carlo package for proton therapy." In: *Physics in Medicine & Biology* 61.20 (2016), p. 7347.

[60] D Maneval, B Ozell, and P Després. "pGPUMCD: an efficient GPU-based Monte Carlo code for accurate proton dose calculations." In: *Physics in Medicine & Biology* 64.8 (2019), p. 085018.

[61] H Wan Chan Tseung, J Ma, and C Beltran. "A fast GPU-based Monte Carlo simulation of proton transport with detailed modeling of nonelastic interactions." In: *Medical physics* 42.6Part1 (2015), pp. 2967–2978.

[62] A Schiavi, M Senzacqua, S Pioli, et al. "Fred: a GPU-accelerated fast-Monte Carlo code for rapid treatment plan recalculation in ion beam therapy." In: *Physics in Medicine & Biology* 62.18 (2017), p. 7482.

[63] J Gajewski, M Garbacz, C Chih-Wei, et al. "Commissioning of GPU-accelerated Monte Carlo code Fred for clinical applications in proton therapy." In: *Frontiers in Physics* (In review).

[64] S Mein, K Choi, B Kopp, et al. "Fast robust dose calculation on GPU for high-precision 1 H, 4 He, 12 C and 16 O ion therapy: The FRoG platform." In: *Scientific reports* 8.1 (2018), pp. 1–12.

[65] KD Choi, SB Mein, B Kopp, et al. "FRoG—A new calculation engine for clinical investigations with proton and carbon ion beams at CNAO." In: *Cancers* 10.11 (2018), p. 395.

[66] S Mein, B Kopp, T Tessonnier, et al. "Dosimetric validation of Monte Carlo and analytical dose engines with raster-scanning 1H, 4He, 12C, and 16O ion-beams using an anthropomorphic phantom." In: *Physica Medica* 64 (2019), pp. 123–131.

[67] T Pawlicki and C-MC Ma. "Monte Carlo simulation for MLC-based intensity-modulated radiotherapy." In: *Medical Dosimetry* 26.2 (2001), pp. 157–168.

[68] Dale L Bailey, Michael N Maisey, David W Townsend, and Peter E Valk. *Positron emission tomography*. Vol. 2. Springer, 2005.

[69] JS Karp, S Surti, ME Daube-Witherspoon, and G Muehllehner. "Benefit of time-of-flight in PET: experimental and clinical results." In: *Journal of Nuclear Medicine* 49.3 (2008), pp. 462–470.

[70] DR Schaart and S Ziegler. "Achieving 10 ps coincidence time resolution in TOF-PET is an impossible dream." In: *Medical Physics* (2020).

[71] *The 10 ps challenge*. https://the10ps-challenge.org/. Accessed: 2020-05-22.

[72] RD Badawi, H Shi, P Hu, et al. "First human imaging studies with the EXPLORER total-body PET scanner." In: *Journal of Nuclear Medicine* 60.3 (2019), pp. 299–303.

[73] SR Cherry, T Jones, JS Karp, et al. "Total-body PET: maximizing sensitivity to create new opportunities for clinical research and patient care." In: *Journal of Nuclear Medicine* 59.1 (2018), pp. 3–12.

[74] Michel Defrise, Paul E Kinahan, and Christian J Michel. "Image reconstruction algorithms in PET." In: *Positron Emission Tomography*. Springer, 2005, pp. 63–91.

[75] A Alessio, P Kinahan, et al. "PET image reconstruction." In: *Nuclear medicine* 1 (2006), pp. 1–22.

[76] S Tong, AM Alessio, and PE Kinahan. "Image reconstruction for PET/CT scanners: past achievements and future challenges." In: *Imaging in medicine* 2.5 (2010), p. 529.

[77] PA Toft. "The Radon transform-theory and implementation." In: (1996).

[78] RM Lewitt. "Multidimensional digital image representations using generalized Kaiser–Bessel window functions." In: *JOSA A* 7.10 (1990), pp. 1834–1846.

[79] RM Lewitt. "Alternatives to voxels for image representation in iterative reconstruction algorithms." In: *Physics in Medicine & Biology* 37.3 (1992), p. 705.

[80] JJ Scheins, H Herzog, and NJ Shah. "Fully-3D PET image reconstruction using scanner-independent, adaptive projection data and highly rotation-symmetric voxel assemblies." In: *IEEE transactions on medical imaging* 30.3 (2011), pp. 879–892.

[81] AJ Reader and H Zaidi. "Advances in PET image reconstruction." In: *PET clinics* 2.2 (2007), pp. 173–190.

[82] A Rahmim, M Lenox, AJ Reader, et al. "Statistical list-mode image reconstruction for the high resolution research tomograph." In: *Physics in Medicine & Biology* 49.18 (2004), p. 4239.

[83] K Thielemans, C Tsoumpas, S Mustafovic, et al. "STIR: software for tomographic image reconstruction release 2." In: *Physics in Medicine & Biology* 57.4 (2012), p. 867.

[84] *Software for Tomographic Image Reconstruction (STIR) website*. http://stir.sourceforge.net/. Accessed: 2020-06-01.

[85] N Efthimiou, E Emond, P Wadhwa, et al. "Implementation and validation of time-of-flight PET image reconstruction module for listmode and sinogram projection data in the STIR library." In: *Physics in Medicine & Biology* 64.3 (2019), p. 035004.

[86] T Merlin, S Stute, D Benoit, et al. "CASToR: a generic data organization and processing code framework for multi-modal and multi-dimensional tomographic reconstruction." In: *Physics in Medicine & Biology* 63.18 (2018), p. 185005.

[87] *Customizable and Advanced Software for Tomographic Reconstruction (CASToR) website*. http://castor-project.org. Accessed: 2019-11-01.

[88] *NiftyRec website*. http://niftyrec.scienceontheweb.net/wordpress/. Accessed: 2020-06-01.

[89] *Occiput.io website*. http://tomographylab.scienceontheweb.net/. Accessed: 2020-06-01.

[90] *Open-source MATLAB Emission Tomography Software (OMEGA) website*. https://github.com/villekf/OMEGA. Accessed: 2020-06-01.

[91] JPJ Carney, DW Townsend, V Rappoport, and B Bendriem. "Method for transforming CT images for attenuation correction in PET/CT imaging." In: *Medical physics* 33.4 (2006), pp. 976–983.

[92] MA Belzunce and AJ Reader. "Time-invariant component-based normalization for a simultaneous PET-MR scanner." In: *Physics in Medicine & Biology* 61.9 (2016), p. 3554.

[93] RL Siddon. "Fast calculation of the exact radiological path for a three-dimensional CT array." In: *Medical physics* 12.2 (1985), pp. 252–255.

[94] PM Joseph. "An improved algorithm for reprojecting rays through pixel images." In: *IEEE transactions on medical imaging* 1.3 (1982), pp. 192–196.

[95] H Zhao and AJ Reader. "Fast ray-tracing technique to calculate line integral paths in voxel arrays." In: *2003 IEEE Nuclear Science Symposium. Conference Record*. Vol. 4. IEEE. 2003, pp. 2808–2812.

[96] S Vandenberghe, P Moskal, and JS Karp. "State of the art in total body PET." In: *EJNMMI* 7.35 (2020).

[97] Szymon Niedźwiecki. "Studies of detection of radiation with use of organic scintillator detectors in view of positron emission tomography." MA thesis. Jagiellonian University, 2011.

[98] Szymon Niedźwiecki. "Double-strip prototype of polymer time-of-flight positron emission tomograph based on multi-level analog electronics." PhD thesis. Jagiellonian University, 2019.

[99] Paweł Moskal, Daria Kisielewska, RY Shopa, Zuzanna Bura, Jyoti Chhokar, C Curceanu, Eryk Czerwiński, Meysam Dadgar, Kamil Dulski, J Gajewski, et al. "Performance assessment of the 2 γ positronium imaging with the total-body PET scanners." In: *EJNMMI physics* 7.1 (2020), pp. 1–16.

[100] *Eljen Technology EJ-230 plastic scintillator*. https://eljentechnology.com/products/plastic-scintillators/ej-228-ej-230. Accessed: 2020-06-15.

[101] G Korcyl, D Alfs, T Bednarski, et al. "Sampling FEE and Triggerless DAQ for the J-PET Scanner." In: *arXiv preprint arXiv:1602.05251* (2016).

[102] M Pałka, P Strzempek, G Korcyl, et al. "Multichannel FPGA based MVT system for high precision time (20 ps RMS) and charge measurement." In: *Journal of Instrumentation* 12.08 (2017), P08001.

[103] G Korcyl, P Białas, C Curceanu, et al. "Evaluation of single-chip, real-time tomographic data processing on FPGA SoC devices." In: *IEEE transactions on medical imaging* 37.11 (2018), pp. 2526–2535.

[104] W Krzemien, A Gajos, K Kacprzak, et al. "J-PET Framework: Software platform for PET tomography data reconstruction and analysis." In: *SoftwareX* 11 (2020), p. 100487.

[105] C Robert, G Dedes, G Battistoni, et al. "Distributions of secondary particles in proton and carbon-ion therapy: a comparison between GATE/Geant4 and FLUKA Monte Carlo codes." In: *Physics in Medicine & Biology* 58.9 (2013), p. 2879.

[106] M Moteabbed, S España, and H Paganetti. "Monte Carlo patient study on the comparison of prompt gamma and PET imaging for range verification in proton therapy." In: *Physics in Medicine & Biology* 56.4 (2011), p. 1063.

[107] KC Jones, F Vander Stappen, CM Sehgal, and S Avery. "Acoustic time-of-flight for proton range verification in water." In: *Medical physics* 43.9 (2016), pp. 5213–5224.

[108] S Lehrack, W Assmann, D Bertrand, et al. "Submillimeter ionoacoustic range determination for protons in water at a clinical synchrocyclotron." In: *Physics in Medicine & Biology* 62.17 (2017), p. L20.

[109] K Parodi, Thomas B, and T Haberer. "Comparison between in-beam and offline positron emission tomography imaging of proton and carbon ion therapeutic irradiation at synchrotron-and cyclotron-based facilities." In: *International Journal of Radiation Oncology* Biology* Physics* 71.3 (2008), pp. 945–956.

[110] T Nishio, A Miyatake, T Ogino, et al. "The development and clinical use of a beam ON-LINE PET system mounted on a rotating gantry port in proton therapy." In: *International Journal of Radiation Oncology* Biology* Physics* 76.1 (2010), pp. 277–286.

[111] K Parodi, H Paganetti, HA Shih, et al. "Patient study of in vivo verification of beam delivery and range, using positron emission tomography and computed tomography imaging after proton therapy." In: *International Journal of Radiation Oncology* Biology* Physics* 68.3 (2007), pp. 920–934.

[112] A Miyatake, T Nishio, and T Ogino. "Development of activity pencil beam algorithm using measured distribution data of positron emitter nuclei generated by proton irradiation of targets containing 12C, 16O, and 40Ca nuclei in preparation of clinical application." In: *Medical physics* 38.10 (2011), pp. 5818–5829.

[113] K Frey, J Bauer, D Unholtz, et al. "TPSpet—a TPS-based approach for in vivo dose verification with PET in proton therapy." In: *Physics in Medicine & Biology* 59.1 (2013), p. 1.

[114] J Bauer, W Chen, S Nischwitz, et al. "Improving the modelling of irradiation-induced brain activation for in vivo PET verification of proton therapy." In: *Radiotherapy and Oncology* 128.1 (2018), pp. 101–108.

[115] B Berndt, G Landry, F Schwarz, et al. "Application of single-and dual-energy CT brain tissue segmentation to PET monitoring of proton therapy." In: *Physics in Medicine & Biology* 62.6 (2017), p. 2427.

[116] K Parodi and T Bortfeld. "A filtering approach based on Gaussian–powerlaw convolutions for local PET verification of proton radiotherapy." In: *Physics in Medicine & Biology* 51.8 (2006), p. 1991.

[117] F Attanasi, N Belcari, M Camarda, et al. "Experimental validation of the filtering approach for dose monitoring in proton therapy at low energy." In: *Physica Medica* 24.2 (2008), pp. 102–106.

[118] F Attanasi, A Knopf, K Parodi, et al. "Extension and validation of an analytical model for in vivo PET verification of proton therapy—a phantom and clinical study." In: *Physics in Medicine & Biology* 56.16 (2011), p. 5079.

[119] T Inaniwa, T Kohno, F Yamagata, et al. "Maximum likelihood estimation of proton irradiated field and deposited dose distribution." In: *Medical physics* 34.5 (2007), pp. 1684–1692.

[120] E Fourkal, J Fan, and I Veltchev. "Absolute dose reconstruction in proton therapy using PET imaging modality: feasibility study." In: *Physics in Medicine & Biology* 54.11 (2009), N217.

[121] S Remmele, J Hesser, H Paganetti, and T Bortfeld. "A deconvolution approach for PET-based dose reconstruction in proton radiotherapy." In: *Physics in Medicine & Biology* 56.23 (2011), p. 7601.

[122] I Pshenichnov, I Mishustin, and W Greiner. "Distributions of positron-emitting nuclei in proton and carbon-ion therapy studied with GEANT4." In: *Physics in Medicine & Biology* 51.23 (2006), p. 6099.

[123] P Dendooven, HJT Buitenhuis, F Diblen, et al. "Short-lived positron emitters in beam-on PET imaging during proton therapy." In: *Physics in Medicine & Biology* 60.23 (2015), p. 8923.

[124] G Shakirin, H Braess, F Fiedler, et al. "Implementation and workflow for PET monitoring of therapeutic ion irradiation: a comparison of in-beam, in-room, and off-line techniques." In: *Physics in Medicine & Biology* 56.5 (2011), p. 1281.

[125] Y Hishikawa, K Kagawa, M Murakami, et al. "Usefulness of positron-emission tomographic images after proton therapy." In: *International Journal of Radiation Oncology* Biology* Physics* 53.5 (2002), pp. 1388–1391.

[126] A Knopf, K Parodi, H Paganetti, et al. "Quantitative assessment of the physical potential of proton beam range verification with PET/CT." In: *Physics in Medicine & Biology* 53.15 (2008), p. 4137.

[127] A Knopf, K Parodi, T Bortfeld, et al. "Systematic analysis of biological and physical limitations of proton beam range verification with offline PET/CT scans." In: *Physics in Medicine & Biology* 54.14 (2009), p. 4477.

[128] AC Knopf, K Parodi, H Paganetti, et al. "Accuracy of proton beam range verification using post-treatment positron emission tomography/computed tomography as function of treatment site." In: *International Journal of Radiation Oncology* Biology* Physics* 79.1 (2011), pp. 297–304.

[129] SP Nischwitz, J Bauer, T Welzel, et al. "Clinical implementation and range evaluation of in vivo PET dosimetry for particle irradiation in patients with primary glioma." In: *Radiotherapy and Oncology* 115.2 (2015), pp. 179–185.

[130] Jo Handrack, T Tessonnier, W Chen, et al. "Sensitivity of post treatment positron emission tomography/computed tomography to detect inter-fractional range variations in scanned ion beam therapy." In: *Acta Oncologica* 56.11 (2017), pp. 1451–1458.

[131] WC Hsi, DJ Indelicato, C Vargas, et al. "In vivo verification of proton beam path by using post-treatment PET/CT imaging." In: *Medical physics* 36.9Part1 (2009), pp. 4136–4146.

[132] X Zhu, S España, J Daartz, et al. "Monitoring proton radiation therapy with in-room PET imaging." In: *Physics in Medicine & Biology* 56.13 (2011), p. 4041.

[133] CH Min, X Zhu, BA Winey, et al. "Clinical application of in-room positron emission tomography for in vivo treatment monitoring in proton radiation therapy." In: *International Journal of Radiation Oncology* Biology* Physics* 86.1 (2013), pp. 183–189.

[134] F Fiedler, G Shakirin, J Skowron, et al. "On the effectiveness of ion range determination from in-beam PET data." In: *Physics in Medicine & Biology* 55.7 (2010), p. 1989.

[135] Y Iseki, H Mizuno, Y Futami, et al. "Positron camera for range verification of heavy-ion radiotherapy." In: *Nuclear Instruments and Methods in Physics Research Section A: Accelerators, Spectrometers, Detectors and Associated Equipment* 515.3 (2003), pp. 840–849.

[136] Yasushi Iseki, Tatuaki Kanai, Mitsutaka Kanazawa, Atsushi Kitagawa, Hideyuki Mizuno, Takehiro Tomitani, Mitsuru Suda, and Eriko Urakabe. "Range verification system using positron emitting beams for heavy-ion radiotherapy." In: *Physics in Medicine & Biology* 49.14 (2004), p. 3179.

[137] A Miyatake, T Nishio, T Ogino, et al. "Measurement and verification of positron emitter nuclei generated at each treatment site by target nuclear fragment reactions in proton therapy." In: *Medical physics* 37.8 (2010), pp. 4445–4455.

[138] Elisa Fiorina, Veronica Ferrero, Guido Baroni, Giuseppe Battistoni, Nicola Belcari, Niccolo Camarlinghi, Piergiorgio Cerello, Mario Ciocca, Micol De Simoni, Marco Donetti, et al. "Detection of inter-fractional morphological changes in proton therapy: a simulation and in-vivo study with the INSIDE in-beam PET." In: *Frontiers in Physics* 8 (2020), p. 660.

[139] AC Kraan, S Muraro, G Battistoni, et al. "Analysis of in-beam PET time-profiles in proton therapy." In: *Journal of Instrumentation* 14.02 (2019), p. C02001.

[140] A Topi, S Muraro, G Battistoni, et al. "Monitoring Proton Therapy Through In-Beam PET: An Experimental Phantom Study." In: *IEEE Transactions on Radiation and Plasma Medical Sciences* (2019).

[141] E Yoshida, H Tashima, T Shinaji, et al. "Development of a whole-body dual ring OpenPET for in-beam PET." In: *IEEE Transactions On Radiation and Plasma Medical Sciences* 1.4 (2017), pp. 293–300.

[142] Taiga Yamaya and Hideaki Tashima. "OpenPET Enabling PET Imaging During Radiotherapy." In: *Personalized Pathway-Activated Systems Imaging in Oncology*. Springer, 2017, pp. 55–84.

[143] P Crespo, G Shakirin, and W Enghardt. "On the detector arrangement for in-beam PET for hadron therapy monitoring." In: *Physics in Medicine & Biology* 51.9 (2006), p. 2143.

[144] H Tashima, E Yoshida, N Inadama, et al. "Development of a small single-ring OpenPET prototype with a novel transformable architecture." In: *Physics in Medicine & Biology* 61.4 (2016), p. 1795.

[145] P Crespo, G Shakirin, F Fiedler, et al. "Direct time-of-flight for quantitative, real-time in-beam PET: a concept and feasibility study." In: *Physics in Medicine & Biology* 52.23 (2007), p. 6795.

[146] HJT Buitenhuis, F Diblen, KW Brzezinski, et al. "Beam-on imaging of short-lived positron emitters during proton therapy." In: *Physics in Medicine & Biology* 62.12 (2017), p. 4654.

[147] K Frey, D Unholtz, J Bauer, et al. "Automation and uncertainty analysis of a method for in-vivo range verification in particle therapy." In: *Physics in Medicine & Biology* 59.19 (2014), p. 5903.

[148] P Kuess, S Helmbrecht, F Fiedler, et al. "Automated evaluation of setup errors in carbon ion therapy using PET: Feasibility study." In: *Medical physics* 40.12 (2013), p. 121718.

[149] AC Kraan, G Battistoni, N Belcari, et al. "Proton range monitoring with in-beam PET: Monte Carlo activity predictions and comparison with cyclotron data." In: *Physica Medica* 30.5 (2014), pp. 559–569.

[150] AC Kraan, G Battistoni, N Belcari, et al. "Online monitoring for proton therapy: a real-time procedure using a planar PET system." In: *Nuclear Instruments and Methods in Physics Research Section A: Accelerators, Spectrometers, Detectors and Associated Equipment* 786 (2015), pp. 120–126.

[151] F Stichelbaut and Y Jongen. "Verification of the proton beam position in the patient by the detection of prompt gamma-rays emission." In: *39th PTCOG meeting, San Francisco*. 2003.

[152] C-H Min, CH Kim, M-Y Youn, and J-W Kim. "Prompt gamma measurements for locating the dose falloff region in the proton therapy." In: *Applied physics letters* 89.18 (2006), p. 183517.

[153] M Pinto, D Dauvergne, N Freud, et al. "Design optimisation of a TOF-based collimated camera prototype for online hadrontherapy monitoring." In: *Physics in Medicine & Biology* 59.24 (2014), p. 7653.

[154] CH Min, HR Lee, CH Kim, and SB Lee. "Development of array-type prompt gamma measurement system for in vivo range verification in proton therapy." In: *Medical physics* 39.4 (2012), pp. 2100–2107.

[155] PC Lopes, P Crespo, H Simões, et al. "Simulation of proton range monitoring in an anthropomorphic phantom using multi-slat collimators and time-of-flight detection of prompt-gamma quanta." In: *Physica Medica* 54 (2018), pp. 1–14.

[156] F Roellinghoff, A Benilov, D Dauvergne, et al. "Real-time proton beam range monitoring by means of prompt-gamma detection with a collimated camera." In: *Physics in Medicine & Biology* 59.5 (2014), p. 1327.

[157] J-W Kim. "Pinhole camera measurements of prompt gamma-rays for detection of beam range variation in proton therapy." In: *Journal of the Korean Physical Society* 55.4 (2009), pp. 1673–1676.

[158] J Smeets, F Roellinghoff, D Prieels, et al. "Prompt gamma imaging with a slit camera for real-time range control in proton therapy." In: *Physics in Medicine & Biology* 57.11 (2012), p. 3371.

[159] I Perali, A Celani, L Bombelli, et al. "Prompt gamma imaging of proton pencil beams at clinical dose rate." In: *Physics in Medicine & Biology* 59.19 (2014), p. 5849.

[160] M Priegnitz, S Helmbrecht, G Janssens, et al. "Measurement of prompt gamma profiles in inhomogeneous targets with a knife-edge slit camera during proton irradiation." In: *Physics in Medicine & Biology* 60.12 (2015), p. 4849.

[161] L Nenoff, M Priegnitz, G Janssens, et al. "Sensitivity of a prompt-gamma slit-camera to detect range shifts for proton treatment verification." In: *Radiotherapy and Oncology* 125.3 (2017), pp. 534–540.

[162] M Priegnitz, S Helmbrecht, G Janssens, et al. "Detection of mixed-range proton pencil beams with a prompt gamma slit camera." In: *Physics in Medicine & Biology* 61.2 (2016), p. 855.

[163] C Richter, G Pausch, S Barczyk, et al. "First clinical application of a prompt gamma based in vivo proton range verification system." In: *Radiotherapy and Oncology* 118.2 (2016), pp. 232–237.

[164] Y Xie, EH Bentefour, G Janssens, et al. "Prompt gamma imaging for in vivo range verification of pencil beam scanning proton therapy." In: *International Journal of Radiation Oncology* Biology* Physics* 99.1 (2017), pp. 210–218.

[165] P Solevi, E Muñoz, C Solaz, et al. "Performance of MACACO Compton telescope for ion-beam therapy monitoring: first test with proton beams." In: *Physics in Medicine & Biology* 61.14 (2016), p. 5149.

[166] T Taya, J Kataoka, A Kishimoto, et al. "First demonstration of real-time gamma imaging by using a handheld Compton camera for particle therapy." In: *Nuclear Instruments and Methods in Physics Research Section A: Accelerators, Spectrometers, Detectors and Associated Equipment* 831 (2016), pp. 355–361.

[167] JC Polf, S Avery, DS Mackin, and S Beddar. "Imaging of prompt gamma rays emitted during delivery of clinical proton beams with a Compton camera: feasibility studies for range verification." In: *Physics in Medicine & Biology* 60.18 (2015), p. 7085.

[168] M McCleskey, W Kaye, DS Mackin, et al. "Evaluation of a multistage CdZnTe Compton camera for prompt γ imaging for proton therapy." In: *Nuclear Instruments and Methods in Physics Research Section A: Accelerators, Spectrometers, Detectors and Associated Equipment* 785 (2015), pp. 163–169.

[169] PG Thirolf, S Aldawood, M Böhmer, et al. "A Compton camera prototype for prompt gamma medical imaging." In: *EPJ Web of Conferences*. Vol. 117. Nuclear Structure. 2016, p. 05005.

[170] F Hueso-González, C Golnik, M Berthel, et al. "Test of Compton camera components for prompt gamma imaging at the ELBE bremsstrahlung beam." In: *Journal of Instrumentation* 9.05 (2014), P05002.

[171] S Kurosawa, H Kubo, K Ueno, et al. "Prompt gamma detection for range verification in proton therapy." In: *Current Applied Physics* 12.2 (2012), pp. 364–368.

[172] M Takahashi, S Kabuki, K Hattori, et al. "Development of an Electron-Tracking Compton Camera using CF_4 gas at high pressure for improved detection efficiency." In: *Nuclear Instruments and Methods in Physics Research Section A: Accelerators, Spectrometers, Detectors and Associated Equipment* 628.1 (2011), pp. 150–153.

[173] E Draeger, D Mackin, S Peterson, et al. "3D prompt gamma imaging for proton beam range verification." In: *Physics in Medicine & Biology* 63.3 (2018), p. 035019.

[174] Cc Golnik, F Hueso-González, A Müller, et al. "Range assessment in particle therapy based on prompt γ-ray timing measurements." In: *Physics in Medicine & Biology* 59.18 (2014), p. 5399.

[175] T Werner, J Berthold, F Hueso-González, et al. "Processing of prompt gamma-ray timing data for proton range measurements at a clinical beam delivery." In: *Physics in Medicine & Biology* 64.10 (2019), p. 105023.

[176] J Krimmer, G Angellier, L Balleyguier, et al. "A cost-effective monitoring technique in particle therapy via uncollimated prompt gamma peak integration." In: *Applied Physics Letters* 110.15 (2017), p. 154102.

[177] JM Verburg and J Seco. "Proton range verification through prompt gamma-ray spectroscopy." In: *Physics in Medicine & Biology* 59.23 (2014), p. 7089.

[178] JM Verburg, M Testa, and J Seco. "Range verification of passively scattered proton beams using prompt gamma-ray detection." In: *Physics in Medicine & Biology* 60.3 (2015), p. 1019.

[179] F Hueso-González, M Rabe, TA Ruggieri, et al. "A full-scale clinical prototype for proton range verification using prompt gamma-ray spectroscopy." In: *Physics in Medicine & Biology* 63.18 (2018), p. 185019.

[180] G Battistoni, F Collamati, E De Lucia, et al. "Design of a tracking device for on-line dose monitoring in hadrontherapy." In: *Nuclear Instruments and Methods in Physics Research Section A: Accelerators, Spectrometers, Detectors and Associated Equipment* 845 (2017), pp. 679–683.

[181] G Traini, G Battistoni, A Bollella, et al. "Design of a new tracking device for on-line beam range monitor in carbon therapy." In: *Physica Medica* 34 (2017), pp. 18–27.

[182] RP Johnson, V Bashkirov, L DeWitt, et al. "A fast experimental scanner for proton CT: technical performance and first experience with phantom scans." In: *IEEE transactions on nuclear science* 63.1 (2015), pp. 52–60.

[183] V Giacometti, G Battistoni, M De Simoni, et al. "Characterisation of the MONDO detector response to neutrons by means of a FLUKA Monte Carlo simulation." In: *Radiation Measurements* 119 (2018), pp. 144–149.

[184] E Gioscio, G Battistoni, A Bochetti, et al. "Development of a novel neutron tracker for the characterisation of secondary neutrons emitted in Particle Therapy." In: *Nuclear Instruments and Methods in Physics Research Section A: Accelerators, Spectrometers, Detectors and Associated Equipment* 958 (2020), p. 162862.

[185] KC Jones, A Witztum, CM Sehgal, and S Avery. "Proton beam characterization by proton-induced acoustic emission: simulation studies." In: *Physics in Medicine & Biology* 59.21 (2014), p. 6549.

[186] KC Jones, W Nie, JCH Chu, et al. "Acoustic-based proton range verification in heterogeneous tissue: simulation studies." In: *Physics in Medicine & Biology* 63.2 (2018), p. 025018.

[187] Jakub Baran, Jan Gajewski, Monika Pawlik-Niedźwiecka, Paweł Moskal, and Antoni Ruciński. "Studies of J-PET detector to monitor range uncertainty in proton therapy." In: *2019 IEEE Nuclear Science Symposium and Medical Imaging Conference (NSS/MIC)*. IEEE, pp. 1–4.

[188] M Lipowski. *Zbior zadań z podstaw techniki swietlnej*. Politechnika Warszawska Press, 1968.

[189] RS Augusto, J Bauer, O Bouhali, et al. "An overview of recent developments in FLUKA PET tools." In: *Physica Medica* 54 (2018), pp. 189–199.

[190] *GATE Monte Carlo software documentation*. https://opengate.readthedocs.io/en/latest/index.html. Accessed: 2020-04-19.

[191] J Smyrski, D Alfs, T Bednarski, et al. "Measurement of gamma quantum interaction point in plastic scintillator with WLS strips." In: *Nuclear Instruments and Methods in Physics Research Section A: Accelerators, Spectrometers, Detectors and Associated Equipment* 851 (2017), pp. 39–42.

[192] L Grevillot, D Bertrand, F Dessy, et al. "A Monte Carlo pencil beam scanning model for proton treatment plan simulation using GATE/GEANT4." In: *Physics in Medicine & Biology* 56.16 (2011), p. 5203.

[193] Jan Gajewski, Magdalena Garbacz, Chih-Wei Chang, Katarzyna Czerska, Marco Durante, Nils Krah, Katarzyna Krzempek, Renata Kopec, Liyong Lin, Natalia Mojzeszek, et al. "Commissioning of GPU-accelerated Monte Carlo code Fred for clinical applications in proton therapy." In: *Frontiers in Physics (Web)* 8 (2021), p. 567300.

[194] Richard Q Twiss and NH Frank. "Orbital stability in a proton synchrotron." In: *Review of Scientific Instruments* 20.1 (1949), pp. 1–17.

[195] *CASToR software documentation*. http://castor-project.org/documentation_v2. Accessed: 2019-11-01.

[196] SR Meikle and RD Badawi. "Quantitative techniques in PET." In: *Positron Emission Tomography*. Springer, 2005, pp. 93–126.

[197] D Wright and S Incerti. "A short guide to choosing physics lists." In: *Geant4 Tutorial at Jefferson Lab, SLAC* (2012).

[198] *GATE Phase Space actor documentation*. https://opengate.readthedocs.io/en/latest/tools_to_interact_with_the_simulation_actors.html#phase-space-actor. Accessed: 2020-04-19.

[199] A Gaitanis, G Kontaxakis, G Spyrou, et al. "PET image reconstruction: A stopping rule for the MLEM algorithm based on properties of the updating coefficients." In: *Computerized Medical Imaging and Graphics* 34.2 (2010), pp. 131–141.

[200] Harald Paganetti. "Range uncertainties in proton therapy and the role of Monte Carlo simulations." In: *Physics in Medicine & Biology* 57.11 (2012), R99.

[201] H Jiang, J Seco, and H Paganetti. "Effects of Hounsfield number conversion on CT based proton Monte Carlo dose calculations." In: *Medical physics* 34.4 (2007), pp. 1439–1449.

[202] *VV software*. https://www.creatis.insa-lyon.fr/rio/vv. Accessed: 2020-05-28.

[203] A Todd-Pokropek, TD Cradduck, and Frank Deconinck. "A file format for the exchange of nuclear medicine image data: a specification of Interfile version 3.3." In: *Nuclear medicine communications* 13.9 (1992), pp. 673–699.

[204] *PLGrid - Polish Grid Infrastructure*. http://www.plgrid.pl/. Accessed: 2020-06-15.

[205] Joseph Yossi Gil and Ron Kimmel. "Efficient dilation, erosion, opening, and closing algorithms." In: *IEEE Transactions on Pattern Analysis and Machine Intelligence* 24.12 (2002), pp. 1606–1617.

[206] Falk Pönisch, Katia Parodi, Bernhard G Hasch, and Wolfgang Enghardt. "The modelling of positron emitter production and PET imaging during carbon ion therapy." In: *Physics in Medicine & Biology* 49.23 (2004), p. 5217.